TROPICAL CYCLONES IN THE SOUTH-WEST INDIAN OCEAN: INTENSITY CHANGES, OCEANIC INTERACTION AND IMPACTS

A. F. Mavume

Department of Oceanography

Thesis submitted in fulfilment of the requirements for the degree of Doctor of Philosophy in the Faculty of Sciences University of Cape Town

In cooperation with Earth Sciences Centre, Oceanography, Göteborg University, Sweden

September 2008

TROPICAL CYCLONES IN THE SOUTH-WEST INDIAN OCEAN: INTENSITY CHANGES, OCEANIC INTERACTION AND IMPACTS

A. F. Mavume

BSc (Math./Phys.), BSc Hons (Phys./Meteo.), MSc (Phys. Ocean.)

Department of Oceanography

Thesis submitted in fulfilment of the requirements for the degree of Doctor of Philosophy in the Faculty of Sciences
University of Cape Town

In cooperation with Earth Sciences Centre, Oceanography, Göteborg University, Sweden

September 2008

Declaration

The work presented in this thesis is, to the best of my knowledge and belief, original except as acknowledged in the text. I hereby declare that I have not submitted this material either in whole or in part for a degree at this or any other institution.

_____
Alberto Francisco Mavume

Acknowledgments

This study has been supported by the Swedish International Development Cooperation Agency (Sida) as part of a project within the bilateral agreement between Sida/SAREC and the Eduardo Mondlane University, Maputo, Mozambique. Support was given for PhD studies on a sandwich basis, presuming halftime work at the UEM, Maputo and halftime abroad, in Cape Town and Gothenburg.

Special thanks to Prof. Francisco Vieira (former Dean), Prof. Amália Uamusse, Dean of the Faculty of Sciences at UEM and Prof. Lars Hernroth, PI's and Almeida Guissamulo, Coordinator, of the Sida/SAREC program: The Development of Biological and Oceanographical Research Capacity and the Implementation of the Master Course in Aquatic Biology and Coastal Ecosystems**,** from which my current support for PhD studies comes.

I would particularly like to acknowledge my sincere appreciation for continuous help given by my supervisors, Dr. Mathieu Rouault, Prof. Johann Lutjeharms and Prof. Geoff Brundrit, Department of Oceanography, University of Cape Town and Prof Lars Rydberg, Department of Oceanography, University of Gothenburg. Their enthusiasm and guidance has been invaluable throughout.

At the University of Cape Town a number of people contributed to my understanding of different topics within Physical Oceanography. Particular thanks go to Dr. Pierrick Penven for his lectures on ocean modelling and to Dr. Jean-Luc Mélice for insight into and application of Wavelet analysis. Also thanks to several people at the Department of Oceanography in Gothenburg, for help with computing facilities and modelling. Ms Agneta Malm is acknowledged for attractive drawings.

Thanks to Prof. Geoff Brundit, Johannes Guddal and the IODE (UNESCO/IOC International Oceanographic Data and Information Exchange Committee) and JCOMM (Joint WMO/IOC Commission for Oceanography and Marine Meteorology) for financial support to attend the Storm Surge Modelling workshops held in Kuantan, Malaysia and Östende, Belgium. Another thanks to IFS (International Foundation for Science) for its financial support to visit Malaysia and present my research work on Tropical Cyclones at the International Science Congress held in Kuala Lumpur, Malaysia. Thanks to the Western Indian Ocean Marine Science Association (WIOMSA), the Intergovernmental Oceanographic Commission (IOC) of UNESCO and the Western Indian Ocean Satellite Application Project (WIOSAP) for their financial support to attend a Satellite Altimetry course held in Malindi, Kenya and for selecting me to be part of the regional network of satellite altimetry experts in WIO. Thanks to Prof. António Mubango (UEM), Prof. Simpson (Bangor, UK) and Prof. Bowers (Bangor, UK) for their earlier invaluable ideas and advice in pursuing a PhD on the subject of Tropical Cyclones and also to the British Council support recommend by Prof Simpson for field measurement programme at Incomáti as part of the Shared River Initiative Project.

I won't forget my colleagues Atanásio Manhique, my room mate in Cape Town, Verónica Dove, Issufo Halo and Michael Mehari, for their encouragement and help during troublesome moments of my visits to Cape Town. Also many thanks to Ms. Rachmat Harris and Ms. Helen King for providing a very kind support on student issues. Jeremy Main and Christo Whittle also aknowledged for their technical assistance

Cyclone track data used in this study were obtained from the Regional Specialized Meteorological Centre of La Réunion (LR-RMSC, 2003) and the Joint Typhoon Warning Center (JTWC, 2006) websites. The QuikSCAT mean fields are produced by NASA Scatterometer Projects and obtained from CERSAT (IFREMER, 2005). The altimeter products were produced by Ssalto/Duacs and

distributed by Aviso with support from Cnes. The TMI data are produced by Remote Sensing Systems (www.remss.com) and sponsored by the NASA Earth Science REASoN DISCOVER Project. The ACSEX data were obtained from the Royal Netherlands Institute for Research (NIOZ, 2003) server. The ACSEX project was funded by the Netherlands Organization for Scientific Research (NWO) and the chief scientist was Dr. Herman Ridderinkhof. Argo data were collected and made freely available by the International Argo Project and the national programs that contribute to it (http://www.argo.ucsd.edu, http://argo.jcommops.org). Argo is a pilot program of the Global Ocean Observing System.

Last but certainly not least, I would like to thank my family for their ceaseless encouragement during the last six years, and to Angélica Monjane and Célia Mandraça for taking care of our daughters Denise and Daisy. I deeply appreciate the support I had from them.

Table of Contents

List of Figures

Chapter 7

Chapter 8

List of Tables

Acronyms

AAIW	Antarctic Intermediate Water
ADEOS	Advanced Earth Observing Satellite
AOML	Atlantic Oceanographic and Meteorological Laboratory
ASW	Arabian Sea Waters
AVISO	Archiving, Validation, and Interpretation of Satellite Oceanographic data
AVHRR	Advanced Very High Resolution Radiometer
ATCF	Automated Tropical Cyclone Forecasting System
BODC	Bristish Oceanographic Data Center
CERSAT	Centre ERS d'Archivage et Traitement
CDW	Circumpolar Deep Water
CLS	Collecte, Localisation, Satellites
CNES	Centre National d'etudes Spaciales
CORIOLIS	Argo Global data Assembly Centre
DMSP	Defense Meteorological Satellite Program
Duacs	Data Unification and Altimeter Combination System
DORIS	Doppler Orbitography and Radio-positioning Integrated by Satellite
EACC	East African Coastal Current
ECC	Equatorial Countercurrent
ENSO	El Nino Southern Oscillation
ESA	European Space Agency
ERS	European Remote Sensing

FNMOC	Fleet Numerical Meteorological center and Oceanographic center
GEOS-3	Geodynamics Experimental Ocean Satellite-3
GPSDR	global position systems demonstration receiver
ICW	Indian Central Water
IFREMER	French Research Institute for Exploitation of the Sea
IDW	Indian Deep Water
INCOIS	Indian National Centre for Ocean Information Services
ITCZ	Intertropical Convergence Zone
ITF	Indonesian Through-Flow
JPL	Joint Propulsion Laboratory
JTWC	Joint Typhoon Warning Center
LR-RSMC	La–Reunion Regional Specialized Meteorological Center
LRA	Laser Retroflector Array
MLD	Mixed Layer Depth
MSW	Maximum Sustained Winds
MSLP	Minimum Sea Level Pressure
NASA	National Aeronautics and Space Admnistration
NEC	North Equatorial Current
NEM	North-East monsoon
NEMC	North East Madagascar Current
NCDC	National Climate Data Center
NCEP	National Center for Atmospheric Research
NODC	National Oceanographic Data Center

NOAA National Oceanic and Atmospheric Admnistration (U.S.A)

NIOZ Netherlands Institut Voor Onderzoek der Zee

NetCDF Network Common Data Format

PO.DAAC Physical Oceanography Distributed Active Archive Center

PRF Pulse Repetition Frequency

QBO Quasi-Biennial zonal wind Oscillation

RA Radar Altimeter

RSW Red Sea Waters

SEASAT SEAfaring SATellite

SEC South Equatorial Current

SEMC South East Madagascar Current

SICC South Indian Ocean Counter Current

SWIO South-West Indian Ocean

SWM South-West Monsoon

SST Sea Surface Temperature

SSH Sea Surface Height

Ssalto Segment Sol multimissions d'ALTimétrie d'Orbitographie

SSW Subtropical Subsurface Water

TMI Tropical Rainafall Measuring Mission (TRMM) Microwave Imager

TRMM Tropical Rainafall Measuring Mission

TRSR Turbo Rogue Space Receiver

WOA05 World Ocean Atlas 2005

WDC World Data Center

List of symbols

Roman symbols

C_d	Drag coefficient
C_e, C_t	Dalton and Stanton numbers
C_p	Specific heat for water
h_{mo}	Initial mixed layer depth
L_t	Latent heat of vaporization
Q_{NET}	Net flux of heat through the sea surface
Q_{SW}, Q_{LW}	Short and long-wave heat flux
Q_{LH}, Q_{SH}	Latent and sensible heat flux
T_S, T_a	Air and water temperature
T_{m+}	Temperature at the bottom of the mixed layer
u_*	Friction velocity
W	Wind-speed
w_e	Vertical entrainment velocity
E_w	Energy flux
B	Buoyancy flux
h_{MO}	Monin-Obukhov depth
γ	Thermocline temperature gradient

Greek symbols

α	Thermal expansion
ρ_a	Air density
ρ_a	Air density
τ_x, τ_y	Wind-stresses in the x and y directions
$\gamma = \partial T / \partial z$	Vertical temperature gradient

Abstract

This study investigates the climatology, intensification and ocean atmosphere interaction in relation to the passage of tropical cyclones (TCs) in the South-West Indian Ocean (SWIO). A Climatology of TCs in the SWIO including landfall in the area of Mozambique and Madagascar was developed for the 1952-2007 and 1980-2007 periods.

Eleven cyclones per year (with Maximum Sustained Winds; MSW>17 ms^{-1}) are formed in the SWIO within the cyclone season (November-April). This is approximately 14 % of the global TC total. Shallow mixed layer depths in the SWIO cause higher sea surface temperatures (SST; typically 28-29˚C) above the 26.5˚C threshold for TC genesis. The most active months are January and February, when the Inter-Tropical Convergence Zone (ITCZ) reaches its southernmost position.

Data from 1980-2007 shows a considerable increase in the numbers of intense TCs (category 3-5; MSW>50 ms^{-1}) during the last 14-year period (1994-2007) compared to the earlier 14-year period (1980-1993); from 36 to 56, and a small decrease in tropical storms (18<MSW<33 ms^{-1}). The increase in intense TCs coincides with an increase in SST of about 0.2˚C in the SWIO and 0.4˚C in the Mozambique Channel.

Most of TCs make landfall in the months of January, February and March. Annual landfall frequency analysis shows an average of 2.5 TCs per year while about 77% of the SWIO TCs remained over the open ocean waters. The analysis shows great geographical variability of cyclone tracks, and consequently the coastlines are considerably affected by the TCs. The northeast coast of Madagascar and the central coast of Mozambique are the most exposed segments in these countries.

Selected TCs under this investigation experienced intensification before landfall. Movement of warm eddies in the Mozambique Channel and surrounding waters and associated sea surface cooling are examined and analysed using satellite

observations for with 15 tropical cyclones between November 1994 and April 2007. Four cases are described in detail. When TCs moved over the warm eddies they rapidly intensified. Sea surface cooling was observed during the passage of these cyclones. Persistence of cooling following the passage of TCs varies from a few days to weeks. Cooling in most cases is correlated with TC strength and maximum cooling in the track of the cyclone reaches 7°C.

Results for the nearest Argo profiling floats were examined and those from TC Japhet were used to model the deepening of the mixed layer along the cyclone track. TC Japhet caused a thermocline deepening from 30 – 65 m, affected by an upwelling velocity of 15 m/day and an entrainment velocity (downward) of 22 m/day (evaluated over a 5 day period). The model used showed total cooling in the surface waters up to 5 kWm^{-2}. The upper ocean conditions prior and after the passage of TCs was also investigated in terms of Tropical Cyclone Heat Potential (TCHP). Results for TC Japhet indicated that TCHP values prior to the storm reached levels well above 50-80 kJ cm^{-2} and the average had decreased by about 10 kJ cm^{-2} after the storm.

Key words *Tropical Cyclones, climatology, intensification, warm eddies, Sea surface cooling, mixed layer model, South West Indian Ocean, Mozambique Channel*

Chapter 1: Introduction

Hazard to the people

Tropical cyclones (TC) are a crucial component of the global equatorial weather systems. On landfall, they frequently cause severe damage in adjacent countries. In the South-West Indian Ocean (SWIO) and the Mozambique Channel they are a major hazard to the central and northern coasts of Mozambique and Madagascar, where landfall with storm winds, torrential rains, and coastal and inland floods takes place on an almost annual basis. Storm surges with a height of up to 5 m may occur along the coast. Thus, they are an issue of great social and economic concern.

Mozambique and Madagascar have coastlines of 2700 and 4800 km, respectively (Figure 1.1). More than 60% of their populations live in coastal areas, which in many places consist of lowlands with sandy beaches, estuaries and mangroves. Survival and everyday life in these areas depend to a large extent on local resources, such as farming and fishing, while infrastructure is weak or even non-existent. In summary, the conditions mean a high vulnerability of both people and landscape to tropical cyclones. Accurate predictions and forecasts of tracks and intensities of tropical cyclones are therefore highly important issues. Knowledge on cyclone behaviour, including areas of landfall and possible future changes are needed to undertake countermeasures such as evacuation of densely populated areas under threat, but also in the long run, for proper land use, for hazard mitigation, for insurance reasons, and in order to build up efficient warning systems.

Since the year 2000 those two countries have been hit by six intense tropical cyclones [in 2000 by Eline and Hudah, in 2003 by Japhet, in 2004 by Gafilo and in 2007 by Favio and Indlala], all of which stand as vivid examples of the large social and economic consequences they bring about: In Mozambique, for

example, floods in the wake of TC Eline alone caused approximately 2 million people to be displaced or otherwise severely affected. About 600 people died. The estimated cost of the Mozambique floods in the year 2000 stood at more than US$167 million in terms of emergency aid funds and in immediate activities in order to rehabilitate the infrastructure and relocate displaced persons (IPCC, 2001).

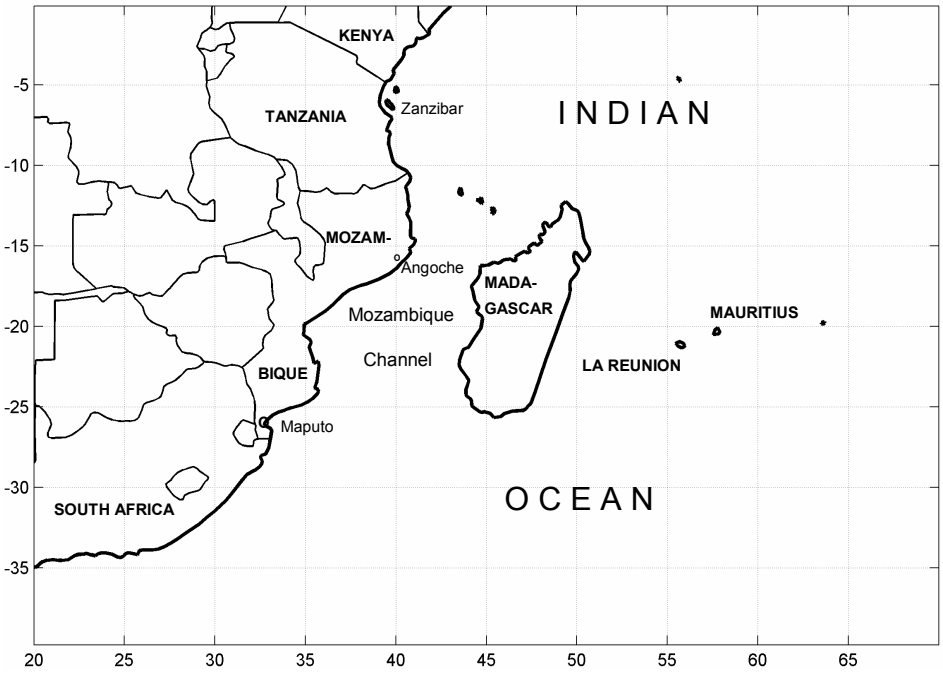

Figure 1.1: Map showing part of the Africa mainland, the Mozambique Channel region and Madagascar, including names of the locations used in the text.

Frequency of tropical cyclones in the area

Most cyclones in the South-West Indian Ocean are formed between 8-15°S, in the area east of 50°E (Ecormier, 1992), and during the period when the Inter-Tropical Convergence Zone (ITCZ) is in its southernmost position, i.e. in between December - March. The total number is about 10 per year. Formation in the Mozambique Channel, which may happen further south (15-20°S) is rare. Such TCs are characterized by rapid development, small size and short life span (Le Borne, 1987). A few cyclones (2-3 per year) enter the Channel across Madagascar, and still fewer, less than one per year, make landfall on the eastern

and western side of the Channel (Tyson and Preston-Whyte, 2000). Some are deflected west and south above Madagascar where they loose energy but the vast majority also decay over water.

Tropical cyclones are formed in several areas of the global ocean, but only over warm tropical waters (Figure 1.2). The South-West Indian Ocean experiences about 15 % of the global total. Inter-annual variations in cyclone frequency are common; for example, there are far fewer TCs in El Niño years (Vitart et al., 2003), one reason for which is believed to be that the westerly wind shear is stronger than normal (Aiyyer and Thorncroft, 2005). In contrast, TCs are more frequent during La Niña years, when westerly wind shear is weaker.

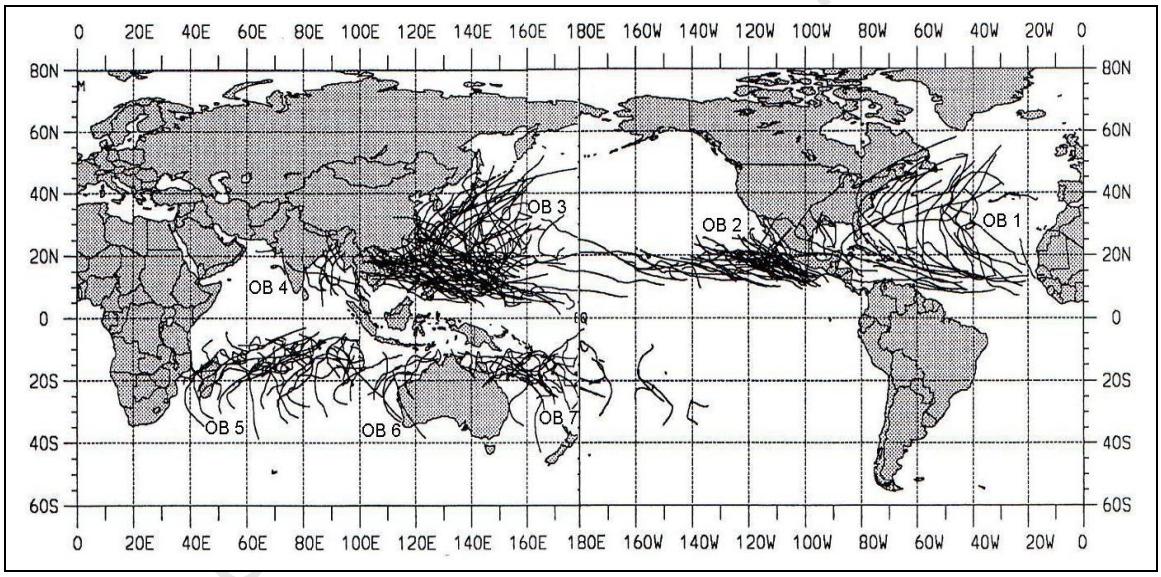

Figure 1.2: Principal tropical cyclone tracks (i.e., maximum sustained winds exceeding 17ms^{-1} for the 3-year period 1988-1990 (adapted from Fink and Speith, 1998). Highlighted are the seven basins where tropical cyclones occur on a regular basis (http://www.aoml.noaa.gov/phod/cyclone/data/seven.html). OB 1: Atlantic basin, including the North Atlantic Ocean, the Gulf of Mexico, and the Caribbean Sea; OB 2: Northeast Pacific basin from Mexico to about the 140 degrees West Longitude; OB 3: Northwest Pacific basin from 180 degrees longitude to Asia including the South China Sea; OB 4: North Indian basin, including the Bay of Bengal and the Arabian Sea; OB 5: South Indian Ocean basin, from Africa to about 100°E; OB 6: Southeast Indian/Australian basin (100°E to 142°E) and OB: Australian/Southwest Pacific basin (142°E to 120°W).

Atmosphere-ocean interaction. *Intensification and sea surface cooling.*

Tropical cyclones, as aforementioned, are formed over a warm ocean surface at temperatures above 27°C, and are driven by latent and (to a lesser extent) sensible heat fluxes from the ocean. The very strong winds related to the cyclone create large-scale mixing (with upward entrainment of underlying waters) and therefore, a rapid cooling of the sea surface (Greatbatch, 1985). Moreover, in the wake of the cyclone, intensive upwelling due to a divergent wind field adds substantially to decrease SSTs (Figure 1.3). In the vicinity of the cyclone track, SST may decrease by as much as 8°C (Emanuel, 1999). In this context, loss of heat due to extreme latent heat flux, has only a minor effect on the cooling itself (10-20%; i.e. Price, 1981, Shay et al., 2000).

Sea surface cooling, in turn, will decrease the latent and sensible heat fluxes. Thus, the pre-cyclone conditions within the surface waters (particularly the depth of the warm surface layer, i.e. the mixed layer depth or thermo-cline depth) play a major role in controlling the intensity and development of the cyclone. A cyclone may intensify or decline, depending on hydrographic features underneath the sea surface.

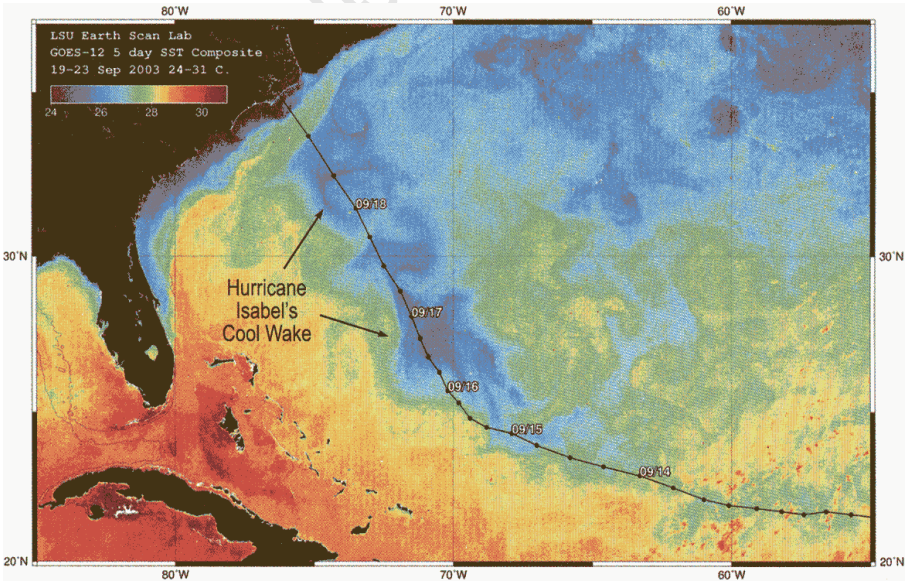

Figure 1.3: Sea surface temperature composite images revealing the cool wake left by Hurricane Isabel on 23 September 2003 (From Lousiana State University Earth Scan Laboratory; more information available at http://www.esl.lsu.sdu).

It was acknowledged at an early stage that the mixed layer depth (MLD) should have a major impact on the genesis (and intensity) of cyclones. A deeper mixed layer might withstand longer. A warm, buoyant and deep mixed layer is the best premise for a cyclone to be sustained or intensified. Leipper and Volgenau (1972) introduced the term Hurricane Heat Potential (HHP) in order to predict the potential for TC formation. However the concept “Cyclone Heat Potential”/or “Tropical Cyclone Heat Potential” hereafter CHP/or TCHP is alternatively used throughout the thesis as is the more commonly used parameter”. Theory for calculation of Cyclone Heat Potential is given in Chapter 6 (Section 6.2).

Satellite observations have improved gradually over the last 30 years, and recent data (from 1992/93 to 1998/99 and onwards) feature better accuracy and resolution in time and space for detailed studies of cyclones. Heavy rainfall may have some impact on SSTs in satellite measurements. Rain from high levels is low in temperature, and may lower the observed SSTs particularly because freshwater is likely to stay on top. A high precipitation also adds to the stability of the surface water. Another impact is that entrainment and upwelling after the passage of a TC contribute to bring nutrients to the surface and thereby to enhance primary production. This has been frequently shown in satellite chlorophyll images.

Earlier interest in cyclones and landfall in the Madagascar and Mozambique region has been very limited. One reason is the lack of ground truth data, with fewer weather stations and buoy data in comparison with all other cyclone areas, and also a lack of local expertise. This is where satellite data can be useful. In addition lack of historical TC data over the South-West Indian Ocean has hampered research on the TCs over the basin. However, the La Reunion – Regional Specialized Meteorological Centre (LR-RSMC) have collected cyclone data since 1950. Since 1993 La Reunion Island has been designated as the WMO Regional Specialized Meteorological Centre/Tropical Cyclones (LR-RSMC/

TC) for the South-West Indian Ocean, extending from African coast out to 90°E, including the Mozambique Channel (WMO, 2006).

Mozambique Channel hydrography. Warm and cold eddies

Mozambique Channel and the region around Madagascar hosts a complex pattern of mesoscale eddies (Figure 1.4). A multidisciplinary cruise, the Agulhas Current Sources Experiment (ACSEX, 2000-2001), was carried out in the Mozambique Channel by researchers from Institute for Marine and Atmospheric Research Utrecht (IMAU), Royal Netherlands Institute for Sea Research (Royal NIOZ), Royal Netherlands Meteorological Institute (KNMI) and the University of Cape Town and it was the first one in 25 years. During ACSEX, two cruises concentrated on the upstream developments in the Mozambique Channel and around Madagascar (De Ruijter et al., 2006). The first cruise in 2000 (ACSEX-I) with focus on current measurements and hydrography have shown that the Channel is dominated by a train of warm, anti-cyclonic eddies progressing pole-ward along the western side (Ridderinkhof and De Ruijter, 2003). East of Madagascar the circulation is dominated by the clear split of the South Equatorial Current into a northern branch and a narrow, warm and intense southern branch. The latter reaches the eastern coast of Madagascar at about 18°S where it bifurcates in a northern and a southern branch. However little is known about the termination the East of Madagascar Current and the data gathered during ACSEX-II in 2001 give no clear evidence of a retroflection of the East of Madagascar Current (de Ruijter et al., 2006). Mesoscale eddies are seen also in this area.

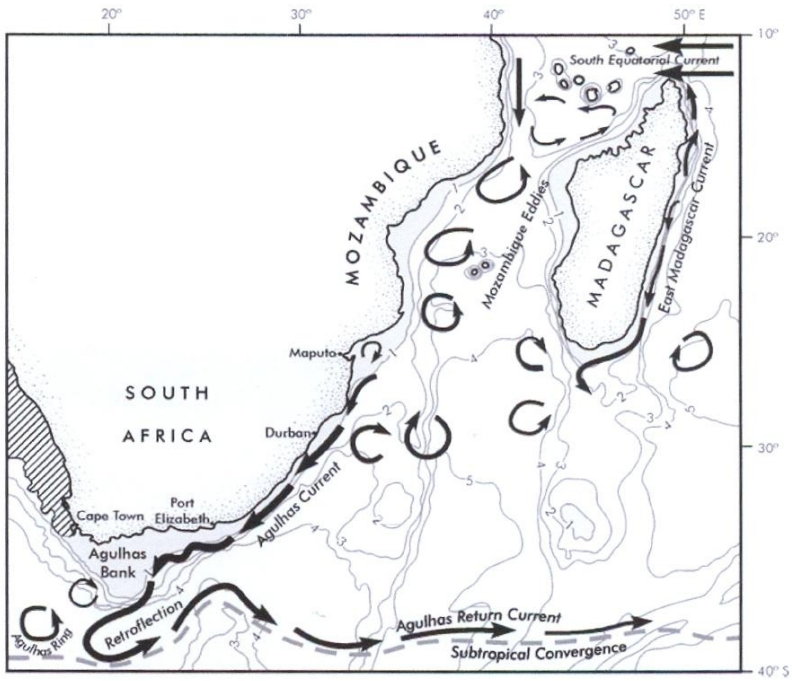

Figure 1.4: The main current system indicating areas of eddies and eddy formation (from Lutjeharms, 2006a).

As already indicated, warm and deep reaching eddies may have a role in intensification of TCs. The ACSEX-I cruise happened to coincide with TC Hudah in early April 2000, during its passage across the SWIO and MC.

In the light of the aforementioned problems related to landfall of tropical cyclones and with the help of a rapidly growing satellite based data set on cyclone tracks and on adjacent ocean and atmospheric data, I have in this thesis established a "climatology atlas" for tropical cyclones in the SWIO (0-40°S, 20-100°E). The atlas (which contains all cyclones in the area back to 1951/52-2007, but with a focus on the recent 28 years, from 1979/80) is used for selection of some recent cyclones for which I study particular features such as rapid intensification and sea surface cooling. In order to place these results into right perspective, it would be essential to indicate what has been known about the climatology of this region in one hand and the tropical cyclones on the other hand, as described in the next two chapters.

Chapter 2 deals with the hydrography and ocean currents of the SWIO; Chapter 3 contains a literature review and common background to cyclone climatology (statistics), sea surface cooling and intensification of tropical cyclones. Chapter 4 identifies the particular research questions dealt with in this thesis. The data sources comprise a large variety of satellite products on SSTs, winds, SSHA, rainfall etc. These sources, including the methodology for use within this thesis are described in Chapter 5. Chapter 6 gives theory for calculations of mixed layer depths and cyclone heat potential. Chapter 7-9 are devoted to results and discussions, Chapter 7 on tropical cyclone climatology, Chapter 8 on the specific features of some cyclones with landfall in Mozambique, and Chapter 9 accounts for calculations of mixing and upwelling in the track of a cyclone. This also includes development of mixed layer depths and upper ocean heat content (i.e. TCHP). Conclusions and recommendations, finally, are presented in Chapter 10.

Chapter 2: South-West Indian Ocean Climatology

2.1 Introduction

Despite its small size in relation to the other oceans, the Indian Ocean is considered by many investigators to be the most complex. It is also less explored and there is a lack of both oceanographic and meteorological data particularly in its southern parts. The northern parts, on the other hand, seem to have received special attention because of the changing wind and surface current patterns associated with the monsoon climate; the South-West Monsoon (SWM) blowing from June to September and the North-East Monsoon (NEM) blowing from November to February. A comprehensive review article by Schott and McCreary (2001) describes the Indian Ocean monsoon climate and its oceanic response. This summary emphasizes the role of the Inter-Tropical Convergence Zone, the movement of which is of particular interest for the formation of tropical cyclones.

2.2 Monsoon climate and the ITCZ

The monsoon climate occurs as part of a larger phenomenon with development of low and high pressure cells over the Asian continent. It is dominated by the Intertropical Convergence Zone (ITCZ), the motion of which is indicated in Figure 2.1. The ITCZ separates the wind circulation between the northern and southern hemispheres (Sikka and Sulochana, 1980). Although a number of definitions of the ITCZ exist, it is climatologically defined as a narrow transition belt, where the global northeast and southeast trades converge, inducing upward motion and rainfall (Wallace and Hobbs, 1977). Strong upward motion and heavy rainfall (see Figure 2.2) is the result of intense heating by sun radiation. The heating also drives a meridional atmospheric circulation known as the Hadley Cell. This cell consists of rising air at the Equator and

descending air at about 30°N and S. The ITCZ (Figure 2.1) has by far its largest range in the Indian Ocean, reaching some 10-15°S in January and 25-30°N in July. The monsoon climate, with northerly winds from December-March and southerly winds from May-September develops in between its end points (Figure 2.1). With few exceptions, tropical cyclones of the Indian Ocean have their origin within the ITCZ, whereas the typical TC season over the southern hemisphere ocean is between December-March and over the northern hemisphere ocean in May-June and September-October. From July-August, the ITCZ is over land and cyclones are rare.

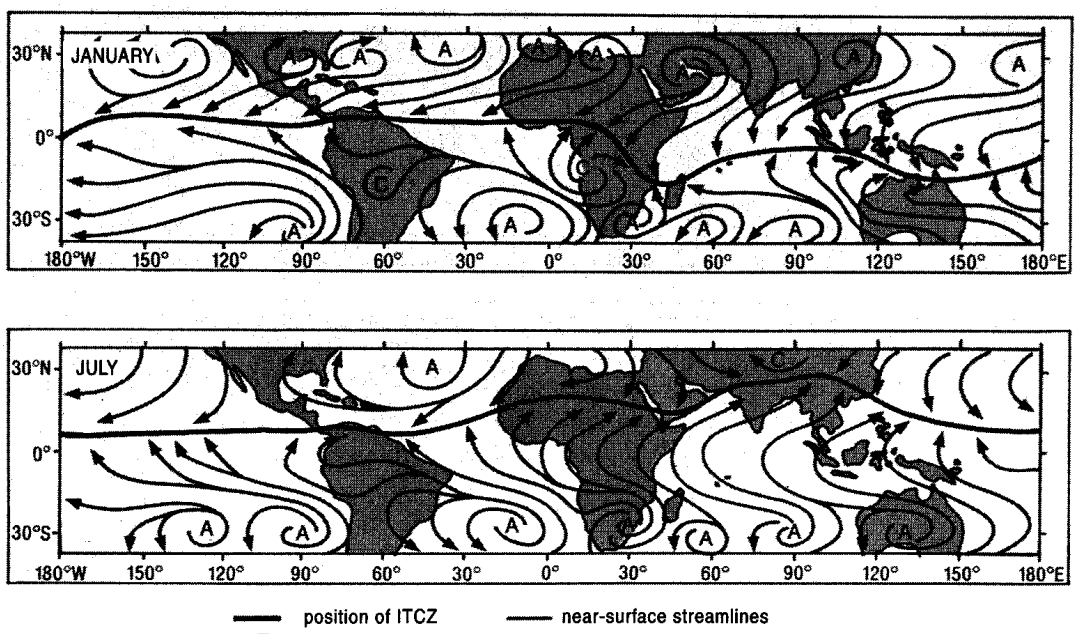

Figure *2.1: Positions of the Intertropical Convergence Zone (ITCZ) including schematic streamlines of near surface flow for the months of January and July. "A" denotes anticyclonic centres, "C" denotes cyclonic centres (from Tyson and Preston-Whyte, 2000, modified after Hastenrath, 1985).*

The extensive meridional shift of the Indian Ocean ITCZ, in comparison with other oceans, stems from the large size of the Asian continent and the correspondingly larger differences between winter and summer temperatures over the continent. In the northern summer (May–September), the ITCZ affects the Indian subcontinent and Southeast Asia, in the southern summer (December–March) it reaches as far as Mozambique and Madagascar. During

the northern summer, the continent of Asia heats up more than the surrounding ocean, causing large differences between land and temperature sea surface temperatures (Asnani, 1993). Heated air over land creates an extensive area of low pressure over north–central Asia and smaller one over India. This low pressure cell along with the Coriolis force, cause intense onshore wind bringing the moisture laden maritime air from the Indian Ocean onto land. As the air streams across land, mountain ridges like the Himalayas and the Indonesian highlands force the air to rise, thus creating abundant rainfall. River runoff into the Bay of Bengal and rainfall over the NE Indian Ocean during the SW Monsoon (Figure 2.2) creates a large pool of fresher surface water in that part of the ocean (see further below).

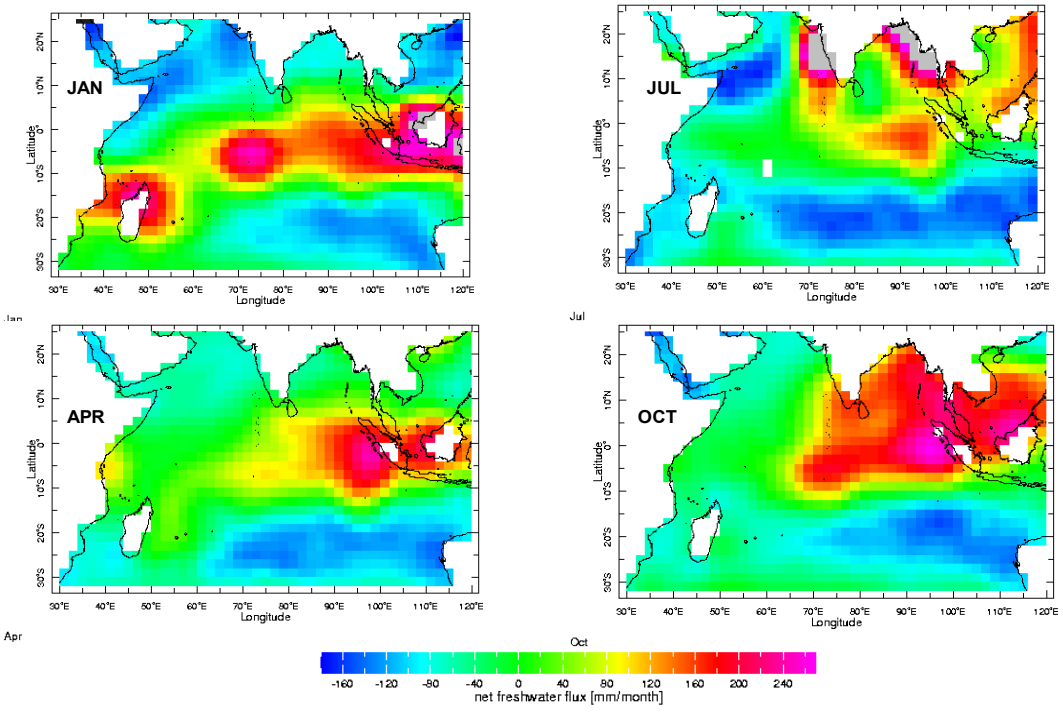

Figure 2.2: Seasonal net freshwater flux, i.e. Precipitation–Evaporation (P-E; COADS climatology (1950–79); from Oberhuber, 1988). The freshwater flux mirrors the movement of the ITCZ, in which precipitation is always dominating. Two areas feature excess evaporation; the Arabian Sea and the South-East Indian Ocean with its almost stationary high pressure cell, seen in Figure 2.1.

From December to March, the airflows reverse, as indicated in Figure 2.1. This reverse coincides with the southernmost position of the ITCZ, during which dry, cold air from the continent blows offshore creating the dry monsoon season. The NE Monsoon exhibits cyclonic curvature into centres of low pressure and is associated with moist, unstable air and light rainfall in East Africa south to northern Mozambique and Madagascar. However, the monsoons are mainly tropical phenomena, which have little direct effect on the weather or climate of southern Africa. What is relevant for southern Africa is the involvement of Indian monsoon air in the ITCZ over Africa in the southern-hemisphere summer (Tyson and Preston-Whyte, 2000).

The climatological wind-field of the Indian Ocean is summarized in Figure 2.3 by Schott and Mc Crary (2001), indicating strong northerly winds over the Arabian Sea and (to a lesser extent) over the Bay of Bengal.

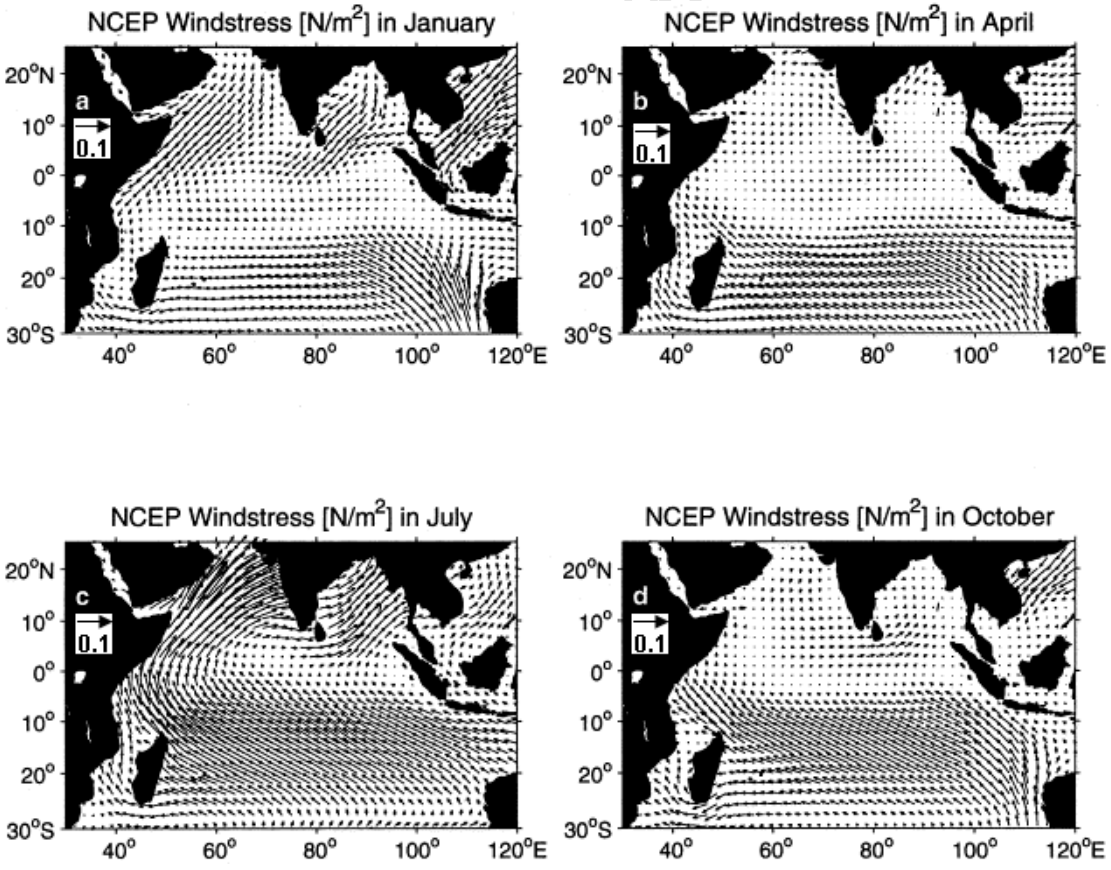

Figure 2.3: Monsoon wind stress fields from NCEP climatology for a) January; b) April; c) July; d) October (From Schott & McCreary, 2001).

In July, the winds are south-westerly over both basins, also with stronger winds over the Arabian Sea during this season in the form of a narrow atmospheric jet, known as the Findlater Jet (Findlater, 1971).

As noted by Schott & McCreary (2001) a unique wind forcing pattern occurs over the Indian Ocean, which is unlike the pattern in other equatorial oceans. It involves the occurrence of semi-annual eastward winds over the Equator, from April-June and from October-November (Figure 2.3). These winds generate an annual-mean zonal equatorial wind stress that is eastward. This may contribute to high surface temperatures along the Equator, in marked contrast to the situation in the other tropical oceans.

2.3 Indian Ocean Circulation

The surface currents in the northern Indian Ocean reverse with the monsoon winds (Figure 2.4a-b; Schott and McCreary, 2001). This has been well established from ship observations for a long time (Cutler & Swallow, 1984).

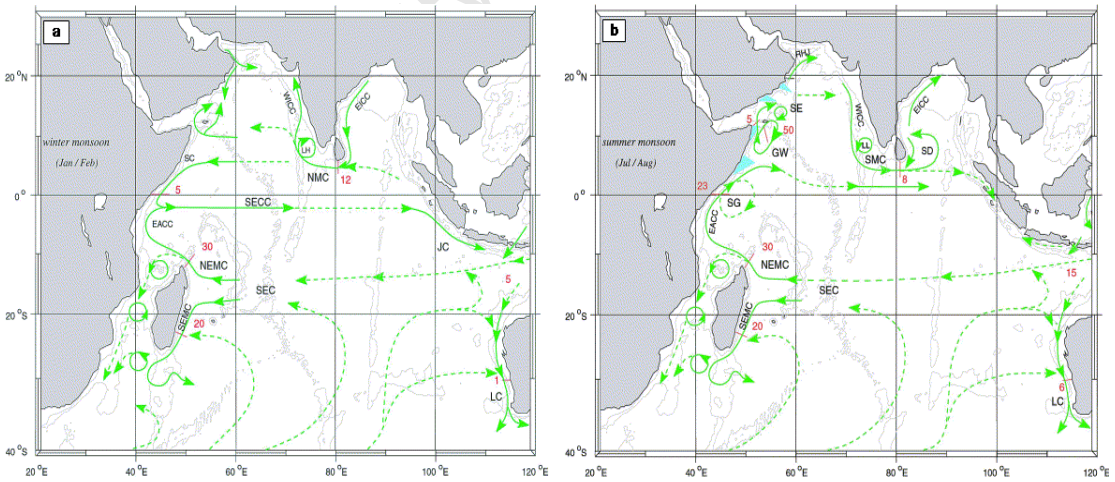

Figure 2.4: Surface currents in the Indian Ocean during (a) the peak North-East Monsoon (Jan/Feb), and (b) the peak South-West Monsoon (Jul/Aug); approximate volume fluxes are indicated in Sv (1 Sv = 10^6 m^3s^{-1}; from Schott and McCreary, 2001).

While the air masses over the northern Indian Ocean experiences strong variability, the conditions south thereof are much more stable. The South-East trade wind dominates with higher wind speed in the eastern part of the ocean and during the southern summer (Figure 2.3). In the Mozambique Channel, mean winds do not ever exceed 5 ms^{-1}.

The North Equatorial Current (NEC) develops from December–February when the NEM is fully established. It runs as a narrow current with a speed of about 0.3 ms^{-1} from Indonesia (Malacca Strait) to southern Sri Lanka (not well indicated in Figure 2.4a), where it increases to 0.5–0.8 ms^{-1} in the region between 60°E and 75°E (Tomczak and Godfrey, 1994; 2003). Schott & McCreary (2001) refer to this current as the North Monsoon Current (NMC) (Figure 2.4a). While the South Equatorial Current (SEC) occupies the region from 10–20°S with velocities rarely exceeding 0.3 ms^{-1}, but with a large transport (see below). Between these westward flows runs the (South) Equatorial Counter Current (SECC) with velocities of 0.5–0.8 ms^{-1} in the west but markedly weaker in the east (Schott and McCreary, 2001). The SECC receives its water from the Somali Current (SC; running south across the Equator) and the East African Coastal Current (EACC; running north up to between 3-4°S). In January, the SECC does not reach beyond 70°E, being opposed by a weak westward flow. As indicated below (Sect 2.3.1) the slightly higher saline and cooler water of the SECC might very well continue underneath a thin layer of relatively fresh water forced westward by excess buoyancy through the ITF (Andersson and Stigebrandt, 2005).

The transition from the NEM to the SWM is characterized by the intense Indian Equatorial Jet, first described by Wyrtki (1973a). During the SWM, the currents north of the Equator change direction totally (Figure 2.1b), and the South-West Monsoon Current (SWM), running east-ward, is developed. The southern Indian Ocean is dominated by the South Equatorial Current. The SEC however, does not change markedly with season, carrying some 50 Sv eastward in

between 10-20°S (Schott and McCreary, 2001; New et al., 2007). It divides into a NE and a SE Madagascar Current (NEMC; SEMC). The NEMC divides on the African East coast. Its northern branch, the EACC seems to be a stable current (20 Sv; Swallow et al., 1991), although it weakens northwards during the NEM and enters the SECC instead of crossing the Equator. The southern part of NEMC enters the northern Mozambique Channel, but seems to become unstable and propagate itself southwards through the channel in the form of warm eddies (see further below).

2.3.1 Upper ocean temperatures and salinities

The Indian Ocean sea surface salinity (Figure 2.5A) is seen to follow the distribution of seasonal precipitation minus evaporation (P-E; Figure 2.2). A remarkable salinity maximum near 30°S is directly related to the minimum P-E (Tomczak and Godfrey, 1994). Minimum salinities, on the other hand also depend on the Indonesian Through-Flow (ITF; Gordon et al., 2003; Andersson and Stigebrandt, 2005) and river runoff, as aforementioned. Lutjeharms (2006) has noted that there are three regions of high salinity water formation in the Northern Indian Ocean: the Arabian Sea, the Red Sea and the Persian Gulf. These high salinity waters penetrate far south into the Indian Ocean at depths down to about 1100 m, creating a dynamic overturning circulation.

The mean sea surface temperatures (Figure 2.5B) indicate high SST in the entire northern Indian Ocean, suggesting a continuation of the western Pacific warm water. Over most of the Equatorial region, annual mean temperatures are above 28°C. However, in the Somali Region, one finds SST down to below 20°C (Tomczak and Godfrey, 1994; 2003), as a result of upwelling during the SWM.

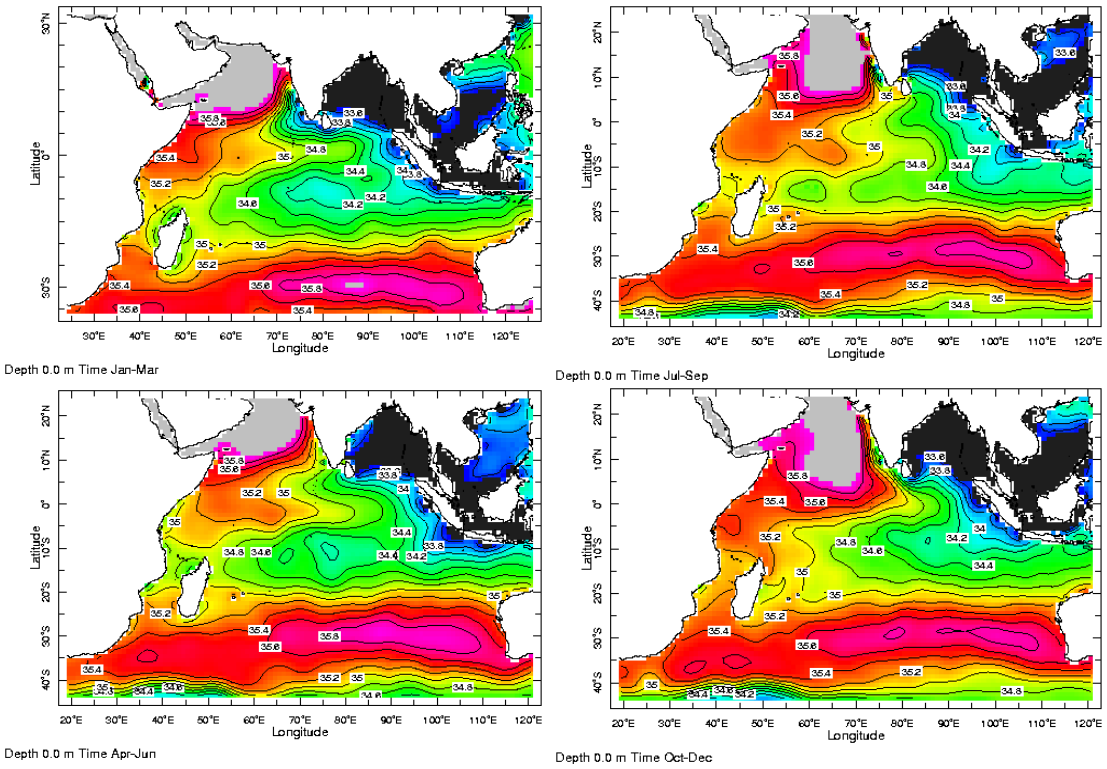

Figure 2.5A: Climatology sea surface salinity based on WOA05 (from interactive website: http://iridl.ldeo.columbia.edu/)

A remarkable feature of seasonal SST cycle in the *northern* Indian Ocean is that the SST maximum does not occur during summer but during the northern spring inter-monsoon period (April-May). Many SST values are more than 28°C everywhere north of the Equator also north of 10-15°S. However, as the southern monsoon develops, mixing and advection of upwelled water reduces summer SSTs to 25-27°C.

During all seasons the SSTs are higher within the Mozambique Channel than in the SWIO east of Madagascar. This difference is most pronounced during the peak cyclone season in the southern ocean (January to March). Also, the salinities are lowest during this period (in the whole of the SWIO). Low salinities (due to rainfall and a larger flux from the east) may contribute to a shallow mixed layer and therefore to higher SSTs, but concomitantly to a more buoyant mixed layer.

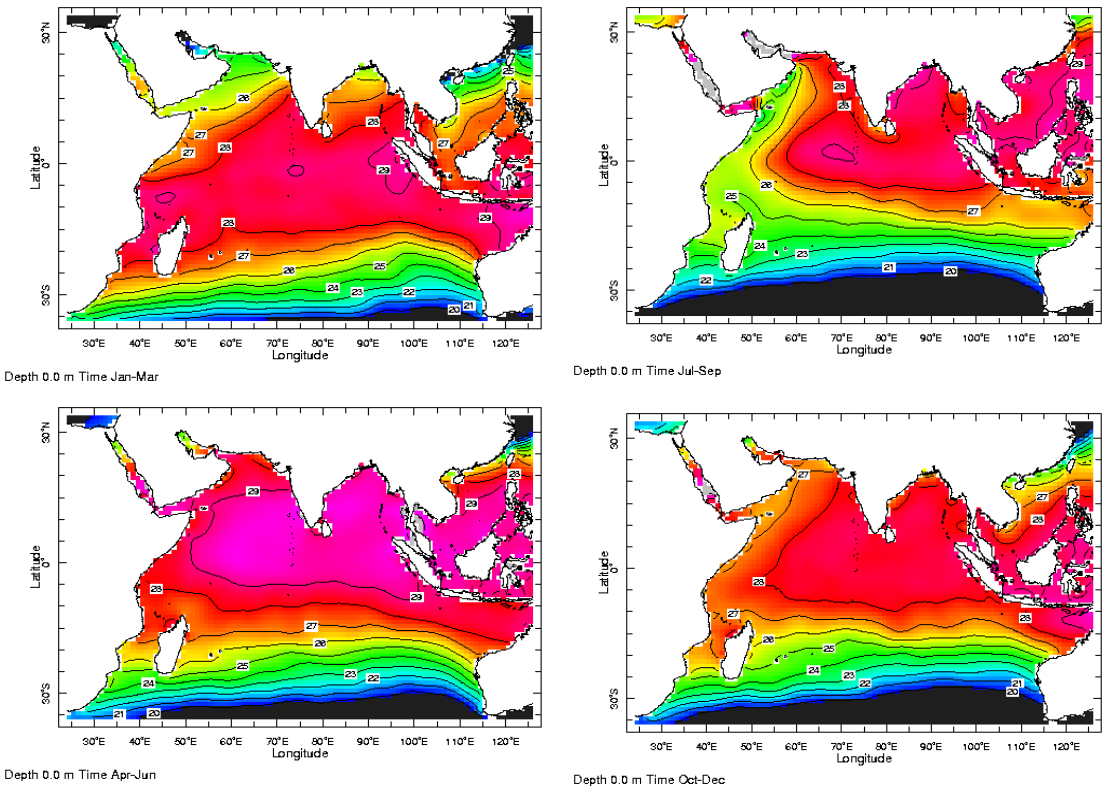

Figure 2.5B: Climatology sea surface temperature from WOA05.

2.4 Climatology of the South-West Indian Ocean

The South-West Indian Ocean (SWIO) includes the coastal and oceanic waters between 0ºS and 40ºS and extends from Africa mainland to 100º E. The bottom topography is rough (Figure 2.6) with large submarine ridges and several islands spread out over the area. Of particular interest is the Mascarene Ridge, rising to near the surface at 60ºE. The South Equatorial Current flows straight across the ridge between 10-20ºS, with several consequences as described below. Madagascar in turn, is a shelter for the Mozambique Channel in several ways (Penven et al., 2006).

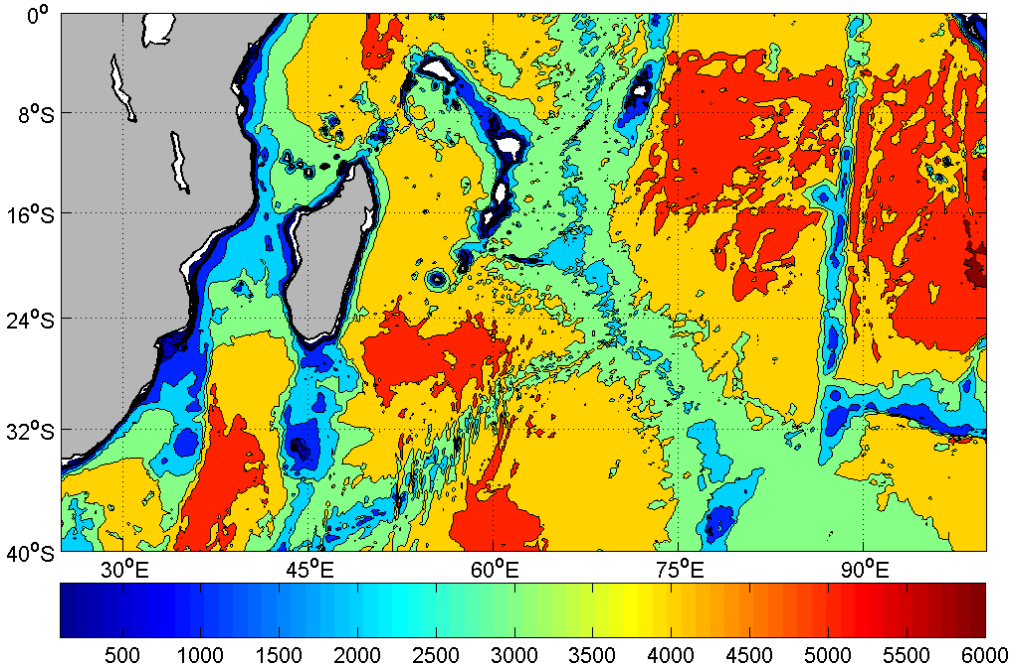

Figure 2.6: Topography of the South-West Indian Ocean indicating frequent occurrence of dynamically important deep-sea ridges. The bottom topography is a subset of ETOPO2 2-mn grid resolution global topography/bathymetry data base (Smith and Sandwell, 1997) and is obtained from the NOAA's National Geophysical Data Center (NGDC).

The general view of the SWIO surface water circulation has been developed by Swallow et al. (1988), Gründlingh et al. (1991) and Stramma and Lutjeharms (1997). Swallow et al. (1988) undertook observations in the region north of Madagascar and further north in the EACC along the east coast of Africa. Volume fluxes are indicated in Figure 2.2. In recent years observations in the Mozambique Channel, to the south of Madagascar and in the region of the Mascarene Ridge, including satellite and ARGO buoy data, have notably improved our basic insight. This recent development is discussed below as a background for understanding TC formation in the area. Particular focus is on mixed layer depths and the occurrence of warm core rings as a source of energy for TCs. However, also the general circulation including the deep waters is taken up.

2.4.1 Wind regime

Lutjeharms (2006) has discussed the general atmospheric circulation over the SWIO, based on work by Ramage (1984) and Taljaard and van Loon (1984). The wind pattern is anticyclonic and clearly weaker in the austral summer (January; Figure 2.7) than in the winter (July).

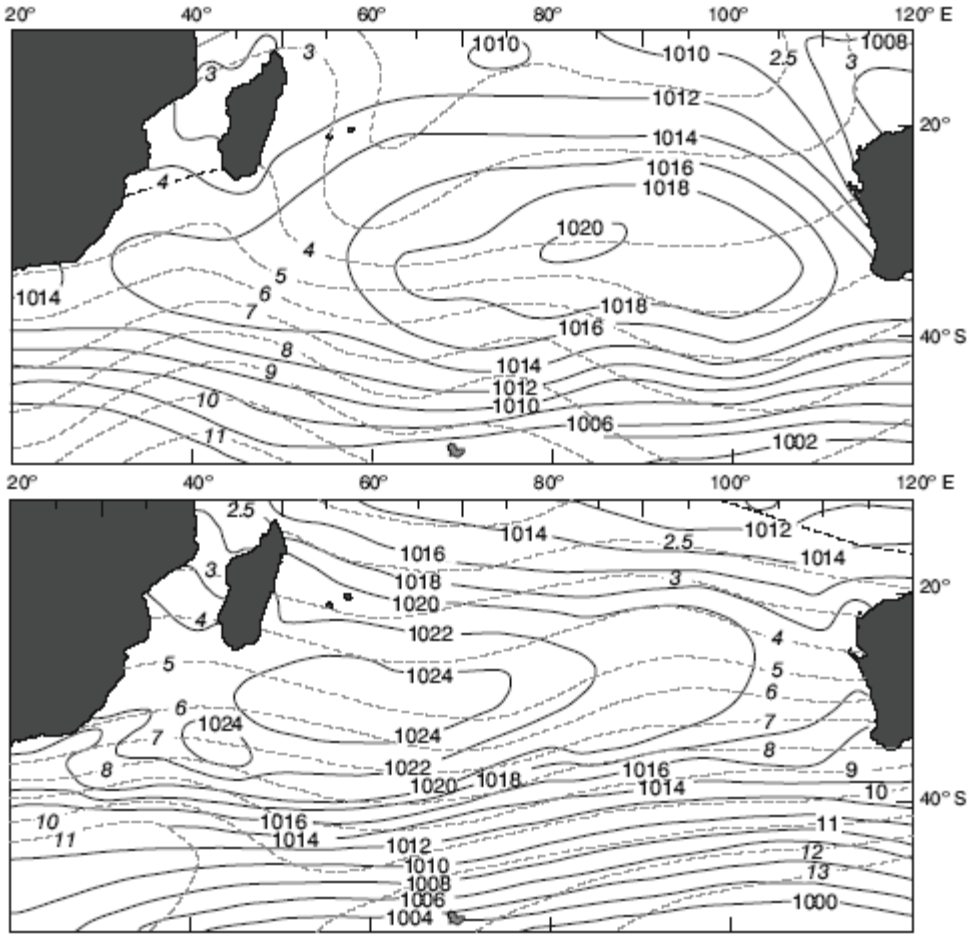

Figure 2.7: *The mean atmospheric pressure at sea level for the South Indian Ocean (full lines) with standard deviations (broken lines), both in hPa (Taljaard and van Loon, 1984). The upper panel represents the months of January; the lower panel July. The seasonal shift of the center of the atmospheric high pressure system substantially changes the wind stress patterns for this ocean region over an annual cycle.*

Wind-stress, shown in Figure 2.3 and air pressure in Figure 2.7, both point at very low winds in the Mozambique Channel. Seasonal means are less than 5

ms^{-1} (Sætre and Jorge da Silva, 1984) with a dominant SE direction. During the peak cyclone season (January-March) the winds are still weaker.

2.4.2 Currents, temperatures and salinities

As mentioned before, ocean circulation in the South-West Indian Ocean is dominated by the South Equatorial Current. According to Schott and McCreary (2001) the transport is of the order of 50 Sv, with small seasonal variations and low surface velocities. The core exists between 10-20ºS, down to about 1000 m. At the Mascarene Ridge (Figure 2.8), the current divides into a southern branch flowing towards Madagascar and a northern branch which goes straight across the ridge in a deeper section (Figure 2.8; New et al., 2007). When the southern branch reaches Madagascar, it divides into northern and southern branch of the East Madagascar Current (see also Section 2.5.4). The northern branch joins the northern part of the SEC (see Figure 2.4).

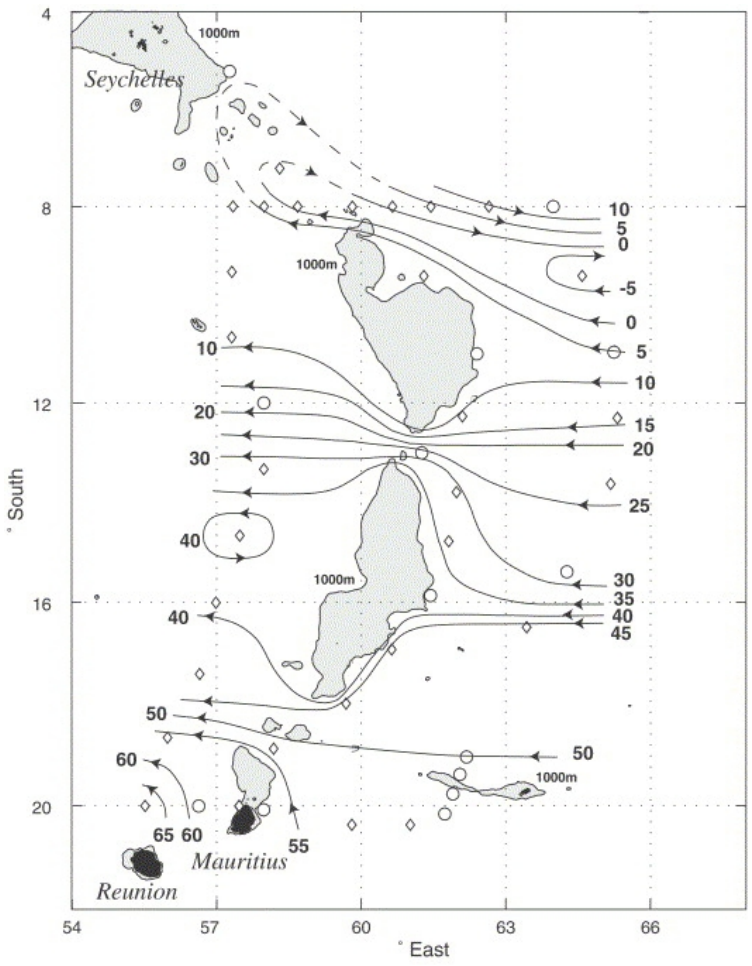

Figure 2.8: Flow pattern of the South Equatorial Current when passing across the Mascarene Ridge, based on observations across the ridge in June-July 2002. CTD/LADCP stations are indicated by diamonds and tidal period stations are indicated by rings, numbers are in Sv (from New et al., 2007). In crossing the Mascarene Ridge, the surface velocities increase from typically 10 cms^{-1} to between 25-50 cms^{-1}. However, the mixed layer depths are not much affected.

According to Tomczak and Godfrey (2003), the large-scale southern hemisphere circulation basically follows Sverdrup dynamics (Figure 2.9), driven by the wind-stress curl, however the path of SEC is more irregular, because of the effects of the underlying topography and Rossby-waves.

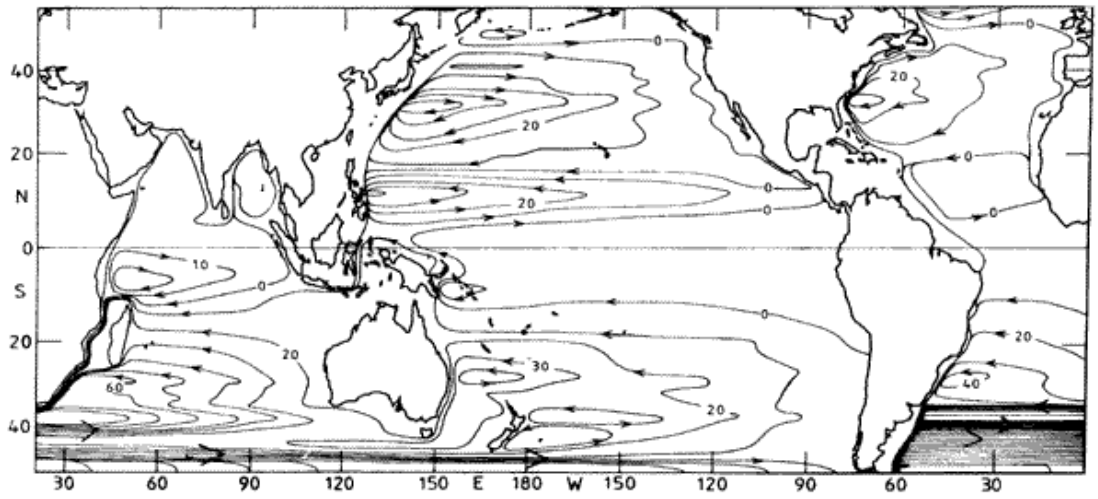

Figure 2.9: Annual mean Sverdrup transports (Tomczak and Godfrey, 2003).

Although the surface circulation of the SWIO is basically wind-driven, thermo-haline forcing as well is certainly important. Figures 2.5a-b showing surface salinities and temperatures, indicate considerable spatial as well as seasonal variations. Minimum salinities and maximum temperatures occur during the southern summer (Jan-Mar), when the ITCZ is at its southernmost position and the trade winds are weak (Figure 2.3). However, despite the weak trades, the South Equatorial Current is at least as strong as during the southern winter (Schott and McCreary, 2001). Freshwater from ITF and other sources (Gordon et al., 2003; Andersson and Stigebrandt, 2005) might in fact contribute to driving of the SEC. Figures 2.10a-c show meridional sections of salinity, temperature and density anomaly (σ_0) east of the Mascarene Ridge. Except for the salinity minimum across the SEC core, the figure also shows "inflows from the sides" of subducting high saline waters from the evaporative dominated SE and NW Indian Ocean and upwelling of cold Antarctic Intermediate Water (AAIW) below the salinity minimum. Figure 2.10c also indicates the current system of the southern Indian Ocean, including the recently perceived South Indian Ocean Counter Current (SICC), flowing eastward from Madagascar at around 25ºS (Palastanga et al., 2006; Siedler et al., 2007).

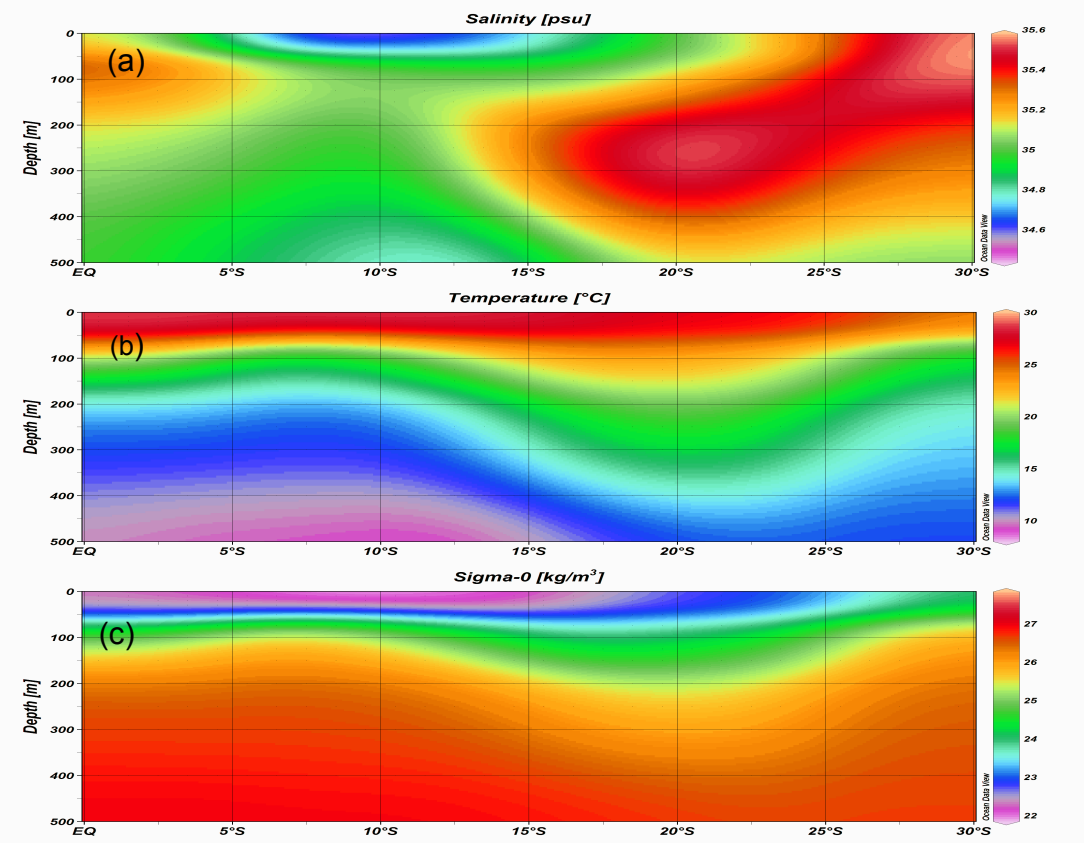

Figure 2.10: (a) Salinity, (b) temperature and (c) density anomaly (Sigma) sections (calculated according to the Ocean Data View-ODV program) east of the Mascarene Ridge (64.5°E, Jan-Mar, data from WOA05), showing the very thin mixed layer in the region from the Equator to about 15°S. Upwelling, forced by Ekman divergence (Schott, 2005) and low saline surface waters may both contribute to the thin mixed layer. This is also the period when the trade wind is at its minimum (see Figure 2.3), i.e. mixing and wind entrainment is also weak.

2.4.3 Water masses

The water masses of the Indian Ocean were discussed extensively by Schott and McCreary (2001) and also in more detail for the south-western part of the ocean, by New et al. (2007). Figure 2.11 shows profiles of salinity and temperature from the Equator to 30ºS along with the Mascarene Ridge. As expected, the differences between the northern and the southern profiles are large. One recognises deep salinity minima, the southern profile at 1000 m related to the Antarctic Intermediate Water (AAIW), and a deep maximum at 700

m near the Equator which is related to Arabian and/or Red Sea Waters (ASW; RSW). A shallow salinity maximum, at a depth of 300 m at 20ºS is related to Subtropical Subsurface Water, created in the south-eastern Indian Ocean, due to high evaporation (Figure 2.2). Shallow salinity maxima at 0-10ºS, indicate a subduction of the SECC underneath a thin layer of fresher water, moving westward (see Sect 2.3.1). Below, in Chapter 2.5, the relationship between these water masses and those closer to Madagascar and in the Mozambique Channel is discussed.

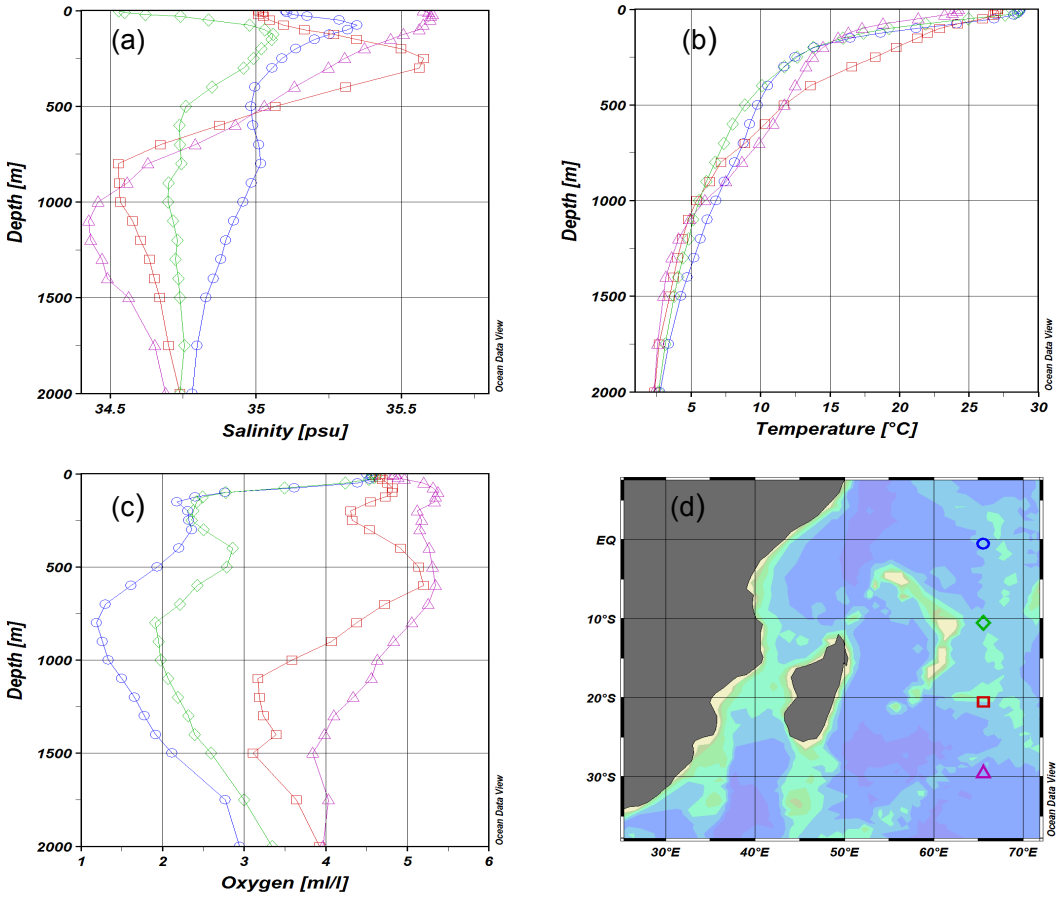

Figure 2.11: (a) Salinity, (b) temperature and (c) oxygen profiles indicating the different masses appearing (d) east of the Mascarene Ridge (data from WOA05).

2.5 The Mozambique Channel and around Madagascar

The Mozambique Channel is a wide strait, being 370 km at its narrowest and 600 km at its widest (Figure 2.11). The circulation in the Channel itself has become better known by direct observations during the past decade. Earlier, most information was from Sætre and Jorge da Silva (1984) and Donguy and Piton (1991). Instead of featuring a continuous, intense western boundary current, the Mozambique Current, as thought of in earlier investigations, has now been shown that the circulation is dominated by a train of warm, anti-cyclonic eddies progressing pole-wards along the western side of the channel (Lutjeharms, 2006a; De Ruijter et al., 2002). These and other features are discussed below.

2.5.1. Through-flow. Water masses, salinities and temperatures

In the years 2000-01, a Dutch-South African expedition (Ridderinkhof and De Ruijter, 2002; De Ruijter et al., 2002 and De Ruijter et al., 2003) deployed several current meters in the narrowest part of the Mozambique Channel. While deploying and recovering the instruments they also carried out tracking of eddies moving through the channel from north to south. They found a *net* through-flow of the order 15 Sv with very strong spatial and temporal variability, related to meso-scale eddies created in the narrow parts of the channel. Maximum azimuthal velocities in these anti-cyclonic eddies exceeded 1 ms^{-1}. At least some eddies seemed to reach from the surface to the bottom (>2000 m). The mean southward movement (of eddies) was estimated at 4.5 km/day (=20 Sv if averaged over 800 m x 500 km width). De Ruijter et al. (2002) also discussed deep water flows, entering from the south having found two cores of deep water (AAIW and North Atlantic Deep Water, NADW) flowing northward in the channel at 1000 m and at 2500 m respectively, and that the northward flux into the channel is about 5 Sv; AAIW (3 Sv) and NADW (2 Sv).

As mentioned before, the volume flux in the part of the SEC, which flows north of Madagascar is of the order of 30 Sv (Swallow et al., 1988). However, the surface

current maps of Schott and McCreary (Fig 2.4) do not indicate to what extent waters from the SEC enter the Mozambique Channel, but estimates of the flow in the EACC indicate that the major part (23 Sv) of the flux north of Madagascar continues northwards towards the Equator, indicating that less than 10 Sv should enter the Mozambique Channel (assuming no vertical mixing). To reach the level of 15 Sv or more going south-wards through the Mozambique Channel, would thus imply a strong vertical mixing in the channel including an upward transport of some 5-10 Sv. The aforementioned deep-water flows might be a response to deep mixing induced by the meso-scale eddies mentioned above.

Profiles of salinity, temperature, oxygen, nitrate and phosphate, for the period Jan-Mar based on WOA05 climatology are shown in Figure 2.12a-c for the northern, central and southern part of the channel, respectively. The surface waters in the northern part of the channel (Figure 2.12a) include SEC water of different origin, with smaller portions of AAIW (S=34.3-34.7, T~2-7°C). Subtropical Subsurface Water (SSW; see Figures 2.10a and 2.11, Section 2.4.3) joins the SEC in the eastern Indian Ocean evaporation area (Fig. 2.3) and flows westward while rising to about 200 m only to the north of MC. Together with Indian Central Water (ICW) just below, it creates the core of SEC (with a linear T/S relationship from 14°C/35.15 to 7°C/34.80). Underneath is water of constant salinity 34.75 and temperatures decreasing from 6-2°C. Indian Deep Water (IDW) finally, according to Schott and McCreary (2001) flows just above the Circumpolar Deep Water. It is oxygen poor with salinities of 34.75 (compared to about 34.7 for the CDW) with somewhat higher temperatures (2-2.5°C), than the CDW. As mentioned before, low surface salinities in the northern part of the channel, but also around Madagascar, indicate high rainfall in the area (Figure 2.2) during this part of the year, when the ITCZ is passing through (see also Ogallo, 1988; Nicholson and Kim, 1997).

During the peak cyclone season, from January-March, the northern Mozambique Channel, north of the narrows, features mixed layer depths of 20-30 m, which is

less than normal for non-upwelling tropical areas. Even further south in the channel (Figure 2.12b-c), the conditions are similar.

Mean SST ranges from 27-28ºC, which is well above the global latitude average (Figure 3.1a - global mean map). A thin mixed layer and high temperatures in combination may be explained by low wind-stress (Figure 2.3) and large rainfall (Figure 2.2), factors which are both decreasing the depth of the mixed layer (see Chapter 6, Section 6.1-The Monin Obukhov depth). It is obvious that variations in the mixed layer depth will play a major role for cyclone predictions. Shallow mixed layers, on one hand, indicate that the development of a cyclone should be readily hampered. On the other hand, the surface water is more easily heated if the mixed layer is shallow, and in the channel, SSTs according to satellite data, may readily increase to beyond 30ºC during the southern summer.

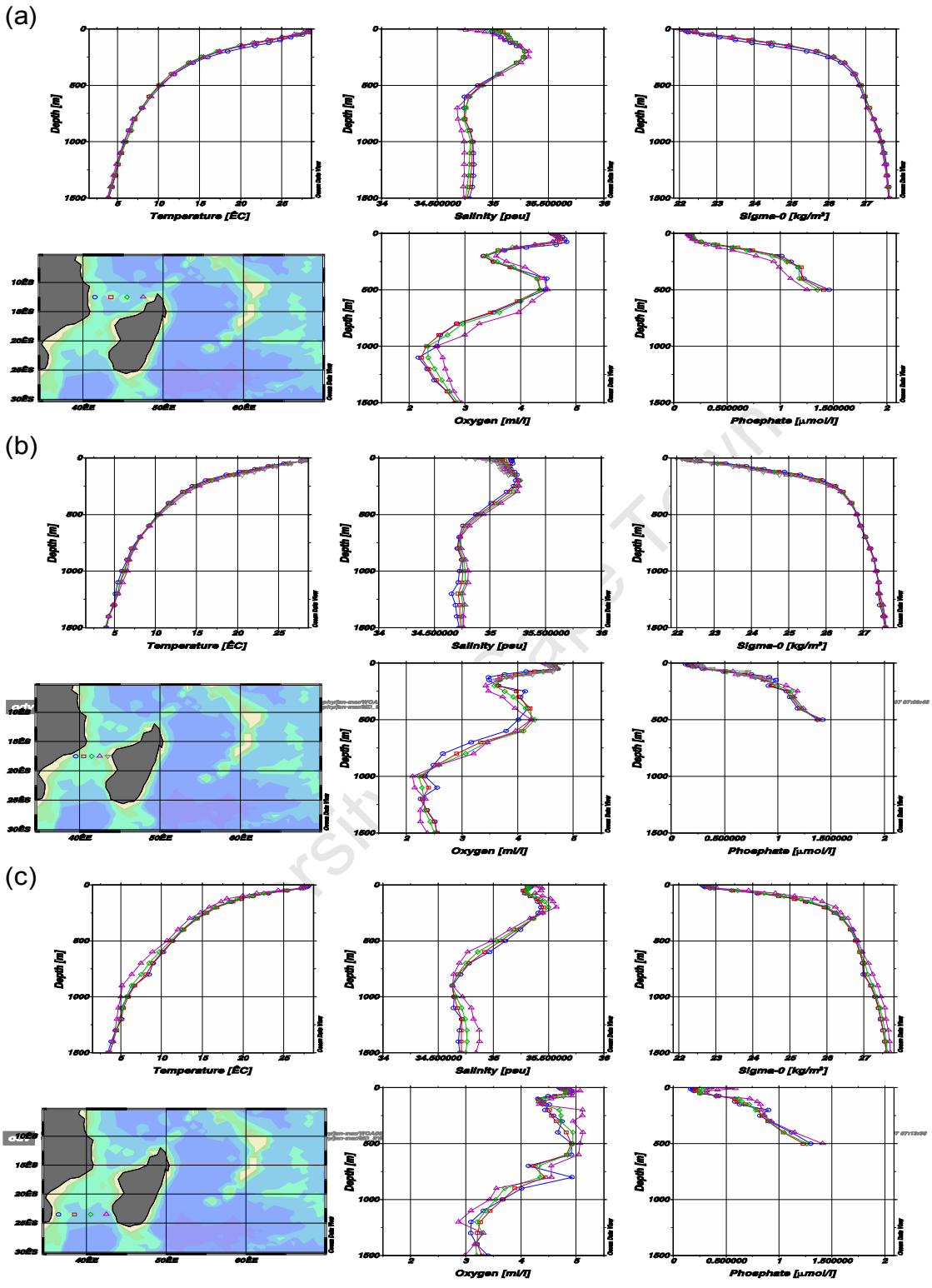

Figure 2.12: Climatology data on (a-c) salinity, temperature, sigma, oxygen, nitrate and phosphate, period January-March, Mozambique Channel (data from WOA05).

Thus, as both genesis and intensification takes place in the area, it is likely that the processes need either a substantially higher SST than normally quoted (26-27ºC) or that “warm core eddies” can contribute. Below, a background is given to the latter subject.

2.5.2 Mozambique eddies

Currents in the Mozambique Channel have classically been understood to be dominated by a strong western boundary current, the Mozambique Current (Lutjeharms, 2006a; Lutjeharms, 2006b). Sketches of circulation in the past have shown different flow patterns (e.g Harris, 1972; Sætre and Jorge da Silva, 1984). This interpretation, based largely on non-synoptic hydrographic observations and ships’ drift (Sætre, 1985; Lutjeharms et al., 2000), has been proven too simplistic. Using data from a recent hydrographic cruise, the Agulhas Current Sources Experiment (ACSEX-I; De Ruijter et al., 2002) and satellite altimetry it was shown that the continuous Mozambique Current is actually a train of eddies, moving slowly southwards through the channel (Lutjeharms, 2006a, de Ruijter et al., 2002).

Eddy behaviour in the Mozambique Channel has two distinct features. First, the anticyclonic-eddies (warm) are larger than cyclonic eddies (cold) and hence dominate the flow. Second, these eddies appears to be affected by the bottom topography (Schouten et al., 2003). As aforementioned train of anticyclonic-eddies is a new concept employed to characterize the major part of flow through the Mozambique Channel. The Mozambique eddies are formed at the narrows of the Mozambique Channel and propagate southward past the African continental shelf (Ridderinkhof and de Ruijter, 2003; Schouten et al., 2003; Figure 2.13).

Most of the reported eddy activity in the Mozambique Channel is related to the western side of it (e.g Schouten et al., 2003; Lutjeharms, 2006a; Lutjeharms, 2006b). Spatial and temporal observational coverage of eddies in the past was

severely limited by the difficulty of sampling using conventional ship borne instruments (Robinson, 2004). The use of satellite data has revealed considerable variability in the Mozambique Channel (Figure 2.14). Analyses of altimetry data show (Lutjeharms et al., 2000; Lutjeharms, 2006a) that flow characteristics on the western side and eastern side of Mozambique Channel are very different.

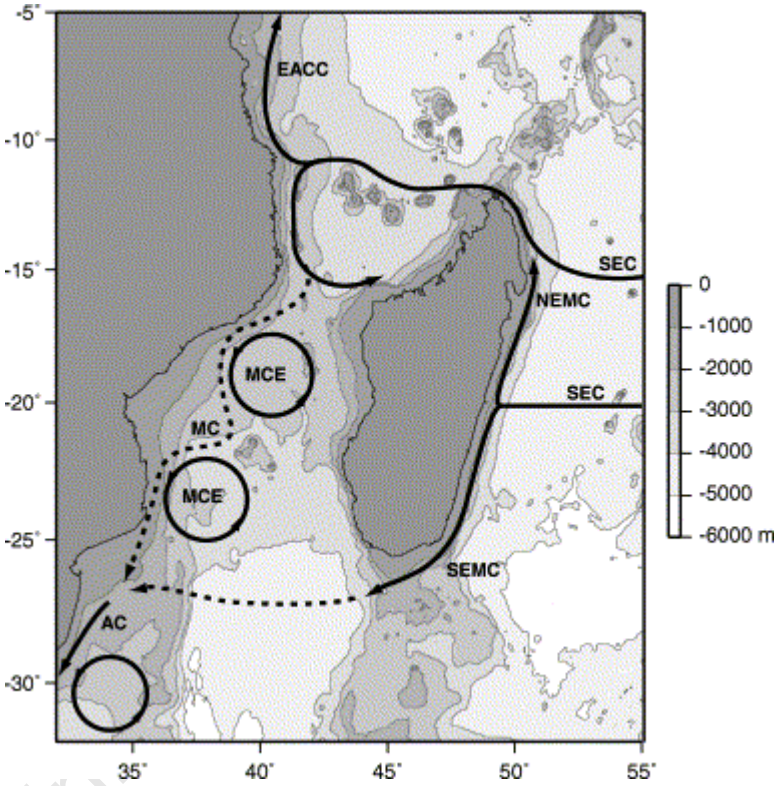

Figure 2.13: Formation and advection of MC eddies (Schouten et al., 2003).

The current variability, or eddy kinetic energy, on the western side is very high whereas that on the eastern side is very low. This flow representation highlights (Lutjeharms, 2006a) two important considerations; i) the flow agrees well with the concept of a train of energetic eddies continuously moving poleward along the western shelf, also supported by modelling studies (Biastoch and Krauss, 1999), and ii) few direct observations are available on the eastern side of the channel, but these few are useful and, with surface drift measurement from ships, indicate (Sætre, 1985; Lutjeharms et al., 2000) that in general the currents in this region

are weak and variable. These flow patterns in the Mozambique Channel could conceivably have marked effects on passing tropical cyclones prior to landfall, which may intensify when the adjacent areas are associated with the presence of warm eddies.

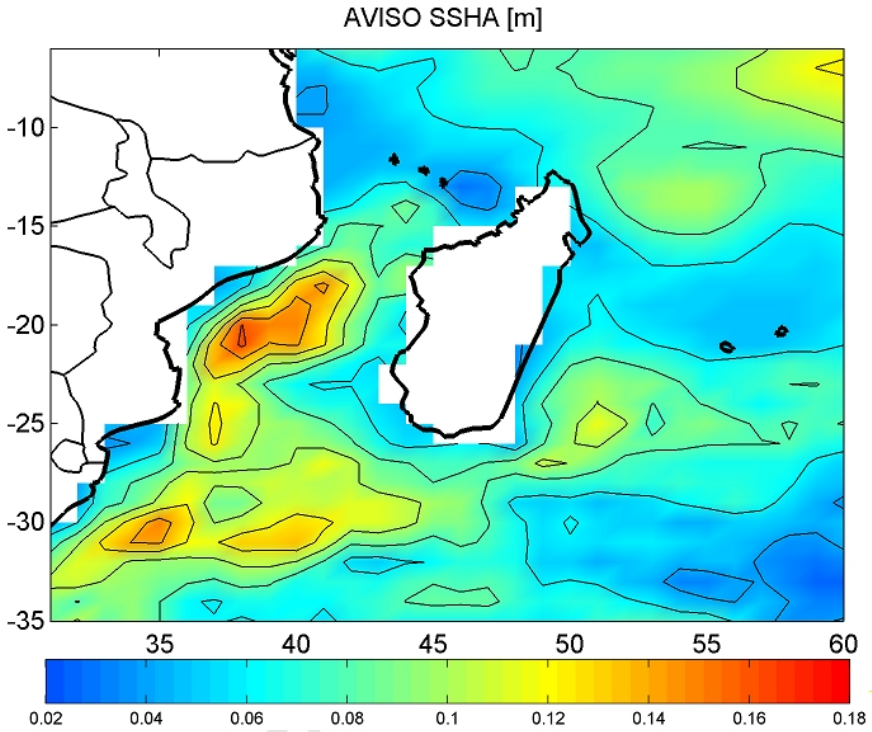

Figure 2.14: Sea level variability in the area of Mozambique Channel and Madagascar. AVISO seasonal variance SSHA (JFM) taken from 1993-2004 mean.

How representative are these warm features in the Mozambique Channel and how is their thermal structure is distributed? Schouten et al. (2003) have analyzed the characteristics of these eddies using a combination of in-situ observations and satellite altimetry. Their results indicate that these eddies have cross sections of about 350 km with a strong barotropic component, extending all the way to the sea floor with maximum surface speeds of 2 ms^{-1}. They also analyzed 6 years of gridded TOPEX/Poseidon and ERS-1/2 altimeter data and tracked eddies manually following the positive SSH (warm eddies) anomalies through the channel. About 4 are formed per year with a net southward transport of about 15-18 Sv in the upper 1500 m (Schouten et al., 2002b; 2003; de Ruijter

et al., 2002; Ridderinkhof and de Ruijter, 2003; Penven et al., 2006) and were found to propagate from around 15°S in the channel towards 35°S, near the Agulhas Current (Figure 2.15).

The spatial scale of eddies (300-350 km) tracked in the Mozambique Channel is comparable to those measured in similar studies in the North Brazil Current (eg. Fratantoni et al., 1995; Goñi and Johns, 2001) and Agulhas Rings in the south-eastern Atlantic (Byrne et al., 1995; Schouten et al., 2000). Schouten et al. (2003) provided some statistics on the Mozambique eddies. The authors found that the average maximum SSH anomaly associated with these eddies increases from about 20 cm (Figure 2.15b) in the northern part of the Channel to 35 cm in the central and southern regions. They also argued that this increase is more than can be accounted by the gradient of the potential vorticity field.

Such presence of energetic eddies in the western corridor of Mozambique Channel is a strong indication of a potentially important source of energy for passing tropical cyclones. Assuming a depth where mixing due to cyclonic winds would be prevalent, say 80 m or more, the temperature difference in an eddy and outside it might be about 5ºC (De Ruijter et al., 2002) making these eddies potentially a rich source of energy for cyclone strengthening.

Using measured AVISO surface eddy kinetic energy data Penven et al. (2006) confirmed five characteristic areas of high eddy variability in the South-West Indian Ocean: the Mozambique Channel (Cheney et al., 1983), the region south-east of Madagascar (Lutjeharms et al., 2000), the Agulhas retroflection and the Agulhas return current (Lutjeharms and Ansorge, 2001; Boebel et al., 2003). On the other hand, within the Mozambique Channel, the central region seems to have high eddy activity and perhaps higher EKE compared to northern and southern regions.

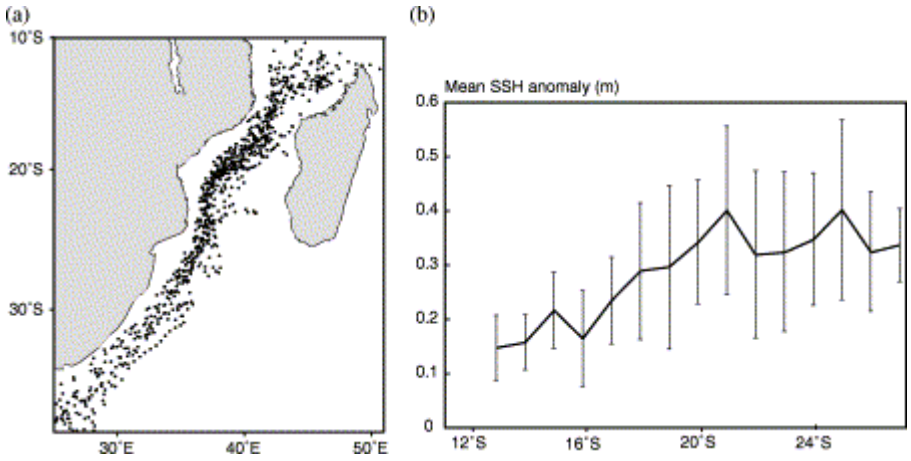

Figure 2.15: (a) paths of 25 Mozambique eddies that were tracked between 1995 and 2000. (b) Mean SSH expression of the Mozambique eddies along their way south (Schouten et al., 2003). The vertical bars show one standard deviation over the observed 25 eddies.

2.5.3 The Delagoa Bight lee eddy

A large cyclonic eddy, named the Delagoa Bight eddy, has since long been recognized and well-documented in the southern part of the Mozambique Channel (Lutjeharms and Jorge da Silva, 1988). The centre of the eddy is at approximately 33.5°E, 26.3°S east of Maputo Bay (Chapter 3, Figure 3.9) in the Mozambique Channel. Information available suggests that this could be a trapped lee eddy, driven by the rapid flow of adjacent waters along the Mozambican coast (Lutjeharms, 2006a). Over a period of 23 years it has been observed 11 times (Martin, 1981). It has been suggested (Lutjeharms, 2006a) that upwelling in the core of the eddy occurs from depths of at least 900 m. This seems to be quite reasonable (cf Chapter 3-Figure 3.9)

A huge and infrequent meander movement with a limited life span over the Mozambique Plateau and apparently associated with this eddy has been described using thermal infrared images (Sætre and Jorge da Silva, 1984). Such movement has also been confirmed by altimetry observations and it is believed that a small fraction of the Mozambique eddies may owe their origin in the Delagoa Bight. Eddies observed directly south of the channel, over the northern Mozambique Plateau (Gründlingh, 1984; Lutjeharms, 2006a) but also over the

northern Natal Valley (Lutjeharms, 2006a) may therefore have their origin either in the channel narrows or the Delagoa Bight. These eddies have diameters of 100 km or more and an elevation of their 10°C isotherm of 270 m at the eddy centre. Circular transports of up to 18 Sv have been observed (Gründlingh, 1984). These eddies are as energetic as rings from western boundary currents (Lutjeharms, 2006a).

2.5.4 East Madagascar currents

The island of Madagascar in the South-West Indian Ocean (Figures 1.1; 1.4) is separated from the African continent by the Mozambique Channel and surrounded by tropical waters with high sea surface temperatures (Figure 2.12a-c; Figure 2.16a-c). The island is affected by monsoon rains and tropical cyclones, particularly when the ITCZ reaches it southernmost position. The island extends 1580 km from north-south and is 500 km wide. Coastal plains on the western side give way to a plateau with mountains higher than 1500 m on the eastern side. Its regionally shifting climate is classified by Donque (1975) and Williams (1990).

The weather is determined by dynamic interaction between trade winds, monsoon flow (in summer) and subtropical anticyclones. While the northwest part is notoriously rainy, the leeward, southwest part is mostly dry (Nassor and Jury, 1997). Obviously, Madagascar is like a strong shelter for winds and rains moving westward towards Mozambique and the African continent.

The southern branch of the South Equatorial Current, as mentioned, reaches Madagascar between 17º-20ºS (Figure 1.4; Figure 2.13), where it bifurcates (Hellerman and Rosenstein, 1993) into the SEMC (southern branch of the East Madagascar Current), rounding the southern tip of the island (DiMarco et al., 2002), and the NEMC (northern branch of the East Madagascar Current), rounding Cape Amber, in the north.

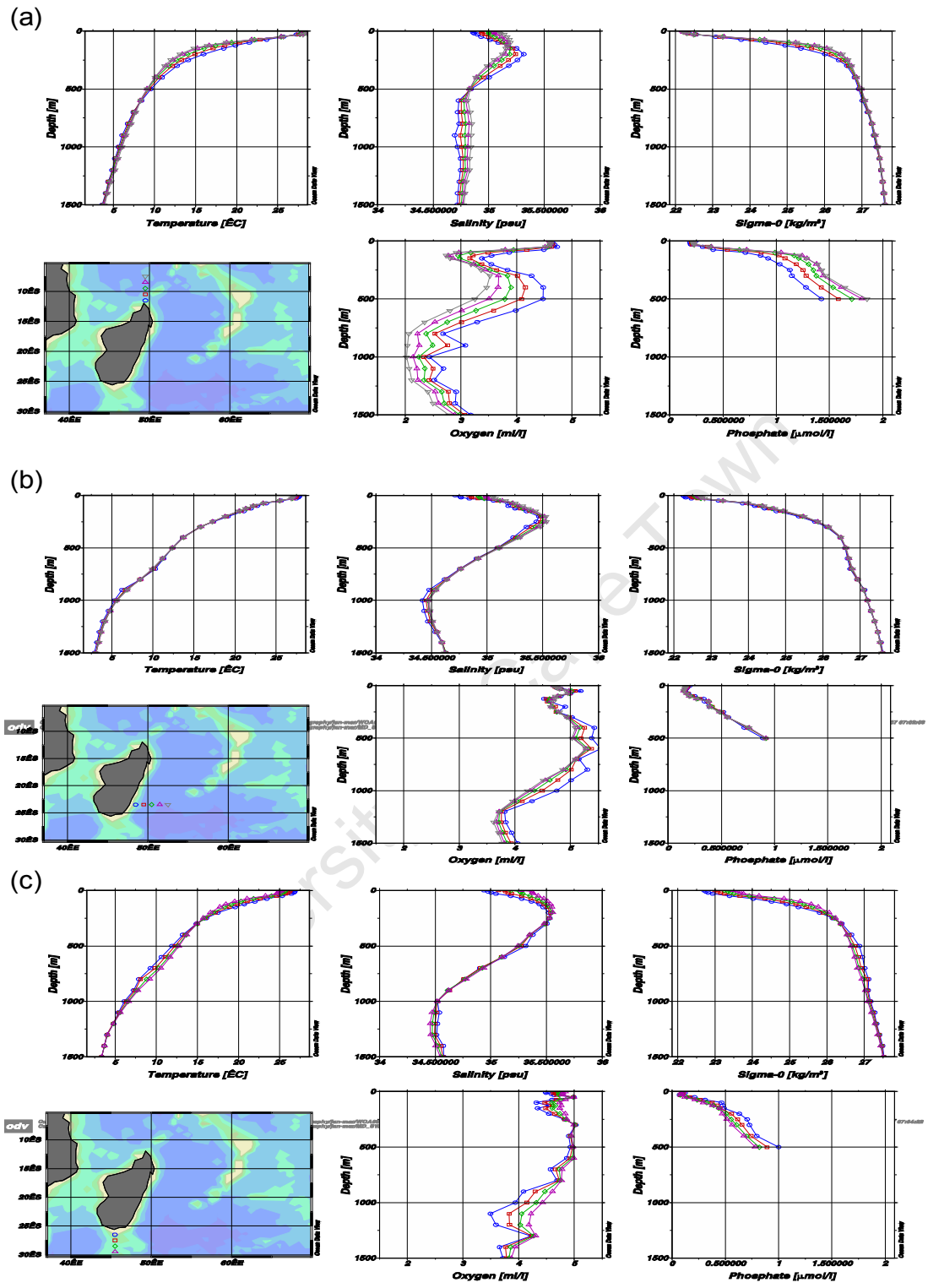

Figure 2.16: Climatology data on (a-c) salinity, temperature, oxygen, sigma, nitrate and phosphate, period Jan-Mar, north, east and south of Madagascar (data from WOA05).

The northern branch of SEC (30 Sv according to Swallow et al., 1988) then, constitutes the core of the East African Coastal Current (Figure 2.4) but also add waters to the Mozambique through-flow. The point where the two branches bifurcate has not been accurately determined and may have a seasonal cycle (Figure 2.13; Lutjeharms, 2006a), shifting north and south. Only recently a retroflection for the EMC and a westerly current were documented (Siedler et al., 2007) outlining the lack of research in the region.

The southern branch of the East Madagascar Current is narrow (~100 km wide), warm and intense and flows southward close to the coast at an average core speed of 0.9 ms^{-1}. This current is known to retroflect (Siedler et al., 2007) and sometimes returns eastward but on many occasions it may extend down to southern tip of the Island acting as a source of vortex dipoles (De Ruijter et al., 2004). Similar to anticyclonic-eddies (warm) observed in the Mozambique Channel the thermal characteristics of the East Madagascar Current along its extension suggest another source of energy which may strongly enhance tropical cyclone strength in the area.

Figure 2.16a-c shows the hydrographic conditions east, north and south of Madagascar. The temperatures are slightly lower on east coast of Madagascar than in the Mozambique Channel, otherwise surface water conditions are much the same with a shallow mixed layer, and low saline surface waters, particularly near the coast.

2.6 Rainfall

Rainfall, as aforementioned is an important parameter in relation to TCs. The main cyclone period in SWIO coincides with the southernmost position of the ITCZ and thereby with heavy rainfall from December to March. This is readily seen from Figure 2.17 showing rainfall climatology based on the TRMM Multi-satellite Precipitation Analysis (TMPA) research product Version 6 3B42 for the

years 1998-2007 (Section 5.4). In recent years the improved accuracy of 3B42 (V6) rainfall data have received considerable interest within rainfall research (e.g. Nazrul Islam and Uyeda, 2006) with strong indication that the (V6) algorithm in curretly providing the best estimate of precipitation in comparison to previous versions. High rainfall (and in addition large runoff from Madagascar) means additional buoyancy to the surface waters and decreasing mixed layer depths. This is particularly seen in the northern part of the Mozambique Channel (Figure 2.17b-c), but also east of Madagascar (Figure 2.17b-e).

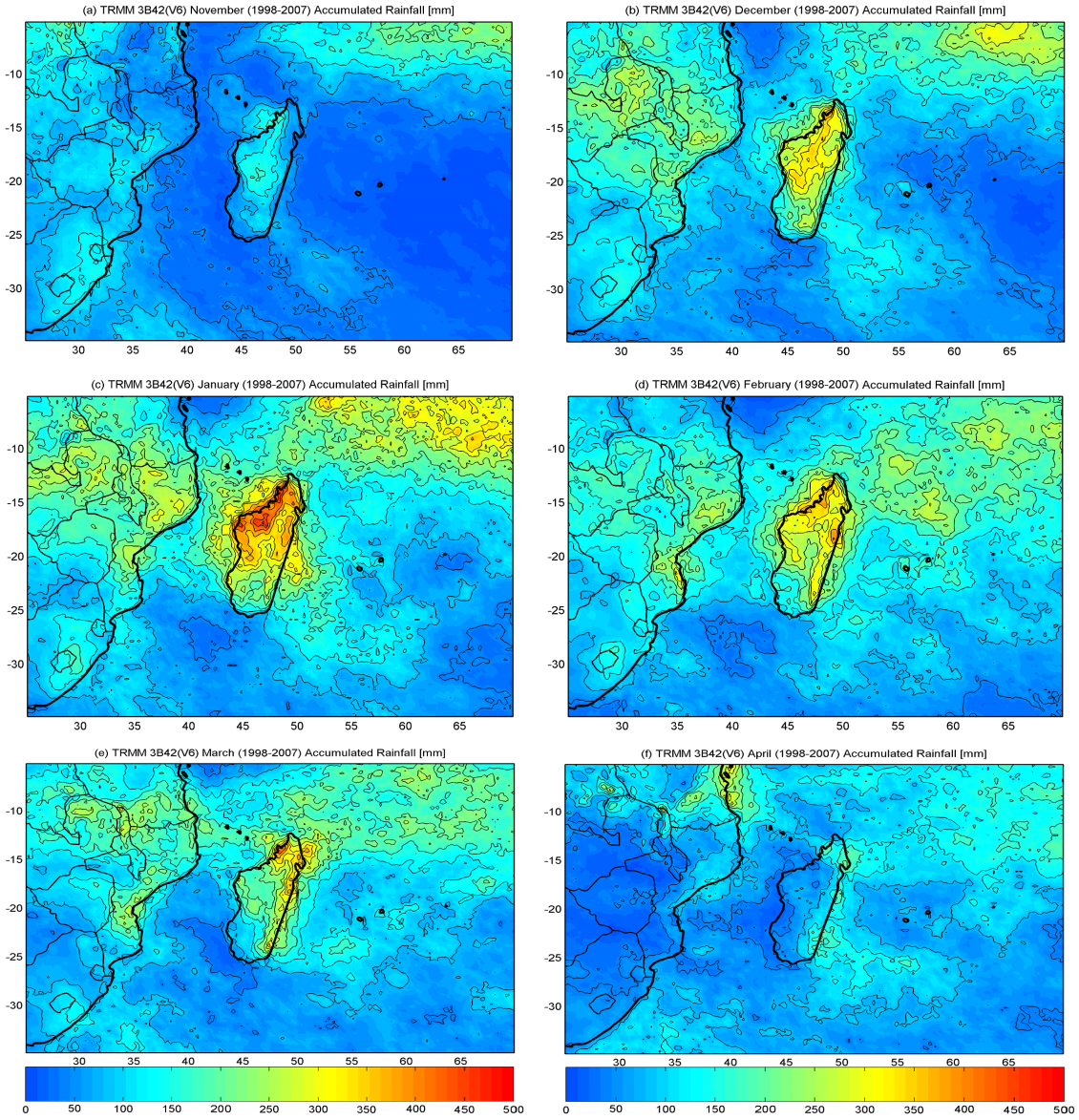

Figure 2.17: (a-f) Monthly 3B42 rainfall climatology (November-April) based on data from 1998-2007.

Chapter 3: Tropical Cyclones

3.1 Introduction

Tropical cyclones, hurricanes or typhoons; all are common names, used to describe the same natural phenomena – one of the most deadly, costly, and destructive weather systems on the Earth (Gill, 1982; Nilsson, 1995). Intensive tropical cyclones produce destructive winds, coastal storm surges, torrential rains and severe floods, usually resulting in serious property damage and loss of human lives. Hurricane Andrew's strike on Florida during August of 1992 caused in excess of $30 billion in direct economic losses, while Hurricane Floyd in 1999 disrupted the lives of 2.5 million of its residents who had to be evacuated (Elsener and Bossak, 2001; Elsener and Jagger, 2004; 2006). On the other hand, tropical cyclones (TCs) may also have positive impacts. Rainfall, if not torrential, in connection with a cyclone is often regarded as a positive effect (Sugg, 1968). Another positive impact has been proposed by Imberger et al. (1979). Imberger et al. have suggested that cyclones, which affect the waters northwest of Australia on average four times per year, induce upwelling and mixing and thus bring additional nutrients to otherwise nutrient poor surface waters.

Tropical cyclone is the generic term for a low pressure system over tropical or subtropical waters with organized convection and a definite cyclonic surface wind circulation (counter-clockwise in the Northern Hemisphere and clockwise in the Southern Hemisphere). In contrast to mid-latitude low pressure systems, which derive their energy from strong horizontal temperature gradients associated with cold or warm fronts, tropical cyclones are driven by latent heat released by the condensation of immense amounts of water vapour within their convective rain bands (Emanuel, 2003).

TCs are classified according to their Maximum Sustained Wind (MSW) at the surface, as either 1-min or 10-min averages. Cyclones with surface winds

between 10 and 17 ms^{-1} are called tropical depressions. Once the MSW exceeds 17 ms^{-1}, the system is assigned a name (in all regions except in the northern Indian Ocean) and the system is called a tropical storm. If the wind increases beyond 33 ms^{-1}, the system is called a hurricane in the Atlantic and the East Pacific, a typhoon in the Western North Pacific (west of 180°E) and a tropical cyclone elsewhere. All cyclones having MSW>17 ms^{-1} are included in the global statistics. Approximately 60 % reach MSW>33 ms^{-1} (see further below).

3.2 Tropical cyclone formation

Tropical cyclones form in the region where the sea surface temperature (SST) exceeds 26-27°C (Palmén, 1948). This strong relationship is readily seen from Figure 3.1, showing regions of formation and mean SSTs. Regions with SSTs lower than the threshold values, and/or a weak ITCZ (e.g South Atlantic; Hsu, 1988) tend to develop very few cyclones. Gray (1968; 1975) has produced a global map of genesis points for all the TCs over the 20 year period, 1952-1971. The regions of cyclogenesis are the Western Atlantic, Eastern Pacific, Western North Pacific, North Indian Ocean, South Indian and Australian/Southwest Pacific. According to Gray about 80 TCs are formed per year over the oceans between 20°N-20°S.

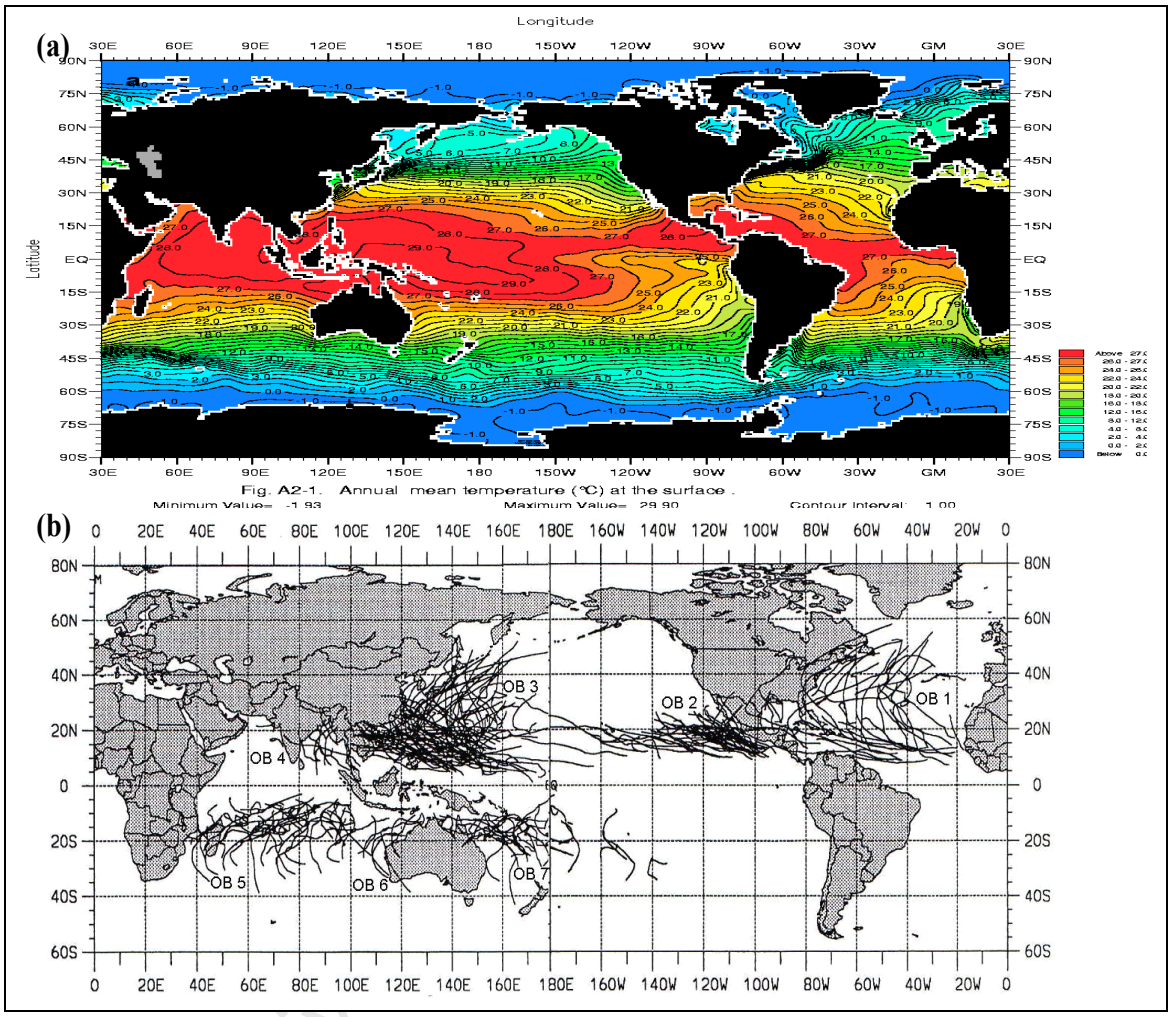

Figure 3.1: (a) *Annual mean temperatures (°C) at the sea surface indicating typical SST conditions, necessary for TC formation. (b) Principal tropical cyclone tracks (adapted from Fink and Speith, 1998).*

TCs do not form within 4-5° of the Equator and very few form poleward of 22°N (Anthes, 1982). The absence of TC formation near the Equator indicates the importance of the Earth's rotation in producing vorticity necessary for storm formation. Henderson-Sellers et al. (1998) while studying TC and global climate change indicated that the favourable conditions for the genesis of a cyclone are (i) large values of low level relative vorticity, (ii) Coriolis parameter (iii) weak vertical shear of horizontal winds (iv) SSTs > 26 °C and a deep thermocline (v) conditional instability through a deep atmospheric layer and (vi) large values of

relative humidity in the lower and middle troposphere. Davidson and Hendon (1989) have shown a progressive vorticity increase on the eastward side of monsoon troughs. The process results in many TC being formed over northern Australia and the south Pacific. McBride and Keenan (1982) have noted the existence of upper troughs during cyclogenesis events which they have suggested would provide favourable genesis conditions. Certainly all those features impact cyclogenesis. However, here focus is on SSTs and upper ocean heat content.

3.2.1 TC structure and life cycle

The structure of a TC (Figure 3.2) covers a range of scales from storm scale to mesoscale, including the size of the low-level cyclonic circulation (such as the outermost closed isobar, or the radius of sustained 15 ms^{-1} gale-force winds), the Radius of Maximum Wind (RMW), the eyewall with its symmetric and asymmetric structures, and both the inner and outer spiral bands. Wang and Wu (2003), have defined TC structure by three components: storm-scale structure, inner-core structure, and spiral bands. The storm-scale structure includes the whole cyclonic circulation with tangential winds larger than 15 ms^{-1}. The inner core structure represents the structure within a radius of twice the RMW, including the deep eyewall clouds, the eye of the storm, and convective asymmetries in the eyewall.

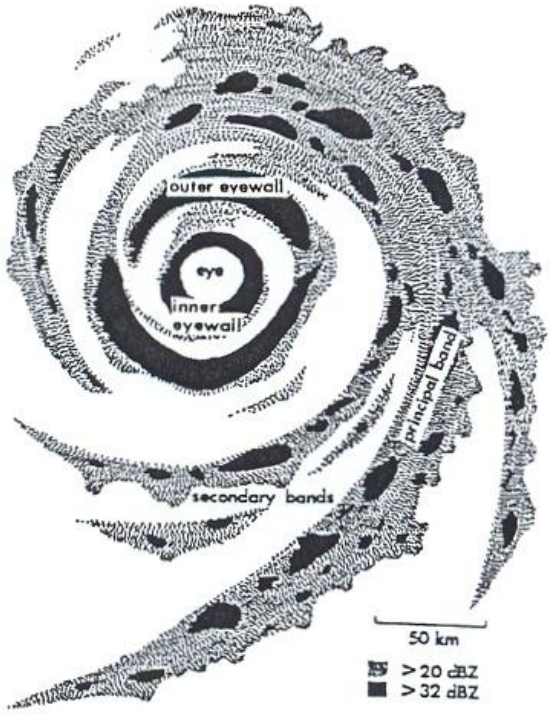

Figure 3.2: Schematic representation of the eye of a mature tropical cyclone. The eyewall convection is separated into an inner and outer eyewall, which is clearly discernible from the radar reflectivity pattern (from Fink and Speth, 1998*)*

TCs have distinct life cycles, several examples of which are described in the literature (e.g Riehl, 1979; Anthes, 1982). For cyclones reaching the level of intense cyclones (i.e. category 3 on the Saffir Simpson scale; see Sect 5.2.2) the life cycle may be divided into four stages. For non-intense cyclones, their development is constrained by one or more of several factors such as being located in an unfavourable atmospheric environment, movement over cooler water or making landfall. One example of such a life cycle is shown in Figure 3.3 starting from the establishment of an environment with required thermodynamic capacity for development. Initiation of a region of sustained convection which may typically stem from a series of thunderstorms, enable the development of a synoptic vortex. The system then becomes self-sustained and capable of intensifying for example because of underlying warm waters with favourable upper ocean heat content. At the climax we have an intense vortex that is able to extract large amounts of energy from the ocean. Decay may take place in an unfavourable environment, because the cyclone is moving into a region with low

sea surface temperatures or over land. It's obvious that a standstill, implying a gradual cooling of the surface waters is self-destructive to a cyclone. Therefore the translation speed (Greatbatch, 1983) is also a primary parameter for the life-cycle. Typical translation speed is 5 ms^{-1}. However, among all stages, rapid intensification is the most important and will be discussed in Section 3.4.

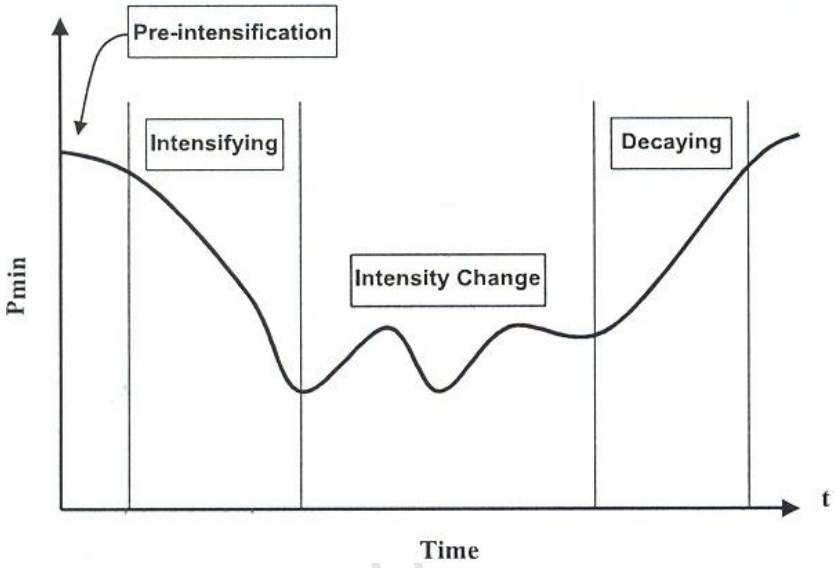

Figure 3.3: *Schematic diagram showing the lifecycle of a tropical cyclone (from Wang and Wu,* 2003*). Pmin indicates the central pressure changes as a function of time.*

3.2.2 Strength and its relationship with intensity

Intensity of a TC is defined from the maximum sustained wind (MSW) or sometimes from the Minimum Sea Level Pressure (MSLP). Many TCs tend to follow an approximately parabolic path around the subtropical anticyclones over the oceans (Figure 2.7, see also Simpson and Riehl, 1981). Winds from these large systems in which TCs are embedded were thought to steer the cyclones. According to this concept the TCs first move westward at low latitudes in the prevailing easterlies. As they leave the easterlies and come under the influence of the westerly winds of high latitudes, they recurve towards northeast in the Northern Hemisphere and southeast in the Southern Hemisphere. On average, TCs reach their greatest intensity shortly before or just at the recurvature point

(Simpson and Riehl, 1981). Analysis on western North Pacific TCs (JTWC, 1994) indicate that weak cyclones typically peak at or near their point of recurvature, while more intense cyclones (e.g Typhoon Ginger in 1997) experience a delay between reaching peak intensity and arriving at their point of recurvature.

Some TCs undergo a second and major stage of intensification after travelling as minimal or even moderate storms for as much as a week. Different from this situation, maximum wind and minimum pressure changes over a period of 1 to 3 days is regarded as up and down oscillations. Merril (1984) pioneered the use of the term strength, which was a measure of the wind speed in an annulus some distance beyond the MSW, which is typically found in the eyewall. Holland and Merril (1984) defined strength as the magnitude of the cyclone circulation in the region outside the inner-core. This definition meant to distinguish the intensity of the TC inner-core from that of the outer circulation. The strength of a system, combined with its track, determines when most preparation should be complete for the oncoming TC, given winds greater than gale force seriously impede outdoor preparation and compromise evacuation safety. A TC with high strength need not have its eyewall pass over land or marine interests to cause substantial damage, and it contributes to a more extensive swath being warned. Higher strengths will increase the magnitude and extent of the storm surge. Hurricane Floyd (1999) forced the evacuation of a record number of people along the Atlantic coast in part due to its impressive strength: hurricane force winds extended 2° of latitude beyond the center.

3.3 Climatology of tropical cyclones

3.3.1 Global occurrence of TCs

Tropical cyclone tracks vary in different ocean basins with respect to cyclone size, intensity and frequency (Frank, 1985). The regions of TC formation are subject to seasonal shifts as a result of the migration of the sun during TC season and the corresponding variations in water temperature (Crutcher and

Quayle, 1974) and wind field. Figure 3.1b shows a very coarse map of the TC regions of the world and the paths of the cyclones. Table 3.1 shows the absolute and relative distribution of TCs within each region, according to Fink and Speth (1998). The western North Pacific including the South China Sea has the greatest number of cyclones. During the period 1968-97 an average of almost 27 disturbances reached storm intensity (>17 ms^{-1}). The global total was 86.7 per year. Matsuura et al. (2003), studying the period from 1971-2000, found an average of 27.2. Although the cyclone season peaks in August, the western North Pacific is the only region where formation takes place throughout the year. The TCs there are also larger than elsewhere. About four typhoons each year reach Super Typhoon Intensity, with MSW>67 ms^{-1} (Fink and Speth, 1998). Factors that promote the frequent genesis of typhoons include a deep warm water body with temperatures of 29-30°C, an active monsoon trough, and persistent upper-level divergence.

Table 3.1: Average numbers of TCs and percentage of global total (i.e peak surface winds of at least 17 ms^{-1}) and their standard deviations (STD) for all tropical ocean basins and for the 30-year period 1968-1997 over ocean basins.

N	Basin	average	percentage	STD
1	North-West Pacific, South China Sea	26.9	31	4.3
2	East Pacific (<180°W)	16.6	19.1	4.6
3	Atlantic (Caribbean Sea, Gulf of Mexico)	9.3	10.7	3.6
4	North Indian Ocean	5.5	6.3	2.2
5	South-East Indian Ocean, South-West Pacific	16.2	18.7	3.9
6	South-West Indian Ocean (<100°E)	12.1	14.0	3.2
	Global	86.7	100	7.9

The North-East Pacific appears to be the second most active region, with an average of 16.6 cyclones per year (Fink and Speth, 1998). In Vadillo et al. (2006), historical analysis of TC data over the last 38 years (1966-2004) indicates a mean of 16.3 TCs per year. Most cyclones dissipate over water north of 20°N and between 120-140°W, because of colder surface waters and increasing wind shear (Figure 3.1a). Fewer cyclones occur in the North Atlantic,

although quite a few reach high intensity. The cyclone season in the Northern Hemisphere is from June to October, but as aforementioned the season is extended in the North-West Pacific. The North Indian Ocean features a twin peak with TCs occurring in April-May and again in October-November, that is in between the monsoon seasons, or when the ITCZ is passing the formation area. However, on the whole there are few cyclones in the North Indian Ocean (Sadhuram, 2004), compared to the other regions. Still, the most disastrous TCs were those hitting the Bay of Bengal, and particularly the densely populated coasts of Bangladesh.

About 16 cyclones per year occur in the South-West Pacific Ocean and another 12 in the South-West Indian Ocean (SWIO), defined as the region west of 100°E (Fink and Speth, 1998). In the SWIO cyclones occur from November-April with a peak in January-February (see also Section 3.3.3). In the South-West Pacific the TC season is from October-May. In the tropical sea north of Australia there is a double peak in January-March, with a distinct minimum in February. Such variations in frequency are strongly related to the ITCZ, which is located mostly north of Australia in these months while it moves to is southernmost position over the continent in February, thus reducing the potential for TC development over the adjacent waters. McBride and Keenan (1982) estimate that some 85% of cyclones in the Australian region have their genesis near the ITCZ.

3.3.2 Interannual variability and trends in relation to global warming

Tropical cyclone activity depends on natural cycles such as the El Niño-Southern Oscillation (ENSO; Pielke and Landsea, 1999), the Atlantic Multidecadal Oscillation (AMO; Goldenberg et al., 2001), the Quasi-Biennial zonal wind Oscillation (QBO; Landsea et al. 1999), the North Atlantic Oscillation (NAO; Elsner et al., 2000) and the Madden-Julian Oscillation (MJO; Madden and Julian, 1994).

Although ENSO seems to play a fundamental role in TC occurrence, its impact is not the same in the different TC regions; El Niño results in increased occurrence of TCs in the South Pacific and in the North-East Pacific, while in the North Atlantic, the Australian region and the North-West Pacific west of 160°E, it is associated with lower frequencies (Landsea, 2000), as expected regarding the SST deviations due to El Niño. An east phase QBO seems to reduce the activity in the Atlantic basin, but the mechanism is not completely clear (Gray, 1984). The role of MJO seems to be relevant in the Pacific basin, with an active MJO associated with more frequent TCs (Sobel and Maloney, 2000). Additionally, TCs exhibit great variability, with significant multidecadal and interannual scales (Landsea, 1996; Elsner and Bossak, 2001).

Trends in frequency and intensity of TCs have been noted by several authors (i.e. Emanuel, 2005; Trenberth et al., 2005; Webster et al., 2005). Emanuel emphasizes a substantial increase in the power of TCs (denoted by the integral of the cubed MSW) over the past 50 years. Webster et al. (2005) find an almost 100% increase in the proportion of the most intense cyclones (Category 4-5), using the period from 1974 to 2005.

However, there are uncertainties concerning the reliability of the tropical cyclone databases (Landsea et al., 2006; Knapp and Kossin, 2007) in relation to long-term trends in TC intensity, and particularly in frequency of extreme TCs. Knapp and Kossin (2007), using a recently launched cyclone data set (HURSAT), find some 5-12% (regional variations) lacking data in the 1980s than in the more recent years. There is an ongoing debate between those who underline the uncertainties, claiming that a link of increasing TC intensity to global warming cannot be shown (eg., Pielke et al. 2005; Landsea et al., 2006) and those who emphasize growing evidence of such a link (e.g. Emanuel, 2005; Webster et al., 2005).

The effect of global warming on the increase in global hurricane intensity has been investigated based on the following chain of hypotheses (Curry et al., 2006): i) Intensity of TCs and frequency of the most intense TCs are increasing globally ii) Average TC intensity increases with higher SSTs iii) Tropical SSTs are increasing globally due to the greenhouse effect.

There should be no doubt about increasing SSTs over the global ocean, although the local variability is large; Webster et al. (2005) show increases in the SSTs of between 0.25-0.5°C in all TC regions over the last 30 years (Figure 3.4), with the SWIO in the upper end. Holland and Webster (2007) discusses 100-year series of SSTs and TCs for the North Atlantic, with an SST increase of 0.7°C. There are few investigations on the relationship between SSTs on one hand and intensity of TCs on the other, but DeMaria and Kaplan (1994) indicate in a study from the North Atlantic, that there is a correlation. Such a positive correlation also seems be the reason why the most intense cyclones are formed in the North-West Pacific, which also has high SSTs (Webster et al., 2005), and in addition, a very large mixed layer depth, compared to other regions (see further in Section 3.3.3).

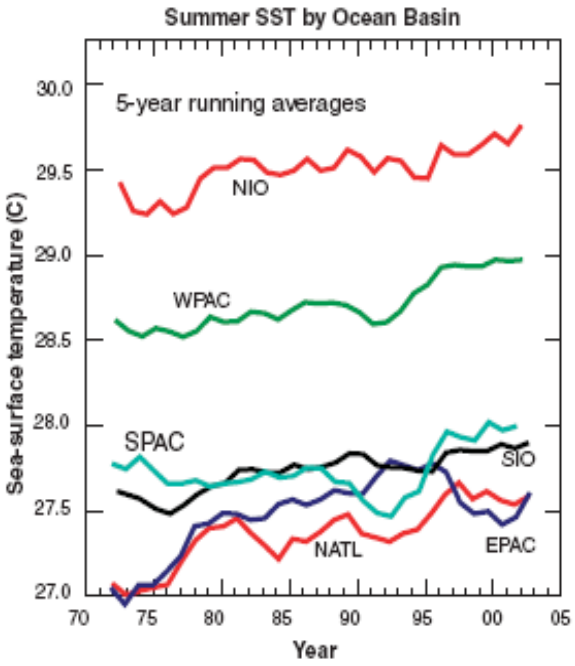

Figure 3.4: *Running 5-year mean SST during TC seasons for the principal regions in which TC occur: North Atlantic Ocean (NATL:* 90-20°*E;* 5-25°*N, June-October), West Pacific Ocean (WPAC:* 120-180°*E,* 5-20°*N, May-December), East Pacific Ocean (EPAC:* 90-120°*W,* 5-20°*N, June-October), South-West Pacific Ocean (SPAC:* 155-180°*E,* 5-20°*S, December-April), North Indian Ocean (NIO:* 55-90°*E,* 5-20°*N, April-May and September-November) and South Indian Ocean (SIO:* 50-115°*E,* 5-20°*S, November-April). [from Webster et al.,* 2005*].*

A choice of a shorter period (i.e. 20 years only, as used Klotzbach, 2006) may result in less debate over the interpretation of data, but the time series may not reflect variability in longer time scale oscillations or provide enough data to establish conclusive evidence for the relationship between TC activity and tropical SST (Sriver and Huber, 2006).

3.3.3 Occurrence of TCs in the SWIO

Most work on TCs in the SWIO has been published in the form of seasonal or annual reports from the WMO, LR-RSMC and JTWC. There are also national reports from the South African Weather Service and Mauritius Meteorological Services (see van Heerden and Taljaard, 1998; Reason and Keibel, 2004). Scientific contributions to climatology of South Indian Ocean cyclones, mainly in relation to QBO, ENSO and MJO variability include Jury and Pathack (1991), Jury (1993), Jury et al. (1999), Xie et al. (2002), Vitart et al. (2003), Reason and Keibel (2004), Landman et al. (2005) and Ho et al. (2006).

The QBO phenomenon is the regular alternation of zonally symmetric westerly and easterly winds in the mean zonal winds of the tropical stratosphere (30 hPa) with a periodicity of 24-30 months (e.g. Xu, 1992). ENSO and the MJO are known as the most dominant modes in tropical low-frequency variability (e.g. Zhang, 2005; Ho et al., 2006). While ENSO has the strongest variability in the Pacific, the MJO activity has the strongest variability in the Indian Ocean. The ENSO is described as an inter-annual oscillation (3-7 years) between a warm and cold phase of the eastern and central Pacific referred to as El Niño and La Niña respectively (e.g. Chu and Wang, 1997). MJO is in turn defined as an intra-seasonal oscillation (30-60 day oscillation), consisting of large-scale (approximately 1000 km across) deep convective tropical rainfall anomalies that propagate slowly eastward from the Indian Ocean, through Indonesia, into the western Pacific, where they decay at around 180°E (Ho et al., 2006).

Jury (1993) has studied synoptic-scale influences on SWIO TC frequency. He found that more cyclones are generated during the easterly phase of the QBO. The SWIO has upper level westerlies as a climatological mean, which are weakened by the east phase of the QBO. In the SWIO, El Niño years appear to reduce the number of TC's during the December-March season. Jury et al. (1999) find that this is explained by the increased subtropical upper-level westerly winds.

Xie et al. (2002) have examined the shallow overturning circulation in the SWIO, and relate the results to the number of TC days. The maximum number is found east of Madagascar (Figure 3.5). Using composites of years with anomalously deep and shallow thermoclines (based on model results), respectively, the authors find a high correlation near 15°S, 60°E. The number of TC days during deep and shallow thermocline years, varies between 4 and 1.

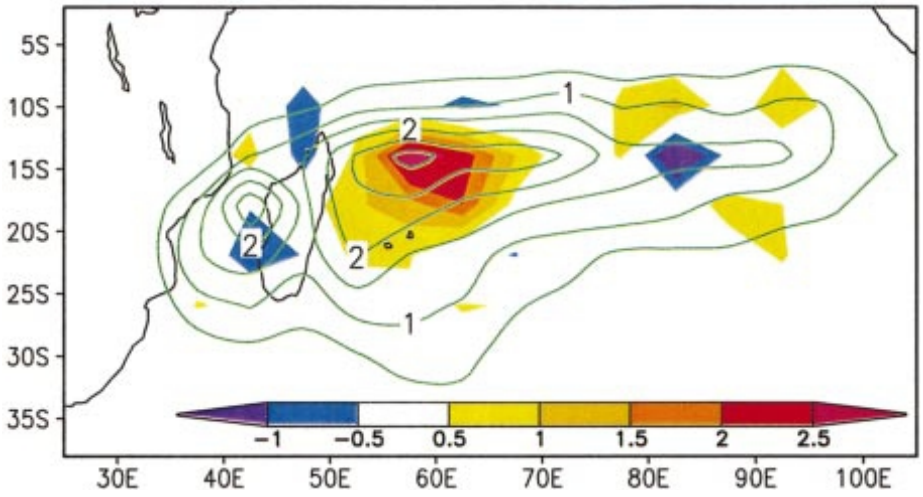

Figure 3.5: *Climatological-mean TC days (contours) in December-April, and the difference (colour shade) between years of an anomalously deep and years of anomalously shallow thermocline in* 8.8-12.8°*S,* 50.8-70.8°*E (from Xie et al.,* 2002*).*

Kuleshov and de Hoedt (2003) find increased number of cyclones between 85°E and 105°E during La Niña years compared to El Niño years. Bessafi and Wheeler (2006) have examined MJO-TC genesis relationship and found that MJO extensively modulates low-level vorticity and vertical wind shear including

the number of TCs, where significantly more (fewer) cyclones form in the active (inactive) phase of MJO.

Ho et al. (2006) have investigated South Indian Ocean (SIO) cyclones using the JTWC data. They found that about 12 TCs are formed in SIO every year (1979-2004; similar to earlier findings). Most of them originate from the region east of Madagascar (50°-100°E, 5°-15°S), and some from the Mozambique Channel. Concerning the effect of ENSO, El Niño means TC genesis increase west of 75°E and decrease east of 75°E, and vice versa. Vitart et al. (2003) have also studied the El Niño/La Niña difference, for example that La Niña years seem to give a more zonal (east to west) movement of the cyclones. The authors also suggest that landfall (for this reason) are more common during La Niña years.

Vitart et al. (2003) evaluated the risk of landfall over Mozambique using both observations and numerical model integrations. They used a 51 year TC record from Neumann et al. (1993) and reanalysis data from NCEP (zonal mean wind, SSTs; Kalnay et al. 1996) to identify predictors and potential physical mechanisms responsible for year to year change in the risk of landfall over Mozambique. According to the results by Vitart et al. (2003) a coupled Global Circulation Model (GCM) with sufficiently high horizontal resolution is capable of predicting a number of landfalls. Landfall is more common during La Niña years, simultaneous with a negative zonal mean flow (averaged for 850-200 hPa). El Niño years have few landfalls and a positive zonal mean flow.

By contrast, operational seasonal forecast systems are currently using horizontal resolutions that are too coarse to properly resolve the trajectory of tropical cyclones. However the TC track predicted by the ECMWF forecasting system indicates that although the model has no skills in explicitly predicting landfall over Mozambique, it has skill in predicting the inter-annual variability of TC tracks. Observations also suggest that ENSO and SWIO SSTs have significant impact on the risk of landfall in Mozambique and hence a dynamical model predicting

the risk of landfall over Mozambique depends strongly on its skill in predicting SSTs over the SWIO and tropical Pacific, according to Vitart et al. (2003).

Landman et al. (2004) have tested a regional model for the SWIO (like Vitart et al., 2003) with the aim to examine its ability to reproduce observed cyclones and their landfall tracks. Their results indicated that the regional model has the ability to simulate tropical cyclone–like vortex tracks across Madagascar and into the Mozambique Channel in a domain that exhibits some control from the eastern boundary. Madagascar also has influence over storms migrating across it and into the channel since it affects the low-level flow. However, the ability of this model to simulate tracks west of the island may depend on the GCM's ability to skilfully simulate the large-scale circulation over the southern Indian Ocean (Vitart and Stockdale, 2001).

Reason and Keibel (2004) have studied the synoptic evolution of TC Eline and its impacts over the southern Africa mainland. They concluded that the very wet conditions in Mozambique and western side of southern Africa and Namibia were caused by Eline. Over southern Namibia, about 25% of the February and March rainfall was due to the passage of ex-TC Eline 2000 km across southern Africa. A strong ridge south of the Mozambique Channel, a preceding trough over southern Africa, and an easterly steering current at mid-levels promoted the unusual evolution and track of Eline. This cyclone was the longest-lived tropical storm observed to date in the region (about 29 days). They also indicated that another precursor for the synoptic conditions was a La Niña episode which produced favourable conditions for this event.

Naeraa and Jury (1997), using ECMWF data, studied the composite structure of TCs Daisy, Geralda and Litanne during 1993/1994 season while landfalling on the east coast of Madagascar. The potentially severe impacts of the three TCs on eastern Madagascar are apparent from their diagnostic analysis. Storm surge signatures of about 6 m and waves up to 10 m were reported to flood the nearest

coast, whilst heavy rainfall up to 500 mm per event inundated 300 000 ha of plantations.

As seen above, several issues concerning the climatology that were investigated on the global scale (Section 3.3.2) have been tested also for TCs in the SWIO. The results indicate relationships between ENSO and positions for formations and landfall, and possibly also in relation to other indices (QBO, MJO). A deeper thermocline favours TC activity (Xie et al., 2002). Increasing number of intense cyclones was also indicated although in the global overview (Webster et al., 2005).

3.3.4 TC genesis, SSTs and cyclone heat potential

Tropical cyclone genesis depends, as mentioned before on a variety of environmental factors. Over the sea, the minimum SST of 26-27°C and a large enough surface water heat content are the most important factors. Palmén (1948) found that TCs in the Northern Hemisphere were formed over the oceans with SST > 26-27°C. Gray (1968; 1979) has emphasized that the 26°C isotherm must extend down to a depth of 60 m for a TC to develop.

The minimum sea surface temperature is readily understood; if the water temperature is lower than the air temperature, sensible heat flux will transfer heat from the ocean. The surface layer will be more stable and the latent heat flux is likely to be lower as the air temperature was lower than SST. A warm enough mixed layer, is needed for at least two reasons; i) to prevent cool deeper water to reach the surface because of wind-mixing, ii) to support strong turbulent heat fluxes into the atmosphere. Leipper and Volgenau (1972) have emphasized the

Cyclone Heat Potential $CHP = \rho_w C_P \int_{z(T_{26})}^{0} T \partial z$ as a way to forecast TC genesis and development. Their results indicated that CHP in the Mexican Gulf waters vary strongly, but also that a certain CHP is needed to sustain a cyclone. Several

authors (e.g. Greatbatch, 1985) have pointed at the importance of the translation speed of the TC. If the cyclone is moving faster, less CHP is needed to sustain it. Today, the CHP is usually referred to as the Tropical Cyclone Heat Potential (TCHP), still using the same formula. As a very rough indication of the TCHP needed to initiate or sustain a tropical cyclone, values such as 50 $kJcm^{-2}$, are suggested.

There are large differences in the number of cyclones generated in different parts of the equatorial ocean (Fink and Speth, 1998). As indicated by the long-term mean SSTs, not only the minimum temperatures, but also the temperature itself, and the CHP may be important for these local variations (Mao et al., 2000; Liu et al., 2006). For example, there are many more cyclones produced in the North-West Atlantic Pacific (30%, Table 3.1) than in the North-West Atlantic (10%) and the South-West Indian Ocean (14%) which seems to correlate well with the occurrence of SSTs>27°C, even if evaluated as annual mean, only (Figure 3.1).

Looking at the seasonal variations in the surface temperature in the South-West Indian Ocean, it is readily seen from Figure 2.5b that SSTs during January-March became a maximum with SSTs>27°C down south to 20-25°S. Given the very thin mixed layer in the cyclone region (Figure 2.10) compared to most other areas of TC formation, one might expect the temperatures in the South-West Indian Ocean to be higher than the 27 or 26-27°C typically used.

By selecting SST data from areas of highest frequencies of cyclone formation in these regions, a high correlation between the number of cyclones and the Cyclone Heat Potential appears (Figure 3.6; Table 3.2). The figure shows temperature and salinity profiles from the regions and Table 3.2 shows CHP (for SST>26°C), bulk estimates of temperatures and depth to the 26°C-isotherm. Mean CHP in the North-West Pacific is 90 kJ cm^{-2}, compared to 36 kJ cm^{-2} for the North-West Atlantic and 39 kJ cm^{-2} for the South-West Indian Ocean.

The SSTs are also much higher in the North-West Pacific than elsewhere and the depth to the 26°C-isotherm about twice as large (Table 3.2). Given that background, one might ask whether the minimum temperatures for cyclone formation (and also the average temperatures) should actually be higher in the Atlantic and the Indian Ocean than in the Pacific, because of the apparently more shallow mixed layers. Particularly, such a hypothesis should apply to the Indian Ocean which comprises less buoyancy in the mixed layer than the Atlantic; in fact one might expect a considerable effect of low salinities due to river runoff from the Amazon and Orinoco River (Ffield, 2006). In the upper 40 m, ΔS in the Atlantic is in fact as large as its ΔT indicating that buoyancy due to salinity is 2-3 times larger than for temperature $(\beta / \alpha = 2.6)$. To investigate the relationship between cyclone formation and sea surface temperatures in the SWIO, TMI weekly SST and track info were combined to give temperatures and lat/long of formation for all cyclones between 1998 and 2005. These results are shown in Section 7.6.

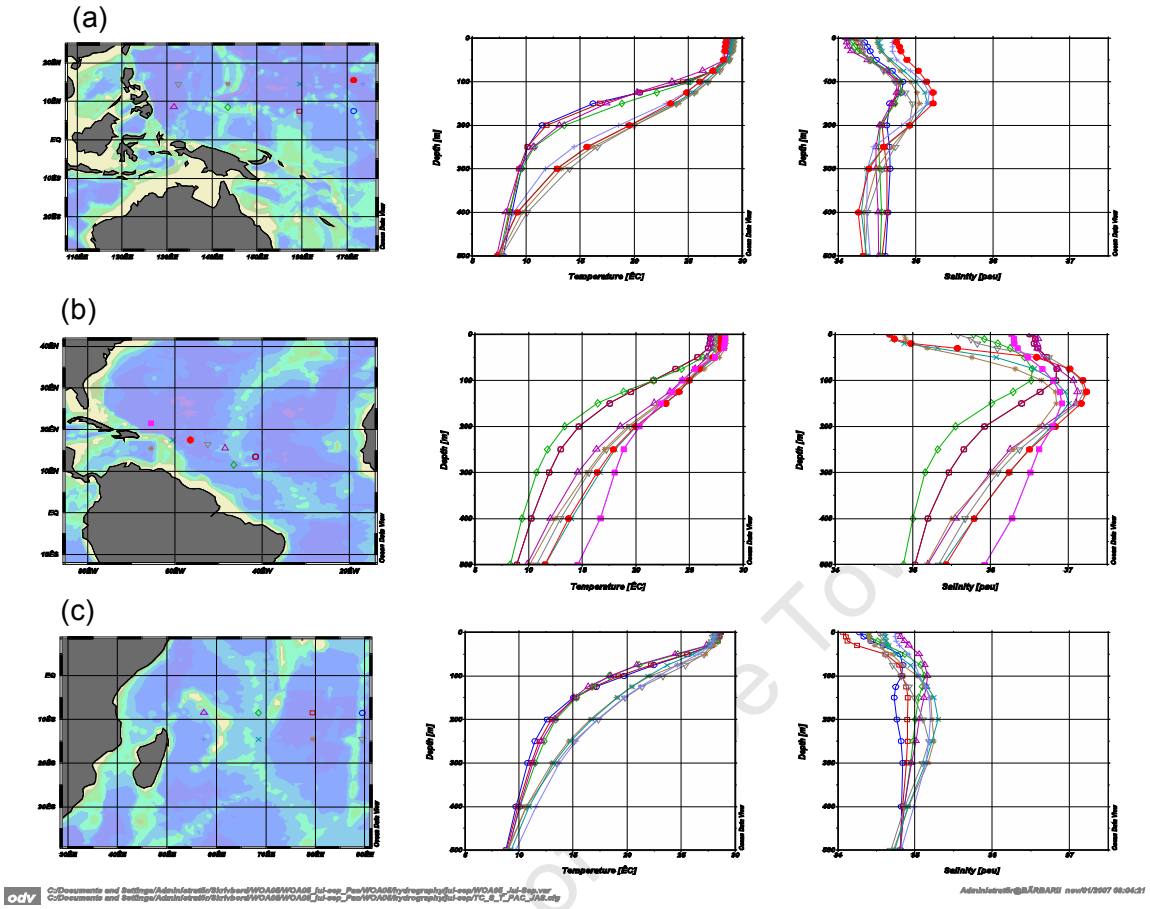

Figure 3.6: Temperature and salinity profiles for the North-West Pacific, North-West Atlantic and South-West Indian Ocean, during the peak cyclone seasons (January-March in the SWIO, July-Sep in North-West Atlantic and North-West Pacific; data from WOA05).

Table 3.2: The SST and long-term mean CHP in some TC regions. $\Delta T = SST - 26^{o}C$ *and* h *is the depth of the 26°C isotherm.*

For *T*=26°C	NW Pacific (Jul-Sep)	NW Atlantic (Jul-Sep)	SW Indian (Jan-Mar)
SST [°C]	28.8	27.9	28.2
ΔT [°C]	2.8	1.9	2.2
h_m [m]	95	60	50
CHP [kJ cm^{-2}]	90	36	39

3.4 Mixing, upwelling and sea surface cooling. Cyclone Intensification

Tropical cyclones, as mentioned above are formed over a warm ocean surface at temperatures above 26-27°C, and are driven by latent and (to a lesser extent) sensible heat fluxes from the ocean. However, strong winds related to the cyclones create large-scale mixing (with upward entrainment of underlying waters) and therefore, a simultaneous cooling of the sea surface underneath the cyclone (Figure 1. 3; Price, 1981). Moreover, in the track of the cyclone, intensive upwelling occurs due to a divergent wind field. Upwelling adds substantially to lowering SSTs (Greatbatch, 1985). In the vicinity of the cyclone track, SST may decrease by as much as 8°C (Emanuel, 1999). In comparison with cooling due to mixing and upwelling, loss of heat due to latent and sensible heat flux, is regarded comparatively small (10-20%; i.e. Price, 1981, Shay et al., 2000), and models of sea surface cooling usually neglect the loss of heat due to turbulent fluxes.

Sea surface cooling, in turn will hamper the latent and sensible heat fluxes. Thus, the pre-cyclone conditions within the surface waters (particularly the depth of the warm surface layer, i.e. the mixed layer depth) play a major role in controlling the intensity and development of the cyclone. A cyclone may intensify or decline, depending on the heat content underneath the sea surface. A deeper mixed layer with larger heat content might withstand longer, the effect of strong winds by hindering deep-going mixing. Leipper and Volgenau (1972) introduced the Cyclone Heat Potential (CHP), a quantity used to predict the potential for TC formation. In their original context, the CHP equals the heat content of the surface waters in which the temperature $T \geq 26^{o}C$, i.e.

$$CHP = \rho_w C_P \int_{z(T_{26})}^{0} T \partial z$$

where ρ_w is the water density and C_P the heat capacity of seawater. While, originally, calculations of the CHP (or TCHP) were based on buoy data and hydrographic cruises, the possibilities of using satellite data on sea surface

temperatures (SST) and even altimetry data has improved. Chambers et al. (1997) employed sea surface height anomaly data (SSHA, Δh) as a proxy for the ocean water heat storage anomaly, ΔH, i.e.

$$\Delta H = \frac{\rho_w C_P}{\alpha} \Delta h$$

while Shay et al. (2000) used a similar approach for explaining cyclone intensification (α is the heat expansion coefficient); areas of Δh >0 were shown to be related to warm core rings, to a deeper mixed layer, and to more efficient in release of heat to the atmosphere. The basis for their approach is the relationship between horizontal differences in steric height, Δh_s and corresponding variations in the temperature profile, where h is the level of no motion, and ΔT is the mean temperature difference:

$$\Delta h_s = \alpha \Delta T h$$

The subject is further discussed in Sect 3.4.2, but it's worth while to mention that the approach is subject to constraints, for example that in several TC regions, the salinity is almost as important as is the temperature for the stability of the water and it's likely that it's the stability of the mixed layer, rather than the temperature alone that prevents the surface water from cooling. However, one can foresee that SSHA in combination with SST might be used also for predictions of cyclone formation, as well as for studies of the relationship between TCHP/SST on one hand and cyclone frequency on the other.

As indicated above, there are three basic processes involved in cooling of surface waters underneath a moving cyclone; i) vertical entrainment due to wind-mixing, ii) upwelling due to wind divergence iii) net heat loss due to large turbulent fluxes at the sea surface. In addition, as TCs bring about extreme rainfall, which is also cold, rain may occasionally affect the SSTs. Cooling processes are discussed below in Sect 3.4.1. Intensification and decay in relation to SSTs and tropical cyclone heat potential is elaborated in Sect 3.4.2.

3.4.1 Sea surface cooling

Sea surface cooling is a process of utmost importance for the development of a tropical cyclone. If cooling is large, the cyclone is likely to decay, because not enough latent heat can be transferred from the sea surface. Sea surface cooling of the order of 1°C takes place in large areas around the cyclone (typically 1-250 kms), whereas, in the cold wake in the vicinity of the track, the SSTs may be much more decreased. As mentioned before, cooling of 7-9°C has been reported (Sakaida et al., 1998; Walker et al., 2005; Emanuel, 1999). Moist air is imported towards the centre of the TC from the larger area, which means that the large decrease in SST seen in the wake may not apply as a real restriction to intensifying of a TC.

Entrainment and upwelling

The theories developed by Chang and Anthes (1978), by Price (1981; 1983) and by Greatbatch (1983; 1984) have been successfully applied to various cyclones in the North Atlantic Ocean and particularly in the Gulf of Mexico. Several buoys and reconnaissance flights have helped to give necessary background information. Dickey et al. (1998) describes a Category 4 hurricane, Felix (hurricane diameter 300-400 km, translation speed 7 ms^{-1}) passing right across a mooring. Large inertia currents (>100 cm/s at 25 m) were generated with decay scale of 9 days. The mixed layer, strongly heated before the cyclone, increased in depth from 15 to 45 m and the temperatures decreased by 3.5-4°C. Large temperature oscillations with inertia period (15 m, 1.5°C) were seen in the mid-thermocline at 60-70 m depth. Shay et al. (2000) have given a similar description of Category 5 hurricane Opal, with 1-min winds exceeding 60 ms^{-1}. Shay et al. have calculated the turbulent (latent plus sensible) fluxes during a period of rapid intensification (14 h) to a maximum of 2-3000 Wm^{-2}. They also find an uplift of the thermocline in its deeper parts (175-200 m) of about 50 m; indicating the particular effect of upwelling. Sanford et al. (2007) and Lin et al. (2005) and several other papers focus on similar matters including intensification (see next section); further details will be taken up in the discussion (Chapter 8).

Greatbatch (1985) has compared entrainment velocity w_e and Ekman (or upwelling) velocity w_E in the wake of the cyclone. Using information on wind-stress, τ the diameter of the cyclone, Γ and the translation speed υ, he derived a dimensionless number $R_U = H_U/(H_m + \Delta h)$, indicating the relative importance of entrainment and upwelling in affecting the temperatures. H_U measures how much the MLD is reduced due to upwelling, Δh is the increase of the mixed layer due to entrainment and H_m is the undisturbed mixed layer depth before the cyclone). Using a set of numerical experiments by Chang and Anthes (1978), he has shown that the decrease in temperature is a factor $1/(1-R_U)^2$ larger than it would be if the entrainment model by Kraus and Turner (1967) was used.

Turbulent heat fluxes

Price (1981) has pointed out that cooling due to turbulent heat flux is small (10-15%) compared to cooling due to the exchange with the deep water, even though the loss of heat to the atmosphere is still quite large during a cyclone compared to normal values. During rapid intensification of TC Opal, Shay et al. (2000) have estimated (indirectly from the change in upper ocean heat content where cooling due to mixing was known) a net surface heat flux of 2-3000 Wm^{-2} (over a 14 h period). This is well above the flux needed to sustain a cyclone (4 $kcal/cm^2/day \cong 17\ kJ/cm^2/day$; Leipper and Volgenau, 1972) for an average translation speed of 5 ms^{-1}.

The turbulent heat fluxes are usually estimated from bulk equations (Section 6.1) using surface data obtained from numerical weather prediction (NWP), reanalysis outputs (e.g Kalnay et al., 1996; Kanamitsu et al., 2000), from the Comprehensive Ocean-Atmosphere Data Set (COADS; Oberhuber 1988; da Silva et al., 1994; Josey et al., 1999), from satellite data (Schulz et al., 1997; Zhang et al., 2004) or from combinations of these sources (Yu et al., 2004a).

Several studies have focussed on TC fluxes based on satellite observations (Guinn and Schubert, 1993; Schulz et al., 1996; Rogers et al., 1998; Jones et al., 2003). Rogers et al. (1998) have shown that a release of latent heat occurred in the eye-wall region of Hurricane Opal during intensification and decay stage.

Gautam et al. (2005) have analyzed latent heat flux Q_{LH} and precipitation, q_R associated with Hurricane Isabel and found that they are strongly coupled with the intensity variations of the TC along its track. Average values taken within a constant grid size of 5.4° x 5.4° area are found to be low, however; typically Q_{LH} =90-150 Wm^{-2}. When Isabel intensified from Category 2 to 5 latent heat flux values, Q_{LH} increased up to maximum values of about 450 Wm^{-2}. The latent heat flux, Q_{LH} became a maximum around the eye-wall, where maximum rainfall occurs. Also the average and maximum values of q_R and Q_{LH} follow a similar trend and are found to be high during TC intensification and also during the decay period.

Morey et al. (2006) employed a coupled ocean and boundary layer flux model to study the upper ocean response to surface heat and momentum fluxes associated with Hurricane Denis (2005) in the Gulf of Mexico. Model results indicated that surface fluxes are primarily responsible for widespread reduction (0.5°-1.5°C) of SST over the west Florida shelf 100-300 km away from the storm center. Momentum fluxes are responsible for stronger surface cooling (2°C) near the center of the storm. The upper ocean heat loss near the storm centre of more than 200 MJm^{-2} (or roughly 2200 Wm^{-2} if the loss is distributed over 24 h) is primarily due to the vertical flux of heat between the surface layer and the deep ocean. Heat loss to the atmosphere during the storm's passage is approximately 100-150 MJm^{-2}.

Mixing in the ocean, effects on volume and heat flux in global perspective.

An interesting question in relation to the large fluxes of heat during TC events is whether cyclones may contribute substantially to fluxes on the global scale. Using the concept of temperature T as an independent variable (see Walin, 1982), variations in the oceanic temperature field, due to entrainment may be translated into volume and heat fluxes across isotherms. Based on that concept Nilsson (1995; 1996), calculated the average cross isothermal volume flow, produced by cyclones. Nilsson applied the method to Atlantic TCs from 1983-1992. Roughly 20% were selected at random and for each, the cross isothermal volume flow was calculated. The average cross isothermal volume flow describes how the cyclone-induced entrainment redistributes water masses and heat in temperature space (Figure 3.7). The results indicate that the TCs mix water in the temperature interval between 18°C and 29°C. Above 24°C, the cross isothermal volume flow is directed towards lower temperatures and vice versa below 24°C and the strength of this flow is about 0.5×10^6 m^3s^{-1}, whereas the adherent diffusive heat flux is estimated at 4×10^{12} W.

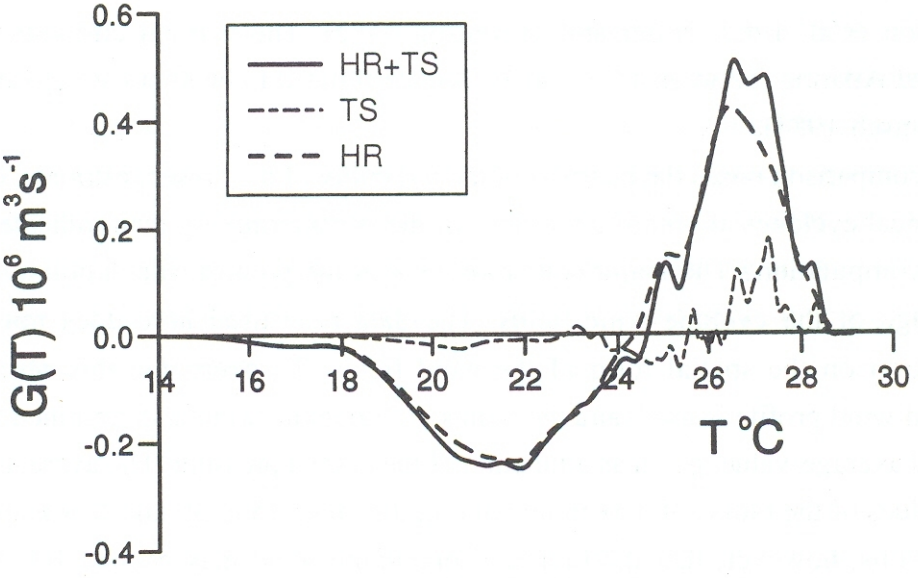

Figure 3.7: Average cross isothermal volume flux by TC-induced entrainment in the Atlantic Ocean between 1983-1992, *G(T). Mixing by tropical storms (TS, wind speed* >18 ms^{-1}*) and Hurricanes (HR, wind speed*>33 ms^{-1}*) are shown separately. Where G(T) is negative, the volume flow across the isotherm is directly towards increasing temperatures, and vice versa where G(T) is positive.*

It's obvious that the fluxes are small if compared to global volume (and even heat transports), however the figure is of interest as it can serve as an indication on how mixing takes place at different levels. Also, the results can be used to compare similar results for individual cyclones.

Cold rain effects on SST and on TC landfalling

Anthes (1982) has discussed estimates of oceanic temperatures changes due to processes other than upwelling and mixing. Among other processes that may affect the oceanic temperature, cooling by heavy precipitation is of some interest. He has estimated the cooling due to precipitation, P, assuming that a temperature change occurs uniformly over a depth H. If ΔT is the temperature difference between the sea and raindrops, the change in sea temperature equals

$$\Delta T_{sea} = \frac{P\Delta T}{P + H}$$

For typical values of P = 0.1 m and ΔT =10°C, and a depth H of 50 m, ΔT_{sea} is only 0.02°C, thus, Anthes concluded that the effect of precipitation on modifying the sea surface temperature is negligible. However, heavy rainfall may also have some impact on SST measurements and the SSTs can be affected because freshwater is likely to stay on top. Liu et al. (2006), while studying the ocean response to TC in northwestern Pacific using Argo/NCEP data, calculated the precipitation rate of the period (10 days) when a cyclone passed and concluded that a freshening of the mixed layer occurred in association with the total rainfall of about 92.7 kg/m^2. Accordingly there should be a decrease of the salinity (following the formula above), of $\Delta S_{sea} = -0.07$ psu, a change which adds to the stability of the surface water. For some of the TCs in the SWIO, rainfall data from the tropical rainfall mission satellite (TRMM) were used for studies of the immediate response to cyclone winds in Chapter 8.

Rainfall is found to be heaviest in a TC's inner core, within a degree latitude from the centre, with lesser amounts further away from the centre (Anthes, 1982). However the actual rainfall falling at a point during the passage of an individual cyclone depends on many factors besides the maximum intensity of rainfall. Anthes (1982) indicated that the location of the point with respect to the storm track, the distribution of rainfall around the storm, the translation velocity of the cyclone, and local effects such as topography and orientation of the coast all are important in producing the observed variability in measured precipitation.

3.4.2 Tropical cyclone intensification

The paper by Shay et al. (2000) describes how warm rings (or warm eddies) can cause rapid TC intensification. An area of warmer water, such as a warm (anticyclonic) eddy, may boost the cyclone by hindering cold water from reaching the surface, thereby sustaining a high turbulent heat flux. The depth of the 26°C isotherm in the core of a warm eddy will reach to greater depths than those of the surroundings (Goñi and Trinanes, 2003). TC Opal intensified with its passage over one such warm eddy, during which the MSW in 14 h increased from 35 to > 60 ms^{-1}. Altimetry-derived fields indicate that the increase in TCHP associated with this warm ring was approximately 30 $kJcm^{-2}$. Goñi and Trinanes give several examples on rapid intensification, i.e. TC Mitch which occurred in the Caribbean Sea in October 1998, intensified from Category 3 TC to a Category 5 TC in 22 hours (1-min sustained winds > 69 ms^{-1}) when its track travelled over a region of warm waters with increased values of TCHP of about 80 $kJcm^{-2}$. TC Bret which occurred in the Gulf of Mexico in August 1999, intensified several times in the South West Gulf over a period of ~36 hours while travelling over two warm feature remnants of a warm ring that had been shed by the Loop Current several months earlier. The increase in TCHP under the track of the TC during this period was also large, about 80 $kJcm^{-2}$. Typhoon Imbudo which occurred in the western Pacific in July 2003, intensified from Category 1 (33 ms^{-1} sustained winds) to Category 4 (66 ms^{-1} sustained winds) during a period of only 12 hours

on 20 July, when its track crossed a region of excess TCHP of almost 100 kJcm^{-2}. The upper ocean exhibited a cooling (decrease of TCHP values) of 60-100 kJcm^{-2}, with SST decreasing by 3-4°C, along the track. Similarly the depth of the 26°C isotherm was lifted by 25-100 m due to mixing, upwelling and latent heat loss (Goñi and Triñanes, 2003).

Lin et al. (2005) and Erb (2006) have shown similar rapid intensifications of two very disastrous cyclones Maemi, and Katrina, respectively. Thus, by exploring sea surface height anomalies (SSHA) it should be possible to predict the potential for tropical cyclone formation, and also to evaluate conditions for a specific cyclone to experience rapid intensification (or decay if a cold eddy is at hand). Sadhuram et al. (2004) have studied the seasonal variability of TCHP in the Bay of Bengal using CTD data from cruises and Levitus climatology (1982), i.e. the World Ocean Atlas. The authors found high values (>30 kcal cm^{-2}) of CHP coinciding with anticyclonic eddies and the low values of CHP (16 kcal cm^{-2}) coinciding with cyclonic eddies. It is also found that TCHP is >14 kcal cm^{-2} over the Andaman Sea and the southern and central Bay of Bengal (where the generation and movement of cyclones take place during post south-west monsoon season, October-November). These are surprisingly low values when comparing to figures appearing elsewhere, but there are at least two factors to consider in addition; i) there are few cyclones in the Bay of Bengal, and probably TCHP is well above the climatology mean, when they appear and ii) there is a lot of freshwater in the Bay of Bengal, particularly in the months of October-November, which means that the surface stability is larger than what appears through the temperature gradient alone.

Altimetry and its use in evaluation of the surface water heat storage and mixed layer depths, and how to estimate TCHP is discussed below. The structure of warm and cold eddies is also indicated. Leipper and Volgenau (1972), as mentioned above first proposed TCHP which is defined as a measure of oceanic heat content from the surface to the depth of the 26°C isotherm. This value is

chosen since it represents a threshold temperature suggested for tropical cyclone genesis by Palmén (1948), which corresponds to mean wet-bulb temperature. The need for a local approach to determine TCHP is elaborated here in terms of the shape of warm and cold eddies, respectively, features typical for the Mozambique Channel.

Eddies, SSHA and TCHP

Unlike their counterparts in the atmosphere, eddies in the ocean are not easily discernible. This is particularly true for warm eddies (or warm core rings). Owing to the dominance of incident sun radiation (Section 6.1), during summer and in the tropics and little wind, the ocean surface here usually exhibits more or less uniform high temperatures.

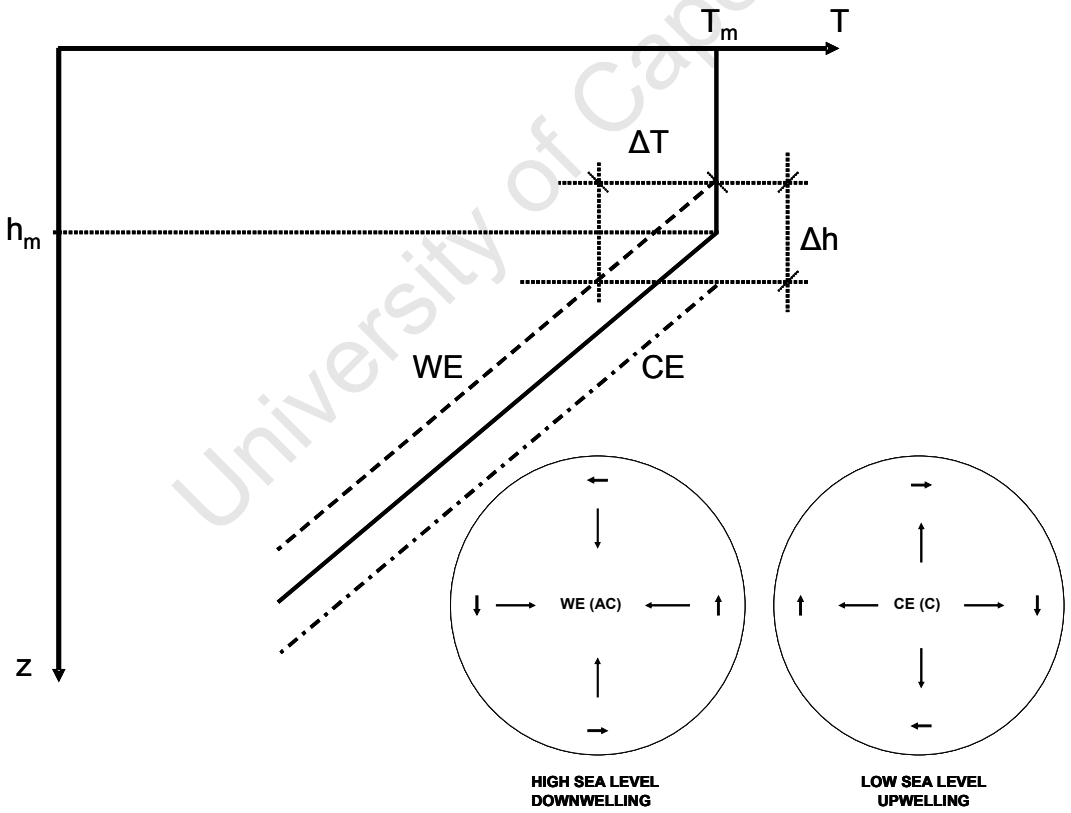

Figure 3.8: Illustration of the temperature profile under a warm (WE) and a cold eddy (CE), respectively. At the surface, the CE is depressed with a cyclonic motion around its centre, while in the WE, the surface is elevated and the motion is anticyclonic.

Eddies are more readily seen by observing the features associated with them, basically sea surface elevation or depression at the centre, and the related rotational velocities. The advent of remote sensing altimetry has provided the opportunity for such assessment. Elevation or depression due to a warm or a cold eddy (Figure 3.8) respectively, can be estimated from altimeter observations.

Figure 3.8 illustrates the features associated with warm and cold eddies, respectively. At the surface, the water in the cold eddy is depressed with a cyclonic motion around its centre, while in a warm eddy, the surface is elevated and the motion is anticyclonic. The cold eddy is associated with a shallow thermocline, the warm eddy with a deep thermocline. Mixing, basically due to winds at the surface will cause entrainment (erosion of the thermocline). Therefore, low surface temperatures will easily appear in a cold eddy (see Figure 3.9A), whereas erosion of the same intensity over an area of a warm eddy will also result in lower temperatures (but not of course to the same degree, because of the deeper thermocline).

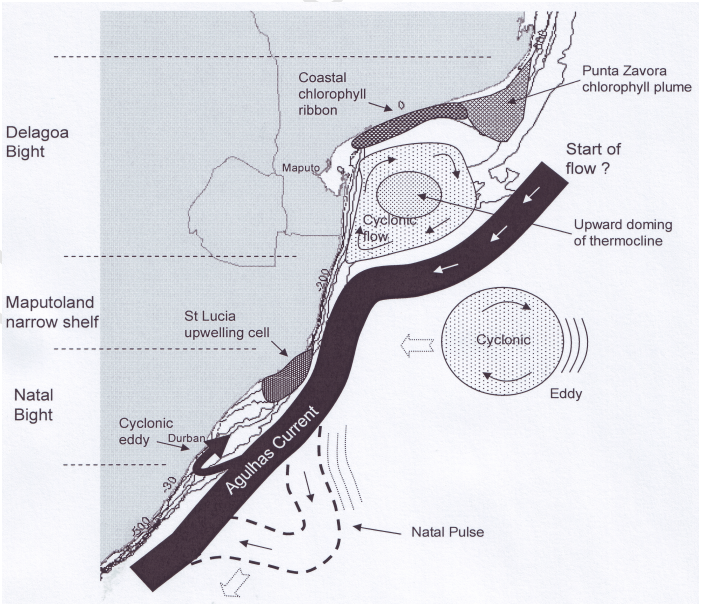

Figure 3.9A: A huge eddy in the Delagoa Bight (from Roberts, 2008) in the southern Mozambique Channel is described by Sætre and Jorge da Silva (1984). A similar large semi-permanent cold eddy, described by Lutjeharms (2006a) seems to exist off the Mozambique coast further north at Angoche (after Lutjeharms and Jorge da Silva, 1985).

However, the warm eddy with its downwelling water may still appear warm at the surface but not because of wind mixing. In case the water in a warm eddy is warmer than its surroundings at the sea surface (which is unlikely), this feature is related to sea surface heat fluxes and surface advection (for this reason the western Pacific is warmer than the eastern).

The difference in sea level or the difference in steric height (dynamic depth) between a cold and a warm eddy $\Delta h_s = \alpha \Delta T h$ is readily calculated if the depth, h to which these eddies reach, is known. For eddies typical of the Mozambique Channel h =1500 m and the difference in temperature between the warm and the cold eddy is ΔT =1°C. Then, one finds Δh_s = 45 cm (see Figure 3.10). If ΔT =1°C, it means a difference in MLD (see Figure 3.9B), Δh =15 m (assuming that $\partial T / \partial z$ =1/15). At the same time, it is obvious that the use of altimetry data for estimating variations in mixed layer depths or cyclone heat potential is quite straightforward, and that the statistic analysis foregoing the work of Goñi and Trinanes (2003) and others is quite satisfactory. Sect 6.2 gives similar but alternative way to obtain a relationship between Δh_s and Δh.

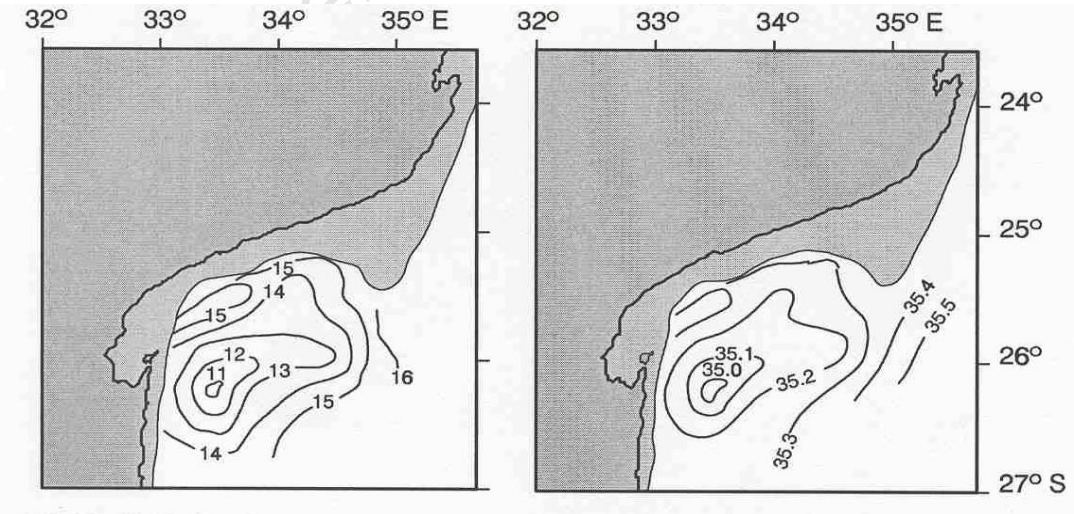

Figure 3.9B: Distribution of the temperature and salinity at a certain depth that show the presence of an eddy in the Delagoa Bight in the southern Mozambique Channel (from Lutjeharms, 2006a).

Current observations undertaken below the thermocline during ACSEX-I revealed the existence of a Mozambique undercurrent flowing along continental slope (Figure 10a). De Ruijter et al. (2002) have found that the current flows equatorward when it moves inshore the eddies and it is characterized by two cores. One is at intermediate level, where speeds range between 0.1 and 0.3 ms^{-1}. It weakens northward (Figure 10b), while carrying Antarctic Intermediate Water (AAIW) along the continental slope. At 24°S it stands out by marked salinity minimum (de Ruijter et al 2002). The other core is below 2000 m, where it has maximum equatorward speeds near 0.2 ms^{-1} (Figure 10a). This narrow jet carries North Atlantic Deep Water (NADW) northward, as can be deduced from its relatively high salinity and high oxygen concentration. The under current is roughly estimated, 5 Sv at 24S of which some 2 Sv is in the NADW-core

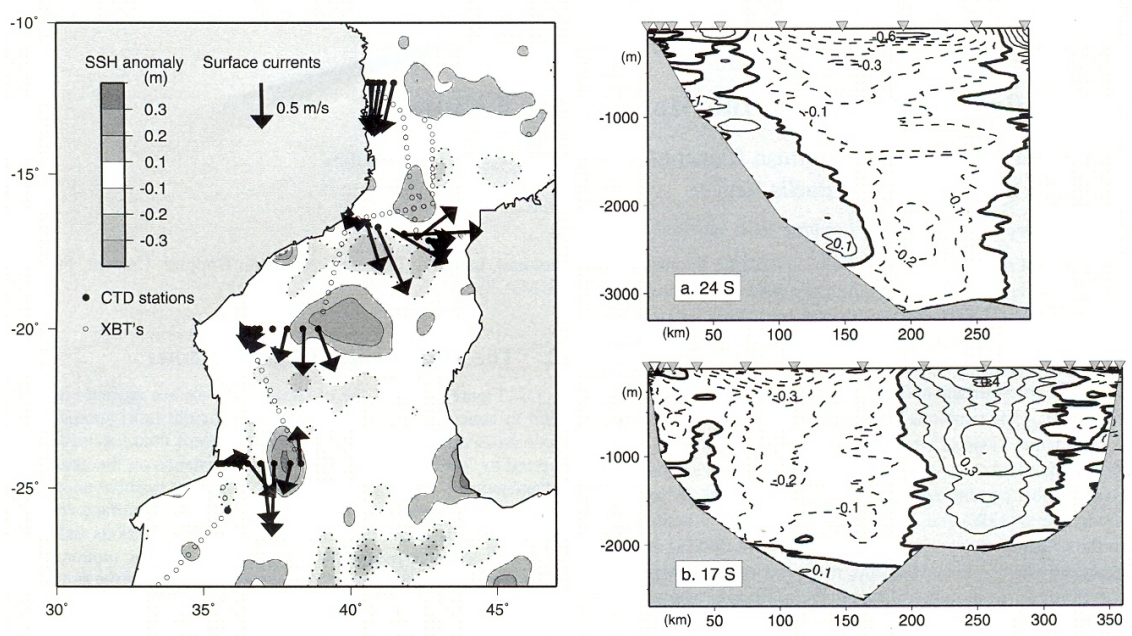

Figure 3.10: (left panel) Surface currents, averaged over the upper 200 m and sea surface height anomalies measured by altimetry (merged T/P and ERS2) during the ACSEX I in the Mozambique Channel (20 March–13 April 2000). (right panel) LADCP observed meridional velocities at (a) 24°S, the centre of the eddy is about 260 km offshore and at (b) 17°S, the anticyclonic eddy appears to fill almost the cross section. Both currents and SSHAs show the dominance of a train of anti-cyclonic eddies in the Channel (from de Ruijter et al., 2002)

Chapter 4: Research questions

1. Globally, climate change has affected research issues in relation to tropical cyclones. Today there is a large interest in how a warmer climate will impact frequency and size of cyclones, but also in how stages of ENSO affect cyclone occurrence. These issues will be addressed here; however some more basic questions concerning the statistics will be given priority. These are;

a. What are the spatial and temporal distributions of tropical cyclone landfalls in the area of Mozambique and Madagascar?

b. What are the typical intensities and frequencies?

c. Is there a change in frequency or intensity during the last 20-30 years or, in landfall over the last 50 years?

2. TCs may form in areas where SSTs $\geq$27°C, with a CHP $\geq$50 kJ cm^{-2} as an additional constraint. The SST conditions may not apply to the SWIO, and particularly not to the Mocambique Channel, where the mixed layer depths are small, compared to other TC regions, typically 30 m only, and with CHP typically less than 50 kJ cm^{-2} during the cyclone season. Shallow mixed layer indicates that one might expect the minimum temperatures to become higher. Thus, SSTs and CHPs are compared to those of other regions of cyclone formation, investigating particularly;

Which are mean and the minimum SSTs required for formation of cyclones in the SWIO and the MC, and what is the relationship to the MLD and the CHP, respectively?

3. Satellite data on SSTs, winds and rainfall from the latest decade are of high quality. Improvements in the satellite observations of sea surface topography and recent ARGO profiles in addition, have improved our possibilities to map the upper ocean structure, and also to understand mixed layer dynamics under shifting conditions (incl. cyclone passages). Investigations of sea surface cooling

in the wake of selected cyclones are carried out here, with the aim to distinguish between the different physical processes (turbulent heat fluxes, wind-mixing and upwelling due to wind divergence), which creates this cooling. Thus,

a. How large is the loss of heat in the surface water in the course of the cyclone passage in the Mozambique Channel?

b. What is the relative importance of cooling due to turbulent heat fluxes, compared to vertical mixing and advection?

c. Is rainfall likely to have an impact on SSTs?

d. If no sign of anomalous SSTs can be seen after a couple of weeks, what is then the impact of the cyclone – is it possible to estimate a "true net heat flux" from the surface water or an overall transport of deep-water towards the surface and relate to a net flux of heat southwards caused by the cyclone?

4. It has been recently shown that warm (and cold) eddies are frequent within the Mozambique Channel (and in the vicinity of Madagascar), and it may be that these features affect intensification of the cyclones. Thus, it may be asked:

a. Does rapid intensification of TCs coincide with warm eddies?

b. Is it possible to indicate the occurrence of rapid intensification from mapping of the sea surface height (as a proxy for CHP) and SST during the passage of particular TCs?

c. What is the role of the atmospheric environmental factors (such as a weak vertical shear) in creating rapid intensification?

It is the overall aim of this thesis also to produce the basis for improved cyclone predictions, such that real time maps of SSTs and SSHAs can be used, for example, in order to determine better based indications for cyclone intensification or decay.

Chapter 5: Data description, Methods and Tools

"Good science is impossible without good data. Checking the quality of your data is therefore as important as using the right tools for their interpretation."
-Matthias Tomczak, *2006*

5.1 Introduction

Chapter 5 discusses data and data sources used in this thesis. Although the study is largely based on satellite products, such as i) surface winds from scatterometry, ii) sea surface heights from altimetry, and iii) SSTs and rainfall from radiometry, other types of data are also employed. These include iv) tropical cyclone track data (giving maximum sustained wind of the cyclone, its position etc), basic statistics for cyclone and a selection of cyclones for case studies, but also v) atmospheric data, and vi) climatology data on e.g. turbulent heat fluxes. Salinity and temperature climatology, Argo data and selected cruise data, are used in addition to verify model studies and to validate satellite data.

There are numerous satellite data and data products available from various sources. These products have been continuously changing over the last 30 years (i.e. the period for which the TCs are studied). Thus, it's obvious that source selection is crucial for the results. The introduction (Section 5.1) deals partly with that problem, but in fact, the selection of relevant data is part of this whole chapter. More information about the data presented in this Chapter is shown in Appendix A (Tables A1-A7).

5.2 Cyclone track data

In order to improve the record on TC track data from the SWIO (with the aim to study land-falling frequency and TC genesis), a merging procedure using LR-RSMC (La Reunion – Regional Specialized Meteorological Centre) and JTWC

(Joint Typhoon Warning Centre) data in combination, has been carried out. This procedure created some basic problems because the two data sources are using different scales for determination of cyclone intensity. The intensity of a tropical cyclone is usually determined on the basis of the Maximum Sustained Wind (MSW; Emanuel, 2005; Olander and Velden, 2007). This, in turn, is estimated, (since the 1970s) from satellite imagery, using the Dvorak technique (Dvorak, 1975). The technique and the adherent scale are explained in Section 5.2.1. However, the periods used for measuring wind speed are different in different regions of the world (but typically either 1-min or 10-min average). This creates a problem when comparing TC track data. The Saffir-Simpson intensity scale (Section 5.2.2), for example was calibrated against ground truth wind data in the North Atlantic TC region (with some regional differences, but using the 1-min average wind). For TCs in the SWIO, the regional TC centre, LR-RSMC adopted a regional *scale* (Section 5.2.2), calibrated against 10-min average wind. A comparison between JTWC (where JTWC hosts a TC record for the SWIO but using the Saffir-Simpson scale) and LR-RSMC data will thus indicate fewer and weaker cyclones (in the SWIO) in the LR-RSMC record.

The Dvorak technique, used to determine MSW and cyclone intensity is based on interpretation of satellite imagery (and data). It has been employed since the 1970s (Dvorak, 1975; 1984), and is explained in current section. Alignment between the Dvorak intensity scale and flight reconnaissance MSW (used in the North Atlantic), including the Saffir-Simpson Scale, used at JTWC and the Regional Scale at LR-RSMC, are also described. Track data are used to study TC landfall frequency and its regional distribution in the SWIO, but also formation areas (and their SSTs) and variability in TC frequency (and intensity) relation to global warming and ENSO-like phenomena. The climatology is also used for selection of some tropical cyclones for special studies in relation to intensification and sea surface cooling.

The primary dataset used here is a subset for the SWIO (0-40°S; 30-100°E) of the best track data from Joint Typhoon Warning Centre (JTWC, 2006) website. It covers the period from 1950-2004. For the most recent TC data (2004-2007), records from Unisys Weather (UNYSIS, 2007) were employed in addition. The second dataset is from La Reunion – Regional Specialized Meteorological Centre (LR-RMSC, 2003), which offers data from 1950-2003 (however, from November 2007, data are available also from 2004-2007). La Reunion provides 6-hourly cyclone position (lat and long), MSW (10-min average) and Minimum Sea Level Pressure (MSLP), while the JTWC archive contains centre locations (lat and long) and MSW (1-min average), also at 6-hourly sampling frequency. MSLP is available, but only from 2002 (Chu et al., 2002). The JTWC best track data are based on (i) the National Climate Data Centre (NCDC) data base, (ii) the Fleet Numerical Meteorological and Oceanographic Centre (FNMOC) data base, and (iii) the Automated Tropical Cyclone Forecasting System (ATCF) data base (Sampson and Schader, 2000).

When merging the two datasets into a unified climatology for the SWIO, it was possible to find missing or erroneous data (even cyclones in some cases!) in both sources. The new product gives TC records in terms of position, translation speed, size, MSW and MSLP (mean sea level pressure), of what is assumed to be all cyclones from 1978-2007, accounting for the difference in estimating MSW, as mentioned before. Cyclone data were collected also for the whole period back to 1950. However, old data are not good enough for comparing statistics between different regions; in fact only the last 20-30 years are really reliable (e.g., Landsea, 2000; Webster et al., 2005; Landsea, et al., 2007).

Because, as mentioned before, the Saffir-Simpson Scale was used with JTWC record, and the Regional Scale with the LR-RSMC record, cyclone intensity comes out different for the same cyclone. A conversion factor is used to make intensity (MSW) data comparable. The two scales, including also the use of Dvorak technique, and other basic issues, are described below in Sect 5.2.1-3.

The new TC Climatology is used to study land-falling frequency and TC genesis in relation to SSTs etc, but also to select some prominent TCs for special studies.

5.2.1 Cyclone intensity. Dvorak Scale

Cyclone Intensity (CI) is defined either in relation to the MSW or from the MSLP at the centre (Sampson et al., 1995; Chu et al., 2002). As mentioned, CI is estimated indirectly from satellite images including infrared imagery. At very rare occasions, ground truth data from buoys (either MSW or MSLP) or Reconnaissance Flight (RF) are available. However, RF are used regularly only in the North Atlantic (and occasionally in the North-West Pacific), which means that for the main part of the TCs in the current region of interest there are no RF data at all. Moreover, as the TC records include data from every six hours along track, it's obvious that even in the case of an existing RF, data are available only for parts of the track.

The satellite era, starting in the late 1960s, made it possible to follow TC tracks and development, and thereafter, satellite imagery has become the basic tool for estimating CI. The commonly used method was developed by the American meteorologist Vern Dvorak. Despite rare RF data (and observations from ships and weather stations) back to the 1950s, it's obvious that records prior to 1950/60s are not very useful, in case one is looking for cyclone statistics and similar issues (e.g. Holland, 1981, 1993; Landsea, 2000). The Dvorak technique has been in use since 1968, but, since then, it has been gradually developed (e.g. Dvorak, 1975; 1984, http://www.aoml.noaa.gov/hrd/tcfaq/H1.html). A recent debate on cyclone intensity/frequency in relation to global warming has been based on 30-year records, typically 1975-2004, but some authors (i.e. Webster et al., 2005) have argued that safe TC track data exist only for the last 20 years. Anyhow, the Dvorak technique to estimate CI is based typically on the following procedures for evaluating signatures from the cloud features, seen from satellite imagery, i.e.;

i. *Several cloud patterns have been established which determine the most common development stages of cyclones.*

ii. *Several cloud parameters are considered, for example the size of spiral bands, the diameter and the shape of the central cloud mass, the diameter and the embedded distance of the eye, the degree of shear.*

iii. *The scheme utilizes the difference between the temperature of the warm eye and the surrounding cold cloud tops and their distributions around the cyclones. The larger the difference, the more intense the cyclone is estimated to be.*

iv. *This analysis compared to that of previous pictures makes it possible to classify the cyclone on an intensity scale. A current intensity number (CI) is allocated to the cyclone.*

Table 5.1: Dvorak Cyclone Intensity (CI) calibrated against MSW (1-min average) and MSLP. Calibration data are according to RF data. The lower MSLP in the North-West Pacific compared to the North Atlantic (NA) is due to lower mean SLP. 10-min MSW is added for comparison with the regional Scale (Table 5.3). A conversion factor of 0.88 is used to obtain 10-min MSW from 1-min MSW.

CI number	MSW (10-min) [Knots]	MSW (1-min) [Knots]	MSLP (NA) [hPa]	MSLP (NWP) [hPa]
1.0	22	25	-	-
1.5	22	25	-	-
2.0	26	30	1009	1000
2.5	31	35	1005	997
3.0	40	45	1000	991
3.5	49	55	994	984
4.0	57	65	987	976
4.5	68	77	979	966
5.0	79	90	970	954
5.5	90	102	960	941
6.0	101	115	948	927
6.5	112	127	935	914
7.0	123	140	921	898
7.5	136	155	906	879
8.0	150	170	890	858

A calibration between the Dvorak CI number, determined from satellite imagery and ground truth data provided by RF is shown in Table 5.1. As seen, there is a rather large difference MSLP between the North-West Pacific TC region and that of the North Atlantic (1-min wind; Martin and Gray, 1993), which is because the mean sea level pressure is some 10 hPa lower in the Western Pacific.

In the South-West Indian Ocean, RF data are not available, and wind data from weather stations are based on 10-min average. Therefore, until recently, different criteria in defining TC intensity are found in the literature (e.g Chaussard and Laplace, 1964; Ecormier, 1992; Camberlin and Shanko, 1998). This led to discrepancies in TC numbers and intensity as the obvious outcome (Jury, 1993). However, in Anonymous (2000), looking at the scarce observations recorded in vicinity of TCs (the likelihood of the centre of a TC passing just right over an observing point being extremely low), it was assessed that the calibration, designed for the North-West Pacific was most appropriate for the SWIO, as suggested by WMO in its Operational Plan. This scale, shown in Table 5.2, was adopted by the La Reunion TC centre (LR-RSMC) in forecasting and recording.

Table 5.2: The South-West Indian Ocean intensity scale (Anonymous, 2000)

System	Cat	Gust	MSW 10-min			Approx. MSLP	Damage
		(kmh^{-1})	(knots)	(ms^{-1})	(kmh^{-1})	(hPa)	
TDi	-	-	<27	<14	<50	1000 - 999	-
TDe	-	-	28-33	14-17	51-62	998 - 996	-
MTS	1	90-124	34-47	17-24	63-88	995 - 983	Minor
STS	2	125-165	48-63	25-32	89-117	984 - 970	Moderate
TC	3	166-233	64-89	33-46	118-165	969 - 940	Major
ITC	4	234-299	90-115	46-59	166-212	941 - 906	Devastating
VITC	5	>300	>115	>59	>212	905 - 858	Extreme

TDi: tropical disturbance; TDe: tropical depression; MTS: moderate tropical storm; STS: severe tropical storm; TC: tropical cyclone; ITC: intense tropical; VITC: very intense tropical cyclone

Multiplication factors formerly used in the SWIO were 0.8 (to convert between 1-min and 10-min) and 1.50 (for the ratio of maximum gusts to mean 10-min MSW). According to Anonymous (2000) the conversion factor of 0.8 was revealed to stand quite far from the conversion factors used in other basin centres working with 10-min. The main consequences of modifying the scale of correspondence were to shift the Dvorak intensities towards higher wind speeds. For instance a system getting the current intensity of 4.5, on the Dvorak scale (Table 5.1), which was formerly classified as a severe tropical storm, would now rank as a tropical cyclone (Table 5.2). Intensities of 4.0 or less are for tropical

depressions or storms, those of 4.5 or, more are for TCs. The numbers 6.5 to 8.0 are specifically dedicated for very intense cyclones.

5.2.2 The Saffir-Simpson Scale

Hurricanes (i.e. TCs with MSW > 33 m/s) in the North Atlantic are classified by their damage potential according to the Saffir-Simpson Scale (Simpson and Riehl, 1981). This scale, shown in Table 5.3, was developed in the 1970s by the US National Weather Service to give public officials usable information on the intensity of a storm in progress. The scale has five Hurricane categories, starting with Category 1 at MSW 33 ms^{-1}. Tropical storms are cyclones below Category 1 with wind speeds of 18-32 ms^{-1}. The Saffir Simpson scale has become commonly used for TC track data in combination with the Dvorak technique. For example, JTWC keep their TC track data from SWIO using the Saffir Simpson scale, with 1-min MSW and the MSLP according to the calibration for the North-West Pacific (Table 5.1).

Table 5.3: Saffir-Simpson Scale (Saffir and Simpson, 1974).

System	Cat	MSLP	MSW 1-min			Surge	Damage
		(hPa)	(ms^{-1})	(knots)	(kmh^{-1})	(m)	
T. Depression	TD	-	≤ 17	≤ 34	≤ 61	-	-
T. Storm	TS	-	18-32	34-63	65-115	-	-
Hurricane	1	>980	33-42	64-83	119-151	1-1.5	Minimal
Hurricane	2	979-965	43-49	84-95	155-176	2-2.5	Moderate
Hurricane	3	964-945	50-58	96-113	180-209	3-3.5	Extensive
Hurricane	4	944-920	59-69	114-135	212-248	4-5.5	Extreme
Hurricane	5	<920	>69	>135	>248	>5.5	Catastrophic

1kt=1.852 km/h=0.514 ms^{-1}

Here, when merging of the JTWC and the LR_RSMC data into one TC climatology for the SWIO, it has been taken into account that wind data are based on 1 and 10 min average respectively, using the conversion factor in Table 5.1. Also, because the Saffir Simpson scale is used world wide to classify intensity of TCs, the climatology will refer to intensity according to this scale.

5.2.3 Merged TC climatology

As mentioned before, a tropical cyclone database was constructed by merging JTWC and LR-RSMC for the TC seasons from 1979/1980 to 2006/2007 taking JTWC as a basic sample. To check for systematic differences between JTWC and LR-RSMC time series frequency, a full inspection of all cyclones present in both datasets were performed. From that it was concluded that JTWC had fewer missing values (except for MSLP). Before 1979/80 there were many missing values. In some cases, cyclones had escaped notice completely in one of the databases. However, data back to 1950's were still merged to look at land-falling cyclones alone (some 20% of the total). Thus, two basic data bases were constructed, one for the years 1952-2007, and one for 1980-2007, covering 28 and 56 TC seasons respectively; where the series 1980-2007 runs from November 1979 to April 2007 and the 1952-2007 series covers TCs from November 1951 to April 2007.

Traking of cyclones

All tropical cyclones that reach storm intensity, i.e wind > 17 ms^{-1} are included in the analyses. Tracking and grouping of cyclones were performed manually based on input the data from JTWC and LR-RSMC and a self are constructed tracking program written in Matlab programming language. The method has to account with the variable-length of data which is common in individual cyclones. Much work was needed to organize and perform quality control of these impaired datasets. The results of these analyses were then used to generate statistics on monthly and yearly basis such as genesis locations and rate, geographic distribution, cyclone life time, categories and track orientation. Cyclones appearing outside the cyclone season, i.e. November-April and those with missing wind and pressure observations were discarded (mainly valid for the years 1952-1979). Appendix B2 gives details on the criteria used for temporal distribution of cyclones and their classification. This method is somewhat tedious but it is simple and independent of a fixed dimensional representation of the cyclone data. Alternative methods for tracking includes a number of different

schemes such as nearest-neighbour search (e.g. Blender et al., 1997), numerical prediction schemes with cost minimizing optimizations (Murray & Simmonds, 1991) and image-based feature tracking methods (e.g. Hodges, 1995). Blender et al. (1997) introduced the idea of K-means to cluster cyclone trajectories of fixed length. To apply K-means to cyclone trajectory data, one must convert the variable-length trajectories into fixed-dimentional vectors. This type of vector based clustering has limitations when applied directly to cyclones. Trajectories of different lengths do not admit a fixed-dimentional representation unless truncated in some manner, which results in a potential loss of useful information. To overcome this problem a methodology using curve clustering models has been applied to cyclone clustering in GCM settings (Camargo and Zebiak, 2002). Further details of this method can be found in Gaffney (2004) and Gaffney (2007), where the method was applied to North Atlantic extra-tropical cyclones.

Landfall of cyclones

The original data do not contain a full record of TC events by landfall locations, so a data base of land-falling tropical cyclones (including position, maximum wind, minimum sea level pressure) in the area of Mozambique and Madagascar was also produced. Having focused on tropical cyclone impact at landfall, a statistical approach is made to reproduce landfall locations according to the definition by Emanuel (2003; see below). Conceptual “north, central and south” regions are applied (Figure 5.2) to compute frequencies for each region.

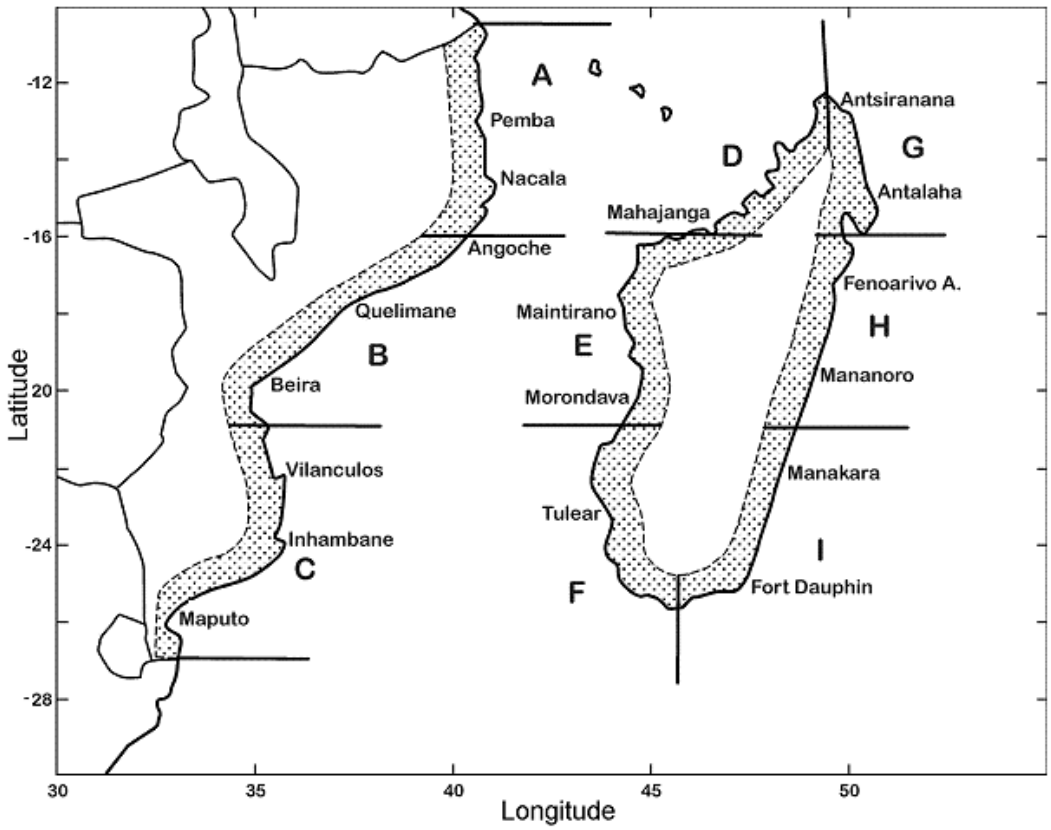

Figure 5.2: Map of the three regions of the Mozambique coast and the six regions of Madagascar's east and west coasts.

Landfall is defined by Emanuel (2003) as the time when the cyclone trajectory is crossing the coastline, with the cyclone going from sea to land. It is assumed that a landfall occurs when all or part of the eyewall passes directly over the coast or an adjacent barrier island. Some tropical cyclones make multiple landfalls. Only TC landfall at the first point of occurrence is considered. Characteristics of landfalling tropical cyclones affecting Mozambique and Madagascar from 1980 and 2007 are discussed in Chapter 7 and listed in the Appendix B5.

Trend analysis

Trends in TCs and SST development and their statistical significance are assessed using linear regression analysis and t-test (MyRegression function; Cardillo, 2007). The statistical significance is then verified by non-parametric

Mann-Kenndal test (Yue et al. 2002). It has been shown that this test has the advantage of not being predicated upon the normal distribution and is insensitive to outliers (Sneyers 1990). Since the Mann-Kenndal test gives only the significance and directions of the trend but not the trend it self, the non-parametric Sen's slope estimator (Sen, 1968) is employed to corroborate the trend obtained by linear regression. Like the Mann-Kendall test, Sen's slope estimator can be applied to data that do not come from a normal distribution, and is not affected by outliers. Details about the functions used can be found at the mathworks site (http://www.mathworks.com/matlabcentral/fileexchange/15473).

Wavelet analysis

A wavelet analysis is applied for the time series of actual TC activity in order to reveal the characteristics of the variability and the periodicity of landfall. The time-frequency characteristics of TC are investigated with the continuous wavelet transform (CWT; Mélice et al., 2001). The continuous wavelet transform (CWT) with the Morlet complex wavelet is used to estimate the time-frequency characteristics of the signals. Torrence and Compo (1998) use the $1/(a)^{1/2}$ normalization. With this kind of normalization the components of the CWT cannot be directly compared to each other. Thus it is compulsory to use the $1/a$ normalization, where a > 0 is the dilatation or scale parameter. A more complete description of CWT method used in this study can be found in Mélice et al. (2001). See also Appendix B4.

5.3 Scatterometry, wind observations

The surface wind field is essential to gain an understanding of ocean surface currents and mixing. Surface winds are also crucial in estimating heat and moisture fluxes between the atmosphere and ocean, and Ekman transports. Wind fields related to TCs have strong temporal and spatial variability. These are usually not sufficiently resolved in Numerical Weather Predictions (NWP). Microwave scatterometers have an advantage over the NWP, in that they provide

more detailed structures of surface wind fields (Liu et al., 1998; Katsaros et al., 2002). The history of scatterometry for wind observations is almost as long as that of the satellites, but resolution enough for use in connection with TCs was not reached until recently, and still there are obvious problems with data accuracy at storm winds and strong rainfall. It seems as if scatterometer winds in intense TCs are still highly underestimated. This is discussed in the present section. In this work, wind data from the SeaWinds scatterometer (QuikSCAT) are employed for the period from 1999-2007. Data are also used to compare kinetic energy input due to wind with the increase of potential energy due to mixing, during a TC event.

Since the early 1990s, several satellites (ERS1/2, NSCAT, and QuikSCAT; e.g. von Ahn et al., 2006) have provided scatterometer data of surface winds over the global oceans with high spatial and temporal resolution. In this thesis, QuikSCAT wind fields are primarily employed. ERS-1/2 wind fields are used complementary.

5.3.1 Principles of operation

Scatterometers, operating on polar-orbiting satellites, provide wind speed and direction through multiple looks (Katsaros et al., 2002) at any one pixel in the swath as the spacecraft travels over the Earth's surface. Microwave pulses are transmitted to the ocean surface and the backscatter power, caused by ripples and waves, received at the instrument, is observed. Instrument history is given in Appendices A-1.1 along with Scatterometer instruments and their characteristics presented in Table A.8. The function of QuikSCAT is indicated in Figure 5.3.

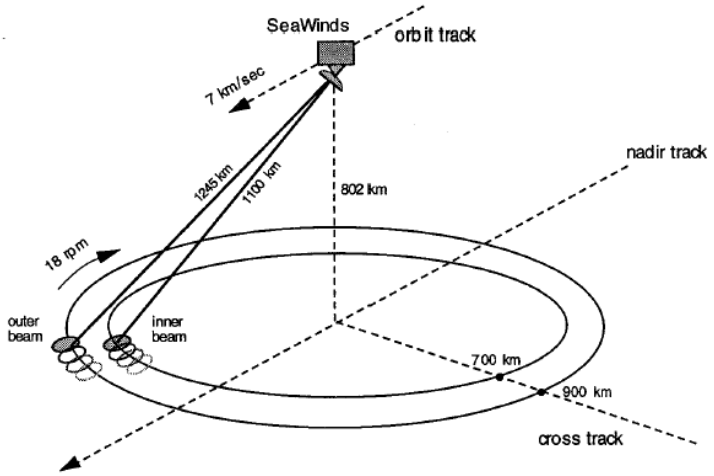

Figure 5.3: NASA QuikSCAT satellite with SeaWinds scatterometer (from Spencer et al., 2000). The satellite employs a 1-m parabolic antenna with twin offset feeds. The antenna is scanning two pencil-beam footprint paths at incident angles of 46° (H-pol) and 54° (V-pol), respectively. The transmitted radar pulse is modulated and the received pulse provides sub-footprint range resolution.

5.3.2 Instrument accuracy

In good weather, data from early scatterometers were shown to be in agreement both with NWP wind fields (e.g., Schroeder et al., 1982; Bentamy et al. 1996) and with in situ measurements (e.g., Bourassa et al., 1997; Freilich and Dunbar, 1999). Quilfen et al. (1998), using ERS data, demonstrated the potential in monitoring TCs, but indicated that the coarse resolution of ERS limited their usefulness. However, QuikSCAT data improved compared to earlier scatterometers; in examining over 5000 collocated QSCAT and buoy data, Wentz et al. (2001) found that, under good weather conditions, there is almost no mean bias in wind speed and only 6° in wind direction.

For moderate weather conditions RMS difference between QuikSCAT and buoy data are 0.3-0.7 ms^{-1} and 3-13°, respectively (Wentz et al., 2001; Bourassa et al., 2003). Under extreme conditions, such as in TCs, Donelan and Pierson (1987) suggest a low-wind cut-off and high-wind saturation. Such limitations have not been clearly proven. However, accuracy for weak winds (< 3 ms^{-1}) and strong

winds (<15 ms^{-1}) and high precipitation, in combination, are uncertain because of the lack of in situ standards. Even with clear indications that rains affect wind retrieval (Yueh et al., 2001), there are few indications of the level of rain at which wind retrieval becomes invalid using existing algorithms (Liu et al., 2002). An exception is a work by Hoffman and Leidner (2005), indicating that for moderate or heavy rain, defined as vertically integrated rain rate of > 2.0 km mm h^{-1}, QuikSCAT data may not be reliable. In addition, data are less useful in the coastal regions due to their coarse spatial resolution. Brown et al. (2005) noted that although new satellite technology will reduce the spatial constrain.

5.3.3 QuickSCAT wind data

The wind datasets used in this study are QuikSCAT mean fields available on CERSAT ftp site at IFREMER and generated from L2B product (swath product of SeaWinds on QuikSCAT scatterometer, distributed by JPL/PO.DAAC), using objective analysis technique based on kriging (Bentamy et al., 1996; 2003). The standard errors of the parameters estimated by this method are also computed and provided as complementary gridded fields. Data constitutes a homogeneous series of daily, weekly and monthly wind fields (in netCDF format), on a global 0.5° x 0.5° resolution. Twice daily global surface winds derived from objective interpolation (Liu, 2002) of observations by QuikSCAT is obtained at JPL ftp site. A subset of these global datasets was made to cover the cyclone area in the SWIO, and to investigate the air-sea interaction during some TC events. It has been shown that the coverage of QuikSCAT makes it the best instrument to provide the synoptic view of wind field over the global ocean within the Scatterometer missions (Liu et al, 2000). The high spatial resolution of its data provides detailed descriptions of small and intense weather systems such as Tropical cyclone Japhet (Figure 5.5) occurred in Mozambique Channel during February-March 2003. The spatial resolution of 0.5° x 0.5° in QuickSCAT allows the delineation of surface wind convergence highlighted in TC Japhet.

Wind data from QuikSCAT were first plotted to see the performance during some intense TCs, featuring Maximum sustained wind (MSW) of between 50 and 60 ms^{-1}, obtained from JTWC/LR-RSMC. The wind speed at 10-m level corresponding to the reference height for QuikSCAT winds (for u eastward, and v northward, velocity components), is given by;

$$U_{10} = \sqrt{u^2 + v^2} \qquad (5.1)$$

Maximum winds using Equation 5.1 was approximately 20 ms^{-1}. Figure 5.4 shows the 10-m wind, U_{10} while TC Japhet reached the level of Intense TC with estimated MSW > 50 ms^{-1} from the tropical cyclone regional centers of JTWC and LR-RSMC (Figure 5.5).

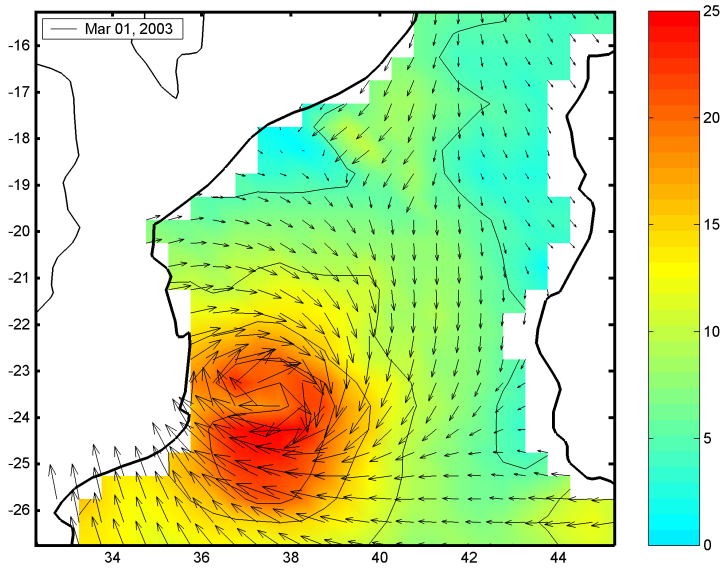

Figure 5.4: Tropical cyclone Japhet on February 28 2003. Black arrows representing wind vectors are superimposed on color image of wind convergence.

To obtain a more relevant figure for the wind-speed the 10-m wind a suggested equation is given in the Appendix A1.3 (Eq. A1.3)

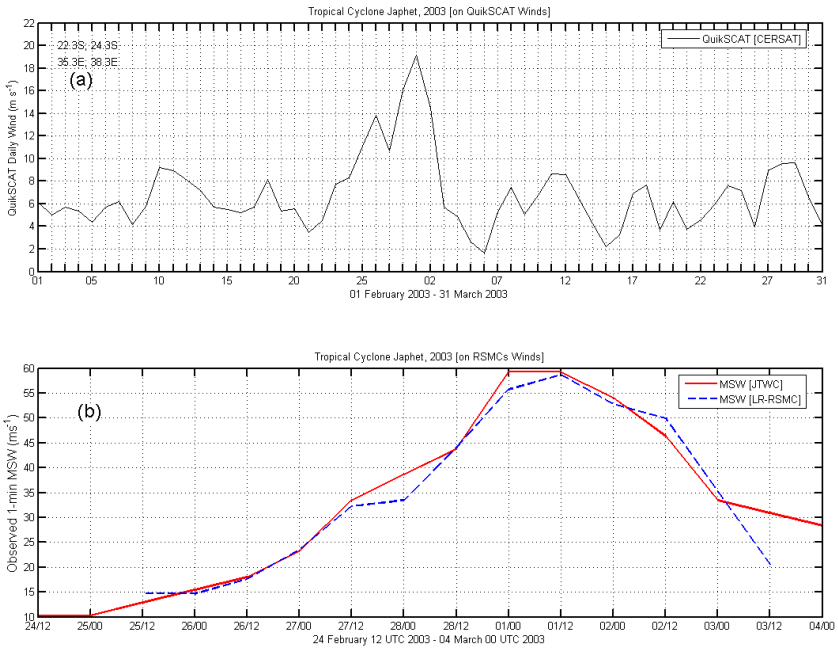

Figure 5.5: (a) QuikSCAT Winds during 01 February to 31 March 2003. According to QuikSCAT data strongest winds locally reaching about 20 ms^{-1}, on 01 March 2003, where present south of Vilanculos shelf in the Mozambique Channel. (b) The maximum sustained winds from JTWC and LR-RSMC were indicating approximately 59 ms^{-1} on 01 March 06 UTC 2003.

Donelan and Pierson (1987) have suggested that under extreme conditions, such as in TCs, a low-wind cut-off and high-wind saturation are likely to occur in QuikSCAT wind retrievals. Also Hoffman and Leidner (2005), have indicated that for moderate or heavy rain, defined as vertically integrated rain rate of > 2.0 km mm h^{-1}, QuikSCAT data may not be reliable.

From the above indications and to some extent it is conceivable to conclude that QuikSCAT/Seawinds may underestimate the wind speed along the cyclone track although still representative.

5.4 Radiometry, sea surface temperatures and rainfall

The use of high resolution radiometer data for observations of SSTs has become extremely important in geophysical research and for weather predictions. Surface temperatures are required to estimate fluxes of heat and moisture and for

monitoring of fisheries resources (Donlon et al., 2002). In the South-West Indian Ocean and in the Mozambique Channel for example, SSTs have been used to study surface currents and the occurrence of fronts and eddies (e.g. Ridderinkhof and de Ruijter, 2003). Radiometry is also used to measure rainfall. The SST observations employed in this thesis belong to Tropical Rainfall Measuring Mission (TRMM) Microwave Imager (TMI). They are basically used to estimate sea surface cooling during TC events, and the upper ocean heat content in combination with altimetry data. In addition, rainfall data from TMI are used to study effects by strong rains on SSTs.

Radiometry is used to measure SSTs and rainfall. This section considers two types of passive radiometers; the IR-radiometer (with wavelengths of 3.5-4.1μ m and 10-12.5 μ m), and the microwave radiometer, operating in the microwave part of spectrum, (with wavelengths of 1.5-300 mm and frequencies from 200 GHz down to 1 GHz). Principles of operation are given in Section 5.4.1. Instrument history is given in Appendices A2.1 along with radiometer instruments and their characteristics presented in Table A.9. The function of TRMM and its primary sensors is indicated in Figure 5.6.

The most widely used IR sensor for measuring SST, and in that sense the most successful, is the AVHRR operated by NOAA, however IR remote sensing account for limitations under cloud conditions (Robinson, 2004). In contrast, microwave penetrates clouds with little attenuation giving an uninterrupted view of the of the ocean surface (Wentz et al., 2000). The primary microwave instruments on TRMM are the TRMM Microwave Imager (TMI) and the precipitation radar (PR) and the Visible and Infrared Radiometer System (VIRS) described in Section 5.4.3., although the sensor of particular importance in this section is the TMI.

5.4.1 Principles of operation: TRMM microwave radiometers

Microwave radiometers have the same fundamental elements of scanning reflector, focusing element, and waveband discriminator and detector as a visible or IR wavelength scanning sensor, but are different in their mode of operation, and also in the design of their components, and focusing capabilities (Robinson, 2004). Principles of operation related to TRMM microwave radiometers sensors are presented in Figure 5.6. The TRMM satellite operates in a precessing orbit, 350 km above the Earth's surface with an inclination of 35°. Its sensors can observe at all local hours and available solar zenith angles over a given location roughly between 40°N-40°S, during 46-day period (Robinson, 2004). The equatorial orbit has a period of 23 days, to better sample the diurnal cycle (Reynolds et al., 2004). The precipitation Radar (PR) on the TRMM satellite is the first instrument designed to measure the reflectivity of rain from space. In essence, the technique is similar to that of land-based rain radars; short pulses are transmitted at microwave frequencies, and the time delay and strength of the echo gives the distance and the intensity of the rain. The differences are that the nearest rain is about 350 km away from the sensor, and scanning must be achieved by electronic steering. The PR surveys a swath of width 220 km at a resolution of ~4.3 km (Kummerow et al., 1998). Furthermore, it is unique in the sense that it gives information on the vertical distribution of rain, with a height resolution of 250 m.

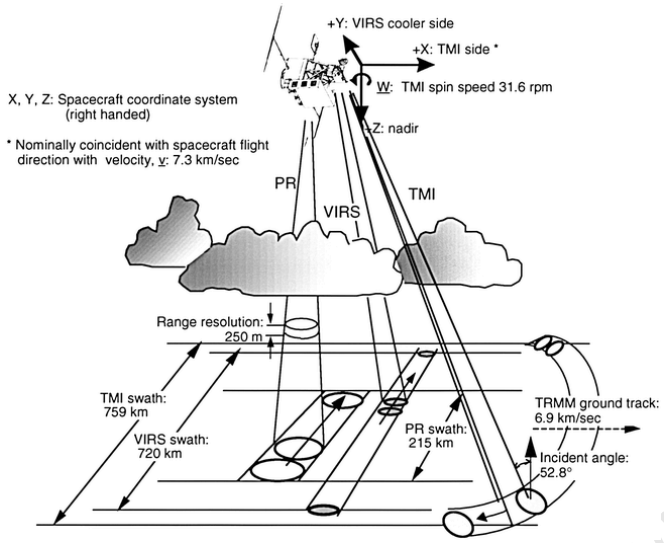

Figure 5.6: TRMM primary sensors: TMI, PR, and VIRS (from Kummerow et al., 1998). The TMI antenna is an offset parabola with an aperture size of 61 cm and focal point length of 50.8 cm. The antenna beam views the earth surface with a nadir angle of 49°, which results in an incident angle of 52.8° at the earth surface. The PR scans in the cross-track direction over ±17° (215-km swath) and in VIRS the swath width resulting from the 350-km orbit and a ±45°scan is 720 km.

The TMI microwave imager, mounted on TRMM is similar in design to the SSM/I which has been flying on the Defence Meteorological Satellites since 1987. The TMI measures the intensity of radiation (brightness temperature) at five wavebands: 10.7, 19.4, 21.3, 37, and 85.5 GHz frequency with a spatial resolution of 25 km x 25 km, providing parameters such as SST, wind speed, atmospheric water vapour, liquid cloud water, and precipitation. These frequencies are identical to those used on the SSMI/ however the 10.7 Ghz channel, suitable for retrieving SST (Wentz and Meissner, 1999) was added in addition, to resolve the heavy rainfall rates that occur in tropical cyclones, inter-tropical Convergence Zone, monsoons and other tropical rain systems. The TMI scans a swath of width 759 km. Its resolution, i.e. the footprint size, is 6 km at highest frequency, increasing to about 50 km for the 10.7 GHz (Robinson, 2004).

5.4.2. Microwave radiometers accuracy

The algorithm for retrieving SSTs from microwave observations is described by Wentz and Meissner (1999). The largest errors in the TMI SST occur near land and at high wind speed (Gentemann et al., 2004). Near land, contamination results in a positive bias of the SST retrievals. Data within 100km from land are excluded in the algorithm development, but the full range of wind observations is included. TMI SSTs has a global accuracy of 0.5°C and has been validated extensively (Gentemann et al., 2004). This study uses the version v04 of TMI SST (September 2006 update; SSM/I web) for the period 1997-2007. A subset of TMI data was made for the SWIO, including daily, 3-day, weekly and monthly SST, winds, rainfall and water vapor.

5.4.3 Data processing. TMI SST and Rainfall

The TRMM/TMI 3-day average SSTs, which are available on a 0.25 x 0.25° grid can be obtained at Remote Sensing Systems home page (RSS, 2005). These are used to study sea surface cooling in the wake of the cyclones for selected TCs. To identify features related to the surface cooling, the change in SST, $\Delta\ SST$ is defined according to;

$$\Delta SST = SST_{pre-cyclone} - SST_{post-cyclone}$$

Three-day average SST is also used to determine initial temperature when cyclones were formed and as an initial SST field in combination with WOA05 vertical profile for mixed layer model simulations during the passage of TC Japhet. The choice of using 3-day averages in most cases is two-fold. Heavy rainfall and appearance of cloud signatures during pre-cyclone and post-cyclone periods lead to conspicuous null regions in the case of daily data. Also a simple average with daily data is taken from ascending pass (day time) or descending pass (night time) which not always have valid data pixels for the same day (Lin et al. 2003a)

Different satellites derived SST data have been employed in this study: SST from TMI (Wentz et al., 2000), Pathfinder Advanced Very High Resoltution Radiometer (AVHRR; Kilpatrick et al. 2001) and Reynolds Optimum Interpolated (OI) SST (Reynolds et al. 2002). The performance of these datasets in detecting sea surface signatures due to tropical cyclones usually differs. Infrared remote sensing is known to have limitations to derive SSTs under cloud conditions. SSTs from IR can be derived only under a clear sky environment. In contrast microwave penetrates clouds with little attenuation giving an interrupted view of the ocean surface (Wentz et al. 2000). The Pathfinder AVHRR SST is a 1° x 1° SST derived from AVHRR (Kilpatrick et al., 2001) while Reynolds OI SST is a 1° x 1° SST derived from AVHRR and *in-situ* SST observations (Reynolds et al. 2002).

Weekly TMI SST has been used to identify the underlying weekly SST from the grid cell that contains the approximate position of the tropical cyclone genesis. As pointed by Bender et al. (1993) and recently by Michaels et al. (2006) selection of SST for genesis is challenging due to the cooling effect on SSTs caused by the TCs over which they are located. Thus a methodology is employed such that the SST the week prior to the storm is used to better represent the SST encountered by each of the cyclones in the record.

Monthly (OI) SST, available from 1982-2007 were used to investigate and discuss possible trends due to global warming and variability of intense cyclones (Sect 3.3.3) in the study area. Climatology maps with monthly TMI and (OI) SST on a 1° x 1° global grid are compared for the period 1998-2005 and in combination with monthly TC trajectories are used to present maps of seasonal distribution and genesis in relation to the sea surface temperatures.

The precipitation data is represented by daily TRMM Multi-satellite Precipitation Analysis (TMPA) 3B42 V6 on a 0.25° x 0.25° global grid although it is also available from TRMM Microwave Imager (TMI) at daily and 3-day averages in the

same resolution. The fundamental limitation of the TMI rainfal dataset is the contamination over land (Wentz et al., 2000). The 3B42 V6 rainfall is based on multi-satellite analysis (MPA, Huffman, 2004) and provides both land and ocean estimates. Huffman et al. (2007) presented two fundamental differences between real-time (RT) and research products. First, the RT product uses TMI precipitation as the calibrator and the research product (3B42 V6) uses TRMM Combined Instrument (TCI), which is considered to be better but is not available in real time. Second, the research product rescales the monthly sums of 3-hourly fields to a monthly gauge analysis, but such a rescaling is not available in real time. Daily TMPA estimates are accumulations of the 3-hourly values. Rainfall data is aimed to evaluate possible influence on the surface water due cold rain and relationship between relationship between TC accumulated rainfall over ocean at TC maximum intensity and over land at landfall or decay. The precipitation over oceans can be inferred from the daily and 3-day averaged TRMM Microwave Imager (TMI) or daily TRMM 3B42data. However, the precipitation over land is determined either from daily TRMM 3B42 or by the historical records of precipitation gauge measurements.

5.5 Satellite altimetry, sea surface heights

Altimeter data are used to estimate sea surface heights on scales from waves and tides to “global change”. An unprecedented development of altimeter instruments has taken place since the 1970s and expectations within the field of satellite-borne radar altimeter are still high (Emery and Thompson, 1998). Early observations had fairly low precision but demonstrated its potential (Huang et al., 1978). Today it is possible to give precise estimates of global sea level increase (Carton et al., 2005; Miller and Douglas, 2006; Beckley et al. 2007). Warm and cold eddies are readily seen in sea surface height data. It is possible to derive surface geostrophic velocities on scales of weeks rather than decades, with relatively better accuracies. In combination with SSTs, sea surface height anomalies (SSHAs) have been used for estimates of the heat content in the upper ocean (Goñi and Trinannes, 2003). The tropical cyclone heat potential (or

TCHP; Chapter 1-3) is a physically relevant variable for TC genesis and intensification. The merged altimetry data described in this section in combination with radiometer data are used to investigate TC intensification including the calculation of TCHP.

The oceanic sea level or the sea surface height is essential in studies of sea surface currents, tides and wave heights but also for long-term changes in relation to global warming. To date most remote measurements of sea surface height have employed microwave techniques such as radar altimeters, scatterometers and synthetic aperture systems. The rapid development of satellite altimetry as a remote sensing capability has provided a wealth of information about the world's ocean, in recent years with focus on mesoscale eddy motion and surface velocities. The altimeter measures the precise height of the sea surface and the development has reach a point where Absolute Dynamic Topography (ADT) is available. Operation principles and accuracy are given below in Section 5.5.1-2. Data processing is given in Section 5.5.3 while the historic development of instruments is given in Appendix A3.1.

5.5.1 The principles of altimetry

Radar altimeters transmit microwave frequency pulses to the sea surface and receive the reflected echoes from the Earth's surface employing a nadir pointing radar. Radar pulses are both scattered and reflected from the sea surface within a footprint of a few kilometres at nadir. The shape of the return radar echo, as a function of time, provides estimates of range, significant wave height and speed.

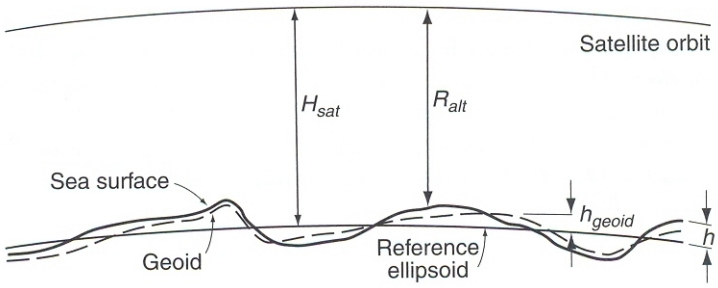

Figure 5.7: The principle of radar altimetry (Robinson, 2004).

The height of the sea surface is estimated by subtracting the altimetric range from the orbital altitude of the satellite (Figure 5.7). The sea surface height (SSH), relative to the reference ellipsoid, comprises; 1) the static *geoid*, which represents the equi-potential surface that the ocean would assume in the absence of currents, winds and tides, 2) height variations due to tides, 3) surface effects from the oceanic response to atmospheric pressure and, 4) dynamic topography associated with currents. The goal to reach is the absolute dynamic topography (ADT) from which it is possible to determine the geostrophic surface velocities. Today with much improved observations of the geoid, ADT data seems accurate for large parts of the open ocean (Brown et al. 2005). However, this thesis makes use of sea surface height anomalies (SSHA), which are still more accurate but where the data used are deviations from the long term mean value (of earlier observations).

5.5.2 Altimetry measurement accuracy

The T/P altimeter is a step ahead in the field of altimetry by making measurements of sea surface height (SSH) to an RMS accuracy of 4.1 cm (1-sec average; Robinson, 2004). Accuracy of the main altimeters is summarized in Table 5.4 by listing the errors associated with the different corrections (where known), and the total error for SSH measured relative to the ellipsoid. The remaining factors which affect the oceanographic application of altimeters are the knowledge of geoid and the accuracy of the tidal correction.

Table 5.4: Approximate RMS measurement accuracy (cm) achieved by different altimeters (from Robinson, 2004)

	SEASAT	GEOSAT	ERS-1/2 RA	T/P*	Geosat-FO	Envisat RA-2
Altimeter instrument noise	10.0	4.0	4.0	1.7	2–3	2.0
Ionosphere correction	3.0			0.5	~5	
Dry troposphere correction	0.7			0.7		0.2–2
Wet troposphere correction	3.0			1.1	~2	1–2
Electromagnetic bias	5.0			2.0		~2
Skewness				1.2		
Orbit	100	50 (10)		2.5	10–15	~3
Total error: SSH 1-sec mean				4.1		
Height error; (~100 km)				~2		

*Jason-1 has very similar accuracy to T/P

5.5.3 Altimeter data processing

Global, 7-day maps of gridded sea surface height anomalies, SSHA (the difference between the observed sea surface height and the mean sea level; a 7-year mean for 1993-99) with a 0.33 x 0.33° were obtained for the period 14 October 1992 - 30 April 2007.

The product combines data from TOPEX/Poseidon (T/P), Jason-1, ERS-1/2 and Envisat satellite altimeters using the method described in Ducet et al. (2000). The data are produced by CNES, in partnership with Ssalto and Duacs. The data are distributed by the AVISO project (http://www.aviso.oceanobs.com/). Despite sampling errors due to differing ground tracks and orbit repeat periods, merged data from multi-missions have the advantage of resolving ocean mesoscale process, which is beyond the capabilities of a single instrument (Fu et al., 2003).

TOPEX data are available over both land and oceans, whereas the POSEIDON data covers the oceans, only (Figure 5.8). The merging process and quality control applied is described in (Fu et al., 2003). The primary data delivery by altimetric mission typically consists of along-track record of SSH at one-second interval, the tidal height estimate at each point and following post-processing of a mature mission with a long enough complete data span to generate a reliable mean topography, the SSHA (Robinson, 2004).

In this study, monthly data at 1° x 1° resolution derived from TOPEX/Poseidon (Jason-1) + ERS-1/2 (Envisat) satellites were used in Chapter 2 to draw a preliminary view of sea level variability (Figure 2.14) in the Mozambique Channel and adjacent waters in relation to the peak months of the cyclone season, that is from January to March.

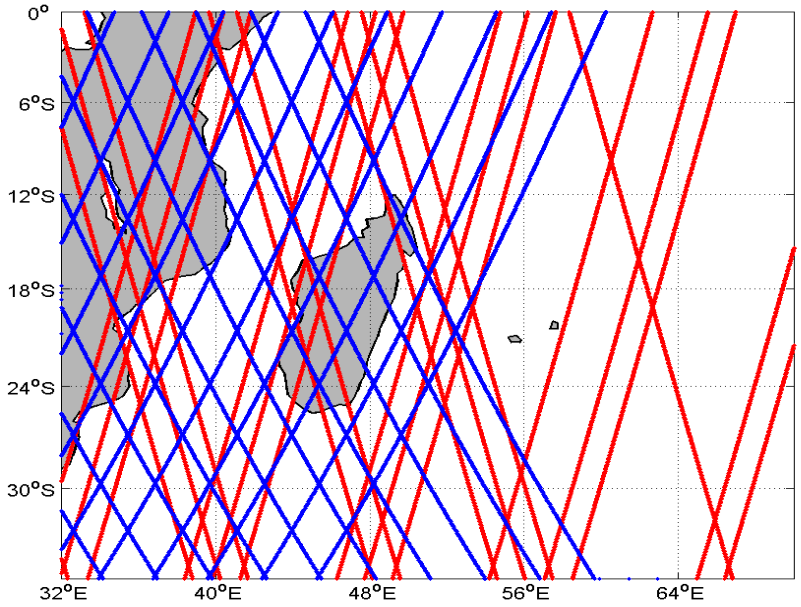

Figure 5.8: The Jason-1 (blue) ground tracks (same as TP) merged with ERS (red) ground tracks (same as ENVISAT) for the South-West Indian Ocean.

The 7-day maps of gridded SSHA are used to identify ocean eddies over the study area during selected pre-cyclone events from 1993 to 2007. An interpolation scheme is also applied to fit both SSHA and TMI SST data allowing for estimation of Tropical Cyclone Heat Potential (TCHP). The theory is described in Section 6.2.

5.6 Atmospheric data and sea surface heat fluxes

Tropical cyclones are affected by several atmospheric parameters (e.g. Gray, 1968; De Maria et al., 2001). Vertical wind shear is one of these parameters, known to have strong effects on both TC genesis, structure and the intensity.

Another important parameter is the relative humidity. The moisture content of a TC and its surrounding environment is crucial for TC growth and intensification. In addition to atmospheric data, also data on sea surface heat fluxes are employed, using OAFlux data (Section 5.6).

5.6.1 NCEP data

The National Centre for Environmental Protection and National Centre for Atmospheric Research (NCEP/NCAR) atmospheric reanalysis data (winds, air temperatures, lower tropospheric relative humidity etc.) extending from 1949 through present have a 2.5° X 2.5° resolution (Kalnay et al., 1996). The NCEP reanalysis uses a global data assimilation system, along with observations from land surface, ship, aircraft, satellite and other data to produce global fields of various meteorological parameters (Kalnay et al., 1996). For this study, the 1979-2006 reanalysis subset of daily average data is used. Winds from the 200, 850 and 1000 hPa and lower tropospheric relative humidity at 850 data were used for studying effects on TC intensification on selected cyclones. Among different kinds of external forcing vertical shear has been considered as a key environmental variable that controls tropical cyclone development. In general, large values of vertical wind shear are detrimental to the formation as well as intensification of individual TCs (e.g Gray, 1968; Zehr, 1992; DeMaria, 1996; DeMaria et al., 2001). The vertical wind shear is defined in this study as the difference between the mean wind vectors of the 200- and 850-hPa levels over an outer region extending from the radius of 200-800 km around the storm center (Chen at al. 2006). Moisture content of a TC and its surrounding environment is also very important. This moist air is necessary because dry environment promotes evaporational cooling, limits clouds, precipitation and latent heat releases within a tropical cyclone (e.g., Emanuel, 1989; Dunion and Velden, 2004). However a moist environment is rich in latent heat, which a cyclone utilizes to intensify. In mentioned above the lower tropospheric relative humidity is taken at 850 hPa to investigate TC intensification.

5.6.2 OAFlux data

The Objectively Analyzed Air-Sea Fluxes (OAFlux) data (latent and sensible heat fluxes) has a 1° X 1° resolution (Yu and Weller, 2007; Yu et al. 2004) extending from January 1985 to December 2006 and has been developed and validated against in situ flux measurements. Latent and sensible heat flux fields are derived from following the procedure by Yu et al. (2004). First, the estimates of the flux-related surface meteorological variables (i.e., wind speed, air humidity, air temperature, and sea surface temperature) are obtained from a synthesis process using an objective analysis. The input data for the synthesis include satellite retrievals and outputs from numerical weather prediction models of the European Centre for Medium-Range Weather Forecast (ECMWF), the ECMWF ReAnalysis-40 (ERA40), and the NOAA's NCEP reanalysis. The latent and sensible heat flux fields are computed by using the variables determined from the synthesis and the state-of-the-art bulk flux algorithm 3.0, developed from the Coupled Ocean-Atmosphere Response Experiment (COARE) by Fairall et al. (2003). The net longwave and shortwave radiations are derived from ISCCP that cover the period from July 1, 1983 through December 31, 2004 with a 3-hour resolution on 2.5°×2.5° grid. This set of surface radiation data is called ISCCP-FD dataset (Zhang et al. 2004). OAFlux (Latent and sensible heat flux fields) and ISCCP (net longwave and shortwave radiations) daily averages have the same spatial and temporal resolution and are available at Woods Hole Oceanographic Institution anonymous ftp server (WHOI, 2007).

5.7 Oceanic data. WOA05, Argo and ACSEX-I

In-situ measurements provide ample opportunities for anyone to experience errors, difficulties and instrument malfunctions. Unlike data from controlled laboratory experiments, earth science data are collected under whatever conditions prevail at the time of the experiment. Remote sensing technology has opened opportunities to study the ocean without even going to sea. However, in-situ measurements and remote sensing must be explored together (Tomczak,

2006). In this study the upper ocean response to tropical cyclones is also investigated using hydrographic data provided from ACSEX-I and ARGO buoys and climatology fields from WOA05 for calculations of the Mixed Layer Depths (MLD). The data used here are presented in Section 5.7.

5.7.1 World Ocean Atlas 2005

World Ocean Atlas 2005 (WOA05) is based on a set of quality-controlled historical profile data for temperature, salinity, dissolved oxygen, and nutrients (phosphate, nitrate, silicate) available from the National Oceanographic Data Center (NODC) and World Data Center (WDC) for Oceanography (refer to Levitus, 1982). Cruise and buoy data from all over the global ocean have been analyzed in a consistent, objective manner and used to produce the aforementioned profiles on a 1° x 1° climatology grid at standard depths down to a maximum of 5500 m. Annual, seasonal, and monthly maps have been derived. Data density, standard deviations etc. are also available as well as original data (in the World Ocean Data Base, WODB). The WOA05 and WODB are used here in several contexts, first in Chapter 2, where the Indian Ocean climatology is presented, but also in connection with intensification and sea surface cooling, where climatology profiles is the point of departure when calculating changes in heat content etc.

5.7.2 Argo profiles

The Argo data used in this study is available at CERSAT ftp site (IFREMER, 2007). Argo is an array of 3000 free-floating buoys making vertical profiles (temperature and salinity) of the upper 2000 m of the ocean once every 10 days (Figure 5.9). For each valid profile, a delayed-mode quality control has been applied following the procedure proposed by Wong et al. (2003). Argo data can also be obtained in delayed mode from two global hubs, one hosted by Coriolis (France) and other by US GODAE. About 90% of profiles are available within 24

hours and almost all within 48 hours. In a few cases, Argo data have been available close to the locations of TCs, whereby it has been possible to obtain a much improved insight in the processes of sea surface cooling.

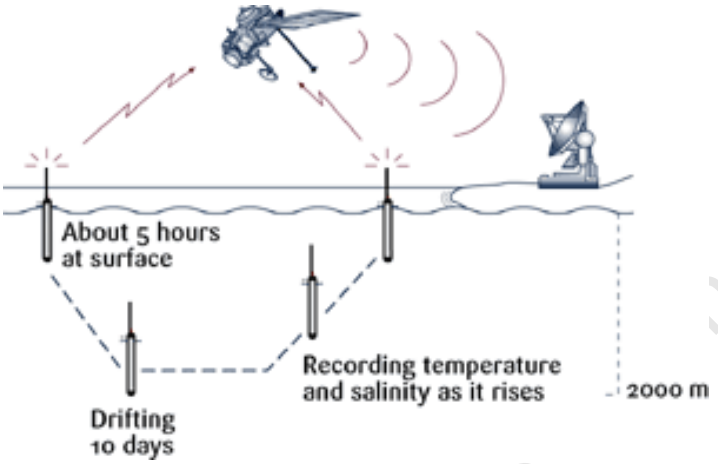

Figure 5.9: Most Argo floats drift at a depth of 1000 m for about 9 days, then they make a profile of temperature and salinity from 2000 m to the surface, after descending. Then they stay at the surface for about 10 hrs, sending the data to a satellite, after that they descend again to resting depth (1000 m).

Temperature data are accurate to ± 0.005 °C and depths to ± 5 m. For salinity there are two answers. The data delivered in real time are sometimes affected by sensor drift. For many floats this drift is small, and the uncorrected salinities are accurate to ± 0.01 psu. However, larger deviations seem to be common. At a later stage salinities are corrected by expert examination, comparing older floats with newly deployed instruments and with ship-based data. Following this delayed-mode correction salinity errors are reduced further (Wong et al., 2003).

5.7.3 ACSEX Cruise Data

The Agulhas Current Sources Experiment (ACSEX) was carried out from Cape Town, South Africa to Victoria, Seychelles during the year 2000. The main research area was the Mozambique Channel where hydrographic observations (e.g CTD, XBT and LADCP) were performed. The purpose of the ACSEX-I was i) to identify the location of the Mozambique Current and to determine it's strength, ii) to test the existence of large scale eddies (see Section 2.5.2) in the area as

suggested by altimetry data, iii) to deploy short term moorings for a period of one week and iv) to deploy moorings for a period of one year, to be recovered in March-April 2001. Hydrographic observations from that cruise coincided during the passage of TC Hudah.

In combination with Argo Profiling float information hydrographic data (salinity, temperature absolute meridional velocities) collected during ACSEX-I Cruise (2000) are employed to provide observations of existing profile pairs before and after the passage of four tropical cyclones during 2000, 2003, 2004 and 2007. The information is given in Appendix C (Tables C5-8).

Chapter 6: Theory on sea surface cooling and Cyclone Heat Potential

6.1 Introduction

The oceanic mixed layer is usually equivalent with the top 20-100 m. This layer is normally well mixed by wind, so that it can be assumed that it has a vertically uniform density, i.e. temperature and salinity. A balance between the flux of buoyancy on one hand and the work done by the wind, on the other apply to this layer (the mechanical energy equation). The mixed layer thickness is the depth, h_m at which a sharp gradient of temperature indicates the start of the thermocline. The bottom of the mixed layer allows a mass vertical flux across it, forced by wind-mixing (entrainment) or wind-divergence (Ekman pumping).

Models for mixed layer depths (either as steady state models or time-dependent for description of its seasonal development in temperate climate) start out from the 1-D model by Kraus and Turner (1967). Their model is based on conservation of volume, heat and mechanical energy, but does not allow for horizontal exchange. Corresponding 3-D numerical models were developed i.e. by Blumberg and Mellor (1983); the Princeton Oceanographic Model (POM) and by Shchepetkin and McWilliams (2005), the Regional Ocean Model System (ROMS) among others.

For the purpose of this thesis however, studying the response of the mixed layer in relation to moving cyclones, a 1-D approach have considerable advantages because of simplicity. Below, in Section 6.1 is described the basic processes related to mixed layer depths, SSTs and moving cyclones. This background is given for the purpose of understanding time dependent and spatial changes of the SSTs, and also to some extent to add knowledge to the efficiency of cyclone mixing and heat transport. In Section 6.2 an expression is derived for estimate of horizontal variations in the tropical cyclone heat potential, TCHP.

6.2 A model for sea surface cooling

The importance of sea surface cooling due to tropical cyclones has been discussed in earlier chapters, mainly in Section 3.4.1. Strong cooling in the wake of a cyclone, mainly due to upward transport of cool thermocline water, is readily seen from daily SST satellite data. Here, the daily SSTs and their evolution throughout a cyclone passage form the basis for a physical interpretation of the basic mixing processes, i.e. entrainment and upwelling. Theory is given for calculations of mixed layer depth (MLD), entrainment velocity, changes in heat content of the mixed layer, and potential energy of the surface waters. The Tropical Cyclone Heat Potential (Section 3.3.4) is evaluated from SST and SSHA data including surface water temperature climatology. Calculations are carried out for one particular cyclone, TC Japhet. This cyclone passed straight across an Argo float, the temperature profiles of which helped greatly in interpretation of the results.

As discussed at length in Section 3. 4, there are three basic processes involved in cooling of surface waters underneath a moving cyclone; i) net heat loss due to very strong turbulent (latent and sensible) heat fluxes at the sea surface, ii) vertical entrainment due to wind-mixing, iii) upwelling due to wind divergence (assuming a 1-D approach, precluding horizontal heat exchange). Theory for the cooling processes is given below.

Cooling due to net flux of heat

The net flux of heat through the sea surface, $Q_{NET} = (Q_S - Q_{LW} - Q_{LH} - Q_{SH})$ consists of the sum of the radiation terms (i.e. short and long-wave heat flux; Q_{SW}, Q_{LW}; 50-250 and 50-70 Wm^{-2}, in the tropics), and the turbulent terms (latent and sensible heat flux; Q_{LH}, Q_{SH}; 100-200 and ±20 Wm^{-2}). Cooling along the cyclone track is due to Q_{LW}, Q_{LH} and Q_{SH}, but dominated by Q_{LH}, because of the very high wind speeds related to cyclones. In the bulk formulas, used to calculate

latent and sensible heat flux (Gill, 1982; Taylor, 2000), these are proportional to the wind-speed, W, according to;

$$Q_{SH} = \rho_a C_p C_t (T_s - T_a) W \qquad (6.1a)$$

$$Q_{LH} = \rho_a C_e L_t (q_s - q_a) W \qquad (6.1b)$$

They are also proportional to the difference in temperature between water and air, $(T_s - T_a)$ and to the difference in specific humidity $(q_s - q_a)$, respectively. While the air density, ρ_a the latent heat of vaporization L_t and the specific heat for water, C_p are well-known quantities, there is a never ending debate on the Dalton and Stanton numbers (C_e, C_t) and a variety of algorithms have been used (Taylor, 2000). Particularly it concerns the Dalton number under stable (when $T_S \geq T_a$) and unstable conditions, respectively, conditions which are highly relevant in cyclone studies. During normal conditions in tropical waters, the latent heat flux typically is 100-200 Wm^{-2}, corresponding to an evaporation w of 3-6 mm/day, where $Q_{LH} = \rho_w L_t w$. It is assumed that in hurricane winds, this number may be several times higher, although this has not been proven. However, even with a very high evaporative loss of heat, it is obvious that the cooling of the mixed layer is mainly due to vertical mixing.

Cooling due to entrainment

Cooling due to entrainment depends on the vertical entrainment velocity, $w_e = (\frac{dh_m}{dt})_{mix}$, defined positive downwards, and the temperature difference, ΔT_m between the mixed layer and that of the ocean below (Figure 6.1). Kraus and Turner (1967) have calculated the deepening of the wind-mixed ocean layer due to entrainment, assuming that a (small) fraction of the wind mixing introduced in the surface water is used to erode cold water from below, into the surface layer.

Cooling due to upwelling

Cooling due to upwelling, or Ekman pumping, is driven by the wind field. Geisler (1970), among others, have developed a theory for upwelling in the wake of a moving cyclone. This process is related to a lifting of the water column, including its interface. If both processes are acting simultaneously, which they are likely to do in the vicinity of the cyclone centre, the total change in depth of the mixed layer, h_m equals;

$$\frac{dh_m}{dt} = w_e - w_E \qquad (6.2)$$

where w_E is the vertical Ekman velocity. The Ekman velocity may be calculated from the equation;

$$w_E = \frac{1}{\rho_w f}\left(\frac{\partial \tau_y}{\partial x} - \frac{\partial \tau_x}{\partial y}\right) \qquad (6.3)$$

where τ_x and τ_y are the wind-stresses in the x and y directions, ρ_w the water density and f the Coriolis parameter (e.g. Gill, 1982). Thus, w_E counteracts the deepening of the wind-mixed layer, but will, nonetheless contribute to lowering of the SSTs.

In the Mozambique Channel, the mixed layer depth (MLD) is small, typically 30 m (see Section 2.5; Figure 2.12). Below the mixed layer, the vertical temperature gradient, $\gamma = \partial T / \partial z$ is typically 1ºC per 10-15 m for the next 100-150 m. This type of profile, with a thin mixed layer and a thick thermocline (Figure 6.1a-b) is employed for the calculations carried out here. Figure 6.1a-b shows two cases for deepening of the ML in the wake of a cyclone; Figure 6.1a for a case assuming that entrainment dominates the cooling, Figure 6.1b for a case where upwelling is also important but where entrainment mixes the surface layer to depths, larger than the initial mixed layer depth h_{mo}. While Figure 6.1a may describe the conditions over a wider area, up to 250-400 km from the cyclone track, Figure 6.1b describes the wake area, in the immediate vicinity of the track (cf Figure 1.3).

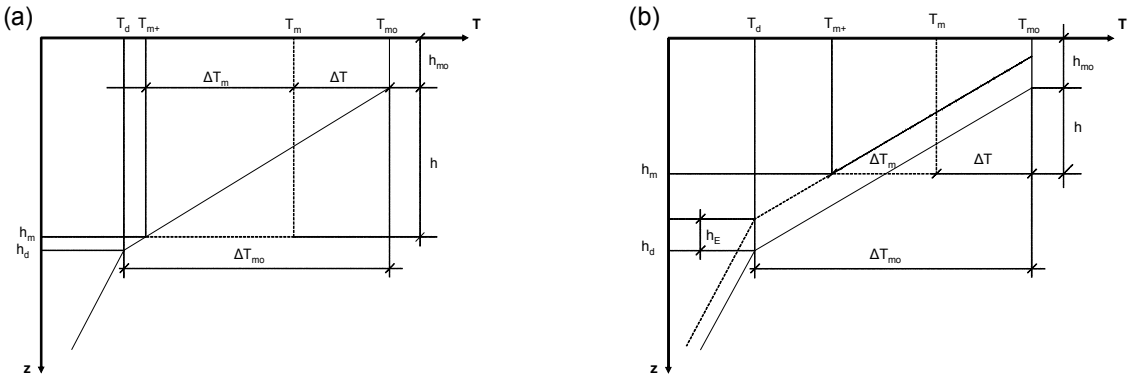

Figure 6.1: Temperature profiles, used to calculate the mixed layer depth, h_m, and other parameters, based on daily SST data. a) shows a case where the change in SST, ΔT, is caused by entrainment, whereas b) shows a case where entrainment and upwelling are both important (where the partly dotted, partly hatched line indicates a case with no entrainment). Case b) produces a thinner mixed layer, for the same SST.

In a model, the temperature profile has a major impact on the cooling; the commonly used two-layer model (Appendix D1) will result in more rapidly decreasing sea surface temperatures than a model with a finite thermocline depth and also in much smaller entrainment velocities. A model based on entrainment alone, for a case where upwelling is also important, will overestimate the entrainment velocity and the final MLD. Upwelling alone, without mixing (the case is illustrated by the hatched line in Figure 6.1b) will have no effect at all on SST as long as $h_{mo} > h_E$.

The mixed layer depth, may be calculated from the mechanical energy equation, balancing increase in potential energy and kinetic energy input by the wind (see Turner, 1973);

$$\frac{1}{2}\alpha g h_m \Delta T_m (w_e - w_E) = m_0 u_*^3 \qquad (6.4a)$$

The work done by the wind (the energy flux of which is $E_w \cong \rho_w u_*^3$), equals the change in potential energy caused by the buoyancy flux from below

$B = g\frac{\Delta\rho}{\rho_w}w = -\alpha g(w_e - w_E)\Delta T_m$. The coefficient $m_0 \cong 0.6$ (see Kato and Phillips, 1969; Turner, 1973) is commonly used (Greatbatch, 1985), but debatable. The friction velocity u_* is related to the wind-stress, τ through $\rho_w u_*^2 = \tau$, in turn determined from the equation $\tau = \rho_a C_d W^2$, where $1000C_d = 0.6 + 0.07W$ in the range $6 \le W \le 26 ms^{-1}$ (Yelland and Taylor, 1996; Smith, 1980). Also C_d is debatable, particularly at high wind speeds.

Net heat flux through the sea surface, Q_{NET} (as an equivalent buoyancy flux) may also be included in Equation 6.4a, which then obtains the following form;

$$\frac{1}{2}\alpha g h_m \Delta T_m (w_e - w_E) = m_0 u_*^3 - \frac{\alpha g h_m}{2\rho_w C_P} Q_{NET} \quad (6.4b)$$

For a stationary MLD, where $w_e = w_E$ one has the Monin-Obukhov depth, where

$$h_{MO} = \frac{2C_P \rho_w m_0 u_*^3}{g\alpha Q_{NET}} \quad (6.5)$$

Thus, it is possible from the Equations (6.2-4) to calculate the evolution of the MLD from input data such as SSTs and wind-stress for various initial conditions. This has been done (Chapter 3.4.1), for example by Greatbatch (1985), in order to evaluate the relative importance of entrainment and upwelling. However, the way chosen here is to assume that entrainment is the dominating cooling process, seen for the whole area, affected by the cyclone. This area is by far larger than the wake in which the very low temperatures are seen, and where advection is likely to be important. Net heat flux is also neglected during the (short) period of the cyclone passage, although this assumption becomes crucial if applied over longer periods and larger areas.

Thus, the MLD, $h_m(x,y,t)$ and the entrainment velocity, $w_e(x,y,t)$ are calculated from the daily sea surface temperature $T_s(x,y,t)$. T_s is assumed equal to the

mixed layer temperature, T_m. Equations for h_m, w_e and change in heat content and potential energy, are derived below.

Mixed layer depth, h_m and entrainment velocity, w_e

Calculation of entrainment velocity according to Figure 6.1a, is carried out assuming heat conservation in the water column as a whole according to;

$$\Delta T(h_{m0} + h) = h\frac{T_{m0} - T_{m+}}{2} + \varepsilon \quad \text{(6.6a)}$$

where $T_{m+} = T_{m0} - \gamma h$ is the temperature at the bottom of the mixed layer (on the deep water side), and $\gamma = (T_{m0} - T_d)/(h_{m0} - h_d)$ is the thermocline temperature gradient. Heat loss to the atmosphere during the cyclone passage is represented by ε, equal to $\int (Q_{NET} / \rho C_P) dt$. By rearranging one obtains;

$$h^2 - \frac{2\Delta T}{\gamma} h = \frac{2\Delta T h_{m0}}{\gamma} - \frac{2\varepsilon}{\gamma}, \text{ or}$$

$$h = \frac{\Delta T}{\gamma} \pm \sqrt{\left\{\frac{\Delta T}{\gamma}\right\}^2 + \frac{2\Delta T h_{m0}}{\gamma} - \frac{2\varepsilon}{\gamma}} \quad \text{(6.6b)}$$

The MLD is calculated from $h_m = h + h_{m0}$ and the entrainment velocity from $w_e = dh/dt$ on a daily basis, where SSTs, $T_s(x, y, t)$ are daily means of day and night-time data. Calculations may be carried out for different period lengths, but for a minimum of 5 days, because SSTs in the core of the cyclone are missing. Various assumptions concerning Q_{NET}, including zero heat loss, are employed. Basically, Q_{NET} is assumed proportional to ΔT. Initial conditions include $h_{m0} = 20 - 30m$, $h_d = 150m$ and $\gamma = 1^o/10m$.

After the cyclone passage, there is a deeper and colder mixed layer. The mean entrainment velocity, evaluated over the area where SSTs are affected by the

cyclone, gives an estimate of the amount of deep water (defined by its temperature) that enters the mixed layer. The change in mixed layer volume, ΔV_{MIX} equals the volume entrained into the mixed layer, $\int_A w_e dA$. The result for a single cyclone may be compared to global estimates, shown in Figure 3.7. The flux of thermocline waters will also bring inorganic nutrients into the mixed layer, thereby promoting primary production. Inorganic nutrients are plentiful, particularly within the lower thermocline (PO_4-P, ca 0.5 µM, NO_3-N, 5 µM; Appendix D2) and is likely to have considerable importance. In Chapter 9, entrainment during the cyclone passage is compared with entrainment under normal conditions (climatology), using Equations 6.4-5. A similar approach might be carried out for the nutrient fluxes.

As mentioned before and discussed in Chapter 3.3.4, the loss of heat to the atmosphere is small, compared to cooling due to upward mixing of cold water. In the wake of a cyclone 80-90% of the temperature *decrease* is caused by mixing (entrainment and upwelling), which means that loss to the atmosphere is hardly discernable in the wake region. Therefore, heat loss to the atmosphere is estimated from calculations of mixed layer heat content (see below) over a 3-week period, assuming that the mixed layer depth and the shape of the temperature profile has returned to climatology a couple of weeks after the cyclone passage. The difference in heat content between the first and the last day, ΔH_1 is compared to the corresponding difference based on climatology ΔH_0 (see next section). Thus, the hypothesis is that the difference in development between ΔH_{mix} and ΔH_{cli} will indicate the loss of heat to the atmosphere due to the cyclone.

Change in surface water heat content $\Delta H_{mix}, \Delta H_{\max}$

As indicated in the preceding section, the change in heat content of the surface waters during the passage of a cyclone may be estimated in different ways

depending on the purpose. A simple way is to estimate the change within the original mixed layer, i.e. $\Delta H_{mix}(z \le h_{m0})$;

$$\Delta H_{mix}(z \le h_{m0}) = \rho_w C_p \Delta T h_{m0} \quad (6.7a)$$

over a time interval, τ. If determined over a longer period (>3 weeks) and compared to the corresponding climatology change, ΔH_{cli}, the difference between the numbers is an estimate of the additional heat flux into the atmosphere, caused by the cyclone. However, this is not satisfactory, because the major heat change at least along with the track, is the loss of heat to deep waters, i.e. the downward heat flux. Equation (6.7a) does not distinguish between atmospheric and deep water flux. An appropriate parameter to calculate, therefore, is the maximum downward heat flux, $\Delta H_{\max}$ which according to Figure 6.1a is

$$\Delta H_{\max} = \rho_w C_P (\Delta T h_{m0} - \frac{\Delta T^2}{2\gamma}) \quad (6.7b)$$

The parameter $\Delta H_{\max}$ may be compared to the heat loss to the atmosphere, indicating their relative cooling effect. Also, the Tropical Cyclone Heat Potential, TCHP, discussed in Section 6.3, if evaluated at different times may be used to estimate mixed layer heat losses.

Potential energy ΔPE

The vertical distance over which the heat exchange takes place is also important and the work to avoid stratification of the water column results in a change in potential energy ΔPE. The change in potential energy was determined by an iterative process, with the following result;

$$\Delta PE \cong g(\frac{1}{2}\Delta\rho(h_{m0}+h)^2 - \frac{43kh^3}{256}) \quad (6.8)$$

A simplified equation of state ($d\rho = -\rho_w \alpha dT$), where α is the thermal expansion coefficient is used to derive the density profile (Figure 6.1a). Thus $\rho_{m+} = \rho_{m0} + kh$,

where, $k = (\rho_{m0} - \rho_d)/(h_{m0} - h_d)$. The change in potential energy will be compared to the input of kinetic energy through the wind $\int_T m_0 u_*^3 dt$ (see Equation 6.4a, b).

6.3 Intensification and cyclone heat potential

As mentioned before, cyclone genesis depends strongly on the SSTs and the mixed layer heat content, expressed for example as TCHP (Section 3.3.4).

$$TCHP = \rho_w C_P \int_{z(T \geq 26)}^{0} (T - 26) \partial z$$

While SSTs are readily obtained from satellite data, the mixed layer heat content and its variations are not readily determined. However, by using the long-term mean stratification, according to WOA05, and the temporal deviations from the mean sea level according to SSHA observations (Section 5.5) in combination it is possible to obtain the temperature field of the upper ocean, and thus to estimate the TCHP. This approach to estimate variations in the mixed layer depth and in heat content was first used by Chambers et al. (1997). Goñi and Trinañes (2003) used a similar approach to estimate the TCHP, including its variations due to cyclone passages. The method employs various techniques to find estimate the level of no motion. A basically similar approach is used here to calculate the TCHP and its variations, with the particular features of the Mozambique Channel eddies (Sections 2.5.2; 3.4.2) as a point of departure.

Relatively large temporal variations of the free surface heights in the Mozambique Channel are shown to be caused by warm and cold eddies (Section 2.5.2). An illustration to mixed layer depth and temperature variations within a warm (WE) and a cold eddy (CE), respectively, is given in Figure 6.2. Downwelling in the WE and upwelling in the CE causes suppression and uplift of the temperature profile, respectively. This was shown to take place down to large depths; in the MC typically to between 1000-2000 m, that is, to the typical depths of the level of no motion in the ocean. Thus, one expects a direct relationship between the deviation of the height of the free surface, Δh from its long term

mean and the deviation of the temperature at a given depth, ΔT from its long term mean.

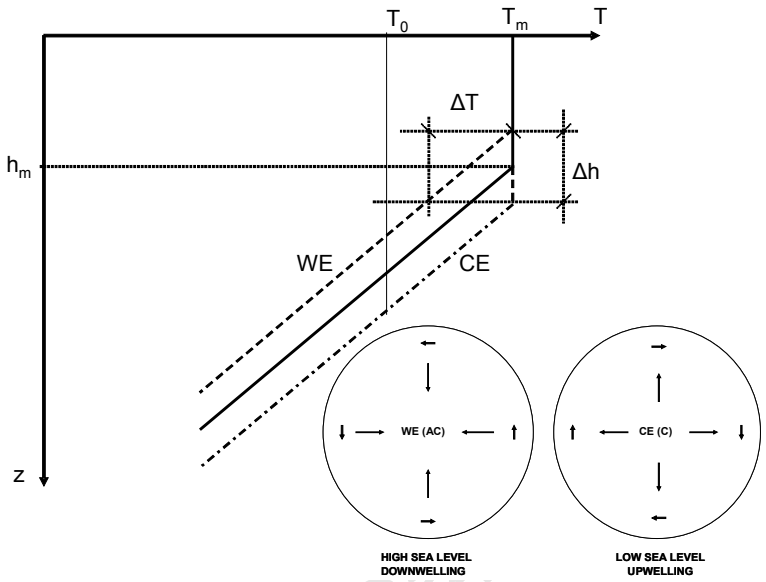

Figure 6.2: TCHP, i.e. the heat content above the depth of the 26°C isotherm (T_0), is larger in the warm (WE) then in cold eddy (CE). Downwelling in the WE and upwelling in the CE create a corresponding suppression or an uplift of the thermocline as illustrated by the hatched lines.

Assuming that $\Delta h = \mathrm{K}\,\Delta T_m$, or $\Delta h = \mathrm{K}\gamma\Delta h_m$ where K is a coefficient, which depends on the temperature expansion coefficient, α and the depth to which the temperature is affected, h and γ is the temperature gradient below the mixed layer. Thus, the tropical cyclone heat potential TCHP (per unit area) may be calculated from;

$$TCHP(h_s) = \rho C_p[(T_{m0} - T_0)(h_{m0} - \Delta h_s / \mathrm{K}\gamma) + (T_{m0} - T_0)^2 / 2\gamma] \qquad (6.9)$$

Using $\mathrm{K} = ٠.٢$ means that a +20 cm SSH anomaly corresponds to a 10 m deeper mixed layer. This can be understood as a deviation in the steric height, $\Delta h_s = \alpha \Delta T h$, caused by a horizontal mean temperature difference of ΔT =1^{0}C vs

the surrounding waters where Δh_s =0, using α=0.2x10^{-3} and h =1000m as depth of the WE.

The tropical cyclone heat potential will be calculated before and after cyclone passages, to investigate increased TCHP in relation to WEs, and also for studying the recovery of the SSTs for comparison with the results obtained from Equation 6.7a.

This chapter has presented the theory on sea surface cooling and on cyclone heat potential which in addition to previous Chapter 3 (Theory on tropical cyclones) and Chapter 5, (Data, methods and tools) are used to address the research questions (Chapter 4) in the next chapters. The results chapters begin with Chapter 7, The Climatology of South-West Indian Ocean cyclones, followed by Chapter 8, Intensification of tropical cyclones and sea surface cooling in the Mozambique Channel and adjacent waters: some examples and, finally by Chapter 9, Sea surface cooling, entrainment and upwelling in the wake of a cyclone. Tropical cyclone heat potential.

Chapter 7: Climatology of South-West Indian Ocean cyclones

7.1 Introduction

This chapter deals with cyclones statistics (TSs and TCs) in the South-West Indian Ocean (SWIO) and particularly in the Mozambique Channel (MC). The investigation employs data from 1952-2007, a period which for quality reasons (see Chapter 5), and as discussed below, is divided into two, 1952-79 and 1980-07. The frequency, i.e the number of cyclones per year and the intensity of the cyclones according to the Saffir-Simpson Scale are studied in relation to their spatial distribution (occurrence, formation areas, tracks and cyclone days) and their temporal development (seasonal and inter-annual). It is reasonable to assume that more intense cyclones also have a much larger impact on sea surface temperatures and upper ocean heat content and therefore that intensity is a very important parameter in relation to i.e. global warming and meridional heat transport. Landfall of cyclones in the Mozambique and Madagascar area is a particular issue. Cyclone climatology was discussed in Section 3.3, both on a global scale and specifically for the SWIO. When relationships to global warming, to ENSO or other climate indices and sea surface temperatures or upper ocean heat content are addressed in addition, it is obvious that the subject grows to levels which are difficult to overview. Then, it's no surprise that experts can forward quite different conclusions (see Chapter 3.3), depending on how the analyses are done, and what period etc. that was chosen.

In Section 7.2 an overview is given, based on all track data from 1952-07. The year to year cyclone frequency (number/year) and the long-term monthly mean distribution are calculated. However, the quality of the data set allows for more detailed investigations, including intensity according to the Saffir-Simpson Scale for the period 1980-07, only. In Section 7.3, the spatial distribution including genesis and preferred tracks are investigated. This background allows for

investigation of inter-annual variability and spatial distribution of cyclones in relation to ENSO (Section 7.4). Section 7.5 deals with relationship to winds, and Section 7.6 particularly with distribution and genesis in relation to sea surface temperatures (SSTs) and upper ocean heat content (TCHP), including effects of global warming. Section 7.7 addresses the occurrence and intensity of cyclones in the Mozambique Channel, with its particularly warm surface waters and eddy occurrence (Section 2.5). Section 7.8 deals with the landfall of cyclones, an issue which was taken up in Section 3.3. Some 20 % of the SWIO cyclones make landfall, either in Mozambique or in Madagascar (or in both). Landfall frequency (including intensity) is studied in terms of temporal development (1952-2007) and SSTs, in relation to ENSO and in relation to formation areas. Regional distribution of landfall is also investigated. Relationship between TC days including variability (Section 7.9) is pinpointed in relation to landfall. The final section, 7.10 is on typical tracks, a matter which is also discussed in Section 7.3 but now evaluated in terms of track tendency and impacts.

7.2 Occurrence and intensity of cyclones - an overview

7.2.1 Quality of data sources. Cyclone frequency in the SWIO 1952-2007

Tropical cyclone statistics for the SWIO (defined as 0-40S, 30-100E) over the past 56 cyclone seasons (1952-2007), was investigated using merged JTWC/LR-RSMC data as discussed in Section 5.2. The annual number of cyclones (from Nov-Apr) for the whole SWIO region and, separately for the Mozambique Channel (MC; 0-40S, 30-50E), is shown in Figure 7.1. The total number of cyclones (TCs+TSs; MSW>17 ms^{-1}) is 633. This count, as aforementioned include all cyclones that spent time in the area as defined above, also those cyclones that were formed outside (i.e. in the east of 100E - of the Indian Ocean). As can be seen, the number is remarkably high in the 1960s for the region as a whole, and from 1950-75 in the MC, compared to the later periods. However, as mentioned in Chapter 5.2, there are uncertainties and missing track data in the early records; satellite imagery and employment of the Dvorak technique was

introduced gradually only from 1968 and was not properly in use until the late 1970s (Section 5.2). Before application of this methodology, the track data contains useful information on landfall areas and cyclone tracks, whereas intensity estimates, as carried out from very scarce wind data, must be considered very uncertain. Therefore, a division of the data into two 28 year periods, before and after 1980, was introduced. Figure 7.2, dividing between 1952-1979 and 1980-2007, indicates the very limited number of wind data from cyclones before 1980. It means that intensity is basically unknown for the earlier period, but also that the count as such (which i.e. assumes exclusion of low wind speed cyclones, TDs <17 ms^{-1}) therefore, is less reliable.

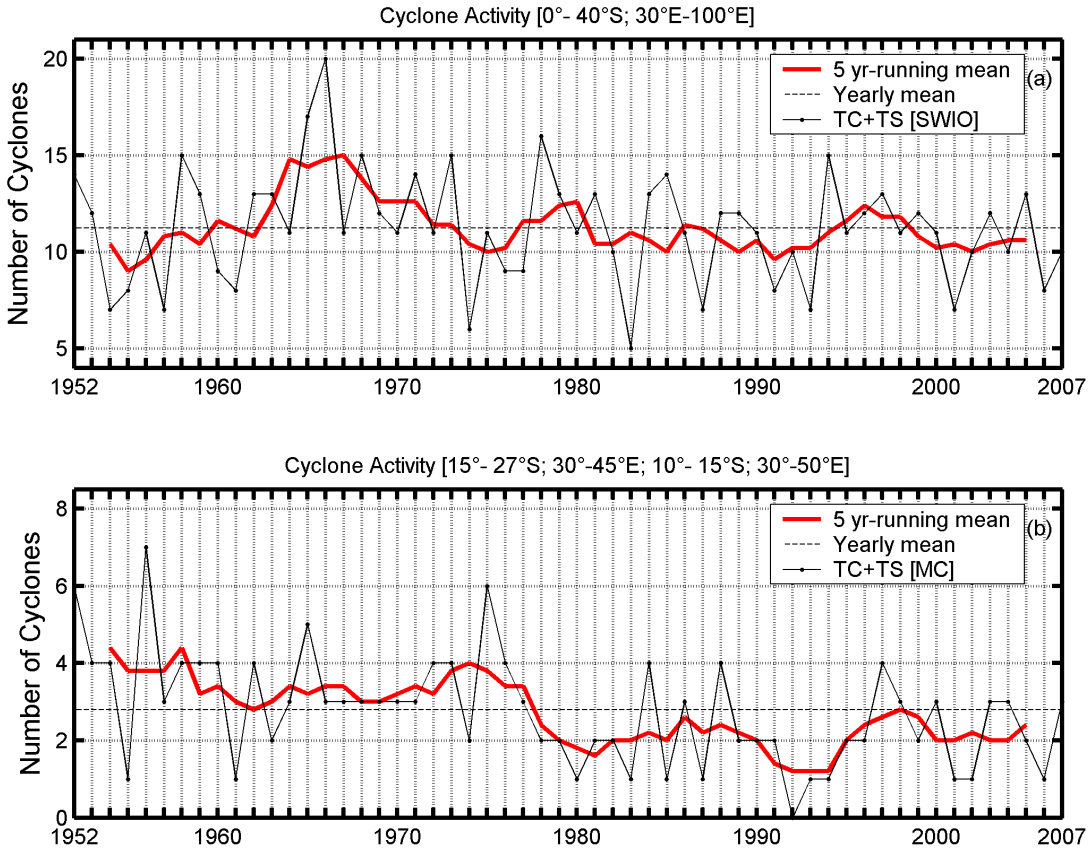

Figure 7.1: Annual number of tropical cyclones (TC+TS) in the South-West Indian Ocean and in the Mozambique Channel (1952-2007).

In the earlier records, 1952-79, exclusion of TDs was based on observed tracks and annual technical reports from the data sources. In the latter record they were

based on real intensity data and therefore, much more consistent. In the forthcoming analysis I will therefore concentrate on data from the latter record, i.e. 1980-2007. However, the earlier period will be employed for TC landfall studies (comprising about 20 % of all cyclones), for which data are considered more consistent.

With the shortcomings in the earlier records in mind, Figure 7.1 indicates a decrease in the number of tropical cyclones; in the SWIO from 330 to 303, in the MC from 97 to 56, between the earlier and the more recent 28-year period. This is still a remarkable result, given that most recent reports on cyclone frequencies in different parts of the world indicate increased number of cyclones (Section 3.3.2), at least for more intense cyclones, and also that this increase is related to global warming.

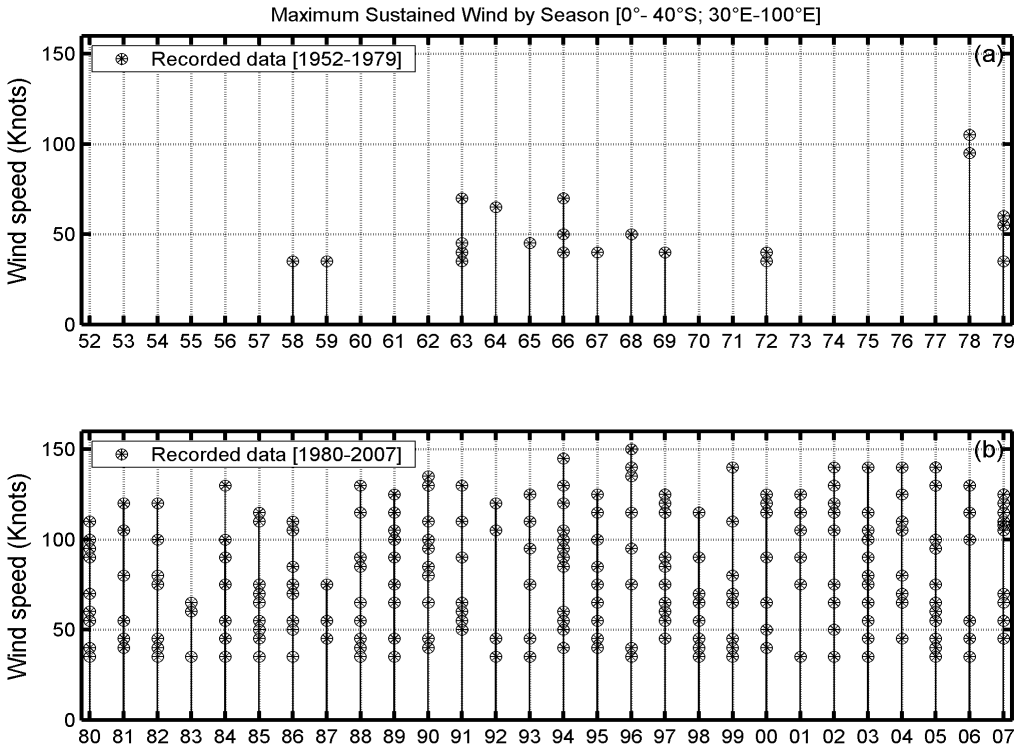

Figure 7.2: Maximum sustained wind (1-min; 1 knot=0.515 ms^{-1}) for all cyclones in the data set (a) 1952-1979 (b) 1980-2007.

Particularly remarkable is the much lower number in the MC, i.e. an area in which control of cyclone occurrence should have been more reliable because of its

smaller size. In the forthcoming investigations of cyclone statistics I will return several times to this question.

7.2.2 Seasonal distribution of cyclones in the SWIO and MC.

Seasonal variation within the cyclone season (in the SWIO from November to April) is one important factor in studying cyclone occurrence. In Section 3.3.1, the cyclone seasons in different regions of the world was discussed and it was indicated that there are large variations also on the monthly time scale depending e.g. on winds and air pressure distribution. Although there is general agreement that the ITCZ (Sections 3.1-3) is a leading factor for generation of cyclones in the SWIO, and that most cyclones appear when the ITCZ reaches its southernmost position in January and February, there are variations in time and space which may be related to e.g. winds and sea surface temperatures and which will be studied in this chapter. Tables 7.1-2 show the total number of cyclones month by month and the corresponding mean frequencies for the periods 1952-79 and 1980-2007 (Appendix B; Tables B1-B4 gives additional information). A separation is done between cyclones in the SWIO as a whole, and in the Mozambique Channel, respectively.

Table 7.1: Total number and frequency of cyclones in the SWIO and in the Mozambique Channel during the period 1952-1979 (November-April)

	Mozambique Channel		South-West Indian Ocean	
Month	All cyclones (TC+TS)		All cyclones (TC+TS)	
	number	frequency	number	frequency
November	3	0.1	17	0.6
December	16	0.6	55	2.0
January	33	1.2	88	3.0
February	28	1.0	82	2.9
March	13	0.5	66	2.4
April	4	0.1	22	0.8
Total/Mean	97	3.5	330	11.8

A comparison between the Tables 7.1 and 7.2 indicates the difference in total number of cyclones and their frequencies; 330 (11.8) for the first 28-y period and 303 (10.8) for the latter period. Relatively few cyclones occur in November and

April, January is the peak month, but cyclones in February are almost as common. December and March have similar frequencies but with a small preponderance in March. Considering that the ITCZ reaches its southernmost position in early February the relationship is obvious. Comparing the recent and the earlier period there is a high consistency in the seasonality, indicating that the old records also makes sense and may be useful, at least for selected purposes, such as landfall studies. As expected, there is also a general agreement on the seasonal distribution as it is presented in Tyson and Preston-Whyte (2000), using data from 1927 to 1984. Comparing the seasonality in the SWIO and in the MC also indicates a similar progression, possibly there is a small chance for later cyclones in the channel. In all, about 20% of the cyclones enter the Mozambique Channel or are generated therein. Relatively few cyclones, though, make their way across Madagascar (see also Section 7.3).

Table 7.2: Total number and frequency of cyclones in the SWIO and in the Mozambique Channel during the period 1980-2007 (November-April). Numbers within parentheses include 10 cyclones with missing intensity data, excluded in the forthcoming analyses (see text).

	Mozambique Channel		South-West Indian Ocean	
Month	All cyclones (TC+TS)		All cyclones (TC+TS)	
	number	frequency	number	frequency
November	2	0.07	28	1.0
December	7	0.25	34	1.2
January	18	0.64	72	2.6
February	16	0.57	72	2.6
March	8	0.29	53	1.9
April	5	0.18	34	1.2
Total/Mean	56	2.0	293 (303)	10.5 (10.8)

The mean frequencies indicated in Tables 7.1-2 are 11.8 and 10.8 cyclones per year, within the cyclone season, compared to 12.1 according to Fink and Speth (1998), using data from 1968-97 (Section 3.3.1), and 11 according to (Dunn, 1985 as well as Karoly and Vicent (1998). However, on average about one more cyclone per year is generated outside the season (see e.g. Figure 5.1), and thus, the cyclone frequency converge at 12 y^{-1}. In the 1980-2007 series, 10 cyclones were removed because of lacking intensity data [7 of which were from 1981 (1 in

November, 4 in December, 1 in January and 1 in February) – the season 1980/81 – 2 from 1982 (2 in December) and 1 from 2001 (November)]. For obvious reasons (lack of intensity data was a rule in that series) no corresponding removal was needed in the earlier record. All forthcoming analyses in this chapter are based on data from the cyclones included in Tables 7.1-2. As explained above, intensity is of major importance and has to be carried along with all types of analyses.

7.2.3 Intensity and seasonal distribution (period 1980-2007)

Figure 7.3 shows the seasonal distribution of cyclones in the SWIO, stratified by intensity according to the Saffir-Simpson Scale (Table 5.3).

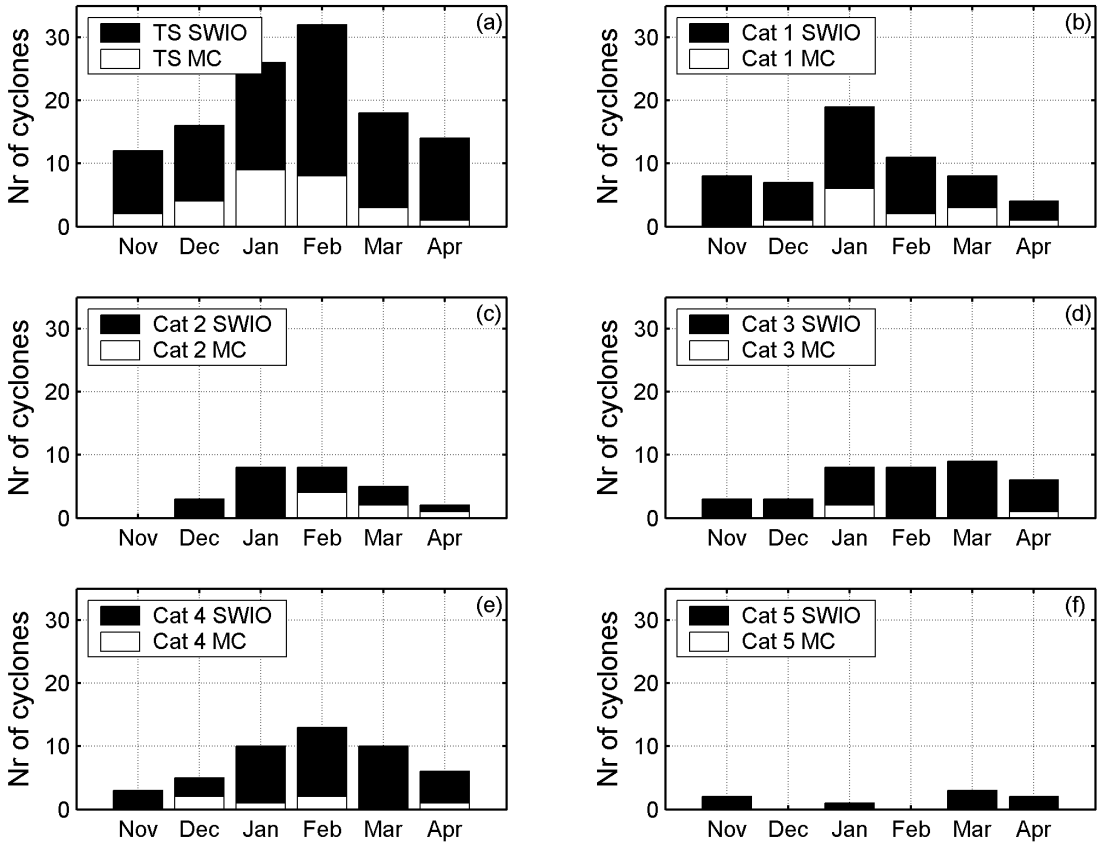

Figure 7.3: Number of tropical cyclones (MSW>17 ms^{-1}) with intensities according to the Saffir-Simpson scale, SWIO and Mozambique Channel, 1980-2007.

In addition, Table 7.3 shows total number and frequency for each TC category, also month by month. From 1980-2007, 118 out of totally 293 cyclones were TS (Table 7.3) and 175 were TC, category 1-5.

Figure 7.3 indicates distinct peaks in January and February for TS and TC category 1. For higher intensities there is a weak displacement of maximum towards March. Category 5 is rare in the SWIO, and absent in the Mozambique Channel, whereas the occurrence among TC category 1-4 seems to be evenly distributed in both areas. As indicated, there are no TCs in the MC during November and two storms only.

From Table 7.3, one might imagine an under-representation of TC category 2-3, but in fact the distribution is almost even for all cyclones with Category 1-4. Only category 5 cyclones with MSW>69 ms^{-1} are rare. Taking into account the uneven ranges of MSW for each category (see 2nd row of Table 7.3) one might conclude that category 3, with MSW in the range 42-49 ms^{-1}, is somewhat less common, while TS and category 1 are slightly more common than the average. This, however, is at least partly because of smaller ranges for category 2-3.

Table 7.3: Occurrence of cyclones (by MSW, ms^{-1}) in the South-West Indian Ocean (number of cyclones and frequency). Period 1980-2007

	TS		Cat1		Cat 2		Cat 3		Cat 4		Cat 5	
	17<MSW<33		33<MSW<42		42<MSW<49		50<MSW<58		59<MSW<69		MSW>69	
	Num	Freq	Num	Freq	Num	Freq	Num	Freq	Num	Freq	Num	Freq
Nov	12	0.43	8	0.29	0	0	3	0.11	3	0.11	2	0.07
Dec	16	0.57	7	0.25	3	0.11	3	0.11	5	0.18	0	0
Jan	26	0.93	19	0.68	8	0.29	8	0.29	10	0.36	1	0.04
Feb	32	1.14	11	0.39	8	0.29	8	0.29	13	0.46	0	0
Mar	18	0.64	8	0.29	5	0.18	9	0.32	10	0.36	3	0.11
Apr	14	0.50	4	0.14	2	0.07	6	0.21	6	0.21	2	0.07
Total	118	4.21	57	2.04	26	0.93	37	1.32	47	1.68	8	0.29

Although the peak frequency of cyclones is in January-February the total number of intense TCs (22; Category 3-5) is higher in March while the total number of weak TCs (27; Category 1-2) is higher in January. On the other hand the highest number of tropical storms in February is 32 (Table 7.3).

Table 7.4 is similar to Table 7.3, but shows statistics in the Mozambique Channel only. There are no category 5 cyclones in the channel and no TCs in November. The intensity distribution is also different from that of the whole SWIO region, with relatively fewer intense cyclones (category 3-5).

Table 7.4: Occurrence of cyclones (by MSW, ms^{-1}) in the Mozambique Channel (number of cyclones and frequency). Period 1980-2007

	TS		Cat 1		Cat 2		Cat 3		Cat 4		Cat 5	
	17<MSW<33		33<MSW<42		42<MSW<49		50<MSW<58		59<MSW<69		MSW>69	
	Num	Freq	Num	Freq	Num	Freq	Num	Freq	Num	Freq	Num	Freq
Nov	2	0.07	0	0.00	0	0	0	0	0	0	0	0
Dec	4	0.14	1	0.04	0	0	0	0	2	0.07	0	0
Jan	9	0.32	6	0.21	0	0	2	0.07	1	0.04	0	0
Feb	8	0.29	2	0.07	4	0.14	0	0	2	0.07	0	0
Mar	3	0.11	3	0.11	2	0.07	0	0	0	0	0	0
Apr	1	0.04	1	0.04	1	0.04	1	0.04	1	0.04	0	0
	27	0.96	13	0.46	7	0.25	3	0.11	6	0.21	0	0

Kimbal and Mulekar (2004), while studying the spatial and temporal distribution of TCs over the North Atlantic have found dual peaks in TSs, categories 1-2, and categories 3-5. After detailed investigations they concluded that local variations in SST related to oceanic processes played a significant role. SST variability may contribute to amplitude differentiation in peak frequency in the SWIO and the MC as well, such that a higher frequency during a certain month is affected both by surface heating related to seasonal development and to variability in winds and thermohaline circulation (see also Xie et al., 2002). The importance of SSTs and upper ocean heat content will be further discussed below.

7.3 Spatial distribution and preferred cyclone tracks

To see where, when and under which conditions the cyclones in the SWIO achieve maximum intensity, a set of maps showing tracks and “along track intensity variations” were produced. This set of figures is shown for all cyclones occurring from 1980 to 2007 in Figures 7.4 a-f. Different symbols are employed to represent the different intensities (TS and TC category 1-5). The period was

further separated into two (1980-93 and 1994-2007) as a basis for a forthcoming interpretation of the relationship between SSTs and mixed layer heat content, on one hand, and formation and intensity of cyclones on the other (Figures 7.5-6 a-f). This division was made following a distinct increase of the mean SSTs in the mid 1990s, as will be shown below.

Movement patterns of SWIO cyclones are indicated in Figures 7.4 a-f. First, most cyclones tend to develop within the Inter-Tropical Convergence Zone (Figure 2.1), or slightly to the south side of this low pressure ridge. Further, the cyclones are known to originate from easterly waves, east of which numerous thunderstorms develop cyclonic airflow due to convergence. Jury et al. (1991) have identified easterly waves crossing the 10-20°S latitude bands east of 55°E. These easterly waves, may organize and propagate scale convection suitable for TC formation. The tracks in Figure 7.4 indicate that cyclones, once they are formed, are steered W-SW in their early stage (along with the slope of the ITCZ). When reaching latitudes south of 15-20°S most cyclones take on a southerly direction and then turn towards SE. Ho et al. (2006), have argued that cyclone movement occurs at the northwestern flank of the South Indian Subtropical High, which seems realistic when comparing the tracks of Figure 7.4. However, there are two high pressure cells in the southern Indian Ocean, and it seems as if cyclones that are formed further east have a tendency to move directly towards the south in between the two high pressure cells (see Figure 2.1), while those formed further west pass west of the second high pressure cell.

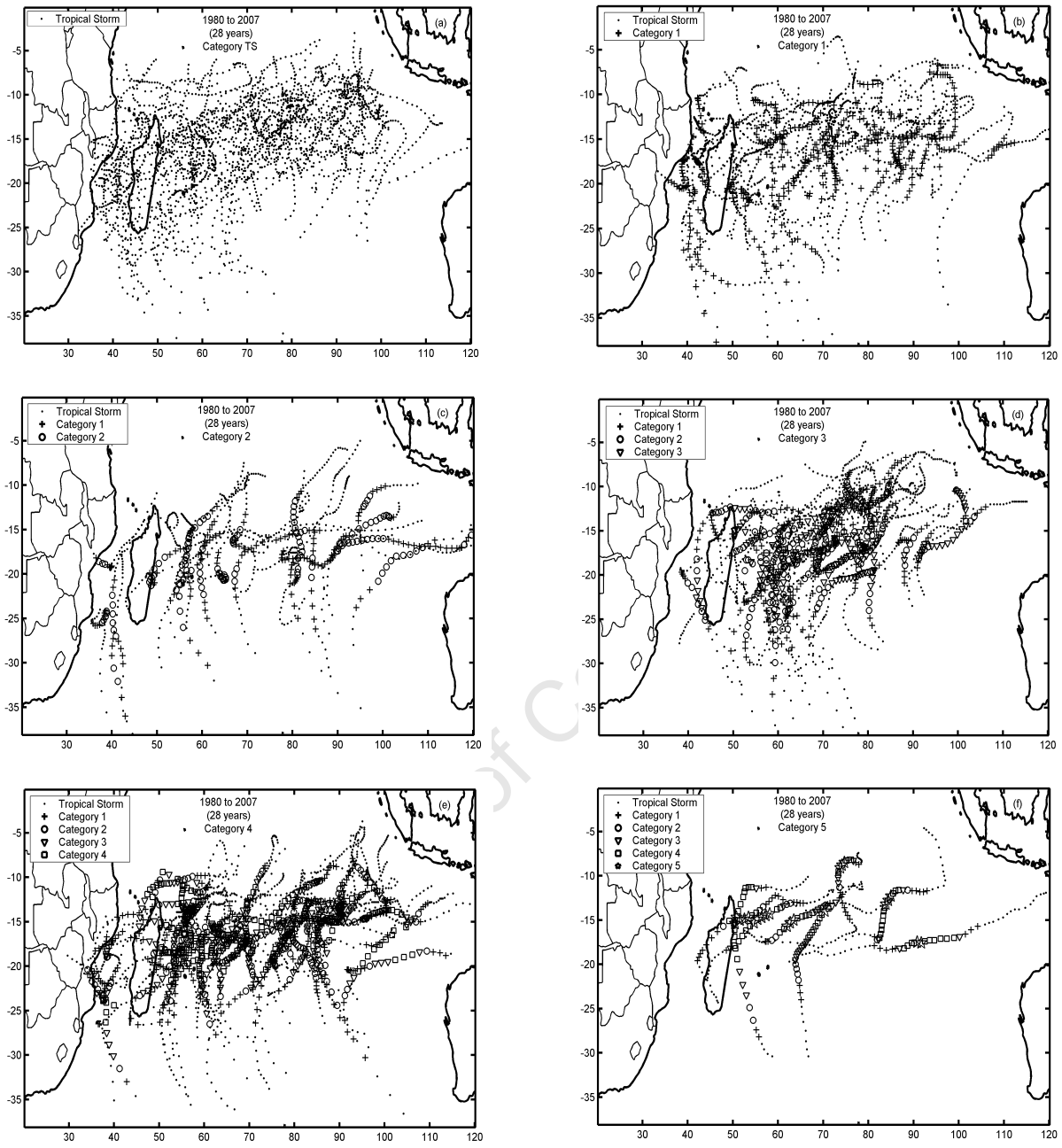

Figure 7.4: Tropical cyclones tracks stratified by maximum intensity according to the Saffir-Simpson scale, TS and Category 1-5 (data from 1980-2007). TC intensity varies along with the track and the intensities are marked by dots which are proportional to "cubed wind force", whereby the figures give a rough estimate of the mixing intensity in different parts of the ocean and for different TC intensity.

Madagascar may also exert some influence on the tracks, and several cyclones take a southerly track up to 1000 km east of the island, an area in which the cyclone density is high south to 20-25°S.

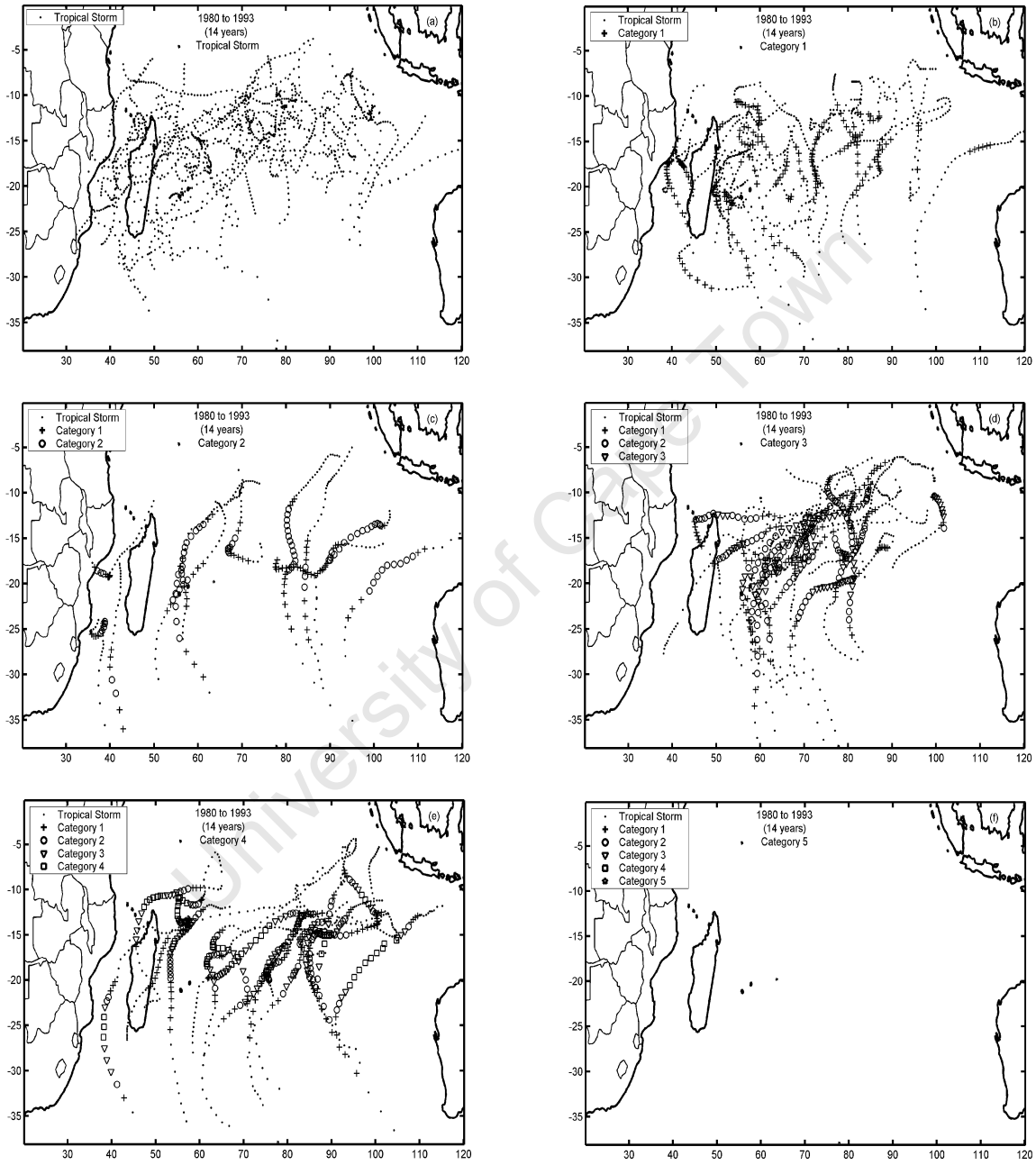

Figure 7.5: Same as Figure 7.4 but for the period 1980-93.

There is also a band of maximum activity, stretching from the Mascarene Ridge (10-18°S; 60E) to about 8-15°S-90°E. This is also along the southern front of low saline and warm water (see Figures 2.5a-b), where buoyancy is stronger than indicated by temperature alone. However, the overall impression is that every cyclone has its own life (as noted by several authors in the past), and that even 300 cyclones are for many purposes not enough to obtain reliable statistics.

Tracks from the two 14-year periods, 1980-93 and 1994-2007 are shown in Figures 7.5-6 a-f. Tropical storms are uniformly distributed across the basin (east of 100°E) and show similar track patterns during the first and the second period (Figures 7.4a, 7.5a, 7.6a). Category 1 cyclones show a uniform distribution for the full period (Figure 7.5b), however there is a shift in the tracks away from Madagascar during the later period (Figures 7.5b, 7.6b). Category 2 tracks feature a meridional pattern during the earlier period but more zonal movements in the latter. Very intense cyclones (category 4-5) show a general increase in frequency during the latter period (Figures 7.5-6e-f). The last 14-y period was more active with a higher landfall frequency (as discussed in Section 7.7).

Category 5 cyclones did not appear at all during the first period (Figures 7.5f), but became frequent during the second period. None of those cyclones however, appeared in the Mozambique Channel, while a few made landfall on the east coast of Madagascar. In relation to Figure 3.5 (Xie et al., 2002) showing the mean annual number of TC days, Figures 7.4-6 add new information, concerning the intensity of the cyclones that appear. The intensity of TCs, rather than the number of TC days should be accounted for, in relation to sea surface temperatures and particularly the mixed layer heat content. The figures indicate that maximum intensity appears over a wider area than the maximum number of TC days. Given that SSTs are reduced by 1-2 ˚C over large areas (due to mixing during a TC passage), TC activity around 15°S may even exert some self-control related to SSTs and mixed layer depths. Spatial density of cyclone days based

on the Saffir-Simpson categories are presented in Section 7.8 and compared with the mean number of TCs as seen in Xie et al. (2002).

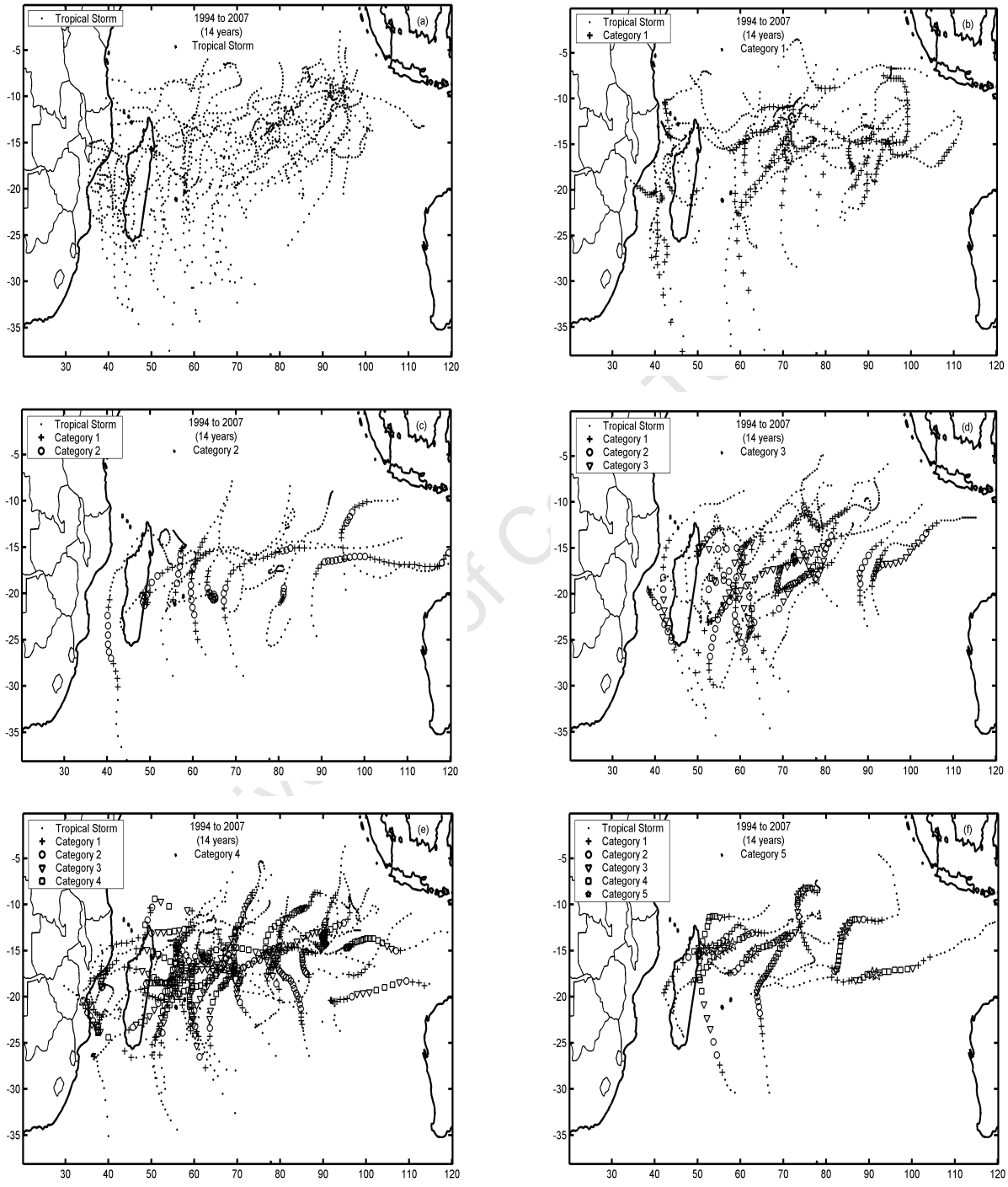

Figure 7.6: Same as Figure 7.4 a-f but for the period 1994-2007.

7.4 Inter-annual and long-term mean seasonal distribution

7.4.1 Inter-annual distribution and ENSO

The annual number of cyclones during 1980 - 2007, with separation between TCs and TSs, is shown in Figure 7.7. As aforementioned, there are some 11 cyclones generated annually within the cyclone season (or about 12 if cyclones outside the season are included), with a maximum number of 15 in 1994, and 13-14 cyclones during 1984, 1985, 1997, 2005. Minimum numbers, 5-7 occurred in 1983, 1987 and 2001. However, some years are dominated by TSs and others by TCs, without obvious correlation, indicating that it is worthwhile to look at intra-TC intensity as well.

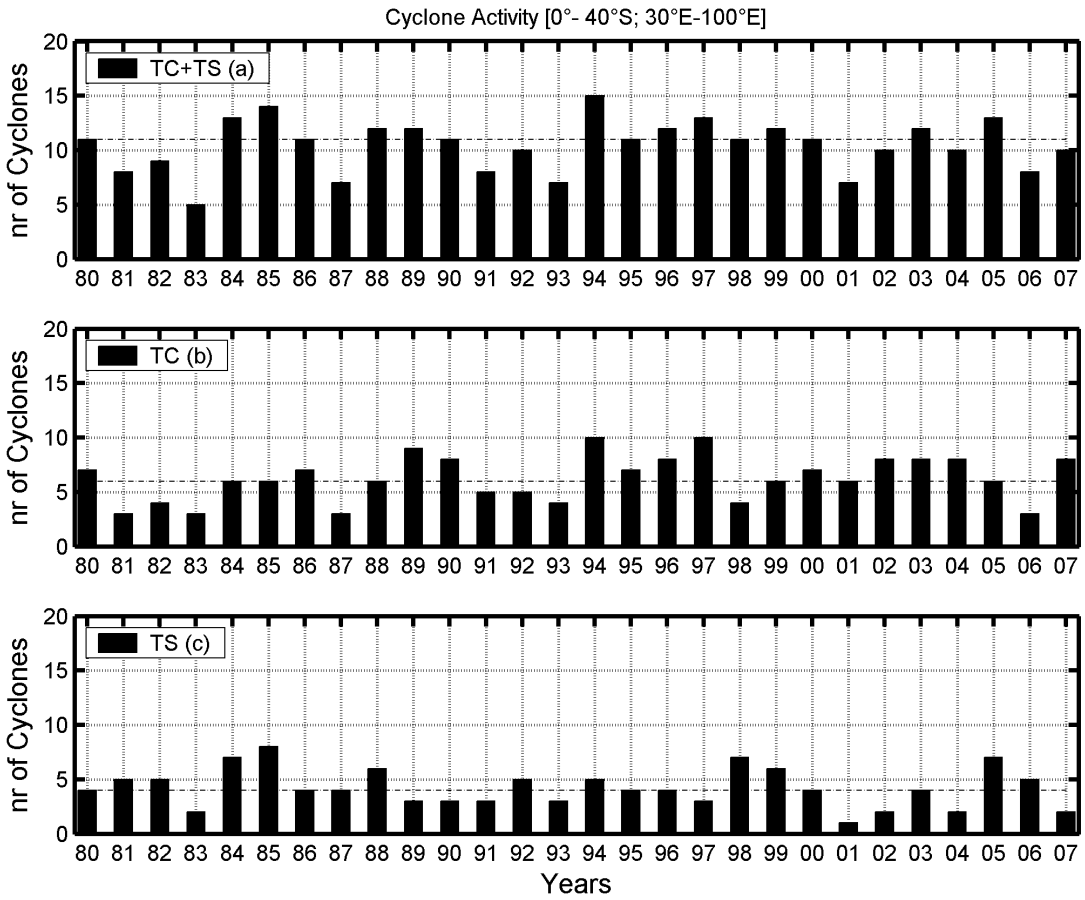

Figure 7.7: Annual number of cyclones in the SWIO (November-April), stratified by TS and TC.

As discussed in Section 3.3.2, Landsea (2000) have pointed out that the number of cyclones is related to the ENSO index, particularly in the North Atlantic (where it is low during El Niño years) and in the North-East Pacific (where it is high). In the South Indian Ocean, ENSO may affect areas of formation (Ho et al., 2006; Kuleshov and de Hoedt, 2003) and track direction (see Section 3.3.3).

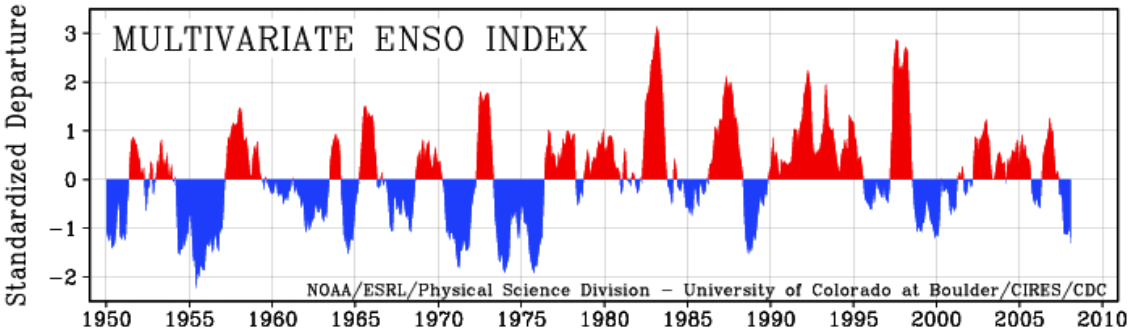

Figure 7.8: ENSO multivariate index from 1950-2007 (source: NOAA/CDC)

An ENSO index is shown in Figure 7.8. Some years with a high number of cyclones are La Niña years others are El Niño years, and vice versa. Compared to Figure 7.7 there is no obvious, general relationship between variations in the total number of cyclones and ENSO variations. However, it is of interest also to look if intensity can play a role, basically if cyclones are more intense during one or the other phase.

As mentioned in Section 3.3.2 the impact of ENSO differs in the different TC regions of the world. Also definitions of El Niño and La Niña differ accordingly (e.g. Trenberth, 1997; Pielke and Landsea, 1999). The forthcoming analysis uses a definition of El Niño and La Niña which is based upon the ONI (Oceanic Niño Index). It is the running 3-month mean of ERSST.v3 SST anomaly for the Niño 3.4 region (i.e., 5N-5S, 120-170W). The events are defined as 5 consecutive months warmer than or equal to +0.5° for El Niño and cooler than or equal to -0.5° for La Niña events (see also Appendix B3, Table B17). Other years which did not meet the criteria are considered as neutral years**.** Statistics (Table 7.1-2) indicate that 178 TCs (about 61%) formed over the region are observed in December-February and 197 TCs (about 67%) are observed in January-March during 1980-2007. Cyclone frequency during El-Niño and La Niña years,

respectively are shown in Table 7.5 for January-March (JFM) being the peak frequency period, and in Table 7.6 for December-February (DJF), when ENSO is at its high phase. Table 7.5 (JFM) shows that out of totally 197 cyclones, 121 (61%) reached the TC level and 76 were tropical storms (TS). During the 28-year period, ITCs (Category 3-5) were 62 while extreme cyclones (Category 4-5) were 36. Only 4 TCs reached category 5.

During the period under consideration (1980-2007), out of the 28 seasons, there were 9 years each for El Niño and La Niña events, while 10 were neutral (Appendix B3, Table B17). The total number of cyclones (TS+TC) is 59, 68 and 70, respectively. Thus, the number of cyclones does not seem to be much affected by ENSO. Looking at tropical storms separately, there is not any obvious correlation either, neither is there any clear tendency among ITCs. Possibly, the current analysis involves too few years, when variations in cyclone activity is evaluated.

Table 7.5: ENSO effects on the number of cyclones and mean frequency in the South-West Indian Ocean, for the peak cyclone period (JFM) 1980-2007.

		TS	Cat 1	Cat 2	Cat 3	Cat 4	Cat 5	Total
El Niño	Number	26	12	4	8	8	1	59
	Mean	2.9	1.3	0.4	0.9	0.9	0.1	6.6
Neutral	Number	21	12	12	10	12	3	70
	Mean	2.1	1.2	1.2	1.0	1.2	0.3	7.1
La Niña	Number	29	14	5	8	12	0	68
	Mean	3.2	1.6	0.6	0.9	1.3	0	7.6
	Total	76	38	21	26	32	4	197
	Mean	2.7	1.4	0.8	0.9	1.1	0.1	7.0

On the other hand Table 7.6 show the statistics for ENSO peak months of DJF which seems to corroborate JFM situation. The total number of cyclones during the peak months are 59, 61 and 58, respectively, thus without any difference between total activity during El Niño and La Niña.

In JFM the mean number of cyclones is generally higher for TS, Category 1, 2 and 4 with no difference significant difference in Category 3 and 5 during La Niña

compared to El Niño years (Table 7.5). If one merge the categories, for weak TCs (Category 1-2) the JFM mean number (1.1) stays higher during La Niña than during El Niño years (0.9) and for intense TCs (Category 3-4) JFM mean number is also higher (0.7) during La Niña than during El Niño years (0.6). Also the overall mean number of cyclones is higher (7.6) during La Niña than during El Niño years (6.6).

Table 7.6: ENSO effects on the number of cyclones and mean frequency in the South-West Indian Ocean, for the high phase of ENSO (DJF) 1980-2007.

		TS	Cat 1	Cat 2	Cat 3	Cat 4	Cat 5	Total
El Niño	Number	28	12	3	9	7	0	59
	Mean	3.1	1.3	0.3	1.0	0.8	0	6.6
Neutral	Number	21	12	11	6	10	1	61
	Mean	2.1	1.2	1.1	0.6	1	0.1	6.1
La Niña	Number	25	13	5	5	10	0	58
	Mean	2.8	1.4	0.6	0.6	1.1	0	6.4
	Total	74	37	19	20	27	1	178
	Mean	2.6	1.3	0.7	0.7	1.0	0	6.4

The peak months, DJF show a slightly different picture with mean number for TS and Category 3 higher during El Niño than during La Niña years while mean number for Category 1, 2 and 4 is higher during La Niña compared to El Niño years. Meanwhile no relative changes in Category 5 are observed in these years (Table 7.6). Considering weak TCs (Category 1-2) the DJF mean number (1.0) stays higher during La Niña than during El Niño years (0.8) and for intense TCs (Category 3-5) the DJF mean number does not change much during La Niña (0.7) compared to El Niño years (0.6). Also the overall mean number of cyclones during La Niña (6.6) and El Niño years (6.4) shows little difference.

Considering the overall (Table 7.2) statistics for DJF (34, 72, 72 cyclones) and JFM (72, 72, 54) mentioned above one can see that the difference in seasonal frequency is strongly influenced by the relatively higher number of cyclones in March compared to December. And more interesting is the fact that the frequency of intense cyclone is higher in March than in any month (Figure 3d-f). These results are in agreement with the idea that on average, the number of

cyclones is higher during La Niña than during El Niño years as indicated in Vitart et al. (2003).

7.4.2 Spatial distribution (tracks/genesis) and ENSO

Cyclone track patterns differ between warm (Niño) and cold (Niña) years and recent studies relying on recent climatology (e.g. Ho et al., 2006) indicate that SIO TC activity increases in the western part of the SIO (west of 75°E) and decrease in eastern part of the SIO (east of 75°E) during El Niño compared to La Niña. Question is how intense tropical cyclones activity and track pattern are related to ENSO in the SWIO? Below, track patterns of ITCs during JFM (peak cyclone season) and DJF (ENSO high phase) are presented and compared below.

Track pattern of Intense tropical cyclones in January-March with ENSO

During JFM and corresponding El Niño years from 1980-2007, 17 ITCs were present in the SWIO (Figure 7.9a), 14 of those were generated northeast of Madagascar (55-90°E and 5-22°S), another two east of 90°E and only one in the MC. During La Niña (Figure 7.9b) 20 ITCs were evident in the basin. Fourteen were generated northeast of Madagascar (55-90°E and 7-22°S) and six east of 90E between 8-20°S approximately. A comparison of Figures 7.9a-b shows that the number of ITCs is higher during La Nina years compared to El Niño. The majority of TCs take on recurving tracks in warm years (Figure 7.9a) but those in cold years tend to move more westward after forming at locations further east (Figure 7.9b).

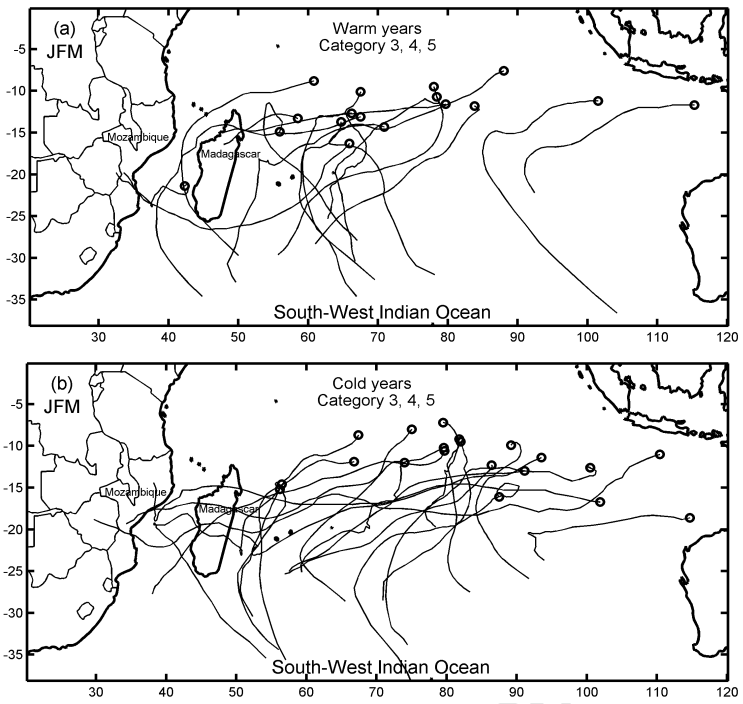

Figure 7.9: January-March tropical cyclone tracks during (a) Warm (El–Niño) years (1982/83, 1986/87, 1987/88, 1991/92, 1994/95, 1997/98, 2002/03, 2004/05) and (b) Cold (La Niña) years (1983/84, 1984/85, 1985/86, 1988/89, 1995/96, 1998/99, 1999/00, 2000/01, 2005/06). These warm and cold episodes are defined according to Ocean Niño Index (see Appendix B17).

Track pattern of Intense Tropical Cyclones in December-February - ENSO

For DJF and corresponding El Niño years, 16 ITCs were displayed in the SWIO (Figure 7.10a), twelve of those were generated northeast of Madagascar (55-90°E and 5-22°S), another three east of 90°E and only one in the MC. During La Niña (Figure 7.10b) 15 ITCs were evident in the SWIO. A number of thirteen were generated in the northeast of Madagascar (55-90°E and 7-22°S) and two east of 90°E between 8-20°S approximately. A comparison between Figure 7.9a and b shows that the number of ITCs does not show significant difference between La Niña years and El Niño years. Similar to Figure 7.9, the majority of TCs take on recurving tracks in warm years (Figure 7.10a) but those in cold years tend to move more westward after forming at locations further east (Figure 7.10b).

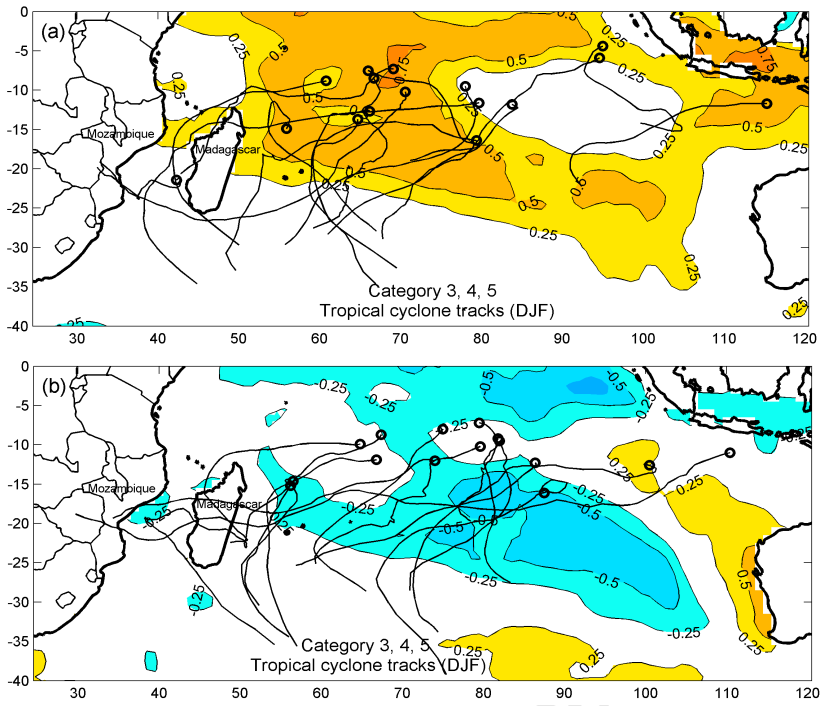

Figure 7.10: December-February SST composite normalized anomalies from mean 1980-2007 with category 3, 4, 5 DJF TC tracks superimposed for the the same El Niño (Top panel) and La Niña years (bottom) as in Figure 7.9.

Considering only JFM where the ITCs are well represented (see Table 7.5-7.7) and assuming that these systems are stratified at 75 degree longitude (Table 7.7), it is shown that 10 (west of 75°) and 7 (east of 75°E) ITCs have appeared during El Niño years. Similarly, 6 (west of 75°E) and 14 (east of 75°E) appeared during La Niña years in JFM. In total 17 ITCs appeared during El Niño years against 20 ITCs during La Niña years.

This suggests a suppressed activity on intense TCs during El Niño years. Hot et al. (2006) have also confirmed the existence of suppressed activity of intense TCs during El Niño. However these authors have recognized that changes in TC activity in the SIO may be attributed to the inclusion of weak intensity systems ($V_{max} \leq$ 32 ms^{-1}) that were counted as TCs.

Table 7.7: Number of ITCs stratified at 75°E

JFM (Warm years)	
10	7
JFM (Cold years)	
6	14

20 E 75 E 120 E

However Table 7.5 does not confirm any influence of these weak systems on ITCs. As mentioned before, ITCs may be suppressed via vertical westerly shear and reduced upper anticyclonic vorticity that are produced during El Niño years (Gray, 1984; Bove et al., 1998; Jury, 1993) hindering TC development. Also the increase in the number of cyclones east of 75°E during La Niña years seems to indicate an increase of cyclones sweeping across Madagascar and Mozambique. Ho et al. (2006), while analyzing variations in tropical cyclone activity in the SIO (including the SWIO) with ENSO found that overall TC passages increase in the Mozambique coastal region and the central mid latitude SIO (60-80°E, 20-40°E), with a decrease south-east of Madagascar and the central east tropical SIO (75-90°E, 10-20°S).

7.4.3 Long-term variability and trends

Sea surface temperatures have increased substantially over the last decades in most surface areas of the ocean (Levitus et al., 2005). Increased SSTs have been suggested as a reason for more intense TCs in several cyclone regions, including the SWIO (Webster et al., 2005). Figure 7.11 shows the SST development in the SWIO and in the Mozambique Channel, since 1982. As can be seen, there is a substantial increase in SSTs from 1995, but only in the MC. When the performing a least-squares linear regression test, trend in SST averaged over the Mozambique Channel (Appendix E1.5) is significantly different

from zero at 95% confidence level, except for the SWIO (Appendix E1.5-1.7; east of Madagascar) where the significance cannot be revealed. Since the linear regression includes t-test, which requires a normal distribution for the dataset, a non-parametric test is used and yields the same result. The non-parametric test used in this work is the Man-Kendall test. More details about these methods in the references described in Section 5.2.3. A comparison for intense TCs (category 3-5) in the MC and the SWIO respectively is shown in Table 7.8.

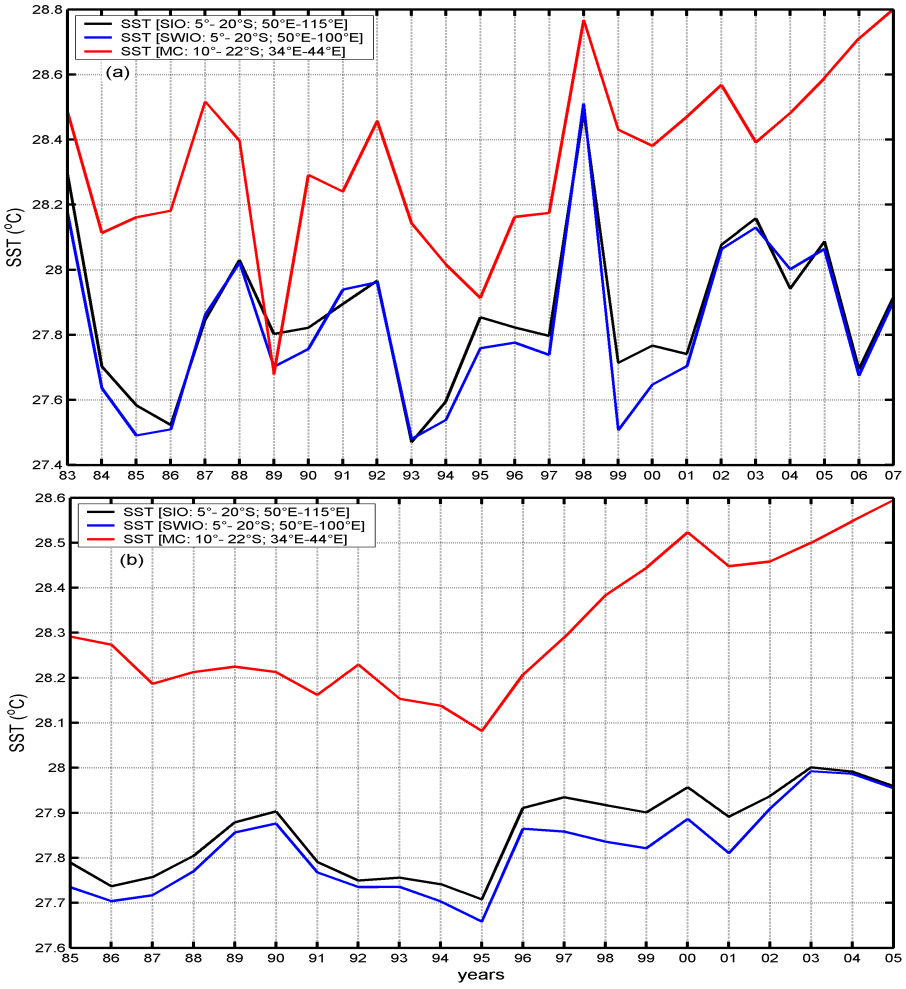

Figure 7.11: Mean (a) and 5-year running mean (b) of SST during the peak cyclone season (November-April) of the South-West Indian Ocean (Africa mainland to 100°E, 0-40°E). Data are a subset of monthly global Optimally Interpolated (OI) sea surface temperature (Reynolds and Smith, 1994) and are obtained from the National Center for Environmental Prediction (NCEP).

The number of intense TCs has increased by more than 50% from the first period (1980-93) compared to the second (1994-2007). A corresponding increase in category 4-5 cyclones was shown by Webster et al. (2005), although over a longer period. These authors also noted a similar amplitude increase in SSTs during the 1970s (Figure 3.4).

Meanwhile the total number of category 4-5 cyclones was higher east of Madagascar than in the Mozambique Channel (Figure 7.7-8e-f), although the Mozambique Channel was particularly warm and the temperatures were well above the SSTs east of Madagascar. The most likely reason for the higher SSTs is that the winds are weaker (Figure 2.3) in the MC which means that there is less mixing (Penven et al., 2006) and therefore a smaller mixed layer depth (see below).

Table 7.8: Number of intense cyclones (category 3-5) in the SWIO and in the MC, during 1980-93 and 1994-2007, respectively.

Area	Period[a,b]	
	1980-1993	1993-2007
Mozambique Channel (only)	2	7
SWIO (east of 50°E)	34	49
Total	36	56

[a,b] Twice 14 years data based on JTWC/LR-RSMC observations (November-April)

An intensity comparison, valid for all cyclones of the SWIO, is shown in Table 7.9. The results indicate an increase in category 4-5 TCs from 17-36 (very intense TCs) and in category 3-5 (intense TCs) from 36-56. The number of Tropical Storms, on the other hand, has decreased. In total, there is an increase from 138 to 155 cyclones.

Table 7.9: Number of cyclones in the SWIO (including MC), separated by category for the periods 1980-93 and 1994-07, respectively. ITC=Category 3-5.

Period	TS	Cat 1-2	Cat 3	Cat 4	Cat 5	ITCs	TCs	All
1980-1993	62	40	19	17	0	36	76	138
1994-2007	56	43	18	28	8	56	99	155
Change (%)	-9.7	+6.9	-5.0	+46.4	-	+35.7	+23.2	+10.9

TS=tropical storm; Cat=Category; TC=tropical cyclone; ITC=intense tropical cyclone

7.5 Wind Climatology and cyclogenesis

As described in Chapter 2.1, the most characteristic feature of the Indian Ocean is its strong monsoon climate, with the northern monsoon dominating from December to February and the southern monsoon from May to September. Although the monsoon climate is much more prominent in the northern Indian Ocean its effects spill over on the southern side of the Equator. When the ITCZ reaches its southernmost position in January and February (see Figure 2.2), northerly winds reach 5-10°S, and the westerly trade winds are pushed southwards, weakening considerably (Figure 2.3). This general picture has been known for a long time, also that the generation of cyclones is highly related to the ITCZ with a majority of cyclones developing within this band of low pressure ridges (Chapter 3.3.1).

However, not until recently, have satellite observations of wind direction and wind speed become good enough to offer a more precise climatology. New wind data from QuikSCAT, running since 1999 (Chapter 5.3), were put together for the years 2000-06; Figure 7.12 shows monthly data for the cyclone season, i.e. from November to April, indicating the successive movement of the ITCZ (as a band of low winds) into the southern Indian Ocean. Simultaneously the trade wind weakens across the ocean, particularly towards Madagascar and in the Mozambique Channel. At the end of the season, in March and April the ITCZ moves northwards, more so towards the African coast, and from April, the southern monsoon starts blowing along the coast.

As discussed in Chapter 3, the wind, and its variations in space and time is one of several variables that may influence the number of cyclones, however, there are also several other factors of importance, all of which are more or less related to each other. The annual cycle of the mean surface wind field and the number of tropical cyclones that formed within the main development region (MDR) are shown in Figure 7.13. The mean surface wind, which is highest during August (winter), decreases sharply and it is lowest during summer (December-April) and

increases again from May to July (winter). January and February are the most active months in terms of cyclogenesis but similar to December and March are associated with lowest values of surface winds. This suggests than intraseasonal variability of factors rather that surface winds are important in determining TC development (e.g. DeMaria et al. 2001). The SST within the MDR is also higher in January-February (Figure 7.14) and in combination with low background wind shear (Figure 7.33) may contribute to enhanced activity.

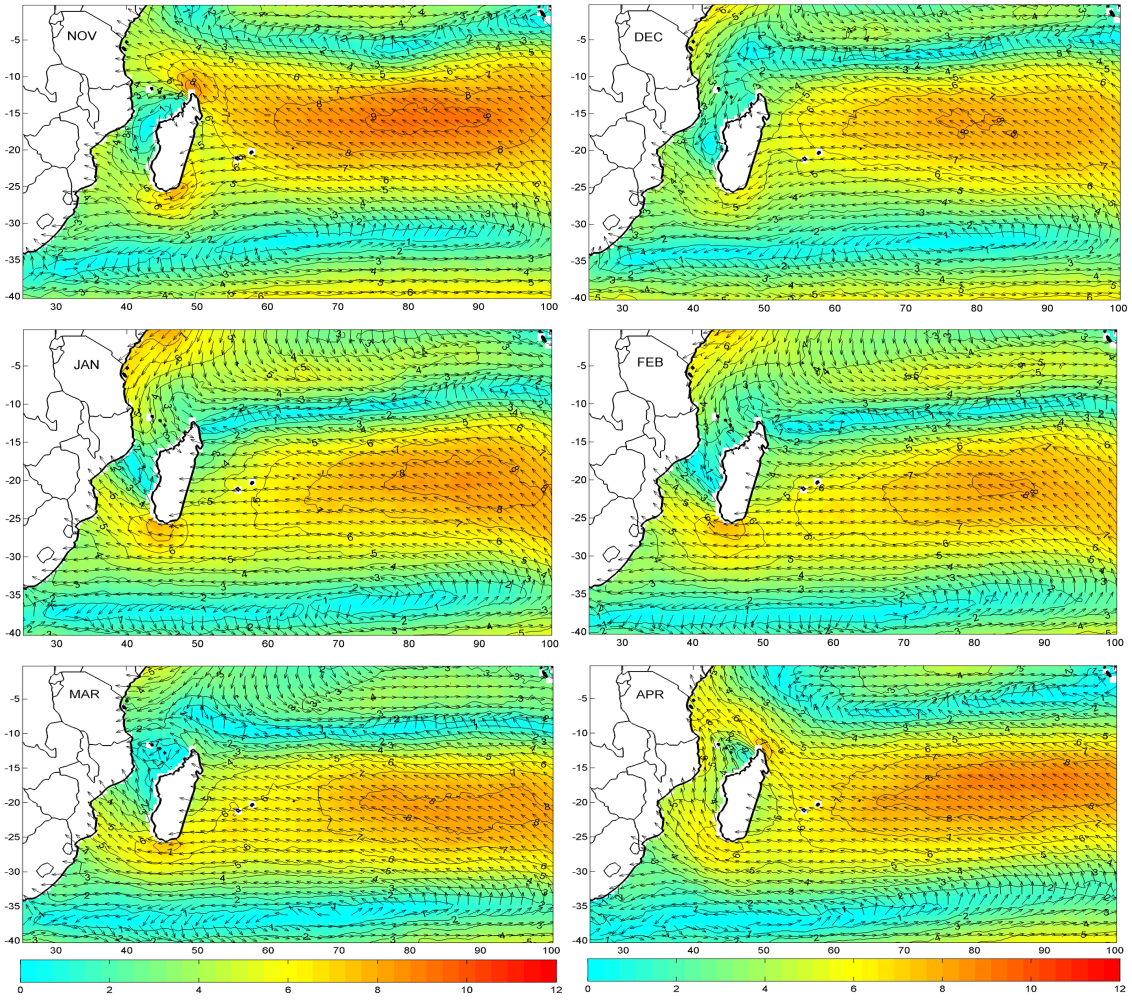

Figure 7.12: Climatological winds of the South-West Indian Ocean from 2000-2006 based on QuikSCAT data. The figure highlights lines of wind convergence (from the equator to about 20°S) reflecting the movement of ITCZ during the cyclone season (November-April). Also the winds in the Mozambique Channel are light during almost all the seasons.

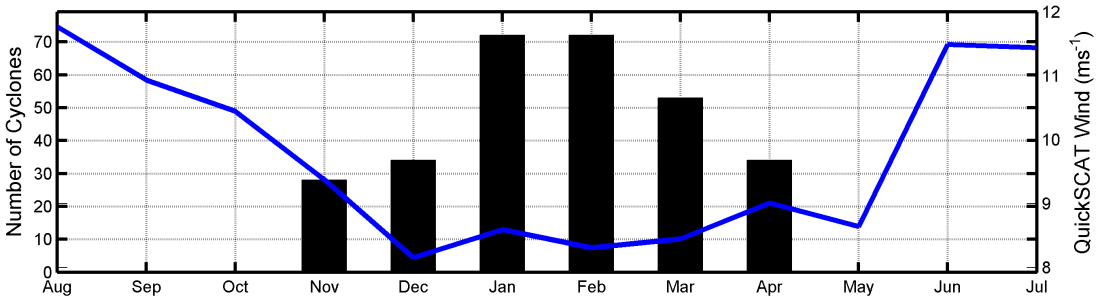

Figure 7.13: Annual cycle of the climatological surface wind (ms^{-1}) averaged within the SWIO (thick blue line) and the total number of cyclones (TC+TS) that formed in the region (shaded bars) over the period of 1980-2007.

7.6 Seasonal distribution and genesis related to SST and TCHP

As indicated before in Figures 7.4-6, cyclones in the SWIO show some preferred seasonal patterns. Figure 7.14 shows, month by month, from November to April the origin (or genesis point) and the track for each cyclone formed during 1980-2007. Most of the cyclones are formed in the area east of Madagascar. Some 10% are formed in the MC, but in terms of genesis density, it is similar to that of the open SWIO. Still, no cyclones at all are formed in the channel during November and April, whereas the density is high from January to March.

In the open SWIO cyclone genesis during November and April takes place further east and north and in February, but also in March, the genesis areas are found further south. The cyclones also reach further south. This pattern should, to some extent depend on the SSTs, the climatology of which is shown in Figure 7.14. The relationship is discussed further below.

It seems as if fewer cyclones have their origin in the easternmost part of the ocean. However, the area selected for counting cyclones, with occurrence in the area west of 100°E matters here; but tropical cyclones with at least a portion of their track within the SWIO, though the genesis location does not necessarily need to be within the SWIO are included in the analysis. As pointed out, the general formation pattern is dominated by the movement of the ITCZ (and

naturally to features such as the seasonal variations in temperatures which follows this motion).

The long-term mean SSTs shown in Figure 7.14 indicate that the temperature for formation of cyclones is above 28°C in the large majority of cases. In the early season, though, there are more cyclones formed in the range between 26.5°C and 28°C. However SST>26.5°C (Palmén, 1948; McBride, 1995) is still the widely accepted empirical threshold for TC formation, although that should apply to the individual case, and not to a long-term mean. The SSTs may be compared with WOA05 data shown in Figure 2.5b for January to March; it is obvious that the two data sets are nearly identical, indicating that errors in terms of TMI SSTs are likely to be small. It is worth pointing out that the salinity climatology, Figure 2.5a, with a tongue of low saline surface waters from the Indonesian side will certainly affect the surface water stability in the genesis area quite substantially. This might help to generate cyclones in the early season (November-December) in the north eastern part of the SWIO. Low salinities may also affect cyclogenesis in the northern MC (contributing to smaller mixed layer depths, higher SSTs and stability).

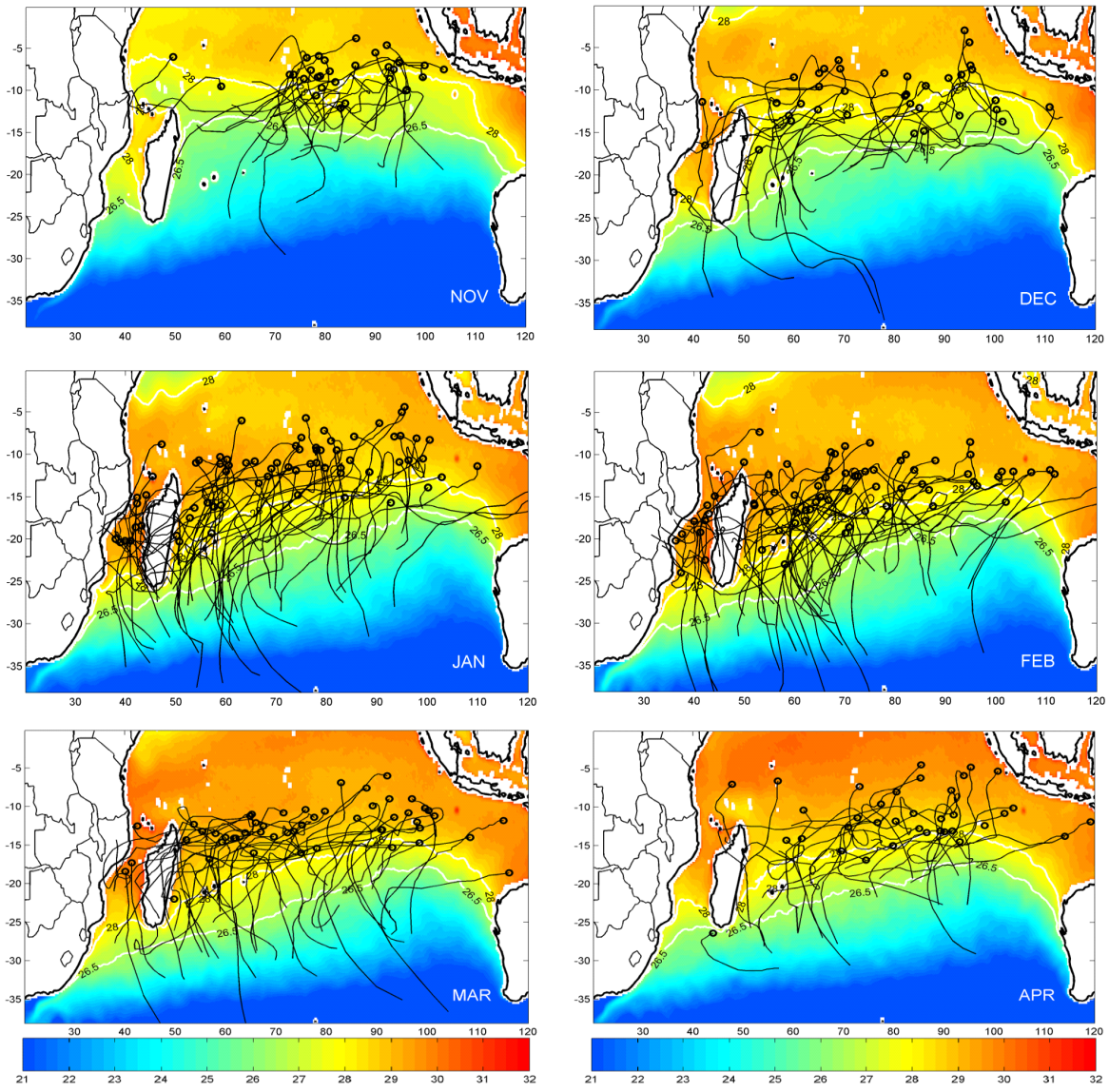

Figure 7.14: Tropical cyclones trajectories for the months of November–April (1980-2007).TC genesis locations are indicated as circles. TMI monthly mean SST (1998-2005) highlights two isotherms. The southernmost isotherm, 26.5°C is the typical SST cut-off in cyclone formation as suggested by Palmén (1948). The northern isotherm, 28°C, is the proposed threshold value for the South-West Indian Ocean under the current investigation.

In Figure 7.15 the positions of formation (genesis coordinates) and SSTs for TCs, based on weekly TMI SST data from the TRMM mission (1998-2005) are shown. As indicated before (Chapter 5), TCs are known to cool the SST over which they are located. Thus

the SST the week prior to the storm was used to better represent the SST encountered at the genesis of each of the cyclones in the record. Formation SSTs are indicated in half degree intervals. Only one cyclone was formed in the interval between 27-27.5°C, and none below that range. Mean genesis SST for all 80 cyclones in the whole SWIO region during that period was 29.2°C. For cyclones within the Mozambique Channel, the mean SST was 29.7°C. We can see that this interpretation increases the genesis SST by about 0.5°C, compared to a relationship based on climatology SSTs (Figure 7.14). Sea surface temperature in relation to longitude indicates that cyclones in the eastern part (80-100°E) are generated at lower temperatures (28.25-29.75°C) than those in the western part (60-80°E), where SSTs are typically 29.25-30.25°C. As mentioned before, lower salinities in the eastern part could to some extent lower the requirements for genesis on temperature.

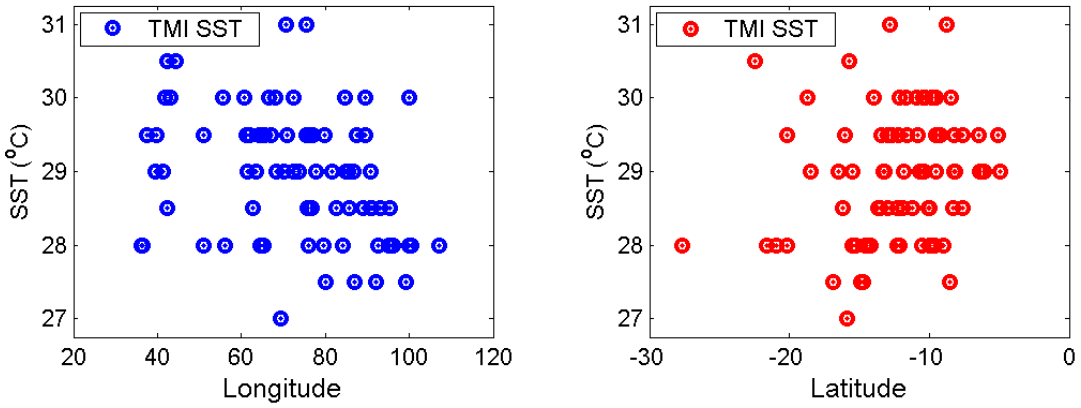

Figure 7.15: Sea surface temperature and genesis location based on cyclone track data and weekly TMI SST data from TRMM mission.

Further exploration of cyclogenesis SSTs needs more detailed information of mixed layer heat content. This is not readily obtained, although improved satellite data on sea level heights (SSHA) has recently been employed to make indirect estimates of mixed layer depth and mixed layer heat content (i.e. Chambers et al. 1997; Goñi and Trinanes, 2003). Leipper and Volgenau (1972) have suggested that prediction of TC formation and intensification should build on a parameter called Tropical Cyclone Heat Potential (TCHP), the integrated heat anomaly from the level of the 26°C isotherm to the surface,

$$TCHP = \rho C_P \int_{z(T_{26})}^{0} (T - 26)\partial z \qquad \text{Eq. (7.1)}$$

The SWIO features a shallow thermocline particularly compared to the North Pacific. According to climatology data from WOA05 mixed layers in the MC are about 30 m, and 40-50 m in the open SWIO (Figure 3.6 and related text). Given that a TCHP of 40 kJ/cm^2 might be a lower limit for sustaining a TC at normal translation speed (i.e. Leipper and Volgenau, 1972) a temperature *T* of at least 29-30°C is needed.

There is also clear evidence of that the SSTs in the SWIO and the Mozambique Channel were larger (ΔT=0.1-0.2°C), and it is likely that this increase (although small if one considers the effect on the TCHP, see Eq. (7.1) has also affected the intensity of the cyclones.

The very small change in SST in relation to the rather dramatic change in the number of intense cyclones is a matter of concern. According to Eq. 7.1 an SST change of 0.1-0.2°C, would affect the TCHP by some 5 %, and this can hardly be the single motivation for a large increase in the number of ITC. However, a possible reason is that the cyclones exert self-control on the oceanic temperatures. An intense cyclone will cause a decrease of the SSTs of ΔT =1°C over a width of 500 km, all along with the track, due to deepening of the mixed layer (see forthcoming chapter).

7.7 Mozambique Channel cyclone intensity

The number of cyclones occurring in the Mozambique Channel is small compared to the number in the SWIO as a whole, and therefore statistics from the channel alone may be misleading. However, Table 7.10 shows intensity-wise a number of TCs in the channel. With about 20% of the total number, for the SWIO only, still the Mozambique Channel features a similar increase for all TCs and a decrease in the TSs.

Table 7.10: Number of cyclones in the Mozambique Channel, separated by category for the periods 1980-93 and 1994-07, respectively. ITC=Category 3-5.

Period	TS	Cat 1-2	Cat 3	Cat 4	Cat 5	ITC	TC	All
1980-1993	15	8	0	2	0	2	10	25
1994-2007	12	12	3	4	0	7	19	31
Change (%)	-20	+33.3	-	+50	-	+71.4	+47.4	+19.4

In summary, the detailed study of changes based on intensity of the cyclones, point at a substantial increase of intense TCs, with a smaller decrease in TSs, similar to that for the whole SWIO region and in the MC. In the next section an investigation is carried out on the relationship with changing temperatures in the surface waters.

Figure 7.14 indicates that most SWIO cyclones are formed in areas where the long-term (monthly) mean SST exceeds 28°C. Very few are formed in the range 26.5<SST< 28°C. Figure 7.16 shows the number of cyclones formed during each month for the intervals 26.5<SST<28°C and 28<SST<29°C intervals, based on climatology data.

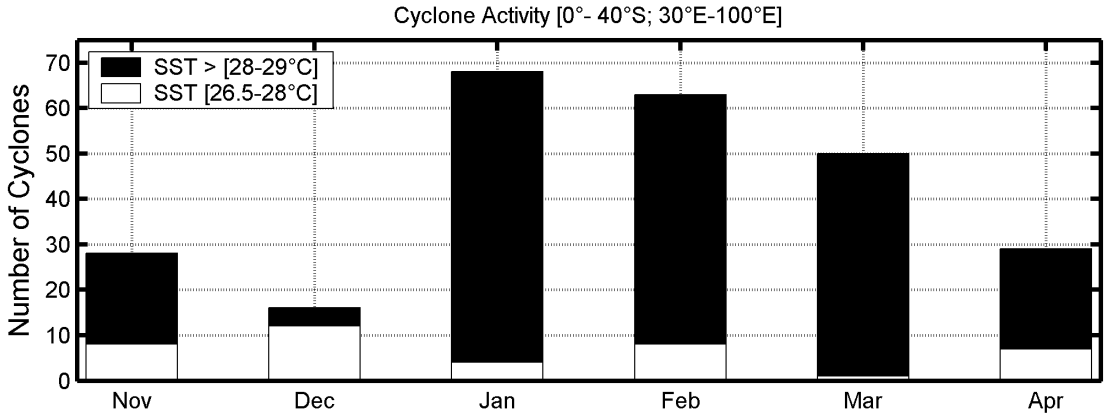

Figure 7.16: Number of cyclones formed each month for the SST binned at 26.5 - 28°C and > 28 - 29°C in the SWIO.

Only in the early and in the late season is, the relative number of TCs forming at lower temperatures is larger. This picture alone is not satisfactory because the cyclones are formed at a certain instant.

7.8 Landfall

7.8.1 Landfall and non-landfall tracks, formation areas

This section is particularly dedicated to land-falling cyclones (for definitions, see Section 5.2.3). As land-falling cyclones are more readily observed, it is expected that the early records, from 1952-1979 should hold relatively reliable data, and they are therefore employed in this section. This section starts by showing tracks of land-falling cyclones using the full record, 1952-2007, divided decade-wise (Figure 7.17a-f), mainly to see where land-falling cyclones originate, but also to identify any long term variability in tracks. As expected, most land-falling cyclones have their origin in the western part of the South-West Indian Ocean or within the Mozambique Channel. There are no striking differences between the decades except for the 1950s, for which it seems that genesis and tracks from the centre of the ocean (from 70-90°E) are more or less missing. The additional fact that no cyclones that are generated east of 65°E reach the coast of Madagascar are probably just indications of shortcomings in these early records. However, there are also more land-falling cyclones in the earlier records (1950s-1970s), most of which with an origin in the Mozambique Channel (as noted before, in Section 7.2.1).

Another particular characteristic which can be seen in these trajectories is that TCs in the past mainly passed through the middle and northern region of Madagascar before recurving south or eventually reaching Mozambique in the African mainland. But in recent years there are some indications that tracks of TCs have changed. Some tropical cyclones have swept further south and made landfall after travelling with unusual trajectories and penetration (e.g., TC Eline (2000); see Reason and Keibel, 2004, and TC Favio (2007); see Klinman and Reason, 2008).

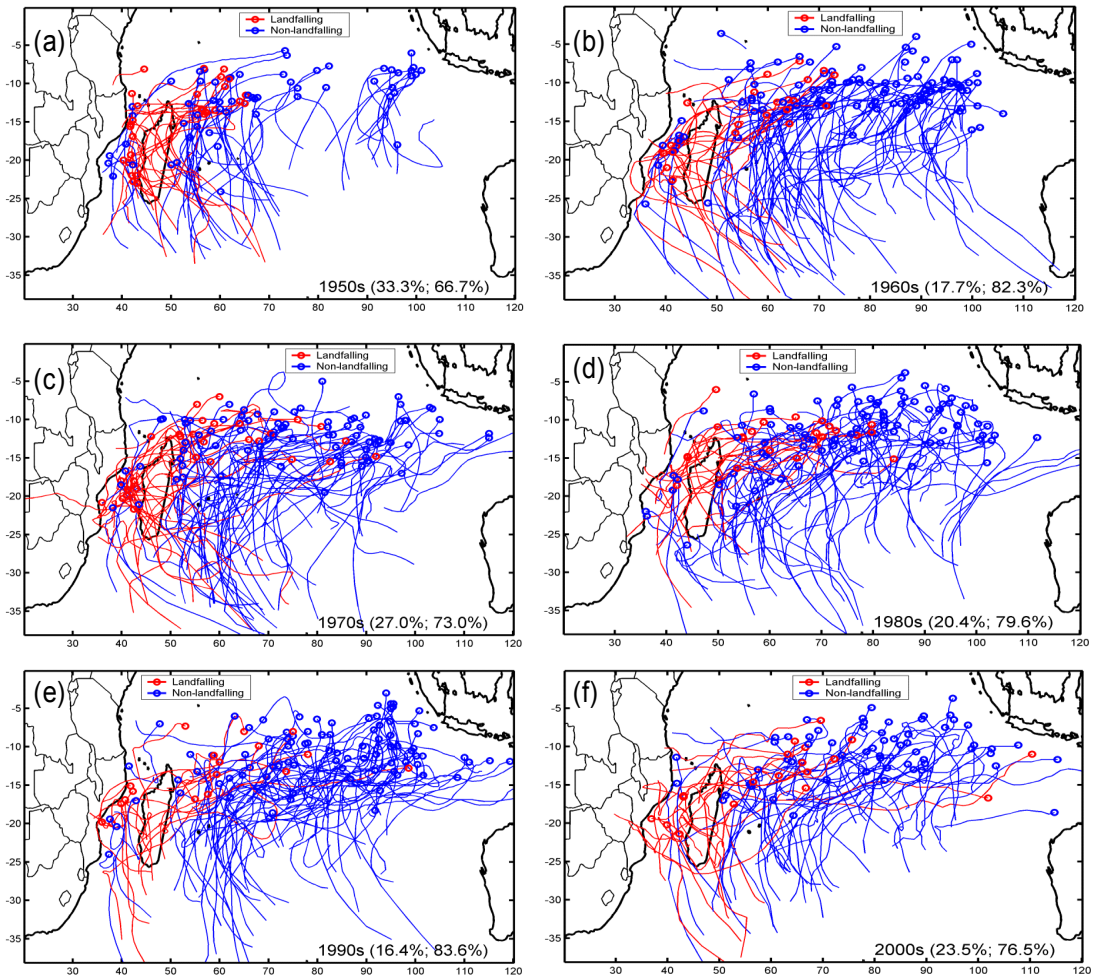

Figure 7.17: Decadal variation of the full tracks of SWIO-landfalling (red) and non-landfalling (blue) TCs. The numbers in parenthesis denote the percentages of TCs that passed over Madagascar and Mozambique to the total number of TCs during each decade.

7.8.2 Landfall 1980-2007, tracks and distribution in time and space

Neumann et al. (1987) and Reading (1989) have defined seven genesis regions worldwide (the North-West Pacific, the East Pacific, the North Atlantic, the North Indian Ocean, the South-West Indian, the South-East Indian and the South-West Pacific Oceans). The regions were further subdivided (e.g. Vega and Binkley, 1993) with reference to large-scale atmospheric and oceanic oscillatory phenomena, taking place in one or the other part of the region (e.g. Ho et al., 2006). Here, for reasons indicated above, the records from the South-West Indian Ocean (50-100°E), and from the

Mozambique Channel, defined as West of 50°E, are compared (Figure 7.18a-b) to identify formation and landfall during the recent period, 1980-2007.

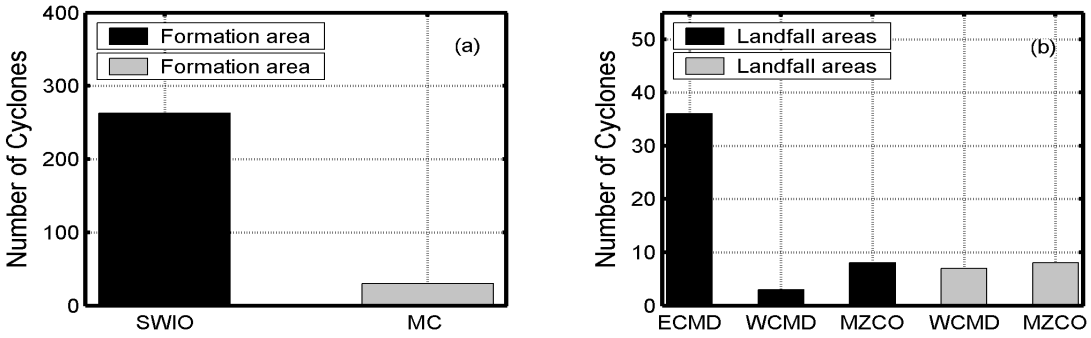

Figure 7.18: (a) Total number of cyclones formed in the SWIO (West of 100°E) and in the Mozambique Channel (West of 50°E), (b) number of cyclones making landfall (ECMD=East Coast of Madagascar; WCMD=West Coast of Madagascar; MZCO=Mozambique Coast) in relation to their origin.

In total 263 (Figure 7.18a) cyclones had their formation area in the SWIO (50-100°E). Of these cyclones, 47 (18%) made landfall, 36 (14%) of which on the east coast of Madagascar, 3 (1%) on the west coast of Madagascar and 8 (3%), finally, on the Mozambique coast (Figure 7.18b). Formation east of Madagascar is less variable, and also well distributed throughout the cyclone season (Figure 7.14a-f). This is also supported by Ho et al. (2006) in their examination of variations in TC activity in the South Indian Ocean during 1979-2004. The authors also found that during El Niño periods TC genesis was shifted westward, enhancing the formation west of 75°E and reducing it east of 75°E. These findings could conceivably lead to identification of new regions of tropical cyclone formation as suggested by Vega and Binkley (1993).

Formation in the Mozambique Channel alone (Figure 7.18b) produced 30 (60%) cyclones in total, of which 7 made landfall on the Mozambique coast and 8 on the west coast of Madagascar. Although few, compared to the total number east of Madagascar, as pointed out, the genesis density is similar to that of the SWIO, or even higher if the period January-March is considered. Jury and Pathack (1991) have felt that the topography of Madagascar (rising 1-3000 m in a North-South axis along 48°E spanning 13-25°S) has an impact on the lower flow fields, deflecting the trades and monsoon

flows pole-ward in the longitude 40-45°E, retarding cyclone formation and appearing to promote an eastward movement of cyclones formed within the Mozambique Channel.

Several studies have documented the existence of year-to-year variations in occurrence, intensity, and tracks in the different cyclone regions (e.g. Shapiro, 1982). Figure 7.19 shows the significant differences in frequency, with which these TCs have affected the Mozambique and Madagascar coasts. The maximum number of landfalls during 1980-2007 was six in 1988. On the other hand, there were no landfalls at all in 1983, 1987, 1999 and 2001. During a few seasons, landfall occurs for half of the total number of TCs (1988 and 2007).

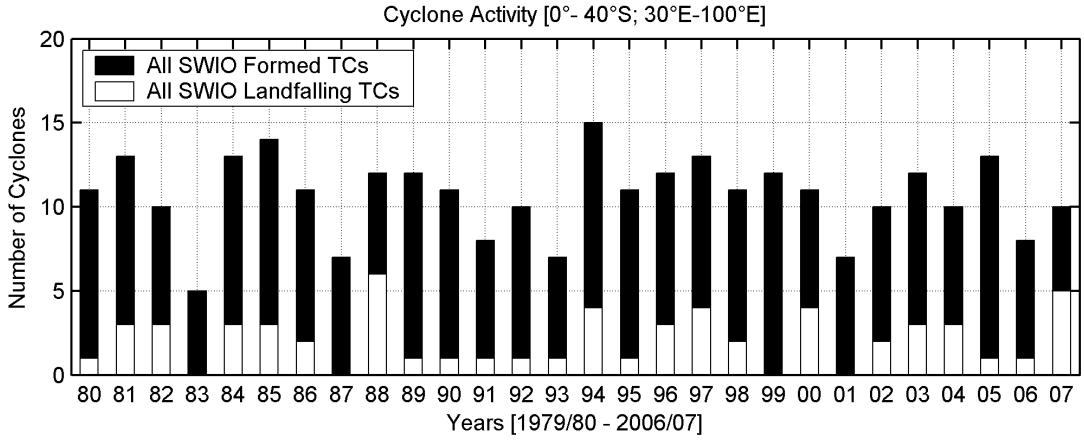

Figure 7.19: Number of all SWIO tropical cyclones formed in the South-West Indian Ocean and the landfall frequency for all TC categories.

7.8.3 Landfall from 1952-2007, tracks and distribution in time and space

According to the merged JTWC/LR-RSMC data (1952-2007), in total 142 cyclones (Figure 7.20) made landfall in Mozambique and Madagascar. This corresponds to 2.5 land-falling cyclones per year (Figure 7.21a; lower dash-dot line). While these were has an impact over land, 489 (or 77%) kept over the ocean where they usually moved at average speeds of 5 ms^{-1} (mean life time of slightly less than 2 weeks). There were 7 cyclones land-falling in 1956, the maximum yearly number in history during the earlier period (1952-1979) and 6 landfalls in 1988, maximum during the recent period

(1980-2007). On the other hand there were no landfall cyclones in 1961, 1983, 1987, 1999 and 2001.

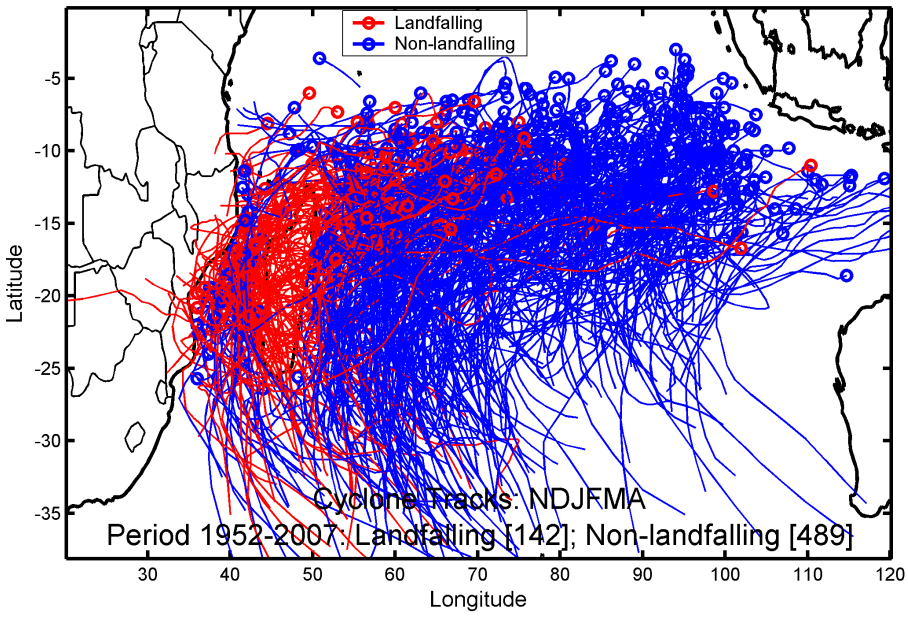

Figure 7.20: TC and TS tracks, November-April 1952-2007. The initial positions of cyclones are marked with a "circle". The number of landfalling and non-land-falling cyclones is highlighted. Only a few cyclones generated east of 80°E made landfall.

Figure 7.17 and 7.20 show the differences between red and blue trajectories or simply landfall and non-landfall TC trajectories were the proportion of no-landfall is relatively high with a tendency to recurve southeast Madagascar. In general TCs spend most of the time over the ocean (source of heat) where they usually move at average speed of 5 ms^{-1}. These differences are likely to do with ENSO-related large-scale circulation response and changes in local SST anomalies including the position of the South Indian subtropical high. This is supported by findings by Ho et al. 2006 for tropical cyclone passages across the SWIO. The reduced (enhanced) TC passage to the southeast of Madagsacar (central midlatitude SIO) are due to earlier recurving of TCs to the east.

The anomalous south-westerlies to the southeast of Madagascar during El Nino periods may inhibit the TCs from propagating further west. In adition TC passage in the central

Indian Ocean seems to be affected by the MJO, which coincides with anomaly patters of steering winds

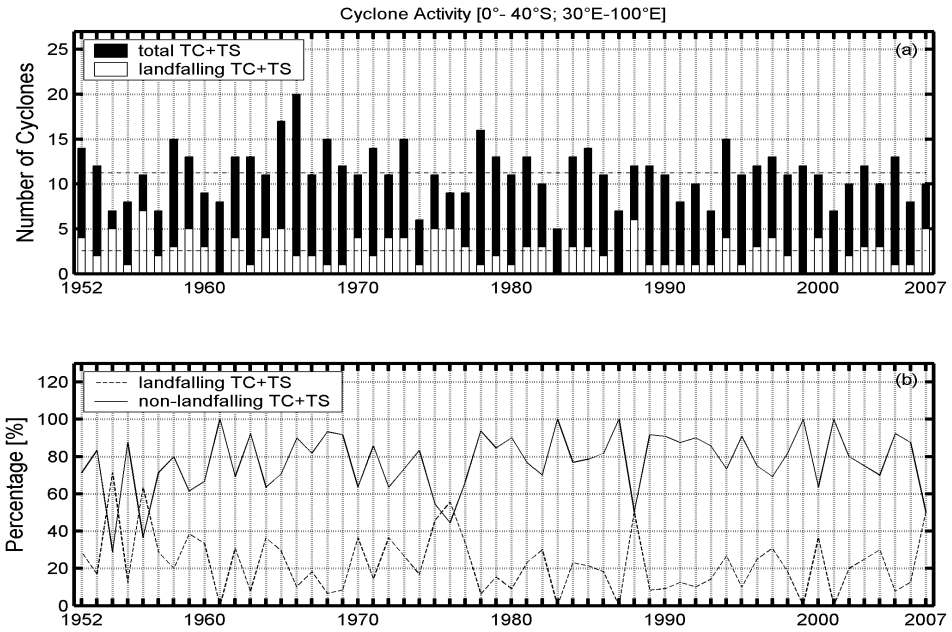

Figure 7.21: (a) Annual variations of cyclones formed over SWIO (including the Mozambique Channel) and land-falling cyclones in the Mozambique and Madagascar mainland's. (b) The percentage of land-falling cyclones (dashed line) and non land-falling cyclones (solid line).

7.8.4 Wavelet analysis of the annual frequency of cyclones

Following the general study of the annual frequency as indicated above, the results in this section show the periodicity of SWIO cyclones as seen from wavelet analysis**.** Figure 7.22a-b gives the amplitude and power spectrum corresponding to different periods obtained using a continuous wavelet transform (CWT) to determine the periodicity of TC occurrence in the basin. Changes in periodicity can be seen around 1956, 1972, 1988 and 2000. Before 1980 the change in periodicity can be seen from a periodicity of 2 to 7 years and after 1980 from 2 to 4 years. Thus, it is apparent from these results that TC landfall activity in the SWIO has a decreasing trend and possesses statistically significant inter-annual variability.

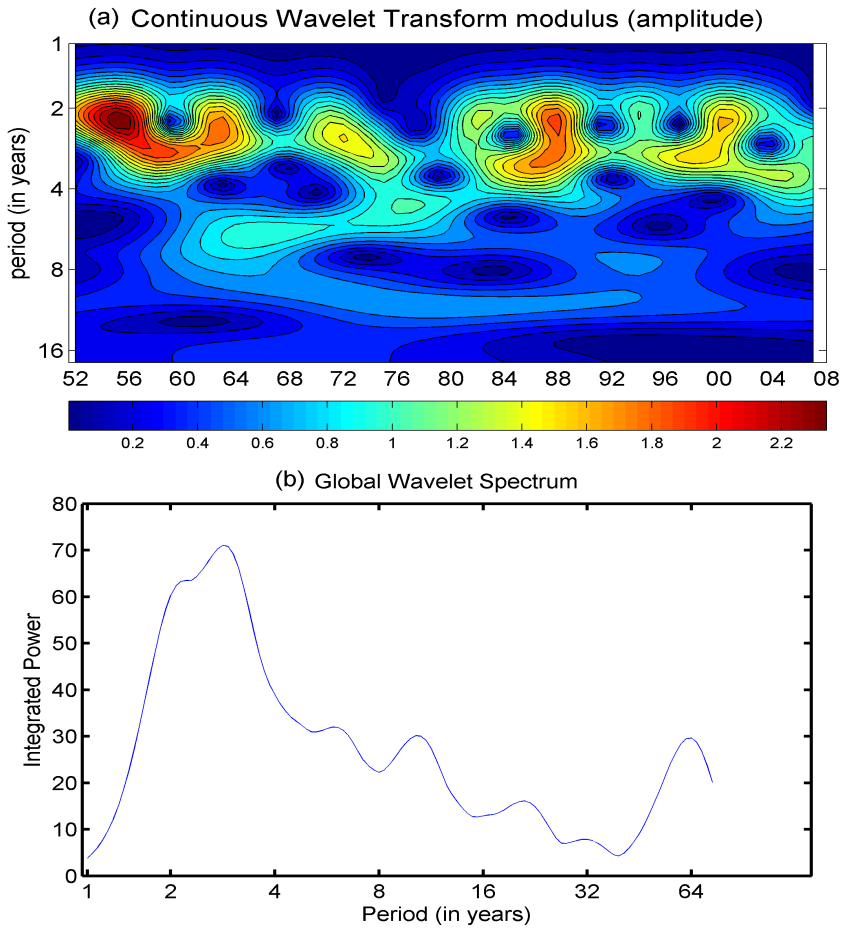

Figure 7.22: Wavelet analysis for landfalling tropical cyclones in Mozambique and Madagascar during the period 1952-2007. (a) The wavelet power spectrum of landfall frequency showing an increase of power at 2-4 year periods since 1950s denoted by the spread of the red and yellow shading. The colour bar represents normalized variances. (b) the global spectrum showing the maximum integrated power around 2-4 years.

The shorter periodicities coincide with the 3 to 7 year period of ENSO (e.g. Chu and Wang, 1997; Ho et al., 2006) suggesting that ENSO may be a factor affecting TCs in the SWIO and landfall is more common during La Niña years (Vitart et al., 2003). However there are only 56 years of data; longer period can therefore not be identified. Nonetheless, the periodicities that are over the 16 years (Figure 7.22b) cannot be explained nor easily related to the other possible large-scale oscillations since there is no power under the edge limit (cone of influence; Figure 7.22a). Integration through the whole period gives an average periodicity of 2.3 years (Figure 7.22b) which indicates where the power spectra are the largest.

7.8.5 Tropical cyclone landfall; locations statistics

In order to assign cyclone landfall locations, the coast of Mozambique has for convenience been divided into three segments, while the coastal areas of Madagascar have bee divided into six segments and comparisons are made among them in terms of TC landfall and thus vulnerability. Preferred landfall strips along the Mozambique and Madagascar which are vulnerable to tropical cyclones are represented by A, B, C, D, E, F, G, H and I (Figure 7.23) for the recent period 1980-2007.

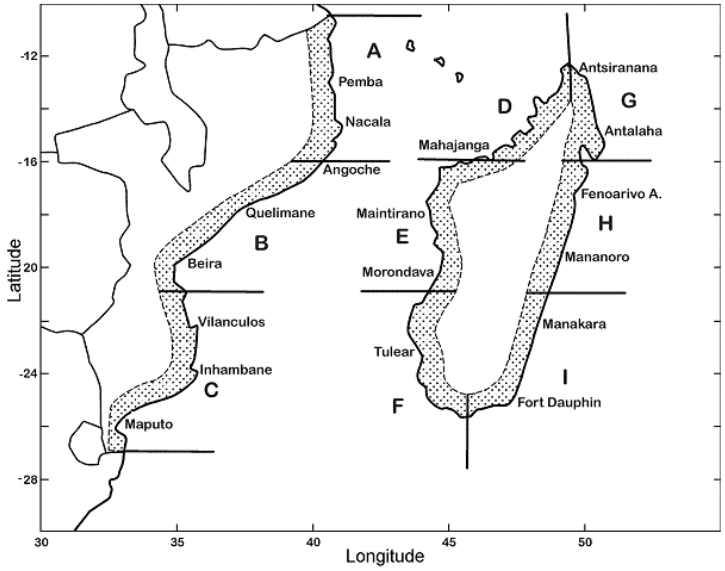

Figure 7.23: Sketch of the 9 regions along the eastern and western coasts of Madagascar and Mozambique coast.

Results in this section are given in relation to cyclones that made landfall over Mozambique and Madagascar with maximum sustained winds (MSW) >17 ms^{-1}. Most cyclones tend to pass over the north-eastern coast of Madagascar, area G (Figure 7.24).

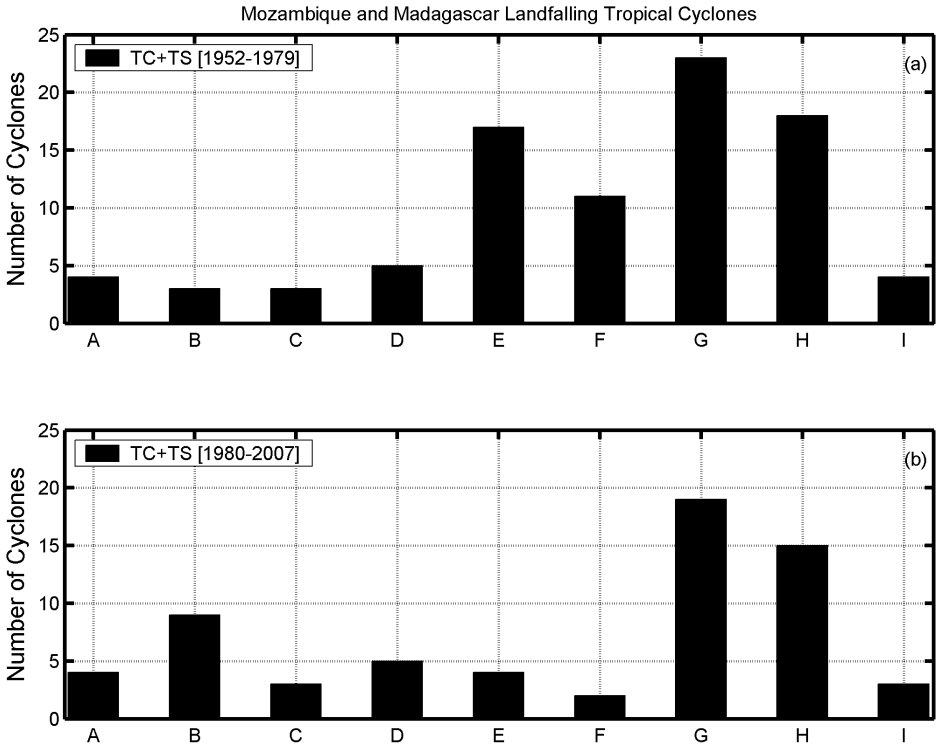

*Figure 7.24: Distribution of tropical cyclone and tropical storms (*TC+TS*) landfalling in each of the 9 regions, (a) from the historical observations; and (b) from the historical observations and recorded merged data available at JTWC/LR-RSMC.*

Figure 7.24 shows in detail the landfall distribution of tropical storms and tropical cyclones in each of the periods 1952-1979 and 1980-2007. Considering the 1980-2007 period the number of landfalling cyclones in Mozambique was 15, 9 made landfall in the central districts of the country (region B) while 4 and 3 made landfall respectively in the southern (region C) and northern region (region A) respectively. Eleven cyclones made landfall on the west coast of Madagascar in region D (5 cyclones) region E (4 cyclones) and region F (2 cyclones). Another 37 cyclones made landfall in the east coast in region G (19 cyclones) region H (15 cyclones) and region I (3 cyclones). Not all cyclones are able to make landfall. As seen, there are some obvious differences in the statistics when comparing the earlier and the more recent period. Areas E and F, on the west coast of Madagascar, were hit by many more cyclones during the first period, and are by few cyclones during the second period. The most likely reason for this difference could be the uncertainities and missing track data found in the earlier records. The later records

are suitable to both TC landfall and intensity studies while the less reliable earlier records may be employed for TC landfall studies with some extent.

7.9 Tropical cyclone days

It was shown in a previous section (Figure 7.20) that tropical cyclones tracks are characterized by high variability covering a great part of the SWIO between the latitudes 5 and 35°S. Figure 7.25a-b show tracks of TC and TS, including the number of cyclone days (and intensity), indicating the most intense activity between 10 and 25°S. This area has been referred to as the main development region (MDR) of TC in the SWIO (Vitart et al. 2003). As previously defined by Webster et al. (2005), tropical storm days are defined as the total number of days (converted into days from 6-hourly observations) of systems that only reached tropical storm intensity while tropical cyclone days refer to systems that attained hurricane status, including the period when a system was at tropical storm intensity. That integration of the life time of each TC along its path gives not only the spatial density but also represents the degree of a TC disaster. The greater the number of TC development days the higher the potential to cause severe damage at landfall. With few exceptions there is a clear decline in the intensity of cyclones when approaching or crossing land (Figure 7.25). Weakening over land in particular, has been generally ascribed to surface friction, a hypothesis that has not been found valid along large mountain ranges (Simpson and Riehl, 1981). These authors argue that the friction of the wildly agitated ocean with large masses of spray in the air is equal to or exceeds that over land. Figure 7.25 shows that the number of TC days increases east of Madagascar. This is roughly in agreement with previously reported work by Xie at al. (2002), the result of which is shown in Figure 3.5. The maximum number of TC days occurs at location north-east of Madagascar (8.8-12.8°S, 50.8-70.8°E) and is just about 3 per year. Figure 7.25 gives a partly different view though, indicating the location of maximum TC activity (including intensity as well), which seems more wide spread, with a similar intensity far eastward in the ocean, due to fewer but more intense cyclones towards east.

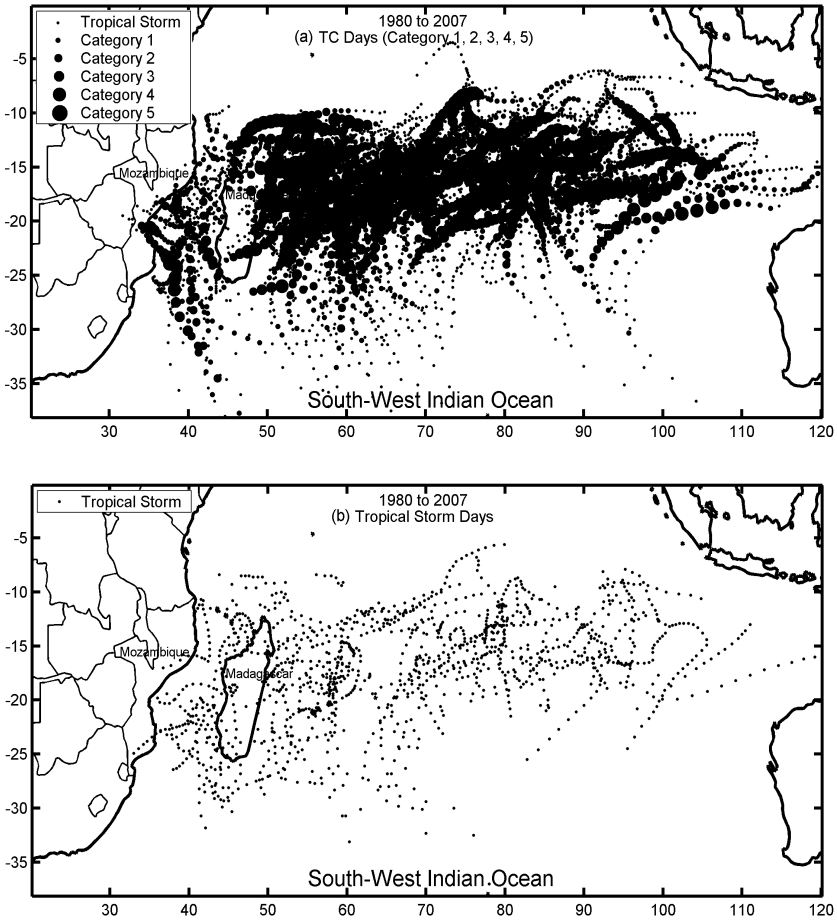

Figure 7.25: Spatial density of (a) tropical cyclone days and (b) storm days. In (a) the intensity is indicated by such that the size of the markers is proportional to (MSW)^3, thereby representing the buoyancy flux.

7.9.1 Variability in tropical cyclone intensity

Figure 7.26 shows the variability in the annual number of TC and storm days in the SWIO. The dataset indicates no apparent trends in total number of cyclone (TC and TS) days and not for weak cyclones (Category 1-2; MSW: 33-49 ms^{-1}). However Category 3-5 (MSW $\geq$ 50 ms^{-1}) TC days seems to indicate a slightly an upward trend mainly contributed by TCs of Category 4 (59 < MSW < 69 ms^{-1}) as discussed in section 7.4.3 (Table 7.7). The least-squares linear regression test is performed here to evaluate trends in tropical cyclones at various categories (Appendix E1.1-1.4). Trends are is significantly different from zero at 95% confidence level for Category 3-5 (increase; Appendix E1.2) and for TS (decrease; Appendix E1.4), except for total activity (Appendix

E1.1) and Category 1-2 (Appendix E1.3) where the significance cannot be revealed. Man-Kendall test is applied and verified the results (see example in Appendix E2.1). More details about these methods in the references described in Section 5.2.3. Such a trend has occurred in the early 1980s and the mid-2000s, consistent with earlier work from Webster et al. (2005) while comparing regional time series for 1970-2004 period and also the recent work by Kuleshov et al. (2008). These authors found an increased number of intense TCs (including the ratio of severe TC days to all TC days) with minimum central pressure of less than 945 hPa (equivalent to MSW $\geq$ 50 ms^{-1}) in the South Indian Ocean.

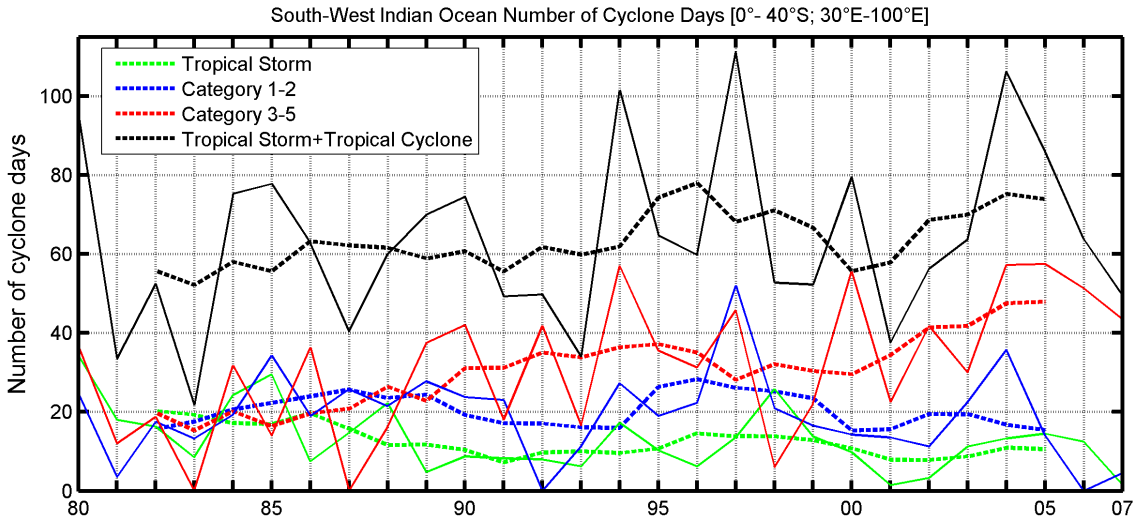

Figure 7.26: Yearly number of TC days (Category 1-2 and Category 3-5) and TS days in the SWIO. Hatched lines show running means

7.10 Typical tracks

Cyclones may show preferred paths depending on varying meteorological and oceanographic conditions during different parts of the seasons. The South Indian subtropical high experiences seasonal migration showing with its southernmost position in August and February-March (Tyson and Preston Whyte, 2000) While its northernmost position is shown in May-July and September-November, longitudinally it exhibits an extreme annual cycle moving 24° eastward from June to December (Tyson and Preston Whyte, 2000). During particular years, cyclones have a tendency to remain over the

water, recurving southward, whereas during other years the tendency may be for cyclones to track westward.

In the case of TC trajectories the grouping was done according to the six-hourly positions over the lifetime of the tropical cyclones from the initial cyclone intensity to the final cyclone intensity. The historical data show that trajectories in the South-West Indian Ocean may be separated into 6 groups;

A: Recurving southward tracks off the Madagascar east coast
B: Recurving-southward land-falling tracks
C: Southward tracks travelling off land and across the Mozambique Channel
D: Westward land-falling and non land-falling tracks
E: South-Eastward land-falling and non land-falling tracks
F: Recurving-random trajectories

Occurrences of the various tracks are shown in Table 7.11. Selection of tracks are done by considering the integrating the six-hourly positions over the lifetime of the tropical cyclones from the initial hurricane intensity to the final hurricane intensity. Although some tracks may also fall into another group, these six groups chosen seem to indicate distinct features.

Table 7.11: Tropical cyclone statistics. Values are based on 6-hourly observations of the total number of cyclone over the SWIO from 1980-2007.

Group type	Number of trajectories	Average	%
A	149	5.3	50.9
B	31	1.1	10.6
C	11	0.4	3.8
D	42	1.5	14.3
E	19	0.7	6.5
F	41	1.5	14.0

Group A: Recurving southward tracks off the Madagascar east coast

About 50 % of all cyclones included in the data set for the period 1980-2007 have this type of trajectory. The number of cyclone days for these cyclones (Figure 7.27) varied

from 4 to 25 days. Initially, these systems move westward mainly above SST>27°C. Specific environmental conditions might have altered their tracks and for instance recurving southward without approaching the coast of Madagascar closely. Of these, coastal brushing and approaching cyclones may have an impact on the coast from induced cyclonic winds along the coast. The trajectories are common during the months of January to February (Figure 7.27b). Tropical storms are most common in this group, followed by Category 3.

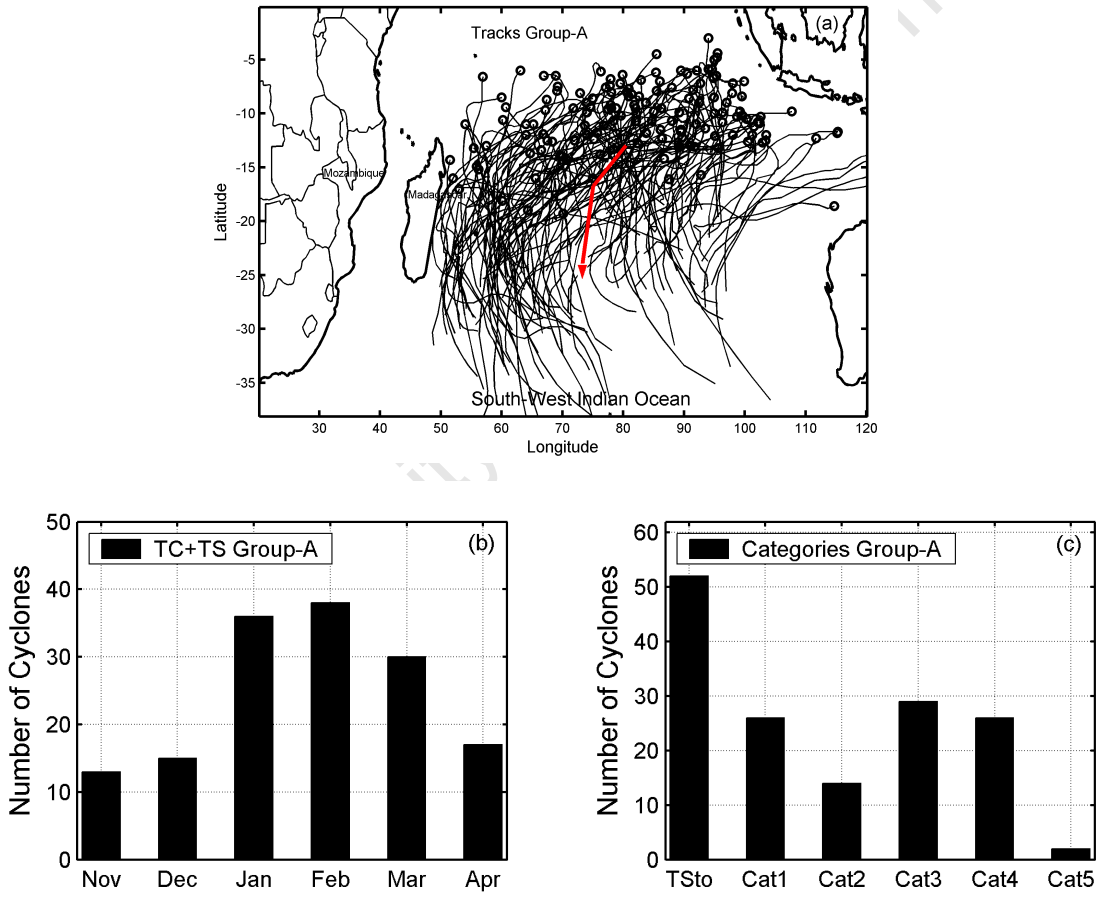

Figure 7.27: (a) Group A of six types of trajectories obtained from the analysis of the 28-years (1980-2007) tropical cyclone data in the South-West Indian Ocean. Red line denotes the average track of this group. (b) the monthly frequency of tropical cyclones and tropical storms and (c) the monthly frequency of TC categories according to the Saffir-Simpson scale.

Group B: Recurving-southward land-falling tracks

The cyclones of Group B have their origin mainly to the north-east of Madagascar moving first, in westerly direction and then curving southward but entering or crossing Madagascar (Figure 7.28). About 10% of the cyclones followed this path. These cyclones have a lifetime of 1 to 19 days with an average of 7. These cyclones crossed land in some cases with multiple landfalls causing great damage to the human population and the infrastructure because of the strong winds and heavy precipitation. Abnormal sea levels are also common. Naeraa and Jury (1997) have reported three TCs in 1994 season (Daisy, Geralda and Litane), which hit the east coast of Madagascar at almost the same point. Rainfall reached 500 mm and 300000 ha were inundated. Storm surges in excess of 6 m were recorded and waves up to 19 m flooded the coastline. These trajectories are most frequent in January and March (Figure 7.28b) and are mostly tropical storms but several TCs of Category 4 (Figure 7.28c).

In average summer (December-March) the South-West Indian Ocean east of Madagascar (10-25°S, 50-70°E) experiences eight tropical cyclone days (Payda 1989; Ecormier 1992). In 1984 22 TC days were observed; in 1994 27 TC days were recorded while the historical record stand at 31 (1971). Often during El Nino years, strengthened subtropical upper-westerly winds limit the potential for development of TC days (0 days in 1967, 1983, 1987; Jury et al., 1999).

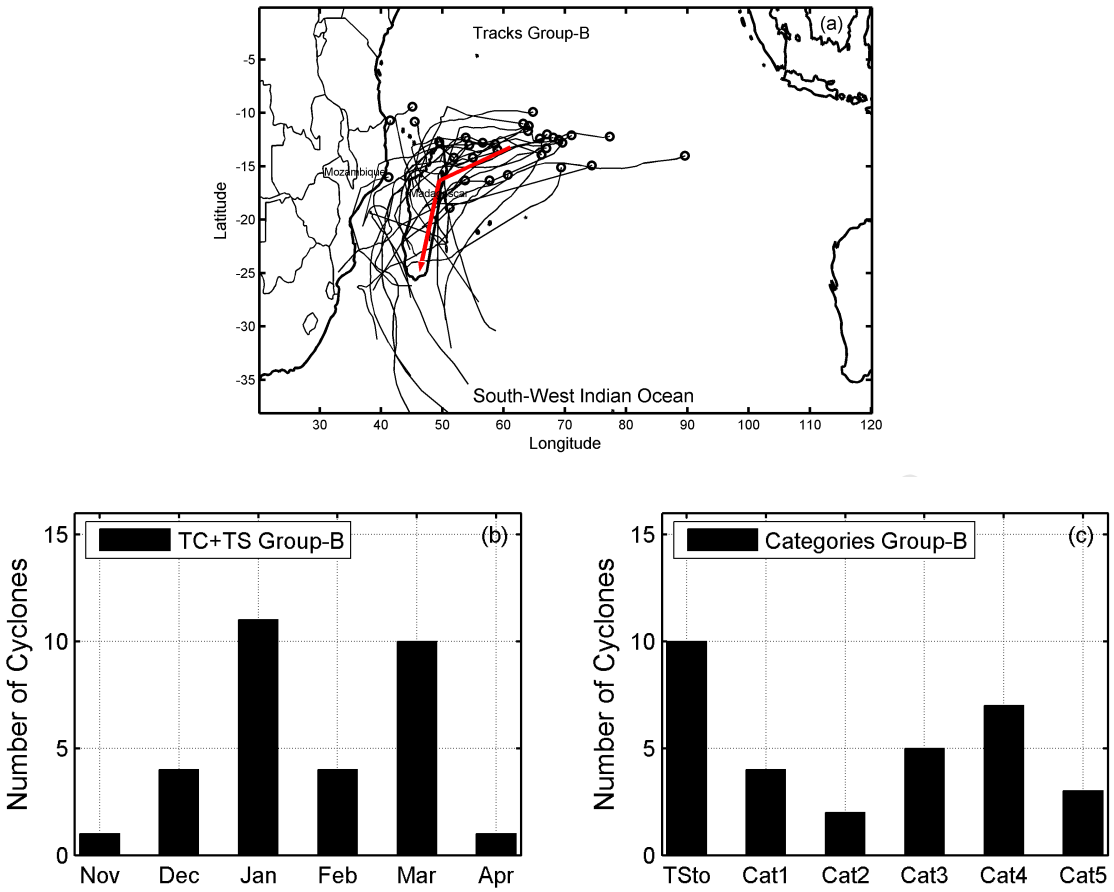

Figure 7.28*: Same as Figure 7.27, but for group B*

Group C: Southward tracks travelling off land and across the Mozambique Channel

Group C comprised the fewest tracks, only about 4 % of the cyclones of the SWIO. These tracks are all towards the south, within the Mozambique Channel (Figure 7.29a). The lifetime of these are even shorter, 2 to 10 TC days only. January and February feature the highest genesis frequency (Figure 7. 29b) and tropical storms and category 2 TCs were prevalent (Figure 7. 29c).

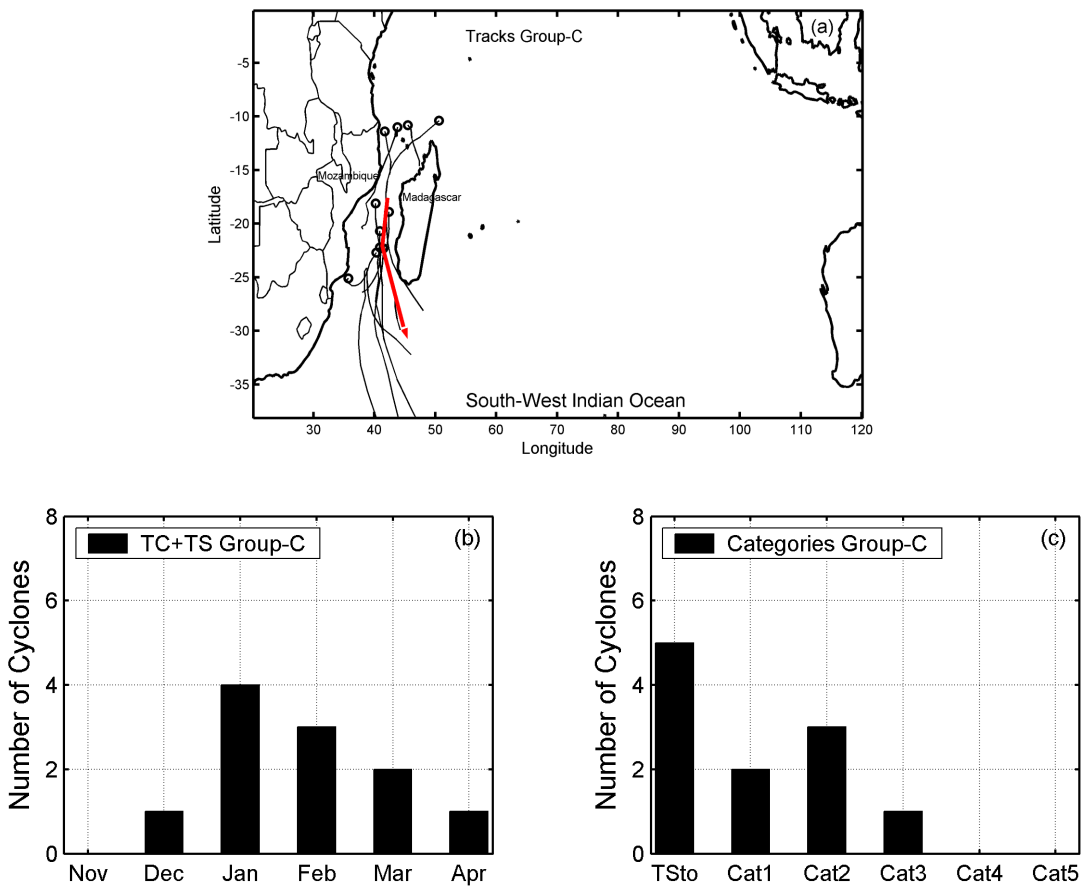

Figure 7.29: Same as Figure 7.27, but for group C

Group D: Westward land-falling and non-landfalling tracks

Group D is characterized by zonal and westward tracks. Fourteen percent of all cyclones have this type of trajectory. The majority of these trajectories were long, and the cyclones had TC days varying 1 to 19 and an average of about 7. This group of trajectories usually crosses land, causing severe damage to coastal infrastructures and inland flooding. Eline in 2000 was one of these longest lived cyclones in history with westward zonal trajectory. As noted by Vitart et al. (2003) landfall associated with this group of trajectories is more common during La Niña years, simultaneous with a negative zonal mean flow (averaged for 850-200 hPa). These trajectories were mostly frequent from November to February (Figure 7.30b). A majority are tropical storms, although TCs of category 1 and 4 are less uncommon (Figure 7.30c).

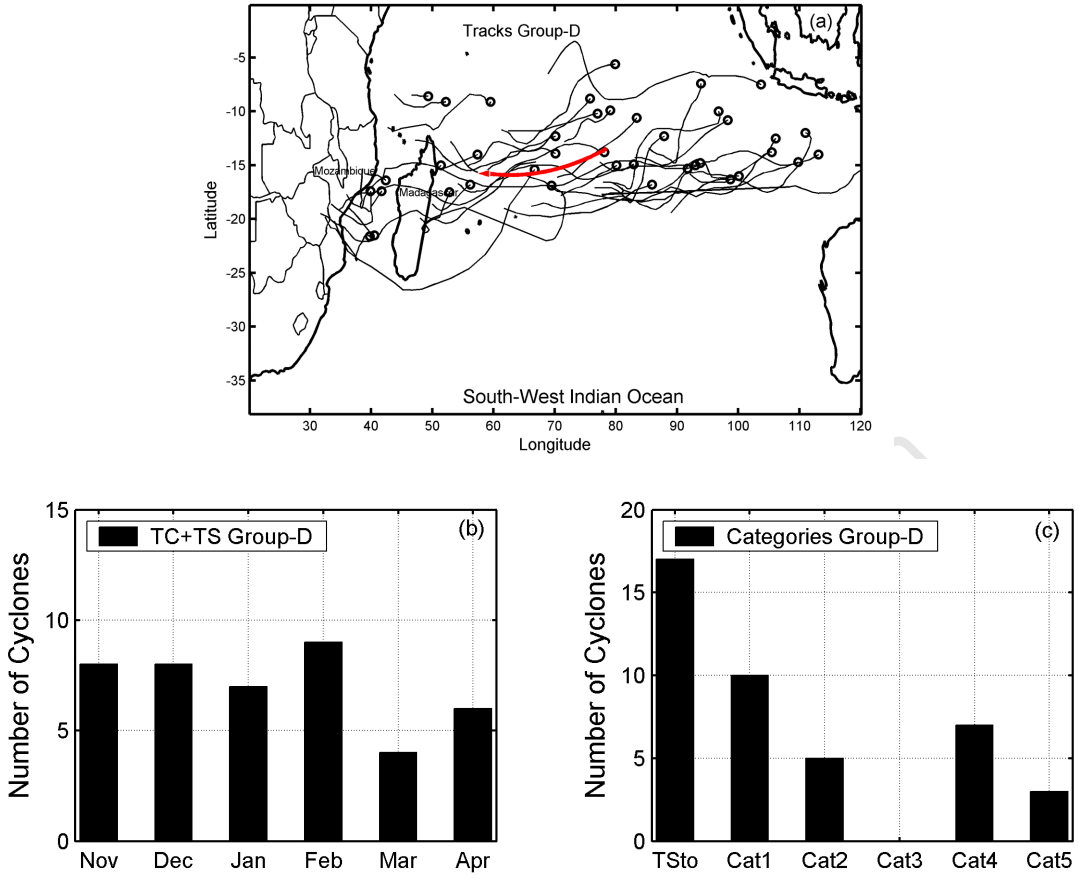

Figure 7.30: Same as Figure 7.27, but for group D

Group E: South-Eastward land-falling and non land-falling tracks

Group E holds the second least number of cyclones, only about 6.5% of all cyclones in the SWIO. Thee tracks are towards southeast (Figure 7.31a), a feature which is rather uncommon; however those off the Mozambique coast and the Madagascar west coast do have such preferred movement. Those off Mozambique tend then to impact Madagascar and are characterized by rapid development, short life-span, and small radius, usually recurving south-eastward as noted previously by Le Borne (1987). Overall TC days varied from 1 to 8 and average of about 4 days but cyclones with less than 48 hours lifetime occur in the MC. The trajectories are most frequent in January and February (Figure 7.31b) and are mostly dominated by tropical storms (Figure 7.31c).

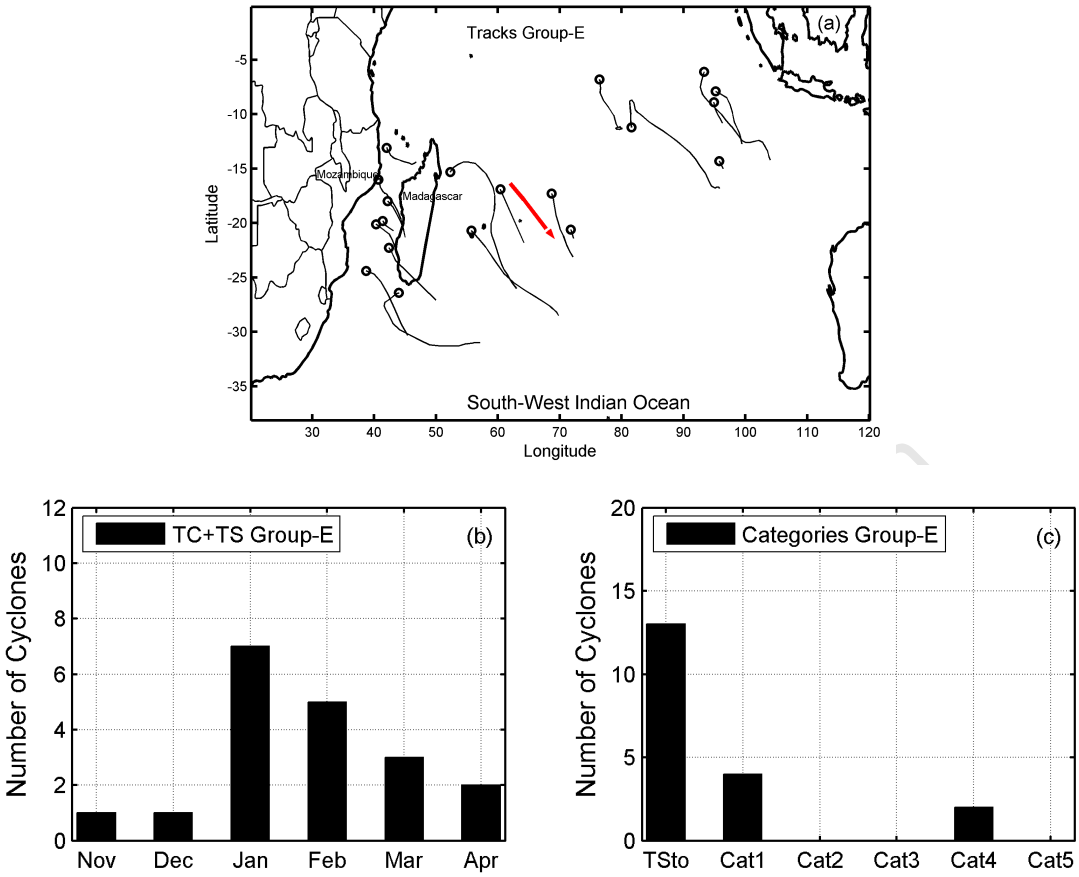

Figure 7.31: Same as Figure 7.27, but for group E

Group F: Recurving-random trajectories

The remaining 14%, Group F have random trajectories (Figure 7.32). Meanderings, zigzags or other uncommon movements appear in this group. Observations and numerical modelling (e.g. Holland and Lander, 1992) suggest that many meanders occur from interactions with mesoscale vortices and convective systems within the cyclone circulation. The majority spends most of the time over the ocean. The number of TC days of this kind varied from 1 to 24 and an average duration was about 6 days. These trajectories are common in February (Figure 7.32b) and are mostly tropical storms and Category 1 (Figure 7.32c).

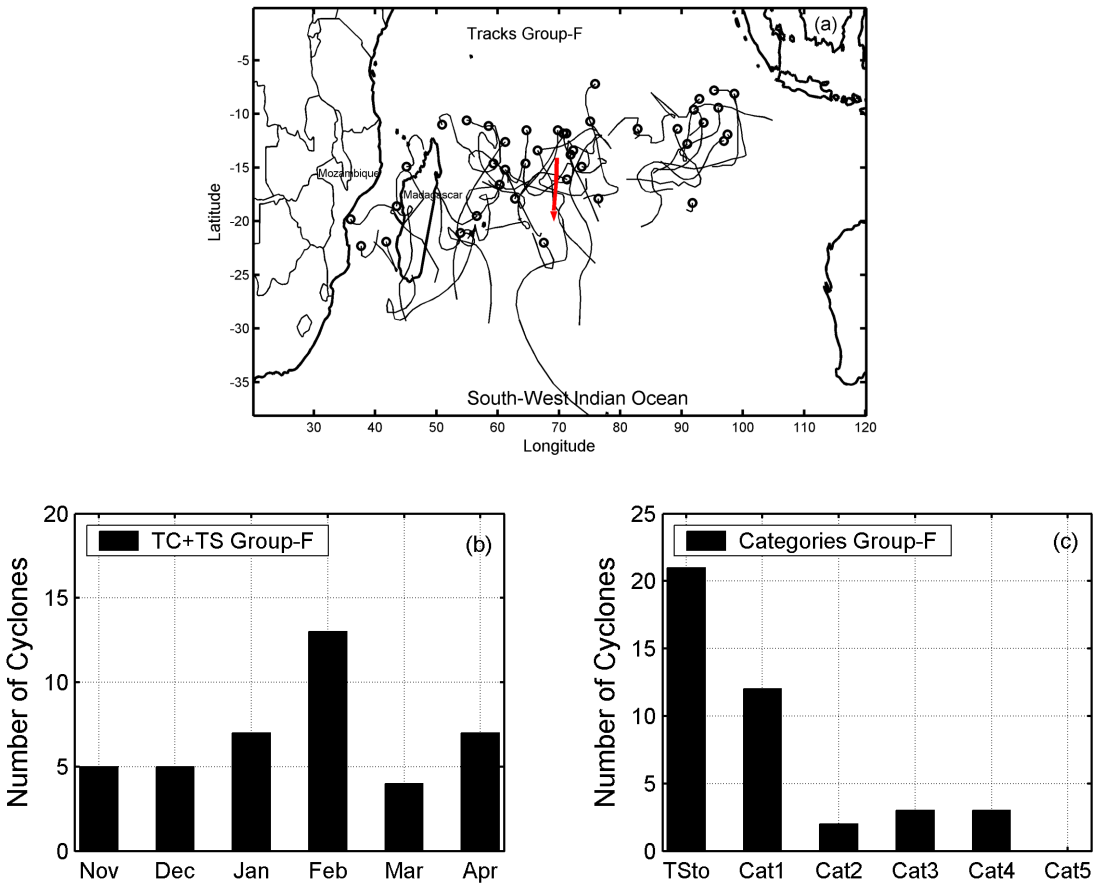

Figure 7.32: Same as Figure 7.27, but for group F

Factors influencing the trajectories

Among several factors which influence the TC tracks, the upper wind circulations around the high-pressure has been suggested as being the most significant (Ho et al., 2006). As discussed by several authors (e.g. Gray, 1968; Zehr, 1992; DeMaria et al., 2001), observations indicate that tropical cyclones form under conditions of a weak shear in the horizontal wind between the lower and upper troposphere. As indicated before (Section 5.X) the wind shear is computed as the difference between the 200 and 850 hPa winds using NCEP/Reanalysis-2 data (Kalnay et al., 1996). Figure 7.33 shows bi-weekly and seasonal monthly wind shear over the South-West Indian Ocean for the period 1979-2005. Low shear values (<10-12 hPa) are associated with higher frequency of TC formation and in combination with the seasonal migration South Indian subtropical high affect the cyclone trajectories.

At the begining and at the end of the cyclone season (November-December and March-April; Figure 7.33a and 7.33c) the subtropical high is well-developed over the SWIO causing the cyclones to stay over higher SSTs and ridge influence, which for instance provides low wind shear further north. On the whole TCs tend to move west and south-west around the north-western flank of the subtropical high favouring mainly group B (Figure 7.28).

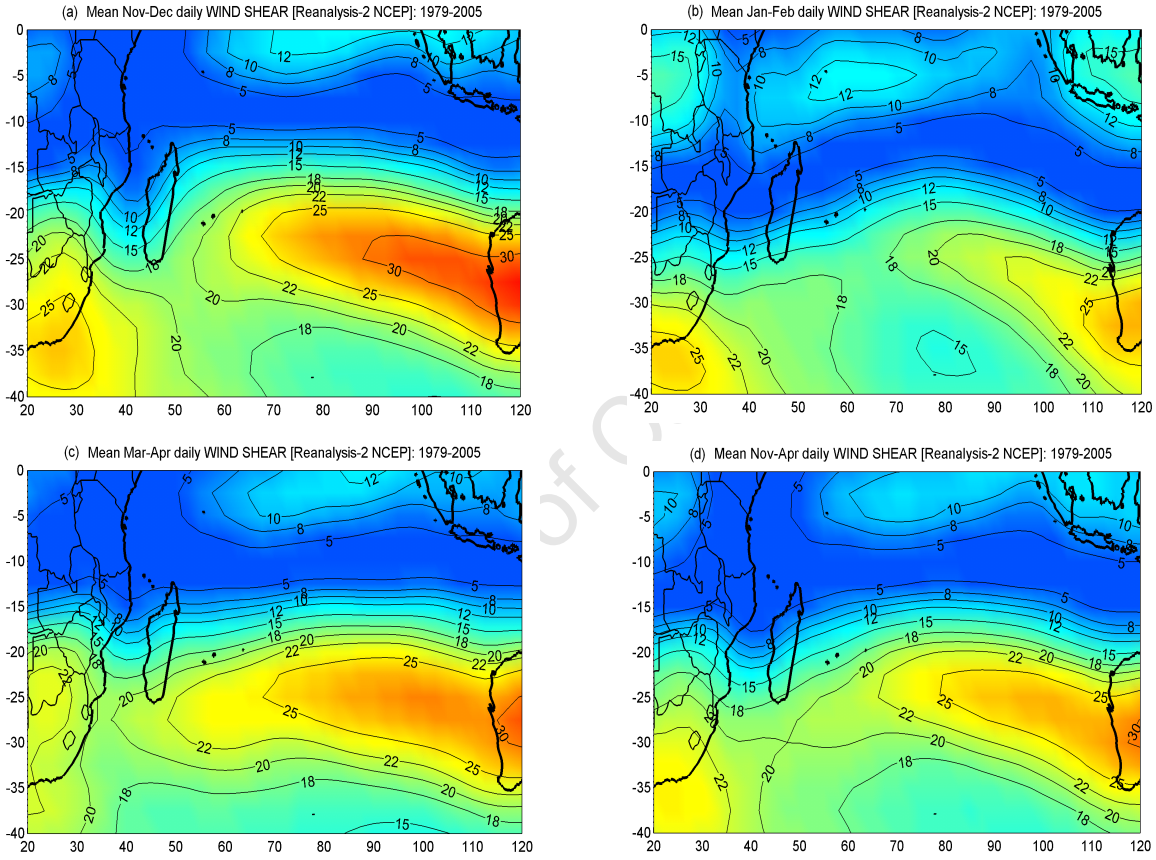

Figure 7.33: Climatological wind shear of the South-West Indian Ocean from 1979-2005 data. The figure shows prevailing conditions during (a) November-December, (b) January-February (c) March-April and, (d) the cyclone season (November-April).

During January-February the subtropical high diminished and the background wind shear dominates above most of the Madagascar and Mozambique. During these months the TCs of group A and D were frequently observed (Figure 7.27-7.30).

7.11 Summary of Chapter

The results from this chapter, which deals with occurrence and intensity of cyclones in the SWIO, has shown (Sections 7.2-6) that overall cyclone intensity has increased considerably over the last 14 years (1994-07) compared to the earlier period (1980-93). Tables 7.8-9 indicate an increase from 36 from 56 Intense Tropical Cyclones, while there was a downward trend in Tropical Storms, from 62 to 56, and an overall increase in cyclones (TS+TC) from 138 to 155. A similar pattern has been documented in other cyclone regions of the world (e.g. Emanuel, 2005a, b; Webster et al., 2005), where the increase is also dominated by ITCs.

While there was a small increase also in the number of cyclones in the recent period, in the longer perspective (from 1952-07), there is a decrease in total number after 1980. This decrease is more accentuated in the Mozambique Channel than in the open SWIO (Figure 7.1b). Tables 7.1-2 indicate a decrease in total number from 330 (1952-79) to 303 (1980-2007). Uncertainties about intensity (basically a lack of MSW data from before the late 1970s (see also Chapter 5) precludes comparison on intensity basis. Therefore, it is reasonable to assume that the number of cyclones has really decreased in the MC (while it is relatively constant in the SWIO), but also that the earlier period contained a larger number of tropical storms and the latter period more of intense cyclones. It is also shown (see further below) that the number of cyclone days has increased (Figure 7.26). Cyclone days are so far less discussed, but this factor is undoubtedly important when considering the TC activity.

There is also clear evidence that the SSTs in the SWIO and the Mozambique Channel increased (by ΔT=0.1-0.2°C) during the most recent period (1994-07) compared to the earlier period. However a similar increase was at hand also during the late 1970s and thereafter (Fig 3.4) and it is likely that also this earlier period (1980-93) was preceded by even lower SSTs as judged from other estimates (i.e. Levitus et al. 2005). It is anticipated that this increase (although small if one considers the effect on the TCHP, which is only some 10% for an increase ΔT=0.2-0.4°C; estimating that this is the increase that took place from the period 1952-79 to the period 1980-07) has affected the

intensity of the cyclones positively. In relation to Section 7.6, Eq 7.1 (showing the TCHP), it is discussed the possibility that the more intense cyclones enables a deepening of the mixed layer, which counteracts more substantial increases of SST. It seems as a good motivation, as to why the number of cyclones is roughly similar, while there is clear evidence that those formed are more intense, and also that the number of cyclone days is increasing. This is not a straightforward issue, however, as generation and occurrence are two different issues, and intensification from a moderate TC to one of high intensity may take place far away from the formation area. Mean genesis SST for 80 cyclones in the SWIO region during from 1998-05 (for which the best data, TMI SST, were available) was 29.2°C (Figure 7.15). For cyclones within the Mozambique Channel, the mean was 29.7°C. No cyclones were formed at SSTs below 27°C and only one below 27.5°C. The data indicates a genesis SST which is 0.5°C above the climatology SSTs according to Figure 7.14.

Sections 7.7-8 deal with the climatological characteristics of TC that made landfall over the Madagascar and Mozambique coastal areas during the period 1952-2007 and also with the intensity of MC cyclones. There is an apparent decrease in landfall since the 1950s in parallel with a decrease in total TC activity in the channel. Considering only the more recent period (1980-2007) there is no apparent change either in total activity or in landfall. However trend analysis for the same period shows a considerable increase in the number of intense tropical cyclones (Category 3-5) during the last 14-year period compared to the earlier 14-year period. As documented from several figures (i.e. Figure 7.16 and 7.20), most cyclones that make landfall are generated within the MC are or in the western part of SWIO, although there are exceptions, i.e. TC Eline (see forthcoming chapter), which moved all across the ocean.

In total eleven cyclones (14 % of the global TC total) per year (with Maximum Sustained Winds; MSW>17 ms^{-1}) are formed in the SWIO within the cyclone season (November-April).

From 1980-2007 the number of land-falling cyclones in Mozambique (MSW>17 ms^{-1}; 1-min average) was 15, a majority of which made landfall in the central region of the

country (Figure 7.23-24). Another 48 cyclones made landfall in Madagascar, 37 of which land-falling on the eastern side, mainly in NE. During the period, 5 intense tropical cyclones made landfall on the Mozambique Coast, while19 hit the coasts of Madagascar. Annual landfall frequency analysis shows an average of 2.5 TCs per year. No landfall cyclones were observed in 1961, 1983, 1987, 1999 and 2001 (Figure 7.21). However, it seems not to be any correlation between frequency in general and that of land-falling cyclones (Figure 7.21). Wavelet analysis indicates a change in periodicity of 2 to 7 years before 1980 and from 2 to 4 years after 1980. These results suggest that TC landfall activity in the SWIO has a decreasing trend and possesses significant inter-annual variability and may be affected by ENSO particularly during La Nina years.

The importance of estimating total number of cyclone days including intensity is demonstrated in Section 7.9. Figure 7.25 gives a rough estimate of total cyclone activity in the SWIO. This figure shows all cyclone tracks, including the cyclone intensity, proportional to $(MSW)^3$, thus giving an integrated impact, or overall cyclone intensity. As seen from the figure this is almost similar in most of the SWIO, in the area between 10 and 20ºS and west of 90ºE, somewhat less strong in the MC, though.

In recent years there have been some indications that cyclone tracks have changed and patterns of landfall may be extend from the northern and central regions to further south in the forthcoming years (IPCC, 2001). However, this is not obvious from Figure 7.17. Tracks of some land-falling tropical cyclones tend to shift further south, also with very unusual trajectories. TC tracks that affected SWIO from 1980-07 were separated in 6 groups (Section 7.10). It is found that about 51% of the SWIO TCs recurves off the Madagascar east coast without making landfall. About 11% were recurving-southward tracks with significant impact over Mozambique and Madagascar coastal areas and 3.8% moved southward tracks travelling off land and across the Mozambique Channel with no direct effect on the coast. TC moving westward (about 14%) had significant on Mozambique and Madagascar while those south-eastward (6.5%) had direct effect on Madagascar. The remaining 14% were recurving-random trajectories also impacted Madagascar and than kept over the open sea.

Stratification of cyclones according to intensity (Figure 7.3) shows that peak frequency for intense cyclones (ITC) occurs in March (22) while the total number of weak cyclones is highest in January (27; Category 1-2). The highest number of tropical storms occurs in February (32). It has been suggested that an increased number of ITC in recent years is the result of larger mixed layer heat content and/or higher SSTs. However, maximum frequency of ITCs in March and of TS in February points towards the opposite, as heat content and SSTs are lower in March than in February. However, other reasons may apply.

The number of ITCs is higher during La Niña years compared to El Niño years (Figure 7.9). Several authors (e.g. Gray, 1984; Bove et al., 1998; Jury, 1993) argued that suppressed activity among ITCs may be attributed to a stronger vertical westerly shear and reduced upper anticyclonic vorticity. Such conditions, which are typical for El Niño years may thus hinder TC development, or even hinder a cyclone from intensifying to an ITC.

Chapter 8: Intensification of tropical cyclones and sea surface cooling in the Mozambique Channel and adjacent waters: Some examples.

In Chapter 3, dealing with various common features of tropical cyclones, it was noted that several scientists found that all cyclones tend to have their own features. Here, the development of some recent intense cyclones, with landfall in Mozambique or Madagascar, is described in detail, based on track data and other remote sensing data, mainly SST and SSHA. Focus is on the reasons for rapid intensification (and, to some extent, decay) and sea surface cooling, features which can be readily related to satellite altimetry sea level data, scatterometer wind data and sea surface temperature and rainfall radiometry, all of which are described in Sections 5.3-5.5. Four cyclones were selected for more detailed description; TC Hudah, TC Japhet, TC Gafilo and TC Favio (Section 8.2-8.5). The selection was done from a total of 15 cyclones (from the data-set 1994-2007), all of which were intense (for easier interpretation of sudden intensification), and some of which also made landfall. Below, and in Section 8.1 it is described how selection was done. This is done with reference to a set of Appendices, showing more details, but also indicating that in this branch, there are no rules without exception, in fact without several exceptions.

An intense tropical cyclone (ITC) features a maximum sustained wind (1-min MSW) of more than 96 knots (50 ms^{-1}), corresponding to a TC, Category 3 according to the Saffir-Simpson scale (Section 5.2.2). Table 8.1 shows the number of cyclones, including intense cyclones and number of land-falling cyclones in the South-West Indian Ocean during the period 1994-07. This period has the most reliable track data, but is also better on remote sensing data in common. As seen from Table 8.1, ITCs represent 36% of the total number, however only 9% made landfall during the period. Still, as aforementioned, in Chapter 7 there were many more ITCs during the last period compared to the period 1980-93.

Several factors affect TC genesis and intensification. One of those is the sea surface temperature. Through interaction between the ocean and the atmosphere, heat is transferred from the ocean to the tropical cyclone, allowing it to become more intense (Section 3.3.4). A higher SST allows for a more efficient transfer of heat and thus for more intense cyclones.

Table 8.1: Intense tropical cyclones (Category 3-5), making landfall and tropical cyclone formation, in the SWIO

Year	Number of ITC	Landfalling ITC	Number of cyclones
1994	6	3	15
1995	4	0	11
1996	4	1	12
1997	4	1	13
1998	1	0	11
1999	2	0	12
2000	5	2	11
2001	3	0	7
2002	6	1	10
2003	4	1	12
2004	4	1	10
2005	4	0	13
2006	3	1	8
2007	6	4	10
Total	56	15	155

The passage of tropical cyclones over ocean also causes upwelling and entrainment, which mixes colder deep water into the warm water at the surface (Section 3.3.4). If the warm layer is shallow, mixing will counteract TC intensification by bringing cool water to the surface thereby reducing the heat flux, particularly if the SST goes below 26°C. On the other hand, if the ocean is heated to larger depths, self-destructive cooling by wind is blocked. This dynamic feedback between TC intensity and SST has been considered important (e.g Emanuel 1999). Particularly the role of warm ocean eddies in the TC-ocean interaction has been underscored in several recent studies (i.e. Shay et al., 2000; Lin et al., 2005). Hurricane Opal (1995) and Katrina (2005) in the Atlantic Ocean and of Typhoon Maemi (2003) in the North West Pacific, are examples in which rapid intensification have occurred in direct relation to the passage of the cyclones across

warm eddies (Section 3.4.1). The high eddy variability and high sea surface temperatures in the Mozambique Channel and east of Madagascar (Section 2.5.2) are good reasons to look in detail for intensification in this area.
Warm eddies are not easily seen from SST data due to continuous surface warming and the prevalence of light winds (Figure 7.12) in the area. This is different from cold eddies, though, which may more readily show up, with their tendency for core upwelling (Section 2.5.2). Employing SST data to identify areas with potential eddy activity is therefore not meaningful. On the other hand measurements of SSHA from satellite have demonstrated to be effective in identifying ocean eddies and quantify eddy characteristics (Hwang et al., 2004; Lin et al., 2005).

The selection done here, combines the high intensity of the cyclones with making landfall (of particular interest for the destructive features of cyclones) and having best available remote sensing data. Thus, the four aforementioned ITCs described in Sections 8.2-5 were picked out. The SSHA altimetry data (see Section 5.5) are crucial to identifying high eddy activity areas where TC are likely to intensify as well as the SST data and even wind data (Section 5.4 and 5.3) in order to evaluate the associated effects of cooling of the surface waters and intensification of cyclones. In Section 8.1 we describe some details on selection and treatment of the remote sensing data.

8. 1 Satellite observations. Methodology

8.1.1 SSHA observations

To identify ocean eddies in the study area, analyses of bi-weekly merged AVISO altimetry data (1/3° Mercator projection grid from the Topography Experiment for Ocean Circulation, TOPEX/Poseidon, Jason-1 and European Remote-Sensing Environmental Satellites, ERS 1 and 2 Ducet et al., 2000) are performed (Appendix C).

As explained in Section 5.5, altimeters measure SSHA along narrow suborbital tracks that are exactly repeated in fixed positions. As the state-of-the-art of the current altimetry algorithm is less accurate in shallow waters (e.g Fu and Cazenave, 2001), the SSHA

measurements in regions of bathymetry< 200 m (see bottom Figure C9-C16 in Appendix C for depths) are not considered. At present, altimeters are not designed to resolve the small scale, rapidly changing features found in coastal ocean circulation. In summary, one might argue that the technique of using SSHA (or SLA) for studying anomalies should be restricted to warm and cold eddies, with meso-scale features.

Here, analysis of SSHA are made seven days prior to the formation of each cyclone and seven days prior to the landfall or dissipation to compare with the development of the ITCs as listed in Table 8.2. Weekly averages of SSHA from 1 Nov 1994 to 30 Apr 2007 are listed in Table C1 (Appendix C). Values of SSHAs for warm and cold eddies including their locations in relation to the cyclone track shown in Table 8.2 are based on Table C1 and Figures C1-15 (Appendix C). The analyses of SSHAs performed between 22 Mar and 9 Apr 2000, 24 Feb and 4 Mar 2003, 1 and 11 Mar 2004, and from 11 – 23 Feb 2007 (those of the four selected land-falling ITCs) are shaded in Table C1. Variations in SSHA in relation to the cyclone track are selected for individual cases in the forthcoming sections (8.2-8.5).

Table 8.2: The 15 ITCs making landfall in the SWIO between November 1994 and April 2007 associated with mesoscale features

			Meteorological observations				Satellite observations		
Year	System	Period	MSW (1-min) [Knots]	MSW (1-min) [ms^{-1}]	MSLP [hPa]	Category (Saffir-Simpson)	Max SSHA MC[cm]	[a]Max SSHA E. Mad [cm]	Location /track
1994	Geralda	25 Jan-5Feb	145	75	892	5	40	10	A-EMD
1994	Litane	05-17 Mar	130	67	910	4	30	10	A-EMD
1994	Nadia	17 Mar-2Apr	120	62	922	4	-30	-20	A-EMD
1996	Bonita	31 Dec-15 Jan	135	69	904	4	20	10	A-EMD , A-MC
1997	Gretelle	18-31 Jan	115	59	927	4	40	20	A-EMD , A-MC
2000	Eline	03-23 Feb	115	59	927	4	30	-10	A-EMD , A-MC
2000	Hudah	22 Mar-09 Apr	125	64	916	4	30	-30	A-EMD , A-MC
2002	Hary	05-14 Mar	140	72	898	5	40	-10	A-EMD
2003	Japhet	24 Feb-04 Mar	115	59	927	4	40	20	A-MC
2004	Gafilo	01-11 Mar	140	72	898	5	40	20	A-EMD , A-MC
2006	Boloetse	22 Jan-06 Feb	100	52	944	3	50	20	A-EMD , A-MC
2007	Bondo	16-26 Dec	135	69	921	4	40	20	A-EMD
2007	Favio	11-23 Feb	120	62	933	4	50	30	A-EMD , A-MC
2007	Indlala	12-16 Mar	120	62	933	3	40	20	A-EMD , A-MC
2007	Jaya	30 Mar-04 Apr	110	57	940	3	20	10	A-EMD , A-MC

[a]Max value next to the track that no eddies are found with 2 degree equator-ward and pole-ward distant from an east-west latitude axis at 20°S. A-EMD=under the track east Madagascar; A-MC under the track in Mozambique Channel

The characteristics of SSHA variability (Figures C1-15) over Mozambique Channel differed from east. There is clear band of very low SSHA (equal or even less than 5 cm) values within the main development region of TCs east of Madagascar. The highest values of SSHA are found in the Mozambique Channel and also the highest variability. There are also more obvious minima in the MC.

8.1.2 SST observations

Sea surface cooling also known as “cold wakes” in the tracks of tropical cyclones have been studied in the past by means of infrared observations (e.g. Stramma et al., 1986; Shay et al., 1992; Monaldo et al., 1997) but the analyses were affected by cloud cover and atmospheric aerosols (i.e. Wentz et al. 2000). The period after (1998-2007) is covered by the TRMM Microwave Imager (TMI) three-day mean SST (Figure C12-16; Appendix C). As aforementioned (Section 5.4.3) one of the important features of TRMM/ TMI microwave retrievals is that the SST can be measured through the clouds. In the absence of TMI SST data for the period 1994-1997, a two day composite products from the NOAA AVHRR satellite data sets was employed (Figure C9-11; Appendix C). The combination of a set of AVHRR images into a composite image made it possible to obtain sufficiently large cloud-free regions for analysis of SST.

The temporal distribution of the consecutive days (fitted with consecutive weeks in SSHA analyses) used in the analysis of three-day mean SST prior to the formation of each cyclone and days after the cyclones is shown in Table C2 (Appendix C). The satellite SST maps for the period prior to and after the passage of the cyclones are shown in Figure C16-31 (Appendix C).

The values and locations of maximum cooling (Max Δ SST) shown in Table 8.3 were obtained by computing the difference between the prior-cyclone and post-cyclone SST fields. SST was more that 28-29 during the period of investigation. There is a positive correlation between Max Δ SST and Max MSW. Although the cooling is generally observed at the location of Max MSW, large areas still indicating similar degree of cooling and in some cases even larger with low MSW. Overall SST cooling found in this

study up to 3°C is relatively low compared to reported maximum of up to between 7-9°C (Sakaida et al., 1998; Walker et al., 2005; Emanuel, 1999), despite the fact that this study have included only ITCs were considered. TC Japhet (described in Section 8.3) was the only exception, with its 7°C maximum cooling. In the case of Japhet, however the strong cooling was most likely due to a low translation speed.

Table 8.3: The fifteen intense tropical cyclones making landfall in the SWIO between November 1994 and April 2007 associated with SST observations

			Meteorological observations					SST observations	
Year	System	Period	MSW (1-min) [Knots]	MSW (1-min) [ms^{-1}]	MSLP [hPa]	Category (Saffir-Simpson)	Trans. speed [ms^{-1}]	Max Δ SST [cm]	Location of Max Δ SST
1994	Geralda	25 Jan-5Feb	145	75	892	5	4.2	-3	-15.2; 52.5, A
1994	Litane	05-17 Mar	130	67	910	4	5.5	-2	-18.4; 54.2, R
1994	Nadia	17 Mar-2Apr	120	62	922	4	6.5	-3	-16.8; 52.1, R
1996	Bonita	31 Dec-15 Jan	135	69	904	4	4.4	-3	-19.0; 50.0, L
1997	Gretelle	18-31 Jan	115	59	927	4	3.6	-1	-22.8; 41.0, L
2000	Eline	03-23 Feb	115	59	927	4	3.1	-4	-22.0; 36.5, A
2000	Hudah	22 Mar-09 Apr	125	64	916	4	7.7	-2	-17.5; 40.5, R
2002	Hary	05-14 Mar	140	72	898	5	4	-3	-12.5; 52.5, L
2003	Japhet	24 Feb-04 Mar	115	59	927	4	0	-7	-23.0; 36.9, A
2004	Gafilo	01-11 Mar	140	72	898	5	4.6	-4	-14.3; 58.4, L
2006	Boloetse	22 Jan-06 Feb	100	52	944	3	6.0	-4	-22.5; 42.5, A
2007	Bondo	16-26 Dec	135	69	921	4	5.7	-3	-9.5; 51.0, A
2007	Favio	11-23 Feb	120	62	933	4	3.6	-3	-25.0; 41.0, A
2007	Indlala	12-16 Mar	120	62	933	3	3.0	-3	-14.0; 55.0, A
2007	Jaya	30 Mar-04 Apr	110	57	940	3	6.0	-2	-15.5; 55.5, A

***L**: Left to the cyclone track; **R**: Right to the track; **A**: Along or under the TC track*
Translation speed of the tropical cyclone (slow, ≤ 4 m/s; medium, 4 – 6 m/s; fast, ≥ 6 m/s, Stramma et al. 1986).

8.1.3 Hydrographic observations

Satellite derived fields of SSTs, shown in Appendix C (Figure C16-31) indicate the occurrence of cold wakes related to TCs, but also cold eddies and upwelling, particularly in the shelf waters. In addition, hydrographic observations, i.e. temperature profiles or sections, for example those that were obtained during the Agulhas Current Sources Experiment (ACSEX; Section 5.7) may help substantially. Such data are used below in relation to TC Hudah (Section 8.2). Also hydrographic data from individual Argo floats, as discussed in Section 5.7 can be used to help identifying warm and cold eddies, and moreover, to see for changes in the upper ocean after a cyclone passage (temperature changes and mixed layer depths can be revealed). Details of hydrographic data used in this study are listed in Appendix C (Table C5-C7).

8.1.4 Rainfall observations

Monthly rainfall climatology was determined from TRMM satellite rainfall data (Section 5.4). Figure 2.17 shows data, averaged for the period from 1 November 1998 to 30 April 2007. Jiang et al. (2008) pointed out that when a TC is over the ocean its rainfall is correlated well with storm intensity (over land, this kind of relationship might be much weaker because of additional factors). In addition tropical cyclones and also storms, can cause heavy rainfall during landfall. The authors emphasize that impacts of TCs such as by floods, are associated not only with the storm's maximum wind intensity but also with its projected movement, its size and rainfall distribution. Examples of rainfall data associated with TCs are examined in the forthcoming sections. There seems to have a close relationship between TC accumulated rainfall over ocean and TC maximum intensity (Figure C2.1, Appendix C1). Whether this relationship is valid over land (Figure C2.2, Appendix C1) need further exploration taking in account several factors such as land topography, storm size, etc. On the other hand a more detailed study including more TCs and extended rainfall data temporal coverage is need for more consistent conclusions.

8.1.5 Vertical wind shear

Large vertical shear is detrimental to genesis and also to intensification of tropical cyclones (Section 5.6.1). It's a source of atmospheric turbulence. If strong, it will dampen the development of cyclones. Mean Nov-Apr vertical shear for 1979-2005 is shown in Figure 8.1. The prominent feature over the SWIO is the area of low shear that extends from 100°E to Mozambique Channel.

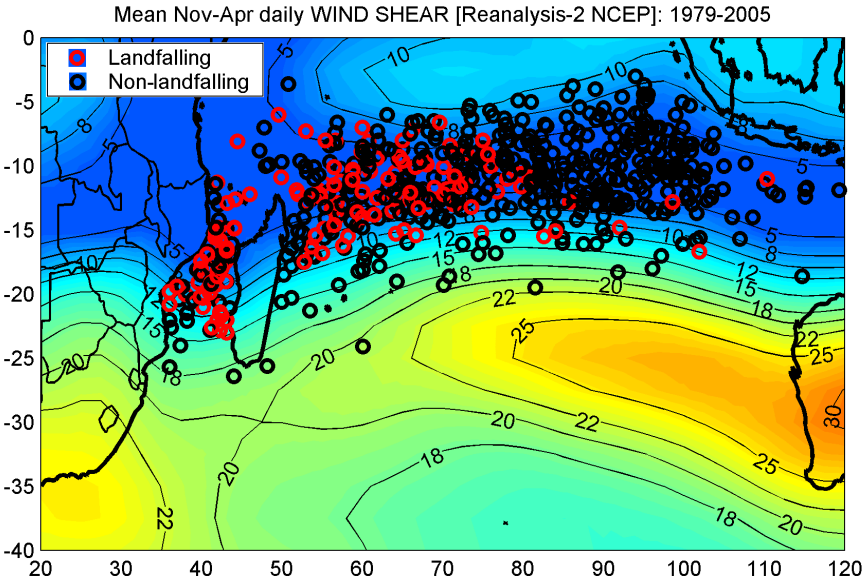

Figure 8.1: Mean vertical shear for November-April 1979-2005. Vertical wind shear is shown as the velocity difference between the 200 and 850 hPa levels (in ms^{-1}). Tropical cyclone genesis locations (red and black circles respectively) are superimposed. Genesis, as seen occurs mainly where the shear is minimum.

This region of low shear, much the same as the area occupied by the ITCZ, with values less than 12 ms^{-1} (as calculated in the interval from 250 to 800 hPa) which covers a large fraction of the main development region (MDR; 8-25°S; 40-100°E) of tropical cyclones indicates that the mean shear pattern of the SWIO is favourable to tropical cyclone development and further intensification (Zehr, 1992; DeMaria, 1996).

8.2 Tropical cyclone Hudah

Genesis of TC Hudah took place within the ITCZ near Australia. The cyclone moved zonally across the ocean and made landfall in the north-east region of Madagascar near the town Antalaha at a MSW>59 ms^{-1} (Category 4) on 2 April, 2000 at 0600 UTC. The track of the cyclone is shown in Figures 8.2-3, indicating bottom topography and SSHA, respectively. Peak intensity before landfall was 64 ms^{-1}, on 1 April 2000 at 1200 UTC.

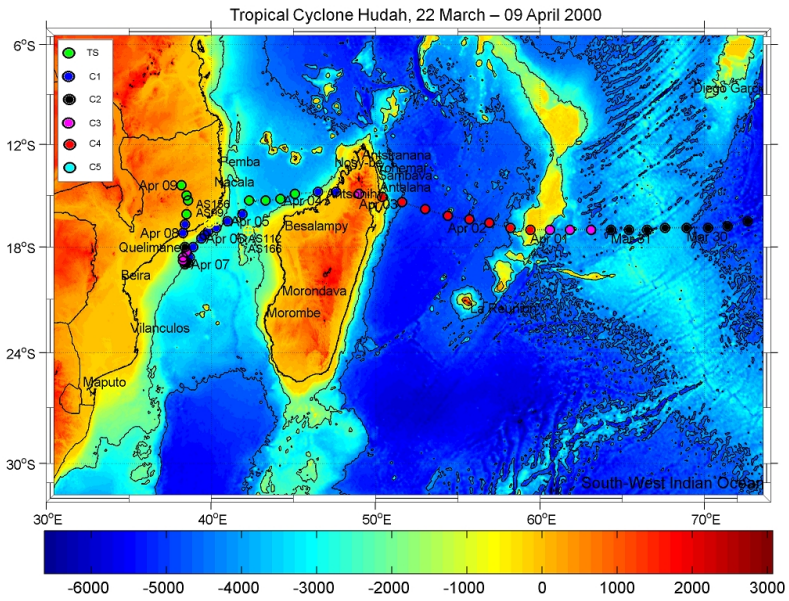

Figure 8.2: Plan view of the study area with ACSEX buoys (yellow circles with crosses), tropical cyclone Hudah path (circles colored marks) overlain the ocean and land topography (ETOPO-2). Cyclone Categories 1-5 are represented by colored circles and dates are next to 6-hourly observations (for dates, see text).

Crossing Madagascar, Hudah weakened significantly and entered the Mozambique Channel as tropical storm on 3 April, only 5 weeks after cyclone Eline had passed through this region, although further south (see bottom Figure C12, Appendix C). Eline was the most long-lived cyclone observed in SWIO in recent years, which tracked almost 2000 km across the southern Africa with a lifetime of 29 days.

On 31 March, the SSHA (Figure 8.3) in the Mozambique Channel indicated the presence of a warm eddy at the narrowest section of the channel. After the eddy encounter, Hudah started intensifying again over the channel particularly on moving south-westward in the warm eddy street of the channel (Section 2.5.2). Thus, Hudah was upgraded to a TC Category 1 (33 ms^{-1}) on 5 April, reaching a new peak intensity of 52 ms^{-1} on 7 April, 2000 at 0600 UTC and made landfall near the district of Pebane, with sustained winds of 41 ms^{-1} on 8 April 2000 at 0600 UTC. It then rapidly lost its intensity over land (Figure 8.3). Total lifetime of Hudah was 18 days, two of which were storm days (MSW<33 ms^{-1}).

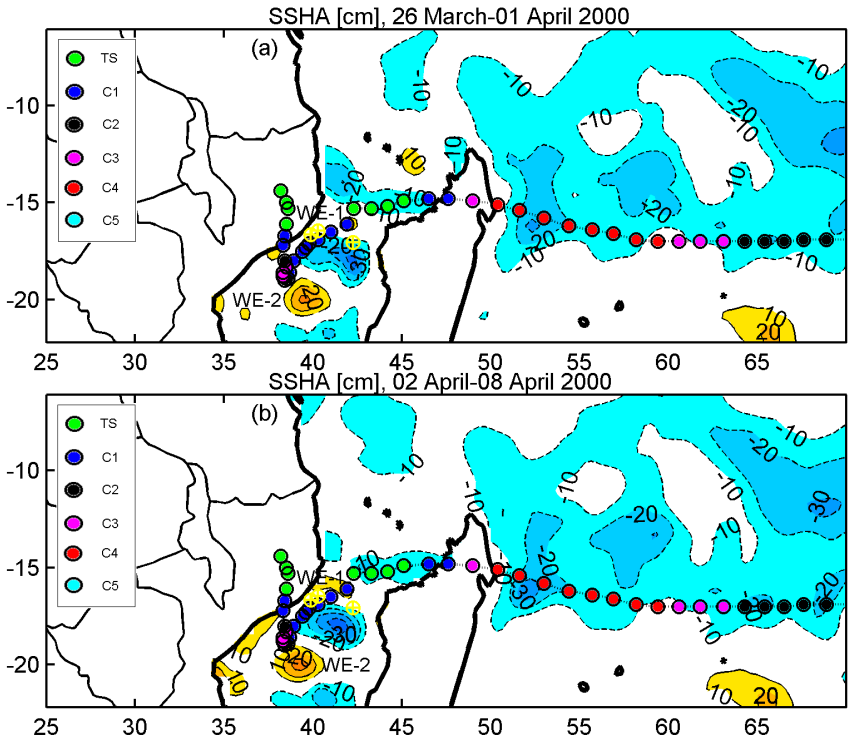

Figure 8.3: AVISO SSHA, deviations from MSL (cm) during the TC Hudah event; (a) 26 March - 1 April and (b) 2 - 8 April 2000 obtained from merged altimeters. Track of the cyclone with intensity according to the Saffir-Simpson Scale (Category 1-5) are indicated. Dates for the cyclone are given in text.

a. SSHA

As mentioned in Chapter 3, sudden intensification of tropical cyclones related to passage of the cyclones over warm eddies has been well demonstrated in Pacific and Atlantic Oceans. In the South-West Indian Ocean no such indications have been demonstrated. Here, Figure 8.3 shows the pre-Hudah SSHA conditions together with the track of the cyclone. Figure 8.4 shows the development of MSW and SLP, according to track data, while the cyclone is passing across the MC. From 2-8 April two warm eddies are seen in the MC: WE-1 is located at the narrows (about 42.5°E; 15.5°E) with an SSHA of 10 cm and a diameter of about 100 km. WE-2 is relatively large (about 250 km) and located in the so-called eddy street of the channel (about 39°E; 20.5°E), with an SSHA ranging from 20-30 cm (Figure 8.3). The passage of TC Hudah across these warm eddies happen to coincide with two stages of intensification; first instance when

the cyclone increased from 35 to 41 ms^{-1} and the second when it increases up to 50 ms^{-1}, as indicated in Figure 8.4.

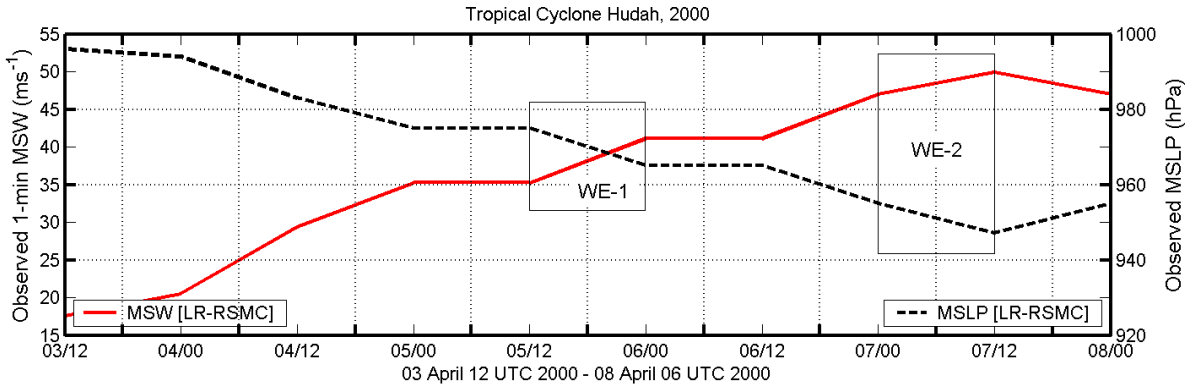

Figure 8.4: Estimated 1-min MSW (solid line) in ms^{-1} and SLP (dashed line) in hPa from 3-8 April 2000 associating TC Hudah with two warm eddies in the Mozambique Channel: WE-1, centered at 42.5°E;15,5°E and WE-2 centered at 39°E; 20.5°E (see Figure 8.2).

Thus, while SSHA in the MC indicated the presence of warm eddies near to the cyclone track, and a consecutive intensification, nothing like that is seen east of Madagascar. Here, cyclone Hudah intensified to a TC Category 4 over a negative SSHA region, so this is a vivid first example that the intensification may have other reasons.

b. SST

A look at the SSTs before and after the passage of Hudah (Figure 8.5) shows that there is a general decrease in the SST, but east of Madagascar it is everywhere low, typically 0.6°C except to the north of the island, and along with the track at 15°*S,* where the decrease is somewhat larger. In this area, TC Hudah passed in the end of March, thus the SST data (from 10 April) are already 12 days old, and that is probably one reason as to why the change is small. It is obvious that within the Mozambique Channel, where the passage took place from about 3-8 April, and the SST data are 4-5 days old, the response is stronger. Near to the land-falling area, the decrease in SST is about 3°C, but not even that is an very large cooling considering the intensity of the cyclone. And even in the channel, the general decrease is less than 1 °C, indicating that the change that is seen could even be the result of seasonal decrease (this is discussed in connection with the recovery of the mixed layer temperatures in Section 9.5). Comparing

SSTs and SSHAs (Figure 8.5 and 8.3) indicates that not even the very low SSHA just to the south of the MC narrows indicating a cold eddy is clearly seen as a lower SST (different from the eddy shown in Section 2.5.2). It is also noted that the changes in the SSHA fields are small comparing “before and after Hudah”, whether the cyclone has affected the area or not. In summary, this set of data may not be enough for understanding cyclone intensification and cooling. It seems as if a higher resolution in time is needed.

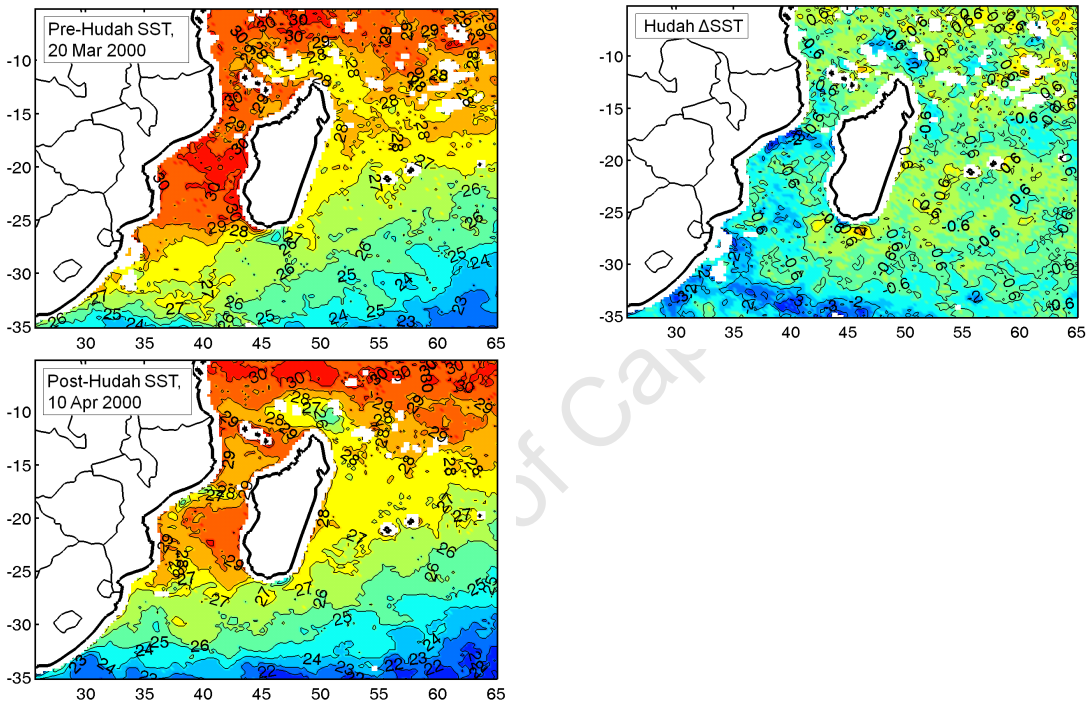

Figure 8.5: Sea surface temperature (TRMM/TMI) data along with cyclone Hudah, showing SSTs before passage (20 March) and after passage (10 April) and the temperature difference, ΔSST between the two.

c. Influence on hydrography

Figure 8.6 shows pre-cyclone and post-cyclone upper-ocean conditions in the narrows of Mozambique Channel, using ACSEX CTD data (Section 5.7). Temperature profiles from 1 and 8 April, is shown in Figure 8.6. The position of this station was some 150 km southeast of the track, apparently outside the wake area, where upwelling and strong cooling was at hand (see below). A cooling is seen, and also a homogenized mixed

layer down to about 45 m. There are also indications of some deeper motions, not very distinct, though.

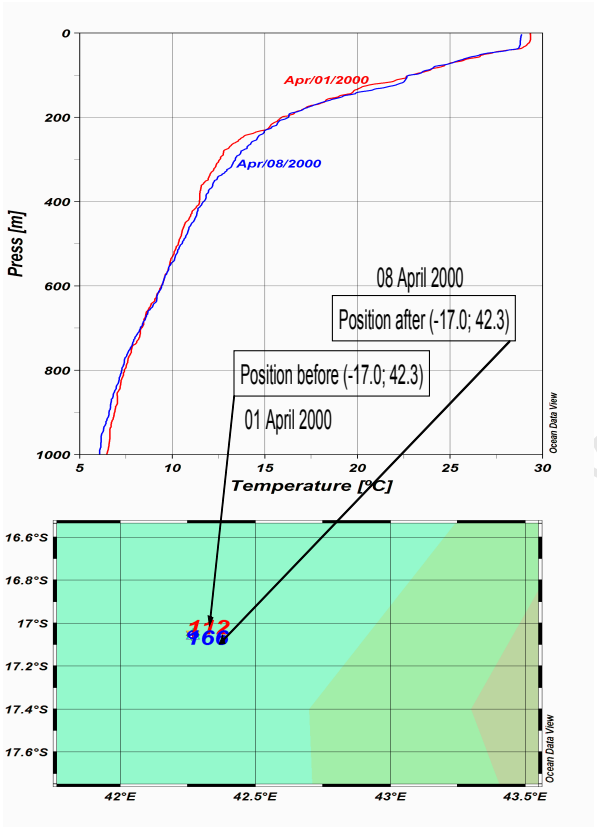

Figure 8.6: Vertical temperature profiles from ASCEX-I cruise (year 2000) taken during Hudah passage at the narrows. The CTD station ID's are 112 (pre-cyclone) and 166 (post-cyclone).

However, after hiding away while Hudah started crossing the MC (on 3 April) , r/v Pelagia from ACSEX started a two day cruise comprising 19 stations taken from the 4 April (13.2°S; 42.6°E) to 6 April 2000 (16.5°S; 40.3°E) trying to follow the cyclone track. The positions of the XBT stations are shown in Figure 8.7, together with the temperature section. On the north south leg, the ship is crossing the track at 15.2°S (250-300 km from the start), in perfect position as indicated from track data, less than two days after the cyclone passed towards west. At this position, the surface temperature is 26°C, thus 3-4°C lower than it was before the cyclone passed, and there are clear signs of upwelling (although not very strong).

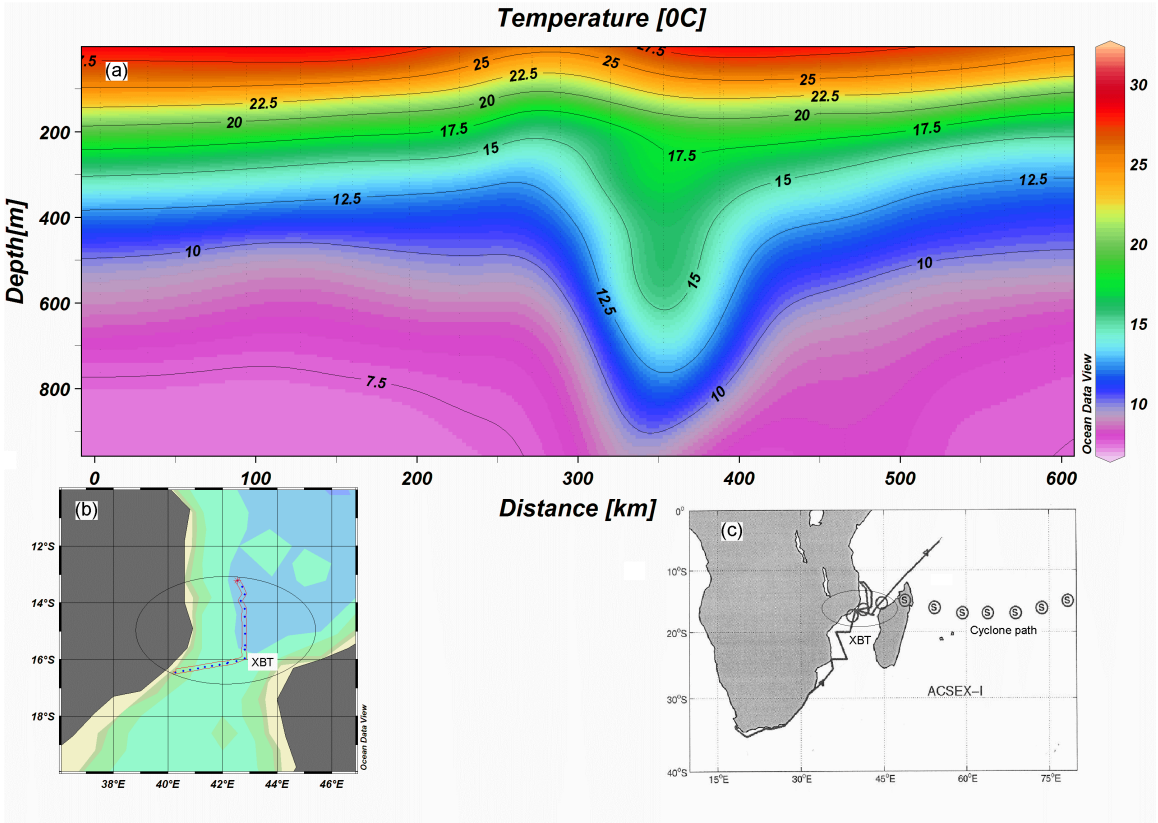

Figure 8.7: (a) Response of the upper portion of the ocean at the narrows of MC next to (b) XBT line, immediately after the passage of (c) tropical cyclone Hudah. Temperature is approximately discontinuous at the boundary and it is lowering down quickly.

At the next station (320 km from the north), the ship track turns almost towards west (Figure 8.7b) and for a distance of about 100 km, there seem to be signs of either a very strong downwelling, or of a warm eddy. However, as seen from Figure 8.3, there is no sign of warm eddy, at least not as judged from the SSHA data. As this strong feature persists for at least 100 km to the west, from 320-420 km, along with the direction of the cyclone (but some 100 km south thereof), it could be related to the cyclone winds which might create downwelling, at least at some distance from the track. Even that, however, seems not very likely; rather, what is seen is the deep water response to strong geostrophic currents, towards south on eastern part and towards north on the western part of this section. Probably these strong currents were caused by the storm winds created by the cyclone, but that relaxation in the surface is too fast to show response in the SSHA. Geostrophic calculations indicate a velocity of the order of 1 ms^{-1} in the warm upper layer for a horizontal temperature gradient 0.6°C/10 km, which is quite reasonable

in this area, which occasionally features very rapid currents (Schouten et al. 2002). At this stage, the nice temperature section indicates a strong decrease in temperature along with track, and a bit of upwelling related to it. The large volume of relatively deep water seen from the second half of the cruise leg, however it may or may not be related to the passage of TC Hudah.

d. Rainfall

Hudah was a Category 4 cyclone when land-falling on the NE coast of Madagascar. According to TRMM data, rainfall signatures associated with maximum wind speed intensity varied from 160-180 mm east of Madagascar (Figure 8.8) and 120-140 mm over the Mozambique Channel. At landfall over Mozambique the associated rainfall was 60-80 mm. The National Institute of Meteorology (INAM, Mozambique) recorded daily rainfall near to the landfall area (at Pebane).

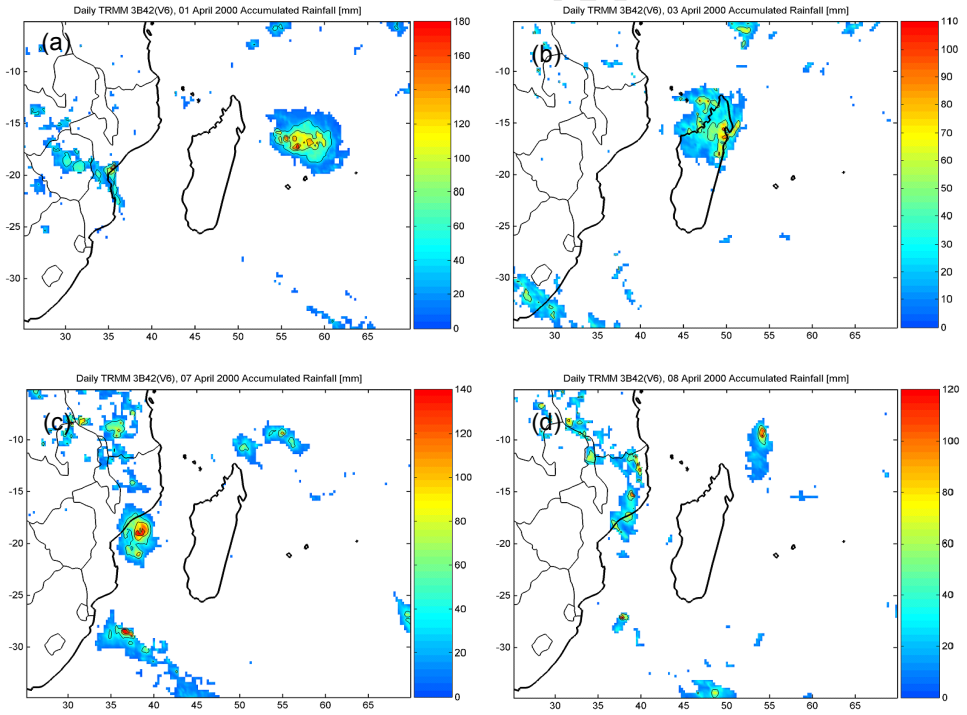

Figure 8.8: Satellite (TRMM 3B42 V6) derived precipitation estimates showing rainfall fields associated with TC Hudah over the study region during the two stages of intensification (a) East Madagascar, (c) Mozambique Channel and at landfall (b) NE coast of Madagascar and (d) Central coast of Mozambique.

On 7 April, this station recorded a very low rainfall (3.2 mm) while on 6, 9 and 10 April it recorded 49, 22.2 mm and 34.2 mm, respectively. On 8 April, landfall day, no data were available. Thus, at present it is not realistic to go further with rainfall data at the moment, and there is little or no possibility to match with TRMM rainfall data in the same period.

8.3 Tropical cyclone Japhet

TC Japhet was a rapidly intensifying ITC, moving westward between 20-22ºS in the Mozambique Channel (i.e. Figure 8.15). It had a short life span of 5-6 days only, starting on 25 February and land-falling in Mozambique with consecutive decay on 2-3 March 2003. The days before Japhet was established, the Mozambique Channel SSTs were very high, about 30ºC on average, and also very stable on a day to day basis (Figure 8.9).

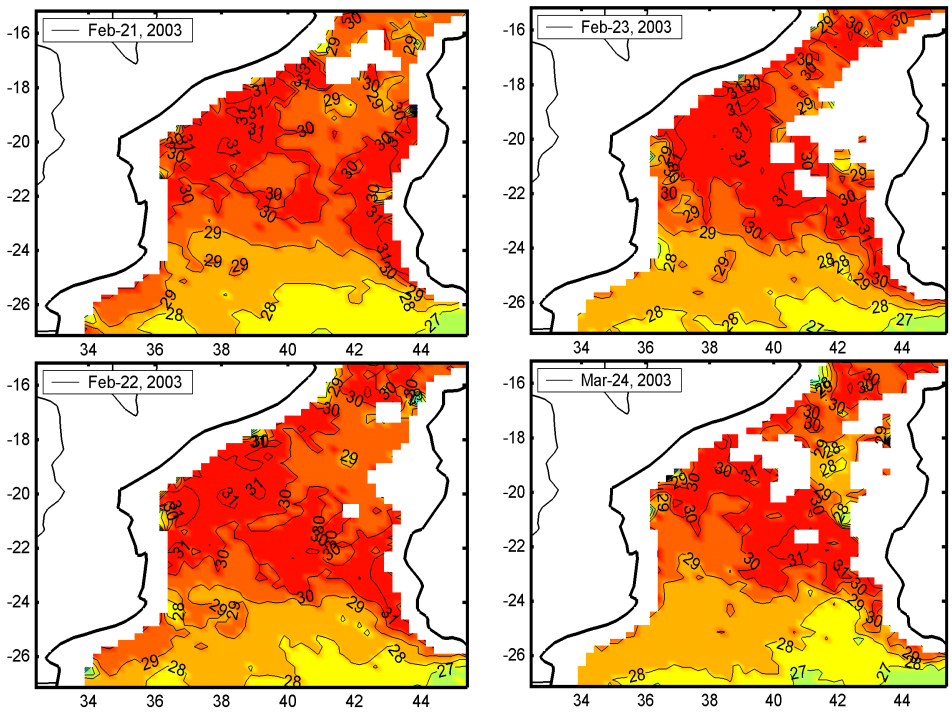

Figure 8.9: Three-day mean TMI SST from 21-24 Feb 2003, ahead of TC Japhet.

However, the winds were increasing in the eastern part of the channel to between 5-10 ms^{-1} (Figure 8.10) and a decrease is seen on the eastern side channel (17-21ºS, E of 41ºE). Otherwise, the SSTs were almost constant throughout this period, and also the winds were below 5 ms^{-1} most of the time.

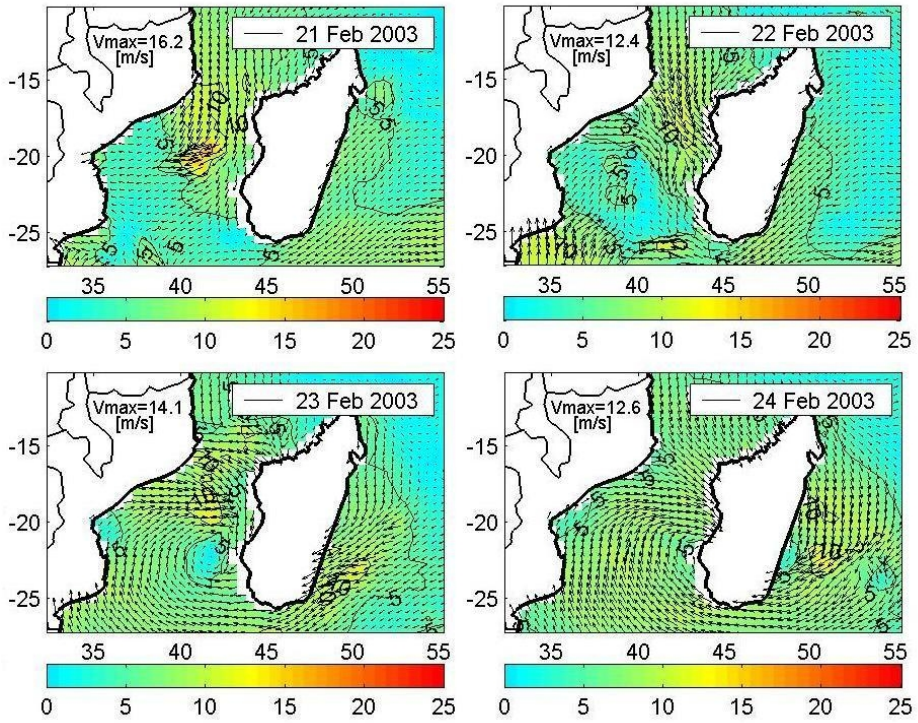

Figure 8.10: QuikSCAT daily mean surface wind from 21-24 February 2003.

From 24 and 25 February, still with moderate winds, SSTs decreased by about 1˚C in the southern parts of the channel (Figure 8.11). Only in the cyclogenesis area (22ºS, 42ºE) SSTs were still >30ºC, as expected because the winds were weak (Figure 8.12) in the genesis area. A day later, TC Japhet was declared a TS with MSW (1-min) increasing from 20 to 40 ms^{-1} between 26 Feb 1200UTC and 28 Feb 0000UTC and then to near 60 ms^{-1} on 28 February (Figure 8.13). During the forthcoming 48 hrs, until afternoon on 2 March, MSW averaged 50 ms^{-1} with maximum of 60 ms^{-1}. As seen from Fig 8.9 rapid intensification took place from 28 Feb 0600 UTC to 28 Feb 2400 UTC. The development is readily seen also in wind data. However, for several reasons as discussed in Section 5.3, the scatterometer wind data are not able to represent the storm winds that appear along with TCs. The comparison with MSW and ground truth observations indicates that the satellite data strongly underestimate the true surface winds. Maximum winds according to TMI are just about 20 ms^{-1} on 28 Feb (Figure 8.12) while track data indicates mean winds of 40-50 ms^{-1} (Figure 8.9) Such circumstances, of

course would violate calculations of entrainment velocities according to the equations given in Chapter 6.

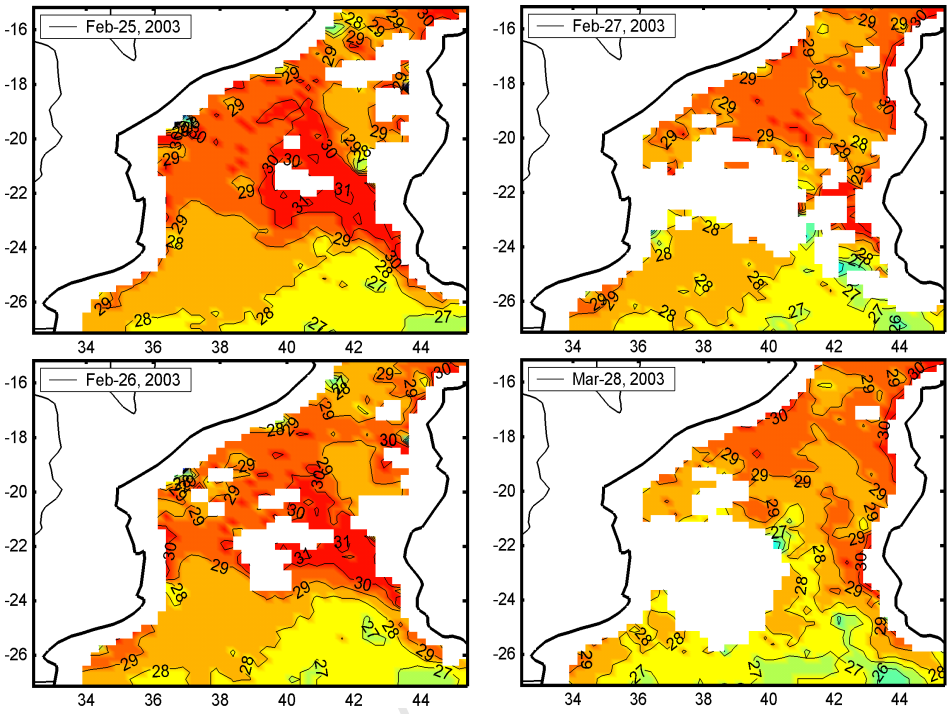

Figure 8.11: Three-day mean TMI SST from 25-28 February 2003.

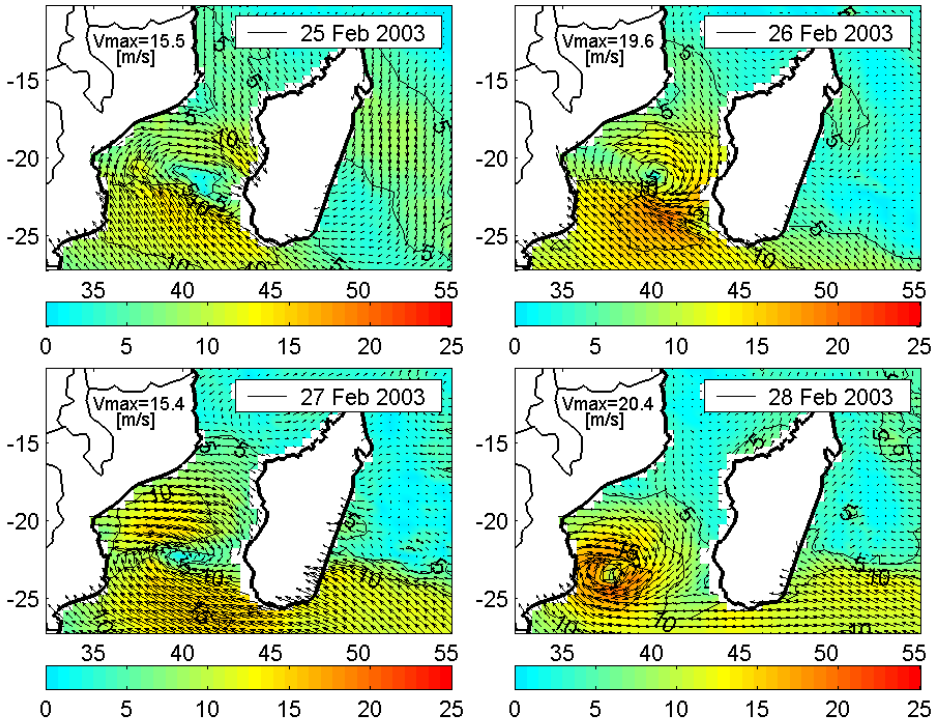

Figure 8.12 QuiSCAT daily mean surface wind from 25-28 February 2003.

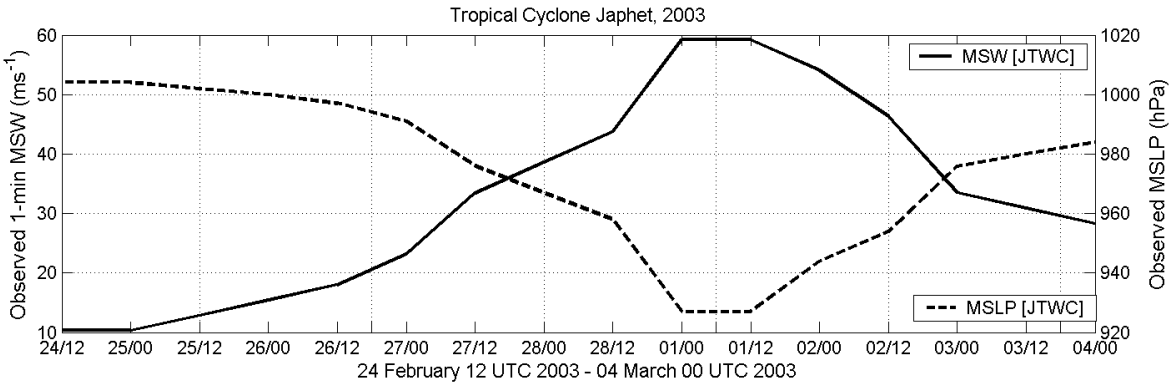

Figure 8.13: Estimated 1-min MSW (solid line) in ms^{-1} and MSLP (dashed line) in hPa from 24 February 12 UTC – 04 March 00 UTC for TC Japhet.

TC Japhet moved almost straight across the channel (Fig 8.14) with landfall in Mozambique on 2 Mar 1800UCT. The track over sea was fulfilled in 5 active cyclone days (25 1800UTC to 02 1800UTC, with a mean E-W translation velocity of 120 km/day,

including a 1-day standstill at 37.5E, 23.5S and the fast westward motion that took place from 25 1800UTC to 26 1200UTC (Figure 8.14).

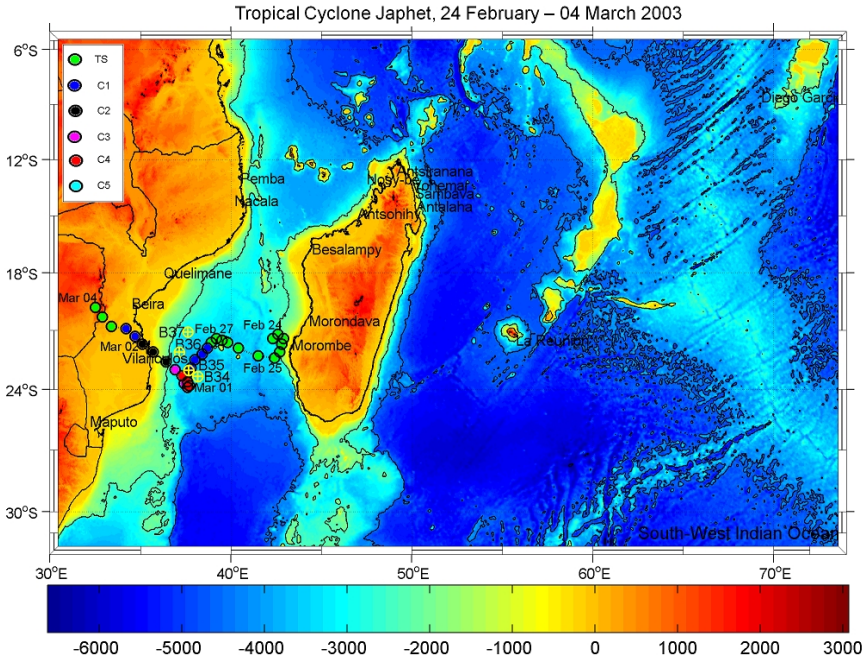

Figure 8.14: Track of TC Japhet. Tropical cyclone centre positions every 6h are indicated by colored circles (for legend, see Figure 8.20). Date beside cyclone centre indicates position at 0000 UTC that day. The positions of three ARGO floats are indicated by yellow crossed circles denoting for B=BODC (British Oceanographic Data Centre). B34: Feb/12/2003 (23.3S; 38.2E); B34: Feb/22/2003 (23.0S; 37.7E) B36: Mar/04/2003 (22.1S; 37.2E); B37: Mar/14/2003 (21.15; 37.6E).

During 6 days, from 24 February to 2 March, there is a continuous decrease of the SSTs (Figure 8.15), with maximum decrease in the wake of 4-7˚C, and a common decrease in the southern Mozambique Channel of ΔT =2-2.5˚C (18-26S, 36-43E).

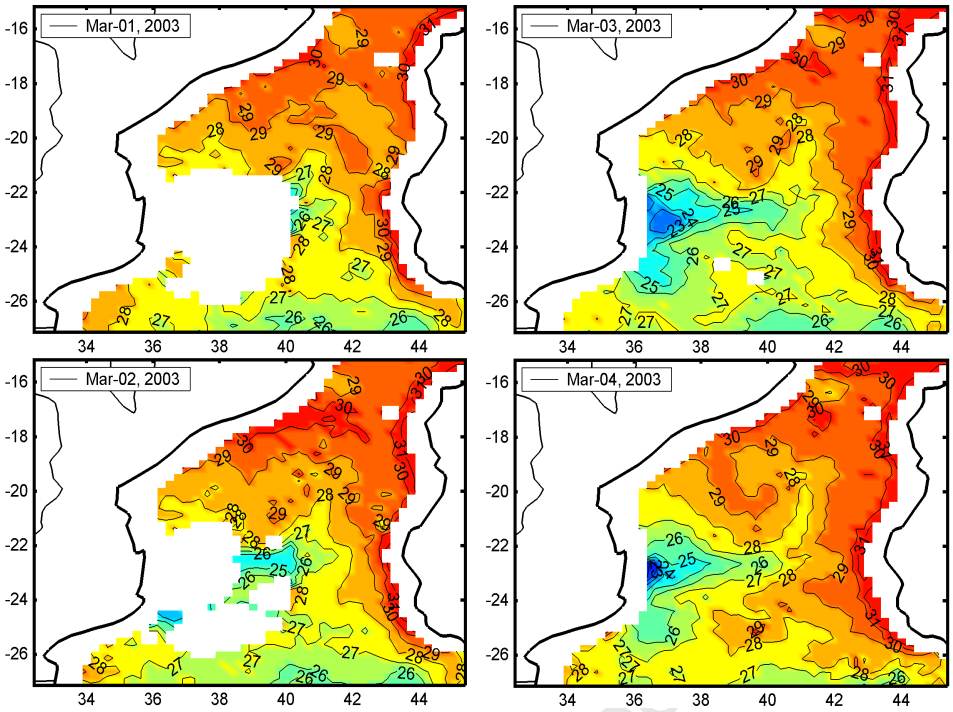

Figure 8.15: Three-day mean TMI SST from 1-4 March 2003

Although clouds and heavy rains (see further below) precludes SST observations in the vicinity of the cyclone, it is obvious from data on 3 March (Figure 8.14) that maximum cooling did not quite coincide with the track of the cyclone. During the 27-28 Feb, maximum cooling took place on the southern side as expected, because of stronger winds to the left. While TC Japhet peaked during its standstill on 1 March (23.5S, 37.3E), maximum cooling seems to have occurred just in front of the cyclone, towards the coast. There is no doubt, however, that this cyclone had a major impact on the surface water temperatures. For the case of TC Japhet this will be considered further in Section 9.5, then including also the recovery period, which continued up to between 15-20 March.

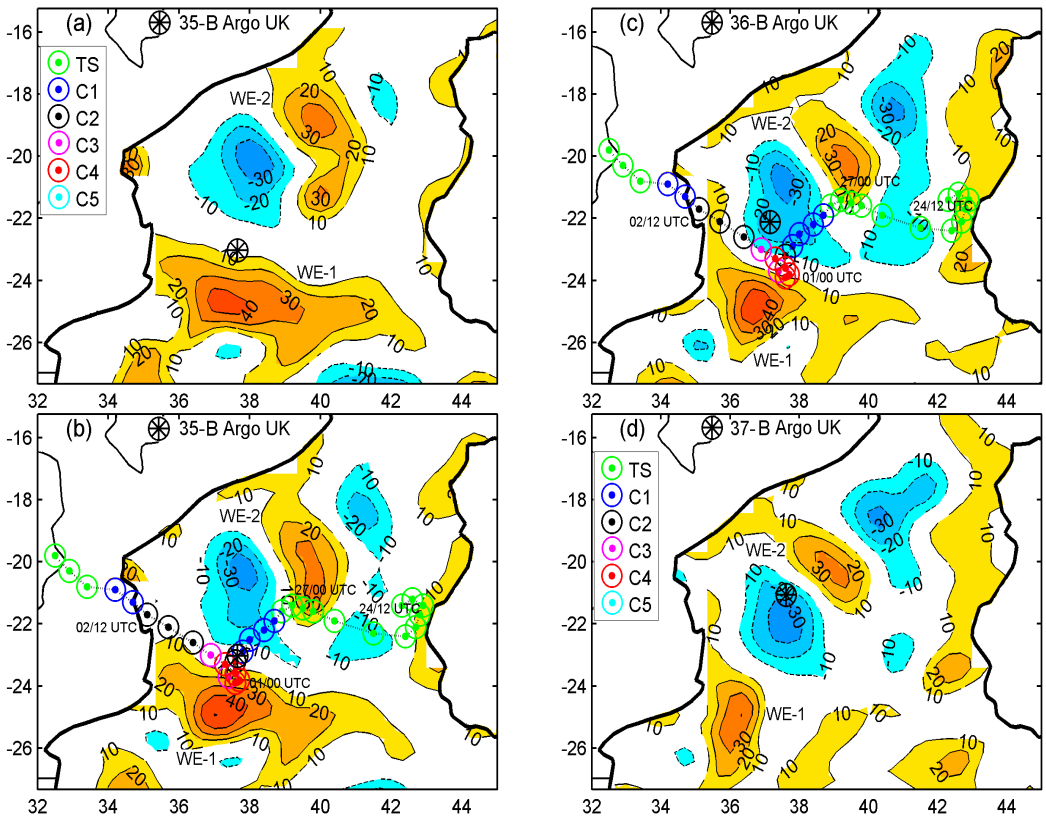

Figure 8.16: Average SSHA showing (a) 16-22 February, (b) 23 February – 1 March, (c) 2–8 March, and (d) 9–15 March. The track of TC Japhet and its intensity according to JTWC is shown with dates inserted. The position of the BODC Argo buoy, discussed in text, is shown on 22 February (35-B in Figures (a) and (b), on 4 March (36-B in Figure (c) and on 14 March (37-B) in Figure (d)).

Sea surface height anomalies, from four 7-periods surrounding the TC Japhet event, are shown in Figure 8.15. Three distinct eddies are seen along the track of the cyclone, two of which are warm and one cold. Table 8.4 shows the movements of these eddies while TC Japhet crossed the channel, and in addition the change in SSTs at the mean positions of the eddies. As seen, there is nothing like exceptionally strong cooling above the cold eddy, and not either seem the waters above warm eddies to be more sheltered against cooling than their surroundings. There is a 3-4˚C decrease over the large eddy (WE-1) on the southern side of the cyclone, less than the maximum of 6-7˚C in the core. Thus this large eddy might have had an effect in hindering the decrease from being even larger as the area was also the centre of the strongest winds on 28 Feb - 1 March. In summary it means that WE-1 might have contributed to the rapid intensification that

took place from 28 Feb 0600UTC. At least it is obvious that the maximum decrease took place to the north of WE-1, where SSHAs were small or even negative. The role of warm eddies in relation to intensity and intensification will be discussed at length in Chapter 9, where a model approach is used to explore the reasons for changing SSTs and heat content in detail.

Table 8.4: Centre positions of three eddies in the vicinity of the track of TC Japhet, and the change in SST at their mean positions.

	23 Feb – 1 Mar		2 – 8 Mar		Mean position		Δ SST
	Lat S	Long E	Lat S	Long E	Lat S	Long E	˚C
WE-1	24.9	37.1	24.9	36.9	24.9	37.0	3-4
CE-1	20.4	37.9	20.8	37.5	20.6	37.7	2-3
WE-2	20.3	39.8	20.1	39.2	20.2	39.6	1-2

While TC Japhet was crossing the channel, there was an ARGO float in the area where the cyclone reached maximum intensity. Temperature data from this float is shown in Figure 8.17, the positions of the float on 22 Feb, 4 and 14 March are shown in Figure 8.12. Further data include salinities for which the data are not quite satisfactory**.** As seen, the profiles before the cyclone event, on 12 and 22 February are typical for the area (Figure 2.12) with SSTs of 28-29˚C and a thin, 20-30 m deep mixed layer. The 20˚C isotherm is at 150 m, and the 26˚C is at 50 m. After the cyclone passage, on 2 March, the mixed layer depth has increased to about 60 m and SST is 26˚C. The bottom of the thermocline is now 60 m shallower, and the 20˚C isotherm is found at 90 m, indicating entrainment of thermocline water into the mixed layer, but also a deep-going upward convection (upwelling). The conditions below the mixed layer are similar on the 12 March (Figure 8.16), however, it is obvious that the mixed layer, is subject to a gravitational restoration giving rise to a very thin but rapidly heating mixed layer

The position of the ARGO float is shown in Figure 8.10. Before the cyclone event, on 22 February the float was in an area between high and low SSHA, while on 2 and 12 March it was within the cold eddy, where the SSHA was about -20 cm at both occasions. As discussed at length in Section 3.4.2 cold eddies are related to a shallower thermocline. In this case, it is obvious that one part of the shallower thermocline after the cyclone is due to the entry of the float into an area of negative SSHA. However, the major part of

the change seems to be caused by upwelling, which in the area of the float may have reached 40-50 m. As aforementioned, this process, as well as the surface wind-mixing and the related temperatures of the mixed layer after the cyclone, are further discussed in Chapter 9.

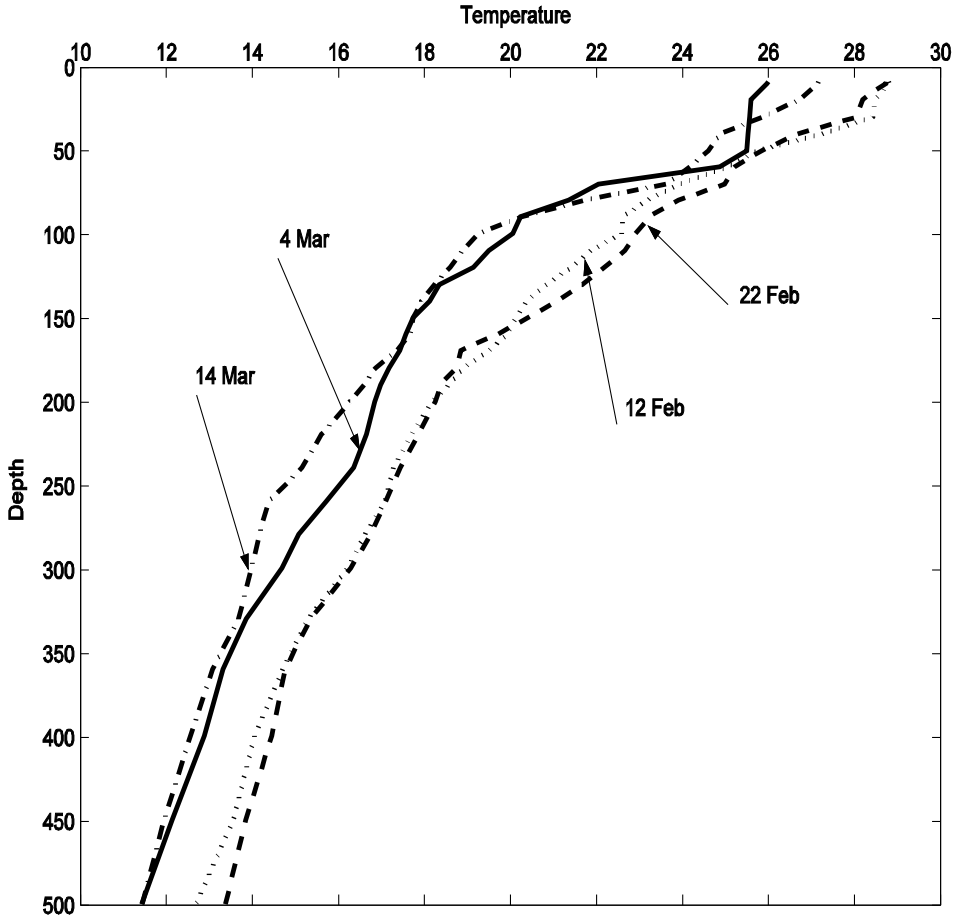

Figure 8.17: Temperature profiles from an ARGO float, travelling across the track of TC Japhet. For positions, see Figure 8.14.

Another important issue concerns the long-term effects of cyclones. Apparently, a single cyclone may affect mixed layer depths and SSTs over vast areas and for quite long periods, even though dramatic losses of heat to the atmosphere (through increased turbulent heat fluxes) are relatively small. In this case, restore of SSTs can be studied on the basis of SSTs after the cyclone has passed. The surface temperatures after Japhet reached what can be considered normal about two weeks later, as indicated in Figures 8.18 (showing SSTs for the period up to 16 March). However, as indicated by the temperature profiles in Figure 8.12, the heated surface layer is thinner (15 m only) and

the SST gives a partly false picture of the restoration. This problem is also further explored in Section 9.5.

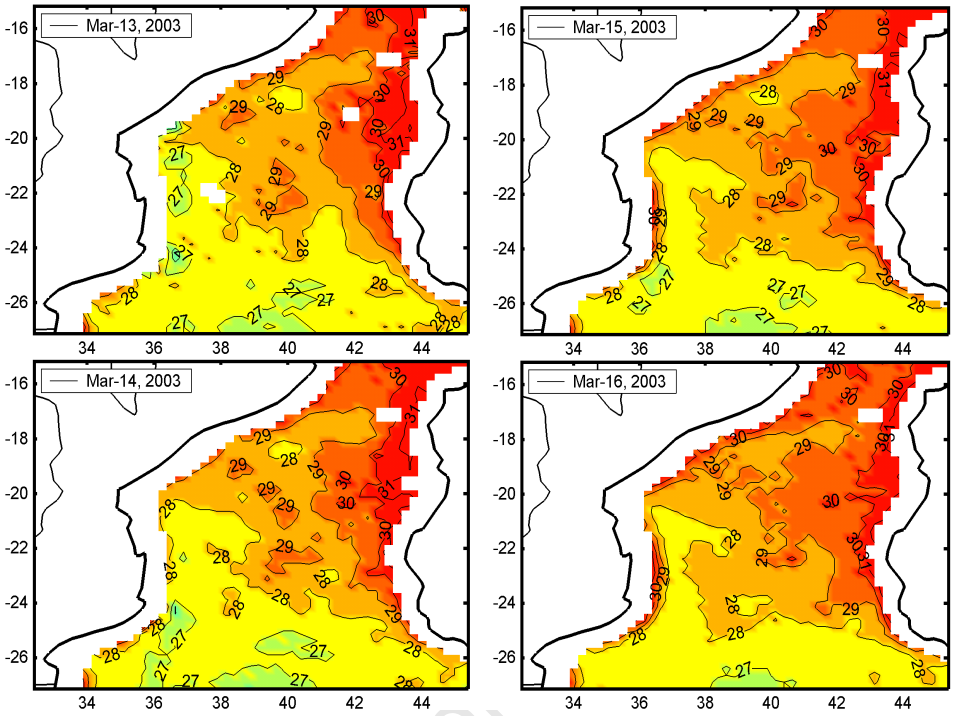

Figure 8.18: Three-day mean TMI SST from 13-16 March 2003, approximately 11-14 days after TC Japhet.

Rainfall data are shown in Figure 8.19 for a couple of days when the TC Japhet peaked. Although even these figures may be impaired by errors, it was expected that rainfall might have some influence on the surface water conditions, i.e. a contribution to cooling by cold rain, and in areas of low wind speed creating thin surface layers of lower density. Evaluation of these more hypothetical possibilities was partly carried, however no results are discussed here.

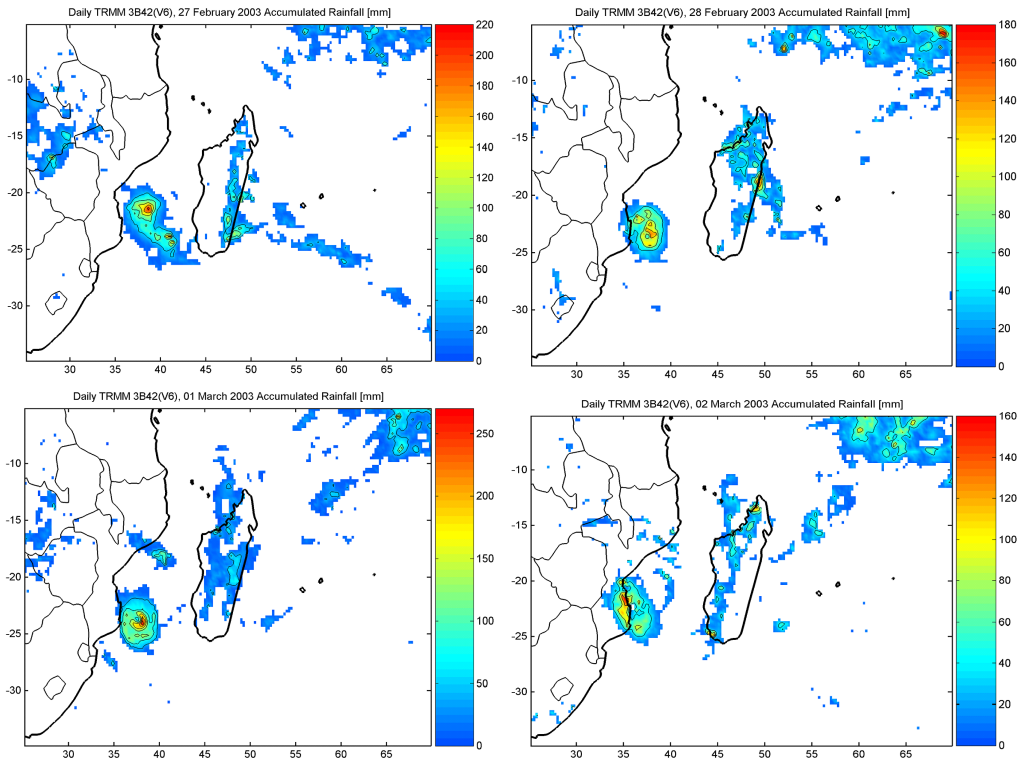

Figure 8.19: Daily rainfall during TC Japhet, 27-28 Feb and 1-2 March, respectively.

8.4 Tropical cyclone Gafilo

Tropical cyclone Gafilo, an extremely destructive Category 5 cyclone, began on March 01, 2004 when it originated as Tropical Disturbance approximately 550 km south of Diego Garcia with its central position located at 11.6°S, 72.2°E at 0600UTC (Figure 8.20). Estimated 1-min MSW was 20 kts (10 ms^{-1}). The system was moving west-southwest at 6 ms^{-1}. On 3 March 0000UTC the, tropical depression intensified to a tropical storm and was named TS Gafilo. In the same day, Gafilo was upgraded to TC (Category 1) at 1800UTC. The day after Gafilo translational speed slowed to 3.6 ms^{-1} turning towards west. Gafilo reached the ITC (Category 3, 50 ms^{-1}) by 1200UTC on 5 March. On 6 March 0600UTC the cyclone peaked at 72 ms^{-1} (Category 5). A very distinct eye <40 km in diameter, was revealed in SSM/I imagery during Gafilo's most intense stage (not shown). Gafilo made landfall near Antalaha, Madagascar on 7 March at 0000UTC, still as a Category 5. After passing across Madagascar into Mozambique Channel on 8 March, under decay, TC Gafilo maintained an intensity of 33 ms^{-1} and continued southwards (Figure 8.20). At approximately 0000UTC on 9 March, Gafilo went

southeast and made landfall a second time in Madagascar, after which a steady decay took place over land.

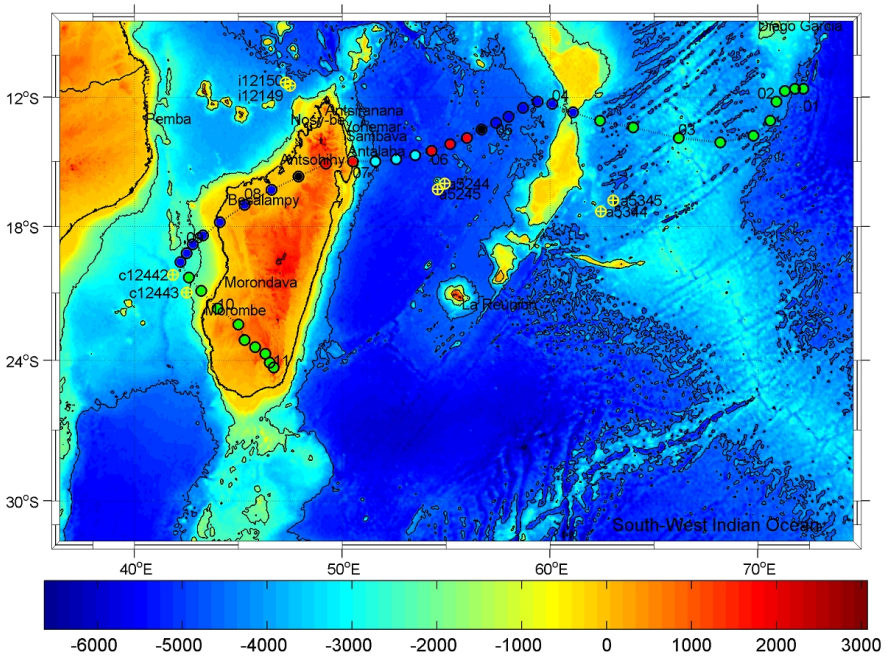

Figure 8.20: Track of TC Gafilo. Tropical cyclone centre positions every 6h are indicated by coloured circles (for legend, see Figure 8.20). Date beside cyclone centre indicates position at 0000 UTC that day. The positions of three ARGO floats are indicated by yellow crossed circles denoting for a=aomol; c=coriolis and i=incois.

Figure 8.21 shows the SSHA during the life cycle of TC Gafilo. Detailed track data are also shown in Table 8.5. TC Gafilo started rapid intensification when entering an area of positive SSHA 4 Mar 1200UTC to 6 Mar 0600UTC, during less than 2 days it changed from a TS to a TC Category 5. According to Figure 8.21 this intensification goes on while the cyclone is moving over large area of positive SSHA (WE-1). On the other hand, when the cyclone moves into the MC, it starts by entering over a large warm eddy (WE-2), without any intensification at all. After about 24 hrs, instead decay is seen, and TC Gafilo, it seems does not either point at any particular role of warm (or cold) eddies.

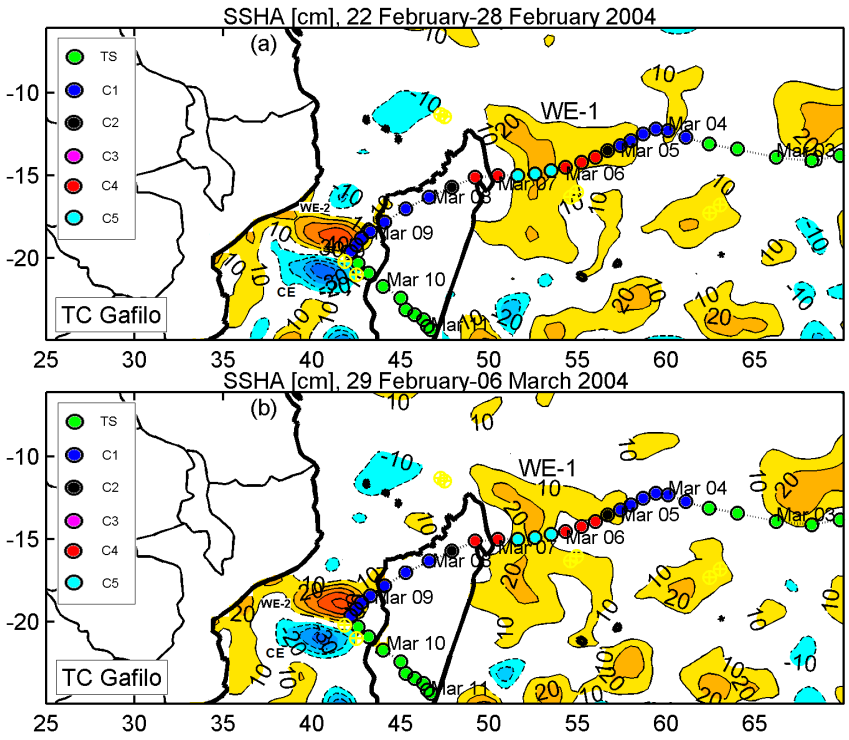

Figure 8.21: AVISO SSHA, deviations from MSL (cm) during the TC Gafilo event; (a) 22 - 28 February 2004 and (b) 29 -06 March 2004 obtained from merged altimeter data. Track of the cyclone with intensity according to the Saffir-Simpson Scale are indicated. Dates for the cyclone are shown near the cyclone track.

Table 8.5: Intensification period of Tropical cyclone Gafilo (1-min MSW)

Date	Latitude	Longitude	MSW(kts)	MSW (ms^{-1})	MSLP (hPa)	Categories
2004030318	-12.7	61.1	65	33.475	976	1
2004030400	-12.3	60.1	65	33.475	976	1
2004030406	-12.2	59.4	65	33.475	976	1
2004030412	-12.5	58.7	75	38.625	967	1
2004030418	-12.9	58	75	38.625	967	1
2004030500	-13.2	57.4	75	38.625	967	1
2004030506	-13.5	56.7	90	46.35	954	2
2004030512	-13.9	56	125	64.375	916	4
2004030518	-14.2	55.2	125	64.375	916	4
2004030600	-14.5	54.3	135	69.525	904	4
2004030606	-14.7	53.5	140	72.1	898	5
2004030612	-14.9	52.6	140	72.1	898	5
2004030618	-15	51.6	140	72.1	898	5

Sea surface temperatures before and after TC Gafilo are shown in Figure 8.22. This figure reveals, as it seems a very large impact of this cyclone on the SSTs. It is obvious that Gafilo exerted a more substantial effect on SST. In the wake of this cyclone, the

SSTs dropped by 3-4°C, and in a belt along with the track of 500-1000 km the drop was at least 1°C. Even on the MC side there is a decrease along the Madagascar coast, however small compared to the decrease on the eastern side. The strongest cooling is found on the southern side of the track. Comparing areas of high (and less high) SSHA with the cooling (ΔSST) it seems as if in this case the high SSHAs on the eastern have also resulted in somewhat lower drop in SSTs. The two eddies in the MC, however, seem not to have affected the SSTs.

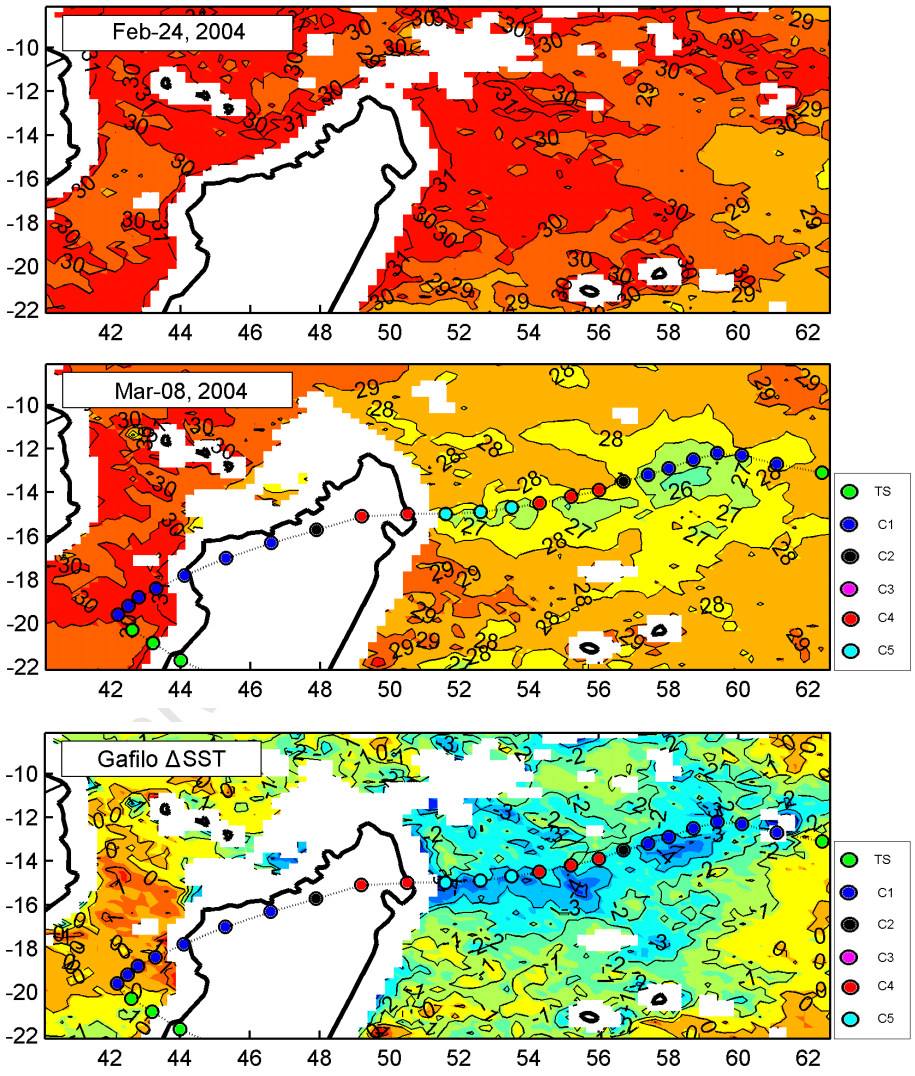

Figure 8.22: Sea surface temperature (TRMM/TMI) data along with cyclone Gafilo, showing SSTs before passage (24 February) and after passage (8 March) and the temperature difference, ΔSST between the occasions.

Conclusions concerning TC Gafilo is that it caused quite strong changes in temperature but also that the relationship between eddies and intensification can be established from this cyclone, either. However, Gafilo showed one of the most obvious along track sea surface cooling, indicating deep-going entrainment and upwelling.

8.5 Tropical cyclone Favio

Cyclone Favio formed on 11 February 2007, 400 km southwest of Diego Garcia (for position of DG, see Fig 8.19), with its central position located at 10.2°S, 70.6°E. Favio took a rare track (Figure 8.23), being the first cyclone, known to have moved westward south of Madagascar. When passing near the southern tip on 19 February, Favio entered the Mozambique Channel, under rapid intensifying from a TC Category 1 to a TC Category 4 (Table 8.6; Fig 8.23). It then took a fast track across the MC while decaying slowly before reaching the coast of Mozambique late on 22 February.

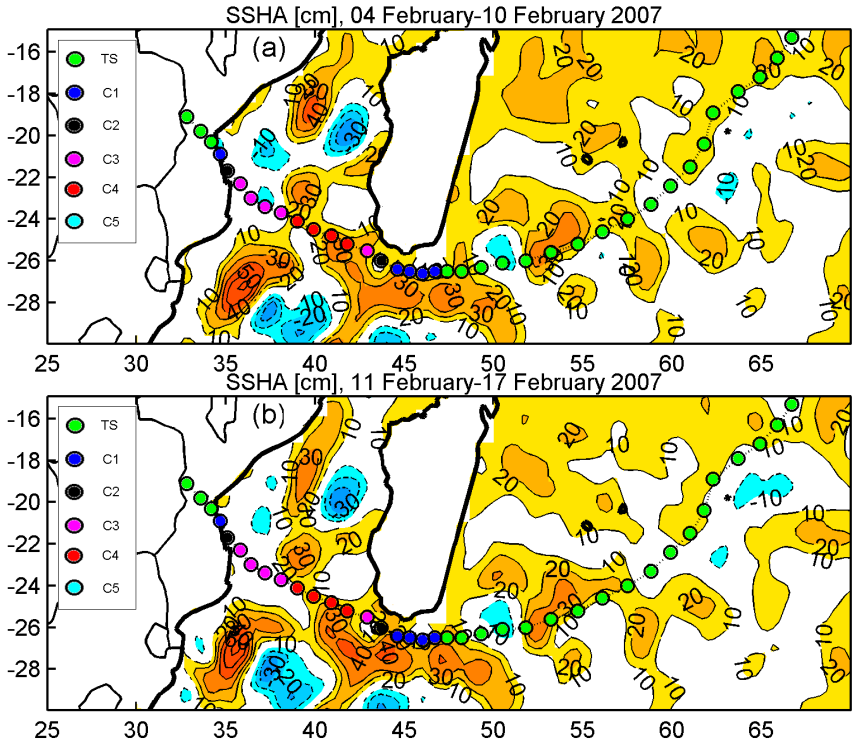

Figure 8.23: AVISO SSHA, deviations from MSL (cm) during the TC Favio event; (a) 04-10 February and (b) 11-17 February 2007 obtained from merged altimeter data. Track of the cyclone with intensity according to the Saffir-Simpson Scale are indicated. Dates for the cyclone are shown in Table 8.6.

Table 8.6: Intensification period of Tropical cyclone Favio (1-min MSW)

Date	Latitude	Longitude	MSW (knots)	MSW (ms^{-1})	MSLP (hPa)	Category
2007021900	-26.5	46.7	65	33	976	1
2007021906	-26.6	46	65	33	976	1
2007021912	-26.5	45.3	75	39	967	1
2007021918	-26.4	44.6	80	41	963	1
2007022000	-26	43.7	90	46	954	2
2007022006	-25.5	42.9	100	52	944	3
2007022012	-25.2	41.8	115	59	927	4
2007022018	-24.8	40.9	115	59	927	4
2007022100	-24.5	39.9	120	62	922	4

TC Favio is passing through waters known for a very high eddy activity (see Section 2.5) where the South East Madagascar Current takes on different direction, as a source current for the Agulhas but also for a South Indian Counter Current moving east at 25ºS. This is also readily seen from Figure 8.18. However, intensification (from TS) is not seen while Favio is crossing the first warm eddy east of Madagascar. Not until it reaches several eddies on the southern tip, rapid intensification takes place. This could possibly be due to the low temperatures east of Madagascar. As seen from Figure 8.23, showing SSTs before and after TC Favio, the temperatures along track of Favio never exceed 28ºC, while the conditions for cyclone formation (and presumably intensification) is restricted (the genesis/SST study in Section 7.6 showed one cyclone only, in data from 1998-05, which formed with SST below 28ºS).

Once entering the MC, the SSTs are higher, generally between 28-30ºC, thus more favourable for intensification. However, not even with this cyclone it is very obvious that intensification is a result of the warm eddies. While crossing the channel, TC Favio experiences both warm and cold eddies, and conclusions on their importance from these data seems difficult to extract.

TC Favio features a very clear wake of low temperatures in the vicinity of the track. Also the widening of the cooling area when landfalling is pronounced (similar to TC Japhet, i.e. Figure 8.14). Looking into sea surface cooling off the track is confusing; in the channel there is a decrease an also it is substantial, typically 1ºC. In the open ocean east of Madagascar, on the other hand, there are as much of increasing as there are

decreasing SSTs. South of the track, the increase in many areas are 1-2ºC, which is really surprising regarding that the Southern Ocean is approaching its winter.

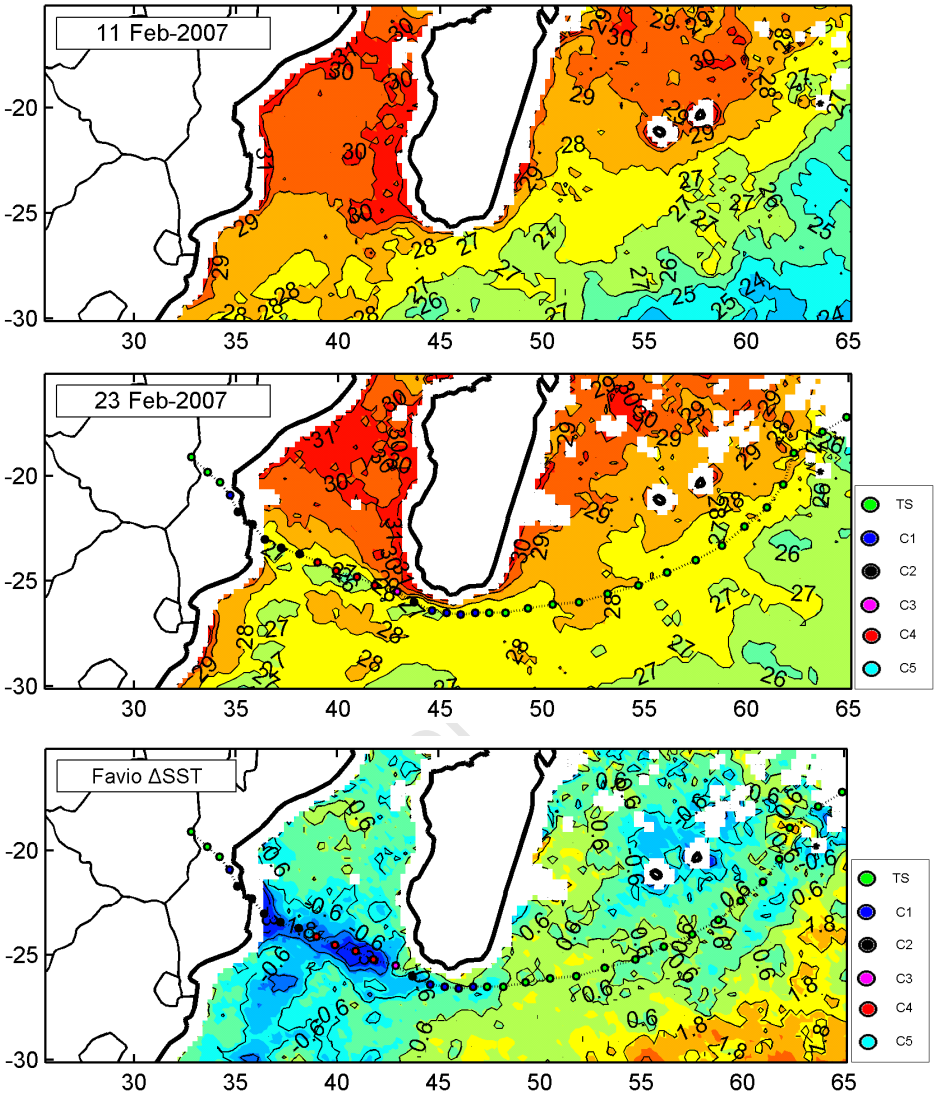

Figure 8.24. Sea surface temperature (TRMM/TMI) data along with cyclone Favio, showing SSTs before and after passage and the temperature difference, ΔSST between the occasions.

8.6 Summary of Chapter

In this chapter, the aim was to obtain an overview of the intense land-falling cyclones which have created much damage to people and infrastructure. Different from in many other TC regions, the control of cyclones in the SWIO is weak, and there is not much

information from meteorological stations, buoys or reconnaissance flights on actual winds, rainfall and ocean hydrography. Therefore, the work in this chapter aimed at seeing how useful the remote sensing data actually are. Analyses of sea surface height anomaly (SSHA) and sea surface temperature (SST) data during the development stages of 15 intense cyclones, with landfall in Mozambique or Madagascar are carried out. Bi-weekly high resolution merged AVISO satellite altimetry data (1/3° Mercator projection grid from Topography Experiment for Ocean Circulation, TOPEX/Poseidon, Jason-1 and European Remote-Sensing Environmental Satellites, ERS 1 and 2 Ducet et al., 2000) allowed for identification of oceanic features in the study area. Further analysis from merged satellite data reveals areas of high eddy activity. Some regions feature more anticyclone eddies (warm eddies; positive sea surface height anomalies), such as the central MC area, others more cyclonic eddies (cold eddies; negative sea surface height anomalies), such as east Madagascar region.

Variability in the MC and East of Madagascar with frequent movement of cold and warm eddies was studied by Schouten et al. (2003). Recent analyses have shown evidence that anticyclonic warm eddies may be linked to the intensification of TCs (Goñi and Triñanes, 2003). Although there is no doubt about the general importance of high values of TCHP in the region, an assessment of these 15 TCs carried out under this investigation did not show a clear tendency for intensification over warm eddies as intensification took place also over cold eddies, similar to what was found in the northwest Pacific Ocean (Lin et al., 2008). Improved knowlegde about the vertical density profile is needed to further understand the role of the ocean in TC intensification in this region.

For instance still, even using the latest information (as described thoroughly in Chapter 5) the observations are not good enough in general for deep going treatment of data. Sea surface height anomalies (SSHA) alone are hardly enough to judge on wheather intensification is likely to occur or not, and even the SSTs seem to have some restrictions, although these data are by far the best for understanding of cyclonic processes.

Analysis of satellite derived fields of SST from TRMM Microwave Imager (TMI) associated with the 15 TCs, indicate the occurrence of cold wakes, at different rates, related to TCs but also cold eddies and upwelling particularly in the shelf waters. Three-day average SST (0.25° X 0.25° spatial resolution) was the best choice to determine sea surface cooling since these data are less affected by extreme weather conditions. Although the TRMM/TMI sensor has all weather capabilities, in the case of daily SST fields cooling cannot be readily obtained during extreme weather because the presence of clouds have a blocking effect. Similarly other SST data sources (MODIS SST, AVHRR SST and OISST) rather than microwave observations were tested (not shown) and showed induced cooling but the SST measurements were frequently blocked by clouds during cyclone periods or simply were unable to detect the cooled surface. This indicates the crucial importance of cloud-free field of view of SST observations.

For one cyclone, TC Japhet, there was an Argo float passing right in the track of the cyclone. This single instrument, which gave 2-4 temperature records in the course of few weeks, has greatly improved the possibilities to interpret other data. Next chapter will deal in detail with the data shown in Section 8.3, and hopefully show that that the situation is still not hopeless. For cyclone Hudah (Section 8.2), there were ship data from just 1-2 days after the cyclone, with a temperature section right across the area where it passed, in the narrows of the Mozambique Channel. These data indicated strong sea surface cooling (3-4˚C) in a wake area of about 100 km width and also some but much less cooling in a much wider area, also highlighting the need for buoys and better coverage with professionally equipped meteorological stations, giving improved rainfall and wind data.

Chapter 9: Sea surface cooling, entrainment and upwelling in the wake of a cyclone. Tropical cyclone heat potential

To become established, a TC requires a Sea Surface Temperature (SST>26-27°C) and a certain, minimum heat content within the ocean surface water. Intensification takes place when enough latent heat is transferred from the ocean to the atmosphere. The amount of this latent heat flux depends both on the SST itself and the amount of heat available in the surface water. However, strong winds related to the TCs result in mixing of cold deep water into the surface waters and upwelling – creating sea surface cooling. These processes reduce the SSTs and the available amount of heat within the surface water. Decay or intensification is the result of the interaction between latent heat flux on one hand and vertical mixing/upwelling on the other. Therefore, both are key factor in predicting cyclone intensity.

9.1 Introduction

As described in Section 8.3, TC Japhet, appearing in the Mozambique Channel in late February 2003, had a short but intensive life-cycle. Increasing winds and TS development took place on 25-26 February, rapid intensification to a TC (category 4) on 28 Feb and then land-falling and decay on 2 March. In all, the cyclone had a life-time of 5 days, from 26 February – 2 March. During these days, there was access to three-day mean SSTs and daily mean wind data. There are also data on sea surface topography in terms of weekly mean SSHA from 19 and 26 February, and 5 and 12 March, respectively. The horizontal resolution (pixel size) is of the order of 30 km.

As discussed in Section 8.3, cooling in relation to TC Japhet was particularly interesting because of the presence of an Argo float which offered four profiles of salinity and temperature (12 and 22 February, 4 and 14 March, respectively) in the immediate vicinity of the track, and near to where the Maximum Sustained Wind (MSW) reached its maximum values. This set of data, including 6 hourly track data makes it possible to

carry out a detailed study of the processes contributing to sea surface cooling as described theoretically in Chapter 6.

In Chapter 6 it was indicated how the change in sea surface temperature in the wake of a cyclone, ΔSST is caused by a combination of upwelling (due to wind divergence - Ekman pumping) and entrainment (wind mixing due to erosion of thermocline waters). Both processes contribute to a net flux of heat out of the mixed layer, the thickness of which is simultaneously increasing (for most cases). If evaluated over several days, the net heat flux through the sea surface (basically loss of heat due to larger than normal latent heat fluxes) also decreases SSTs, although in the wake, as discussed in Section 3.4.1, cooling is to between 80-90% dominated by mixing and upwelling (earlier investigations, mainly on modelling of sea surface cooling and deepening of the mixed layer was also discussed in Section 3.4). However, away from the wake itself, latent heat flux will have relatively larger impact, as the wind becomes weaker and upwelling is taking place only in the vicinity (typically within 100 km) of the cyclone centre.

In Chapter 6, it was shown that the heat fluxes caused by each process can be calculated from data on wind stress and other parameters (Equations 6.1-4). It was also shown how to calculate changes in mixed layer depth, h_m allowing for combinations of upwelling and/or entrainment and/or heat loss to the atmosphere (i.e. Equation 6.6b). The results are strongly dependent on the original temperature profile, exemplified in Chapter 6 by using either a two layer case, with constant temperature in the upper and lower layer (Appendix D1) or a three layer case with a finite thermocline thickness and a linear change in temperature, as shown in Figure 6.1. The latter will allow for deeper penetration because the work needed by the wind to entrain to deeper levels is partly done (the same is true also for the upwelling part and for convection caused by loss of heat to the atmosphere as well).

Figure 6.1 illustrates the difference in cooling by entrainment and cooling by upwelling. Entrainment will affect SSTs and mixed layer temperatures whereas the integrated heat content within the volume of the mixed layer will remain unchanged. Upwelling will

contribute to additional cooling (Figure 6.1b), proportional to the thermocline temperature gradient and the upwelling velocity, w_E ("E" for Ekman). The combined effect is illustrated in Figure 6.1b. Below, the mixed layer depth (MLD), $h_m = h + h_{m0}$ is calculated by assuming, in case a) that cooling is exclusively caused by entrainment then in b) that the effect of net sea surface is added, both cases according to Equation 6.6b. Entrainment velocity, $w_e = dh/dt$, the change in heat content and the maximum heat flux are determined accordingly (Equations 6.7a-b).

9.2 MLD for cooling exclusively due to entrainment

Calculations were carried out using initial MLDs, $h_{m0} = 20 - 50m$, respectively and $\gamma = 1^o/10m$ (the thermocline temperature gradient) implying a temperature of about 15˚C at depths of 175 m (the initial SST, i.e. mixed layer temperature, determines the precise value). Different starting and end days (from 21-25 February to 3-18 March) were employed. To cover the five days when cyclone Japhet peaked, from 26 February – 2 March (see Section 8.3), the best coverage was obtained by using 21 February as starting date and 3 March as end date. It means that changes in MLD and heat were calculated over 10 full days.

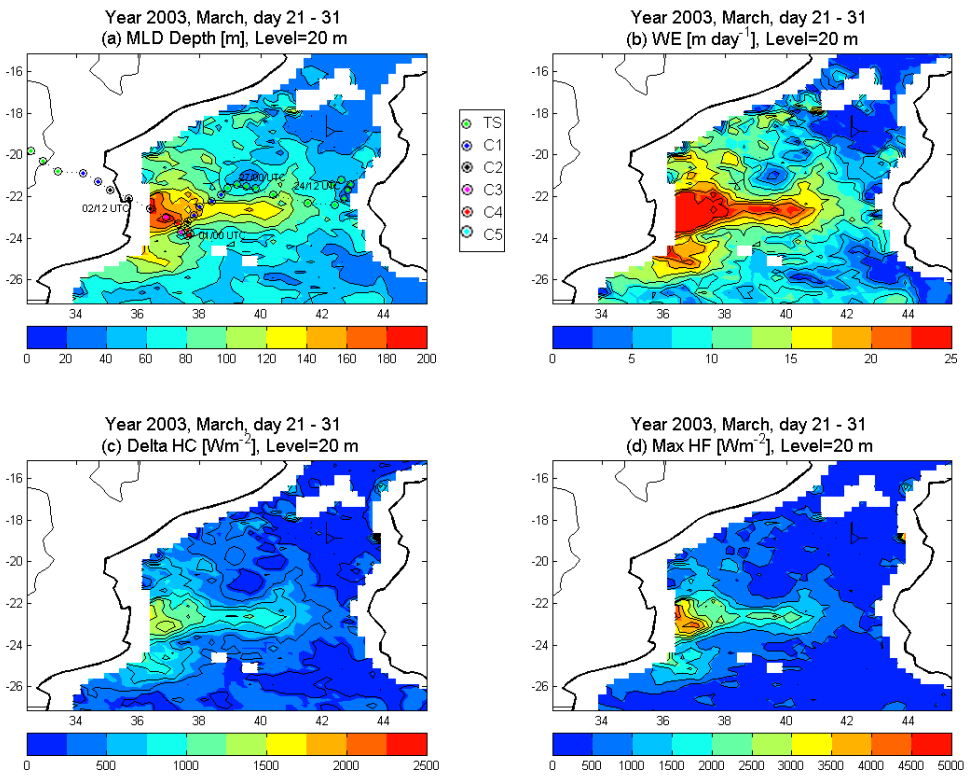

Figure 9.1A: MLD, entrainment velocity, upper 20 m heat loss (delta HC) and Maximum heat flux (Max HF) for h_{m0}=20m (assuming entrainment only).

However, it's assumed that all changes took place over five days only. Thus, entrainment velocities and heat change, as shown in Figure 9.1-3 are calculated per 5 days. Figures 9.1A-B are showing the results for two cases, where $h_{m0} = 20m$ and $30m$ respectively. On 21-25 February the SSTs were higher than 28˚C in most of the Mozambique Channel and large parts along the track of TC Japhet indicated SSTs>30˚C (Chapter 8.3). On 3-4 March, after the cyclone passed, in the core of the cooling area, the SSTs were 4-8˚C lower, indicating deep-going mixing (and upwelling) in that area. The MLDs, according to these calculations (assuming entrainment alone) are approaching 200 m, and the entrainment velocities accordingly reaching some 40 m/ day. The difference between 20 and 30m initial MLD is small, in fact, but MLD is larger in the case of 30 m initial MLD (and still more so if larger initial MLDs are chosen). Mixed layer depths of 200 m in the wake of the cyclone are not realistic. Even with a thinner MLD and a skin temperature (Chapter 5) which overestimates the initial SST. However,

even with those limitations, it's obvious that very large changes in SSTs are hand in the position where TC Japhet spent 24-36 hrs as a category 3-4 cyclone (23.3-23.9°S, 37.4-37.7°E), over water from at least 150 m must have reached the surface.

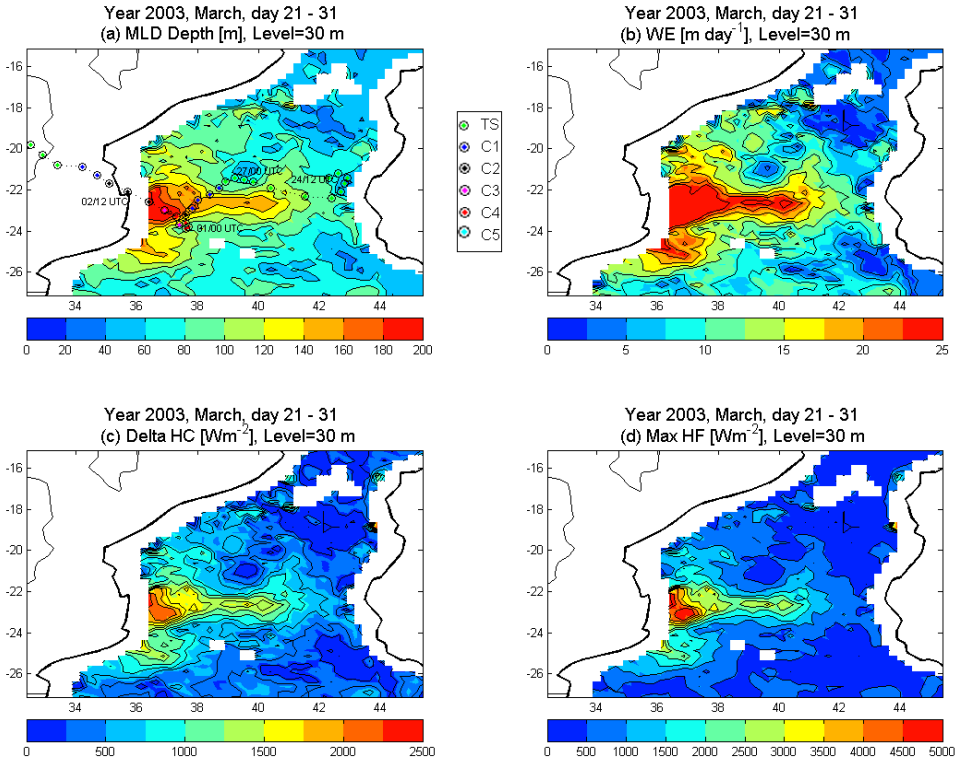

Figure 9.1B: MLD, entrainment velocity, upper 30 m heat loss (delta HC) and Maximum heat flux (Max HF) for h_{m0}=30m (assuming entrainment only).

Even in the rest of the wake, within 200 km, the entrainment velocities are more than 20 m/day. From the track it's obvious the maximum MLD appears south of the track for the first couple of days, but then on the northern eastern side during the last couple of days, but there is a warm core ring also on the south-western flank of the cyclone, which might have had limited cooling on the southern side of the track.

Outside the wake, cooling is typically 1-2˚C, and the corresponding entrainment velocities are also moderate, typically 10 m/day or less. It is interesting to note the none-existent change in MLD and entrainment velocity at 20.5°S, 39.5°E, which coincide obviously with the warm eddy at that position (Chapter 8.3).

Thus, in summary, it seems that TC Japhet gave a very strong response in terms of deep-going mixing, approaching the highest temperature reductions ever reported. This strong response however, as already indicated, may have been an effect of upwelling, which can be active only in a narrow band, where the wind divergence is strong (see Section 10.4). Also it could be due to passage over a cold core ring (not seen at the surface, but with a shallower thermocline with a sharper gradient). Strong latent heat flux in addition, will contribute to cooling as well, and thereby to an overestimate of the MLD. That will be taken into account in Section 9.3.

The lower panels of Figures 9.1a-b show two alternative ways of estimating the heat change within the surface waters. Lower left panels are showing the change within the original mixed layer, ΔH_{mix} i.e for h_{m0} = 20 and 30 m, respectively, whereas the right panels show the maximum heat flux $\Delta H_{\max}$ within the mixed layer, according to Equations 6.7a-b. As seen from the lower left panels, the losses indicated are maximum 1500-2000 Wm^{-2}, over 5 days, corresponding to 65-90 kJ cm^{-2} in the wake. However, maximum heat loss if integrated to larger depths than 30 m, are even larger as indicated in the lower right panels. These are approaching 5000 Wm^{-2}, which corresponds to about 200 kJ cm^{-2}. This is the integrated effect over five days, while in practice the time that the cyclone spent in each part of the area is rather 1 day, the true maximum heat flux might reach 25 kWm^{-2}. However, outside the wake area, the losses are much less, typically less than 1000 Wm^{-2}, although even these numbers are large compared to normal atmospheric and deep water heat exchange.

Of particular interest too, is that a two-layer approximation will produce much smaller entrainment depths. Approximating the MC stratification with a two-layer ocean, where the upper layer is 50 m and the lower layer has a temperature of 20˚C, would result in maximum MLDs of about 140 m only (Appendix D1). In summary, it is very unlikely that entrainment alone can explain the extreme sea surface cooling caused by TC Japhet.

9.3 MLD for entrainment cooling and heat loss to the atmosphere

In Equation 6.6b, a term for net heat loss to the atmosphere was also included, but in the estimates given above, that term was excluded. In Figure 9.2 is shown a solution for MLD, entrainment velocity and heat loss, where the net heat loss is assumed directly proportional to ΔT, such that the term $2\varepsilon/\gamma = \Delta T * 300$ (which means that for i.e. ΔT =6˚C, $Q_{NET} = -300 Wm^{-2}$).

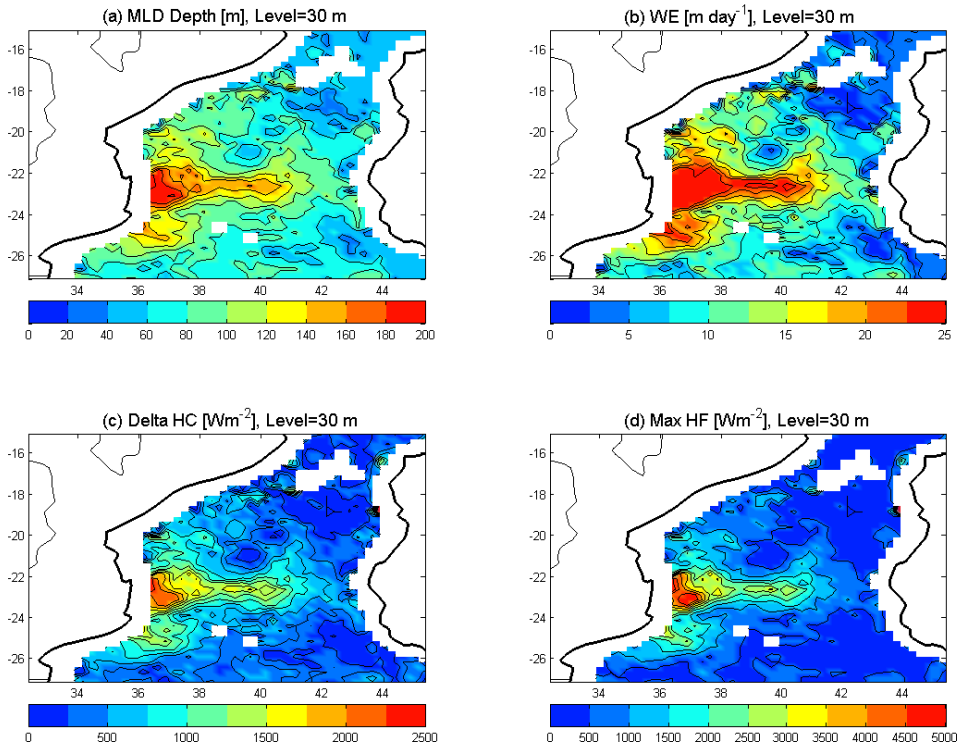

Figure 9.2: MLD, entrainment velocity, upper 30 m heat loss (delta HC) and Maximum heat flux (Max HF) for h_{m0}=30m. Assuming entrainment and a net sea surface heat flux.

As expected, areas with large entrainment depths will be considerably decreased. However, both entrainment velocities and heat fluxes are of the same order in the wake area. Outside the wake area, with entrainment velocities of more than 15 m/day, the heat loss is everywhere less than 1000 Wm^{-2}, but it's obvious that entrainment dominates over the net flux in an area of at least $0.5*10^6 km^2$. This because upwelling, as considered in the next section, is concentrated to the wake area.

9.4 MLD for cooling due entrainment, upwelling and heat loss to the atmosphere

As was discussed in Section 8.3, the relative importance of upwelling and entrainment in the vicinity of the cyclone track is not readily evaluated, unless very accurate wind data, ocean temperature and velocity profiles are available. Satellite winds are available along with TC Japhet (Section 8.3), but estimates are far lower than the true surface winds and the resolution in time and space are not enough. However, an Argo float happened to cross the track of TC Japhet, giving a record of temperature profiles before and after the passage. This opens for an alternative way to estimate upwelling velocities.

Figure 9.3 a-d shows the movement of the Argo float from 22 February to 14 March, and Figure 10.4 the temperature profiles for the dates 12 and 22 February, and 4 and 14 March. The cyclone track is also included. The first two profiles are from before the cyclone, featuring SSTs of 28-28.5˚C and MLD of 25 m. The thermocline gradient is > 0.1 ˚C /m in its upper part, but lowers (about 0.05) further down. The temperature according to the SST figures (Figure 9.5) is about 29˚C, thus slightly above the Argo data. As seen there is also a small gradient in the near surface water. Unfortunately, the salinity sensor was not working satisfactory (and the effect salinity variations on density could not be evaluated).

The next Argo profile shows data from 4 March, indicating a surface temperature of 26˚C and a mixed layer depth of about 65 m. The temperature fits exactly with the observed SST on the same day. In addition a massive uplift of the whole column underneath is seen. The uplift is most likely a direct result of upwelling due to wind divergence, the size of which is between 60-100 m in the whole column down to 1000 m. However, as seen from Figure 9.3 there is a rapid northward movement of the float. In 20 days, the northward movement is 230 km, or 13 cms^{-1} at a depth of 1000m, where the float was resting in between profiling.

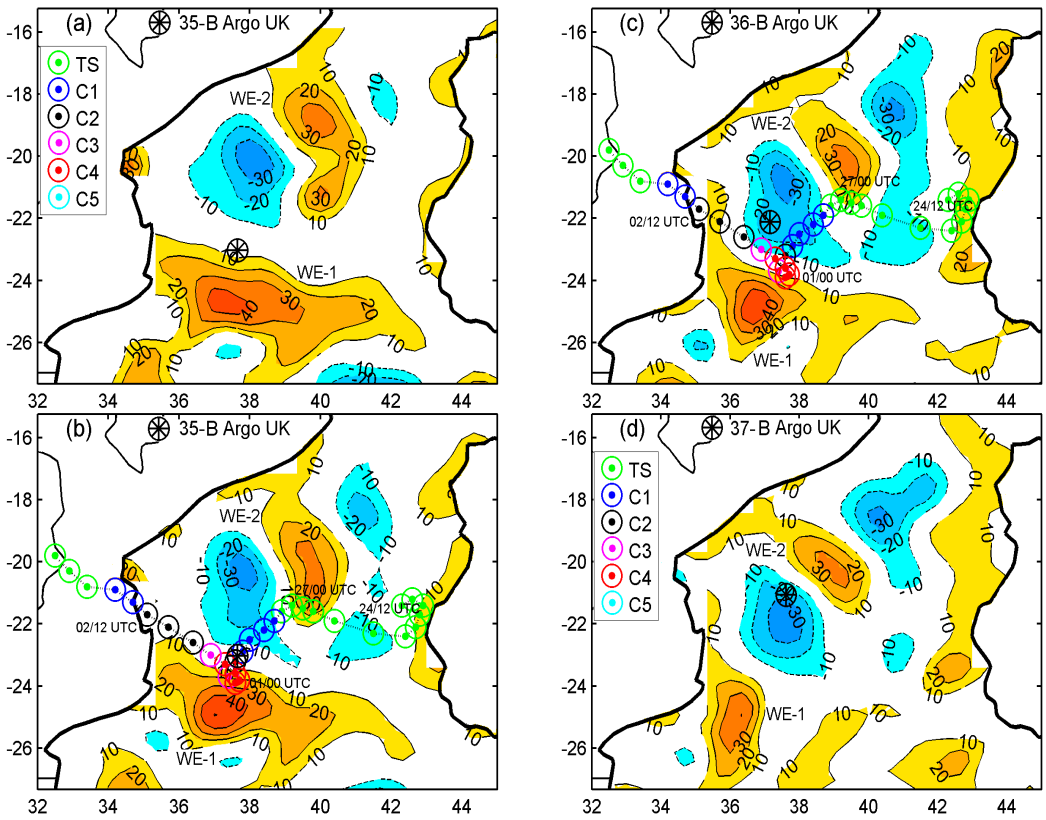

Figure 9.3: The position of the Argo float is shown on 22 February (35; 33.66E; 27.04S) on 4 March (36; 37.16E; 22.12S) and on 14 March (37; 37.50E; 21.10S), and mean SSHA for the periods (a) 16-22 February, (b) 23 February – 1 March, (c) 2–8 March, and (d) 9–15 March.

This motion may have had some impact on the profiles; while the float was in between a warm and a cold eddy on 22 February it entered a cold ring before the next profile and stayed within the ring up to 14 March. The latter two profiles were taken while the SSHA was about 0.2 m, which according to Section 6.3 would correspond to a thermocline 10 m higher up compared to the earlier dates.

This shows that the cold eddy does not explain more than a smaller part of the uplift, and thus that the mixed layer depth, as calculated from the SST change must be reduced by the rate of upwelling. At the position of the Argo float on 4 March, the calculated MLD was 150 m. At the same position, upwelling was in the range of 60-100 m, thus reducing the need for deep entrainment. Instead the situation is similar to that of Figure 6.1b. The case of TC Japhet is illustrated in Figure 9.5. In this case almost all the cold water is brought in from below.

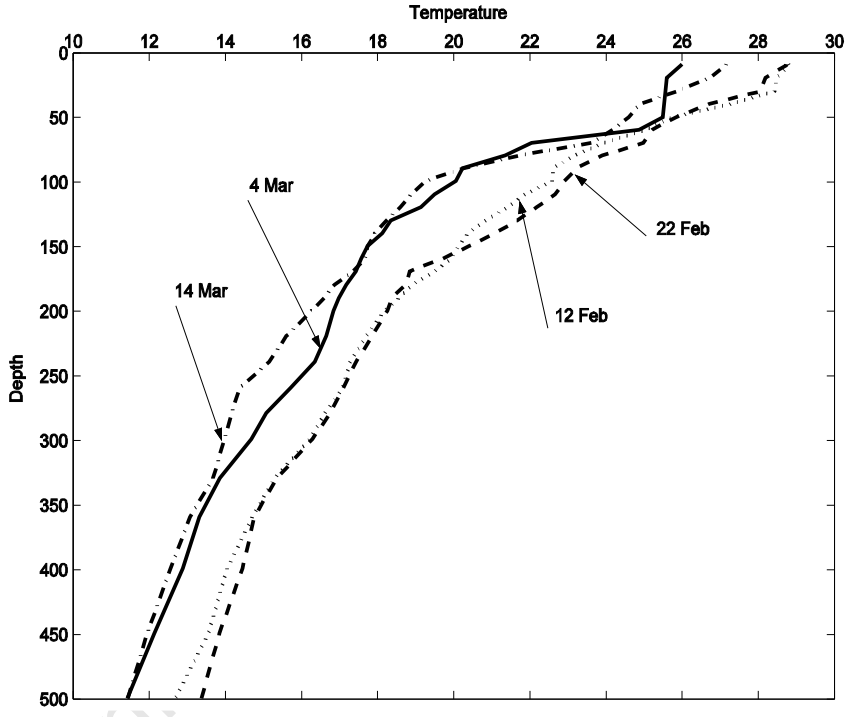

Figure 9.4: Temperature profiles from the Argo float travelling across the track of TC Japhet. Positions are shown in Figure 9.3.

For an average upwelling of 70 m and a temperature difference between the upwelled water that entrains into the surface water of $\Delta T = 3.5^{o}C$ the total cooling from below equals $\rho_w C_p \Delta T h_E \approx 100 kJcm^{-2}$ (or 2500 Wm^{-2}) evaluated over the 5 day period. Thus the Argo buoy data suggest that in the wake itself upwelling heat fluxes are of the same order as entrainment fluxes, possibly larger. Upwelling brings the thermocline towards the surface thereby facilitating entrainment because of small depths (see Equation 6.2). In this case, assuming that the mixed layer deepened from 30 to 65 m, the upwelling

velocity is $w_E \cong 15m/d$ and, then according to Equation 6.2, the entrainment velocity $w_e \approx 22m/d$. These results may be valid in the track area, representing an unusually strong event, where the cyclone spent at least 24, possibly 48 hrs staning more or less in the same position. Outside the track, it is expected that entrainment is the dominating process. However it is notable that the largest work along track is done by the divergence of the wind, which is lifting the interface towards the surface. This is well illustrated in Equation 6.4a.

It is notable that the last profile in Figure 9.4, from 14 March shows a very thin surface layer, partly stratified. It's an indication that the estimates of heat content (which are based on a 30 m mixed layer), will underestimate the recovery time. The temperatures seen in the surface are not reaching 30m, and the impact of the cyclone in terms of heat fluxes may become somewhat overestimated.

9.5 Heat recovery within the surface waters; heat loss from ML due to Tropical Cyclone Japhet

A specific temporal distribution of the consecutive mean days relative to the periods used in the analysis of three-day mean SST and Weekly SSHA following the evolution of TC Japhet is shown in the Table 9.

Table 9: Dates used for the MLD and CHP computations

MLD		CHP	
Mean Day (SST)	Centered dates	Mean Day (SSHA)	Centered dates
21	21 February, 2003	19	19 February, 2003
31	03 March, 2003	26	26 February, 2003
36	08 March, 2003	33	05 March, 2003
41	13 March, 2003	40	12 March, 2003
46	18 March, 2003	47	19 March, 2003

From the SSTs (Section 8.3), it is obvious that a couple of weeks after TC Japhet, the sea surface temperatures had returned to climatology values. Figure 7.14 shows that the mean SST in the southern half of MC (i.e. the area affected by TC Japhet) is 28 -

29˚C in mid-March, while in January and February, it averages about 29˚C. By mid March, 15 days after TC Japhet peaked, Figure 9.5 (right panels) shows SSTs identical with the climatology data. On the other hand, SSTs from before TC Japhet, on 21-22 February (Figure 9.5, left panels) were near 30˚C in the southern MC and 31 in its eastern part, thus corresponding to an excess surface water heat content of $\rho_w C_p \Delta T h_{m0} \cong 12.5 kJcm^{-2}$ (assuming an average MLD of 30 m and an excess temperature $\Delta T = 1^o C$). Some of this loss of heat may have entered the atmosphere as excess evaporative heat flux, but as mentioned several times, this is a small amount, on average not exceeding 1 kJcm^{-2}. Thus, the processes we face are an upward flux of cold water (may be compared to typical values of the meridional overturning circulation) and presumably, an increase of the mixed layer depth.

Figures 9.6A-B are showing alternative calculations for estimates of heat flux. Heat content within the upper 30 m (Figure 9.6A, based on Equation 6.7a) and maximum heat flux (Figure 9.6B, based on Equation 6.7b) have been extended up to where the SSTs may be considered as recovered. The change in heat content mirrors the change in SST, which is decreasing in the course of time.

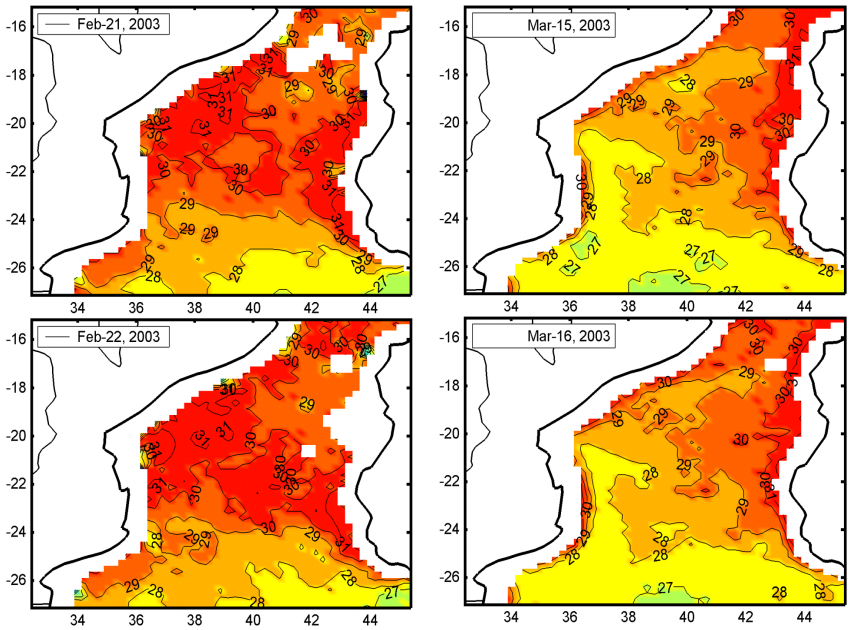

Figure 9.5: SST for two days before TC Japhet (21-22 February) and two days well after the passage (15-16 March). The latter figures mirrors the climatology mean.

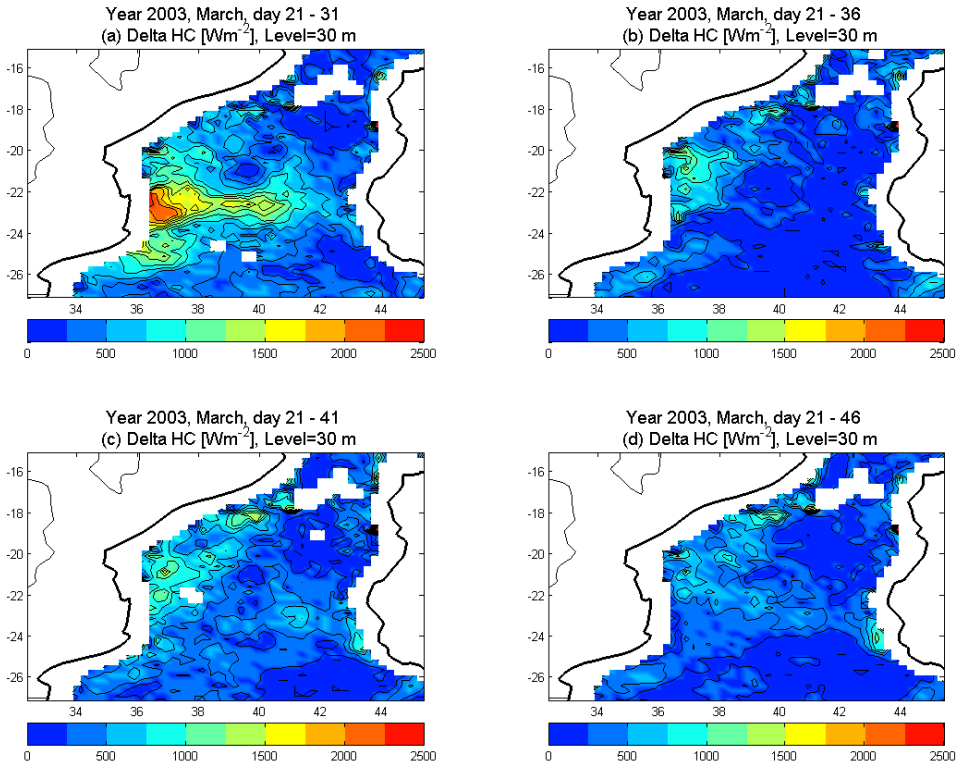

Figure 9.6A: Heat loss in comparison with heat content in the upper 30m on 21 February (day 21), from some different period lengths (to day 31 (3 March), day 36 (8 March), etc.).

Figure 9.6A-B both indicate that the effects of the cyclone on the SSTs are rapidly decreasing. In the area just north of where TC Japhet made landfall, there are some effects up to day 41 (13 March), whereas the wake area lost its signature already on 7 March (Figure 9.7), presumably due to a combination of advection of warm surface water across the wake, and more rapid heating in the wake, where low temperatures can result in surface water stratification and thin heated surface waters. This is seen also in Figure 9.4, where the temperature profile in surface water is almost linear on 14 March. Although a local estimate, only, the very shallow thermocline indicates that any calculation of heat content in the surface water (whatever method is chosen) is likely to overestimate its heat content.

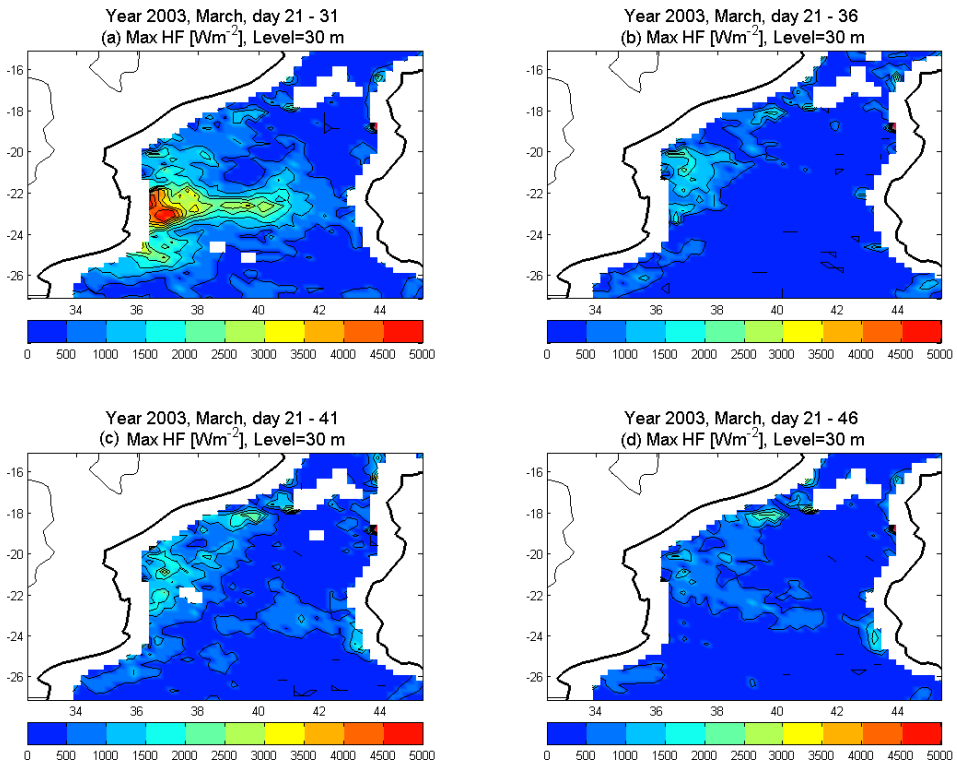

Figure 9.6B: Maximum net heat flux within the mixed layer for the periods, 21 February – 3 March (day 21-31), 21 February - 8 March (day 36), etc.

9.5 Tropical cyclone heat potential

The Tropical Cyclone Heat Potential, as aforementioned, has been used (Section 3.3.4) in order to evaluate the likelihood for cyclone generation and intensification. Basically it represents the heat content in mixed layers where the temperatures exceed 26˚C, i.e. the minimum temperature for tropical cyclone generation.

$$TCHP = \rho_w C_P \int_{z(T\geq 26)}^{0} (T - 26)\partial z$$

Early estimates of TCHP were based on buoy or cruise data, but more recently, satellite data (SSHA and SST) in combination with climatology data have been employed for this purpose. In Section 3.3.4 it was shown that large differences existed in the mean TCHP between different TC regions. While the NW Pacific TCHP averages 90 kJ cm^{-2}, average in the SWIO is only about 40 kJ cm^{-2} (during the cyclone season).

.

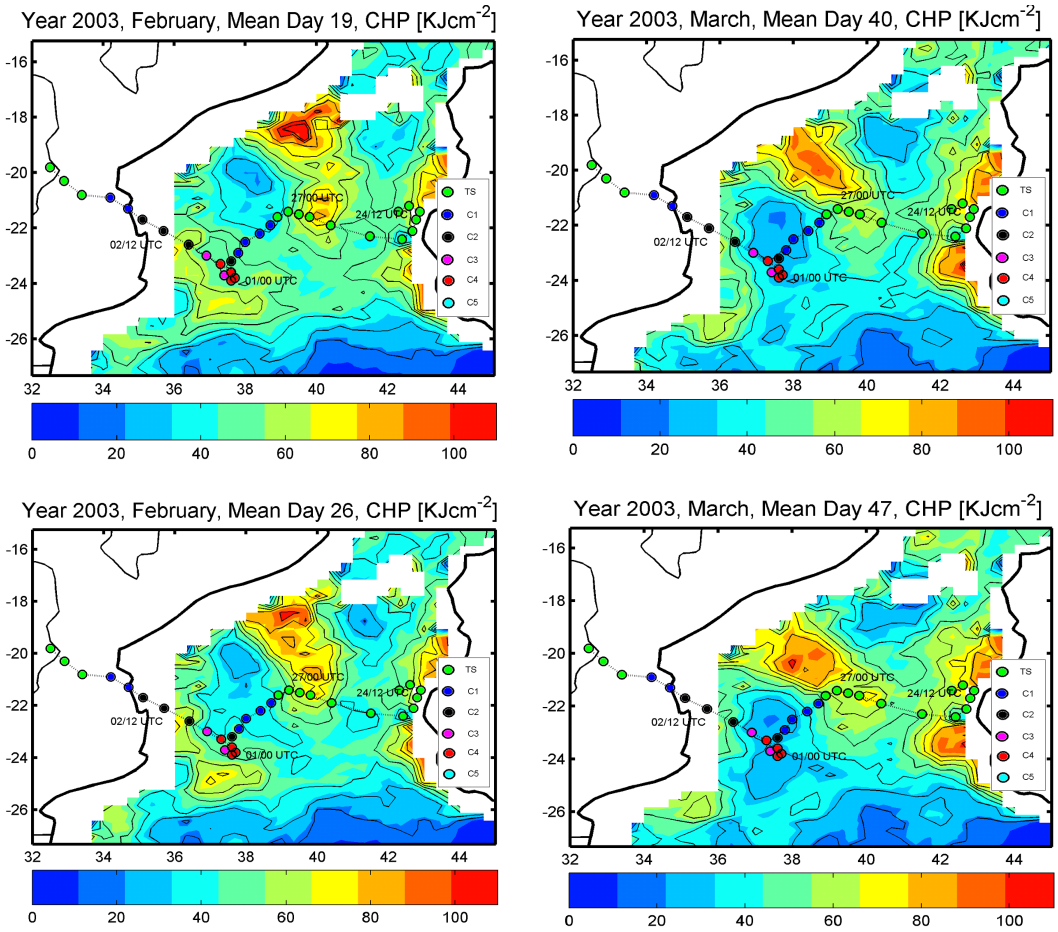

Figure 9.7: The tropical cyclone heat potential at four occasions, two before the TC Japhet, day 19 (19 February) and day 26 (26 February), and two after, day 40 (12 March) and day 47 (19 March).

Here, Equation 6.9 was used to calculate TCHP before and after TC Japhet. In Figure 9.7 results are shown for calculations where the last term in Equation 6.9 was omitted. This term represents the heat content below the mixed layer, and depends on the temperature gradient, $\gamma = dT / dz$. While, in the earlier calculations a mean gradient of 0.1˚Cm^{-1} was used, γ is larger in the upper end of the thermocline, and therefore this term is relatively small, particularly so during the cyclone passage and some time thereafter. Thus, the TCHP mirrors the sea surface temperature but also the existence of warm and cold eddies in the Mozambique Channel. According to Figure 9.3, there are two warm and two cold eddies in the channel. Their effects are readily seen in the plates showing the conditions before the cyclone passage (mean day 19, 19 February and mean

.

day 26, 26 February), although already for the latter, which represents data from 23 February to 1 March, there is a decrease in the TCHP. Before the cyclone, on day 19, most of the channel features TCHP levels >50 kJ cm^{-2}. In the two warm eddies TCHP is about 80 kJ cm^{-2}. A weak later, on day 26, the average TCHP has decreased by about 10 kJ cm^{-2}. There are no dramatic changes in this early cyclone stage, and looking at the results after the passage, on 12 and 19 March (mean day 40 and 47), the potential remains similar in most of the channel, although larger in the vicinity of the warm eddies and smaller with the cold eddies. The difference may reach 50 kJ cm^{-2}. As pointed out before the SSTs were about 1˚C higher than normal, which means an additional 10-15 kJ cm^{-2}.

Although the TCHP may be a good indicator for predicting the risk of cyclogenesis, it's obvious from the above, that the rather radical changes in thermocline features along with a cyclone passage (Figure 9.4) means that estimates of mixed layer heat contents may be questioned.

9.5 Summary of Chapter

The calculations of oceanic response caused by TC Japhet was based on the changes in SST as observed by twice daily SST data, which together with the model made it possible to estimate the flux of water from below needed to cool down the surface. By chance, there was an Argo float available in the area, and for that reason, the temperature profiles before and after TC Japhet could be used to estimate upwelling impact in relation to entrainment, in the wake of the cyclone. The upwelling velocity was $w_E \cong 15m/d$ and, then according to Equation 6.2, the entrainment velocity $w_e \approx 22m/d$, evaluated as mean values over a 5 day period. That is entrainment eroded 110 m, while upwelling lifted the column 75 m. The net velocity, then, is downward, throughout the period causing a deepening of the mixed of 35 m, from 30 m to 65 m. This efficient mixing goes on in the wake of the track, only. One might anticipate that strong upwelling is limited to an

.

area less than 100 km away from track. Outside, wind mixing is still efficient in large areas (up to 500 km away) as seen from the cooling caused by the cyclone. However, in these areas the entrainment velocities are much lower, typically $w_e \approx 1m/d$ (averaged as above, over 5 days).

A few weeks after the passage of the cyclone, which affected most of the southern part of the MC, the SSTs were back on the climatology level (Figure 9.5). This recovery was studied here by estimating change in heat content in the surface waters. Three different approaches used including calculations of the TCHP. None of them, however, is actually satisfactory, and the reason for that is that the SST alone is not a good indicator of mixed layer heat content after a cyclone passage. The thermocline features are greatly changed.

However, in the end of the day, cyclones have an impact on the SSTs which is more profound than what can be seen from the SSTs themselves. There is also an important mixing, probably of some global impact as well (advection and vertical transports = mixing). This was discussed in Section 7.11. The aim was to derive actually, some estimates of the net mixing caused by cyclones in the SWIO, but that will become an issue for the future.

The upper ocean heat content is estimated by a parameter, the tropical cyclone heat potential (TCHP), which can be indirectly computed from altimetry derived Sea surface Height anomaly fields. Evidence is presented that the genesis or intensification of cyclones in the region could be also linked to favourable environmental oceanic factors. Average TCHP in the SWIO is about 40 kJ cm^{-2} and the average background shear during the cyclone season is less than 12 ms^{-1}. There are common oceanic features present at the time of genesis (e.g Japhet) or intensification (e.g. Eline, Hudah, Japhet, Favio; see also Appendix C - Figure C1-C8) with high Tropical Cyclone Heat Potencial (upper ocean heat content) and sea surface temperatures (e.g. Appendix C - Figure C9-C16) in the Mozambique Channel (MC), belonging to Mozambique Channel eddies.

.

However, despite the low number of occurrence of TCs in this region, it is evident that during their relatively short sojourn over the MC the increase of wind intensity of these cyclones took place predominantely over the waters of warm eddies. The presence of these warm eddies thus established an additional energy source - apart from other atmospheric influences for cyclones that cross these features and may create an extra potential for cyclones over the Mozambique Channel. The TCHP taken for the duration of two of these cyclones (Eline and Hudah; not shown) and Japhet (shown) intensified particularly when their tracks went over the waters of warm eddies. The mean values of TCHP under the track of these cyclones while they travel through the MC were above the threshold value of 60 kJ cm^{-2}. This value`has been reported to be needed to sustain tropical cyclone winds (DeMaria et al., 2001) and also found to be linked to intensification in statistical models used in the tropical Atlantic (Mainelli et al., 2008). From the examples shown here, the correlation with wind speed increase appeared to be linked to TCHP and SST, meaning that the upper ocean heat content could be considered as a predictor for the risk of cyclogenesis and intensity changes.

.

Chapter 10: Conclusions with comments. Future work

Two merged cyclone track data records are used in this thesis, one covering the period from 1952-07, and one from 1980-07. The latter contains data on maximum sustainable wind (MSW) as estimated using the Dvorak technique, in turn based on weather satellites. Thereby, for the more recent data, it has been possible to study statistics in relation to intensity, according to the Saffir Simpson scale. Data prior to 1980 are mainly on tracks, but also include landfall information.

Statistics of cyclones was studied in Chapter 7 from a great many viewpoints, including i.e. global warming, El Niño phenomena, preferred tracks and landfall sites and cyclogenesis SSTs. In Chapter 8, a selection of Intense Tropical Cyclones (ITCs; Category 3-5) from the most recent period (1994-07) is done. The aim is to give examples, particularly from land-falling ITCs, on how far it is possible to reach in terms of understanding cyclone genesis and intensification, including sea surface cooling, using remote sensing data (for example whether it is possible to see relationships with the upper ocean heat content, roughly what is CHP or TCHP). Four ITCs are discussed in detail. Chapter 9 finally deals with sea surface cooling, entrainment and upwelling in the wake of TC Japhet, based on theory in Chapter 6. Also, some calculations of CHP/TCHP are performed. A common theme, throughout the thesis, is to make use of recent, high quality satellite data products, for SSTs, for SSHAs, for rainfall and other data.

The most important findings from Chapter 7 concern the long-term development of cyclone frequency which has some outstanding features. First, there is a distinct increase in the number of ITCs in the South-West Indian Ocean, from 36 to 56 between the periods 1980-93 and 1994-07. In the Mozambique Channel, the increase is from 2 to 7 (Tables 7.3-5). There is also a small increase in the total number of cyclones (TS+TC), from 138 to 155, and a somewhat larger increase in the number of TC days, from 60 to 72. The total number appearing

.

from 1980-07 is 303 (10 of which were excluded in the statistics presented in Chapter 7, because of missing track data). The total number corresponds to a frequency of 10.8 cyclones per season (November-April). About 1 cyclone per year appears outside the cyclone season. However, statistics for the period 1952-79 shows a larger number of cyclones, totally 330, thus indicating a long-term downward trend. This result is corroborated by a more distinct downward trend in the number of land-falling cyclones; 83 for the period 1952-79 and 59 from 1980-2007 (track data from the earlier period were not good enough to judge about intensity).

The increase in cyclone intensity during the most recent period (1994-07) is roughly simultaneous with an increase of the average SST, which in the SWIO is about 0.1˚C and in the MC about 0.2˚C compared to the earlier period (1980-93). This increase in SST is identified as a possible reason for the intensity increase, corroborated by similar results in other cyclone regions. However, the increase is so small that it has a marginal influence on the CHP/ TCHP. In fact, it is not enough to explain the large increase in ITCs. Thus it is proposed that the increase of more intense cyclones causes a deeper oceanic mixed layer, which counteracts more substantial increases of the SST. In other words, the cyclones exert a self-control on the tropical ocean SSTs, whereas a thin mixed layer is correlated with more but less intense cyclones and vice-versa (presuming that this conclusion is restricted to a particular region).This hypothesis needs further work to be proven (see below), particularly wind variations (affecting mixed layer depths/TCHP as well as the vertical shear) has to be employed more rigorously.

The employment of high resolution SST data (TRMM/TMI) made it possible to determine SST at the point of TC genesis. On average, the temperature for genesis was 29.2˚C for the SWIO and 29.7˚C for the MC. Very few cyclones (3%) were formed for SSTs below 28˚C and none below 27.5˚C. These comparatively high SSTs for genesis is proposed to be due to small mixed layer depths, typically 30-40 m. Therefore, also the average TCHP, about 40 kJ cm^{-2},

.

is low compared to most other cyclone regions. However, TMI data showed about 0.5˚C higher average formation temperature than indicated by climatology SST data (WOA05). Also here, it is necessary to do more detailed studies, where Argo floats can be of large help (see below)

Stratification of cyclones according to intensity shows that peak frequency for ITCs is in March while the peak for weak cyclones (Category 1-2) is in January. The peak for tropical storms is in February. This rather odd distribution is not readily explained from upper layer heat content, which maximise in February, and in fact contradicts that increasing number of ITCs should be the result of a warmer upper ocean. The number of ITCs is higher during La Niña years compared to El Niño years. Suppressed activity among ITCs may be attributed to a stronger vertical shear and reduced upper anticyclonic vorticity. Such conditions, which are typical for El Niño years may thus hinder TC development, or even hinder a cyclone from intensifying to an ITC.

Landfall of cyclones occurs in Madagascar and Mozambique. During 1980-2007, 15 cyclones made landfall in Mozambique, mainly in the central region, and 48 in Madagascar, mainly in the north east region. As aforementioned, there were more cyclones making landfall in the earlier period, from 1952-79, than in more recent years, but recent years have brought about more intense cyclones. A surprising and not understood phenomena is that among the relatively few cyclones that are formed within the MC (10% of total), most of them make landfall in Mozambique, those that are entering the channel across or north of Madagascar takes a more southern or south-easterly track.

Local prediction and follow up of cyclones in the SWIO region is weak. There is not much information from meteorological stations, buoys or reconnaissance flights. Therefore, one important goal of this thesis was to explore remote sensing data to see if that could improve our knowledge on local TC behavior. However, even the most recent satellite data are not alone good enough for deep

.

going analyses. Sea surface height anomalies and temperatures seem not enough to judge on whether genesis and intensification is likely to occur or not, nor is it, at the present level very useful for predicting intensification in relation to warm eddies. SST data also have restrictions, although these data are by far the best for understanding of cyclonic processes. This, as aforementioned is a subject for more future work.

For one cyclone (TC Japhet), there was an Argo float passing right under the track. The instrument, which gave four vertical temperature profiles in connection with the cyclone, greatly improved the possibilities to explore the SST and SSHA data, as well. For another cyclone, TC Hudah, there were ship data from just 1-2 days after the cyclone, with a temperature section right across the area where it passed, in the narrows of the Mozambique Channel. These data indicated strong sea surface cooling (3-4˚C) in a wake area of about 100 km width and also some, but much less cooling in a much wider area. Apparently, there is a need for buoys (for met and ocean data) and a denser net of meteorological stations, also giving improved rainfall and wind data, if progress shall be possible.

Calculations of oceanic response caused by TC Japhet (Chapter 9) were based on the changes in SST. Argo float temperature profiles in addition to SSHA and SST data made it possible to estimate upwelling in relation to entrainment, in the wake of the cyclone. The upwelling velocity related to this cyclone was $w_E \cong 15m/d$, the entrainment velocity $w_e \approx 22m/d$. The figures are mean values over a 5 day period. The difference, $7m/d$ is the velocity by which deepening of the mixed layer occurs, in this case from 30 m to 65 m. This efficient mixing takes place in the wake of the track, only. Strong upwelling is limited to an area less than 100 km from track (ship data from crossing the wake of TC Hudah, described in Chapter 8 indicated a total width of about 100 km for a similar intensity). Entrainment is still efficient up to 500 km away from the track. However, in these areas the entrainment velocities are much lower, typically

.

$w_e \approx 1m/d$. This was corroborated by profile data from some other Argo floats, recording at some 100-200 km distance from the track.

A few weeks after the passage of TC Japhet, SSTs were back on the climatology level. This recovery was studied here by estimating change in heat content in the surface waters. Different approaches were used including calculations of the CHP/TCHP. None was satisfactory; the reason is that the SST alone is not a good indicator of mixed layer heat content after a cyclone passage.

Tropical cyclones have an impact on the SSTs which is more profound than is seen from the SSTs themselves. There is also an important mixing, probably of some global impact as well. This was discussed in Chapter 7. The aim was to derive estimates of the net heat flux caused by cyclones in the SWIO, but that will become another issue for the future, although in fact all issues are parts of the same problem, the lack of ground truth data, particularly so in this region of the world.

Therefore, in the end it seems that the embryo to a data base (as indicated in the Appendices of this thesis) is now continuously improved. Real time maps of SSTs and SSHAs can be used, for example, in order to determine better based indications for cyclone intensification and decay. With parallel efforts to set a network of buoys and meteorological stations in place at least in the landfall region, future studies on tropical cyclones may be much more efficient. This is also needed to make more safe predictions in order to avoid disasters such as those caused by TC Eline in year 2000.

Last, a website can be established on the basis of the work of this thesis to monitor SST and SSHA in real time, including information from buoys and meteorological stations, in the Mozambique Channel and adjacent waters.

.

Chapter 11: References

Aiyyer, A. R. and Thorncroft, C. (2006). Climatology of vertical wind shear over the tropical Atlantic. *J. Climate,* **19**, 2969-2983.

Andersson, H. C. and Stigebrandt, A. (2005). Regulation of the Indonesian throughflow by baroclinic draining of the North Australian Basin. *Deep-Sea Res*. I, **52**, 2214-2233.

Anonymous (1984). The oceanological conditions in the western part of the Mozambique [sic] Channel in February-March 1980. Geodätische und geophysikalische Veröffentlichungen, IV, 163 811 pp.

Anonymous (2000). Cyclone Season 1999-2000. South-West Indian Ocean. Meteo France. BP 4–97491 SAINTE-CLOTILDE Cedex-France.

Anonymous (2006). Annual tropical cyclone report (2006). U.S. Naval Maritime Forecast Center/ JTWC Pearl Harbor, Hawaii.

Anthes, R. A. (1982). Tropical cyclones, their evolution, structure and effects. Met. Mon. 19, 41 *Amer. Meteorological Soc.* Boston, 208 pp.

Asnani. G. C. (1993). Tropical Meteorology. Volume I. *Noble Printers Pvt. Ltd*., Pune (India). 603pp.

Atkinson, G. D. and Holliday, C. R. (1977). Tropical cyclone minimum sea-level pressure and maximum sustained wind relationship for the western North Pacific. *Mon. Wea. Rev.*, **105**, 421-427.

Attema, E. P. W. (1991). The active microwave instrument on board the ERS-1 satellite. *Proc. IEEE*, **79**, 791-799.

AVISO project (Archiving, Validation, and Interpretation of Satellite Oceanographic) web page. (2003). www.aviso.oceanobs.com/, consulted in January, 2003.

Beckley, B. D., Lemoine, F. G., Luthcke, S. B., Ray, R. D. and Zelensky, N. P. (2007). A reassessment of global and regional mean sea level trends from TOPEX and Jason-1 altimetry based on revised reference frame and orbits. *Geophys. Res., Lett.,* **34**, L14608, doi: 10.1029/2007GLO30002.

.

Bender, M. A., Ginis, I. and Kurihara, Y. (1993). Numerical simulations of tropical cyclone-ocean interaction with a high resolution coupled climate model, *J. Geophys. Res*., **98**, 23245 - 23263.

Bentamy, A., Katsaros, K B., Alberto, M., Drennan, W. M., Forde, E. B. and Roquet, H. (2003). Satellite Estimates of wind speed and latent heat flux over the global oceans, *J. Climate,* **16**, 637-656.

Bentamy A., Quilfen, Y., Gohin, F., Grima, N., Lenaour, M. and Servain. J. (1996). Determination and validation of average wind fields from ERS-1 scatterometer measurements. *The Global Atmosphere and Ocean System*, Vol **4**, pp. 1-29

Bergeron, T. (1954). The problem of tropical hurricanes. *Quart. J. Roy. Meteor. Soc*., **80**, 131-164.

Bessafi, M. and Wheeler, M. C. (2006). Modulation of south Indian Ocean tropical cyclone by the Madden-Julian oscillation and convectively-coupled equatorial waves. *Mon. Wea. Rev*., **134**, 638-656

Biastoch, A. and Krauss, W. (1999). The role of mesoscale eddies in the source regions of the Agulhas Current. *J. Phys. Oceanogr*., **29**, 2303-2317.

Blender, R., Fraedrich, K. and Lunkeit, F. (1997). Identification of cyclone-track regimes in the North Atlantic. *Quart J. Royal Meteor. Soc*., **123**, 727–741.

Blumberg, A. and Mellor, G. (1983). Diagnostic and prognostic numerical circulation studies of the south Atlantic bight. *J. Geophys. Res.*, **88**, 4579-4592.

Boebel, O., Rossby, T., Lutjeharms, J. R. E., Zenk, W. and Barron, C. (2003). Path and variability of the Agulhas Return Current. *Deep-Sea Res*. II, **50**, pp. 35–56.

Bourassa, M. A., Freilich, L.M., Legler, D.M., Liu, W.T. and O'Brien J.J. (1997). Wind observations from new satellite and research vessels agree. *Eos Trans., AGU*, **78**, 597, 602.

Bourassa, M. A., Legler, D. M., O'Brien, J. J. and Smith, S. R. (2003). SeaWinds Validation with Research Vessels. *J. Geophys. Res.,* **108**, doi: 10.1029/2001JC001081.

Bove, M.C., Elsner, J.B., Landsea, C.W., Niu, X. and O'Brien, J.J. (1998). Effects of El Niño on U.S. Landfalling Hurricanes. Revisited. *Bull. Amer. Meteor. Soc*., **79**, 2477-2482.

.

Brown, C. W., Connor, L. N., Lillibridge, J. L., Nalli, N. R. and Legeckis, R. V. (2005). Introduction to Satellte Sensors, Observations and Techniques. R. L. Miller (eds). Remote Sensing of Coastal Aquatic Environment, 21-50. 2005 Springer.

Byrne D. A., Gordon, A. L. and Haxby, W. F. (1995). Agulhas eddies: a synoptic view using Geosat ERM data. *J.Phys. Oceanogr.,* **25**, 902–917.

Carton, J. A., Giese, B. S. and Grodsky, S. A. (2005). Sea level rise and the warming of the oceans in a simple Ocean Data Assimilation (SODA) ocean reanalysis. *J. Geophys. Res.*, **110.**

Camargo, S. J. and S. E. Zebiak, 2002: Improving the detection and tracking of tropical cyclones in atmospheric general circulation models. *Weather and Forecasting*, **17**(6): 1152-1162.

Camberlin, P. and Shanko, D. (1998). The effects of the Southwest Indian Ocean Tropical Cyclones on Ethiopian drought. Centre de Recherches de Climatologie, CNRS ESA 5080. Université de Bourgogne, BP 138. 21004 Dijon Cedex, France.

Cardillo G. (2007). MyRegression: a simple function on LS linear regression with many informative outputs (http://www.mathworks.com/matlabcentral/ fileexchange /15473).

Chambers, D. P., Tapley, B. D., Stewart, R. H. (1997). Long-period ocean heat storage rates and basin-scale heat fluxes from TOPEX. *J. Geophys. Res*., **102**, 10525-10533.

Chassaurd, A. and Laplace, L. (1964). Les Cyclones du Sud-Ouest de l'Ocean Indien, Memorial de la Meteorologie Nacional. Paris, no. **49**, 161 pp.

Chang, S. W. and Anthes, R. A. (1978). Numerical simulation of the ocean's nonlinear baroclinic response to translating hurricanes. *J. Phys. Oceanogr*., **8**, 468-480.

Chelton, D. B. (2001). Report of the high-resolution ocean topography science working group meeting. Reference 2001–4, College of Oceanic and Atmospheric Sciences, Oregon State University, Corvallis, Oregon, October 2001, 224 pp.

Chen, S. S., Knaff, J. A. and Marks, F. D. (2006). Effects of vertical wind shear and storm motion on tropical cyclone rainfall asymmetries deduced from TRMM. *Mon. Wea. Rev.*, **134**, 3190-3208.

.

Cheney, R. E., Marsh, J. G. and Becley, B. D. (1983). Global mesoscale variability from collinear tracks of SEASAT altimeter data. *J. Geophys. Res*., **88**, 4343-4354.

Chu, J. H., Sampson, C. R., Levine, A. S. and Fukada, E. (2002). The Joint Typhoon Warning Center Tropical Cyclone Best Tracks, 1945-2000. Naval Research Laboratory Reference Number NRL/MR/7540-02-16.

Chu, P. C., Veneziano, J. M., Fan, C. W. (2000b). Response of the South China Sea to Tropical Cyclone Ernie. *J. Geophys. Res.,* **105**, 13991-14009.

Chu, P.-S., and J. Wang. (1997). Tropical cyclone occurrences in the vicinity of Hawaii: Are the differences between El Niño and non-El Niño years significant? *J. Climate,* **10,** 2683-2689.

Crutcher, H. L. and Quayle, R. G. (1974). Mariners worldwide climatic guide to tropical storms at sea. Washington: Naval Weather Service, NAVAIR 50-1C-61, Asheville, NC.

Curry J. A., Webster, P. J. and Holland, G. J. (2006). Mixing politics and science in testing the hypothesis that greenhouse warming is causing a global increase in hurricane intensity. *Bull. Amer. Meteor. Soc*., **87**, 1025-1038.

Cutler, A. N. and Swallow, J.C. (1984). Surface currents of the Indian Ocean (to 25S, 100E). Compiled from historical data archieved by the Meteorological Office, Bracknell, UK. Wormley, UK, Institute of Oceanographic Sciences Report 187, 8pp. 36 & charts.

Da Silva, A. M., Young, C. C. and Levitus, S. (1994). Atlas of surface marine data 1994. Vol. 2, National Oceanic and Atmospheric Administration, 419 pp.

Daubechies, I. (1992). Ten lectures on wavelets. Society for industrial and applied Mathematics Press, vol 16 of CBMS-NSF Regional Conference Series in Applied Mathematics, Philadephia USA, pp 357.

Davidson, N. E. and Hendon, H. H. (1989). Downstream development in the Southern Hemisphere monsoon during FGGE/WMONEX. *Mon. Wea. Rev.,* **117**, 1458-70.

DeMaria, M. and Kaplan, J. (1994). A Statistical Hurricane Intensity Prediction Scheme (SHIPS) for the Atlantic Basin. *Wea. Forecasting,* **9,** 209-220.

DeMaria, M. (1996). A history of hurricane forecasting for the Atlantic basin. Contribution to Historical Essays on Meteorology, 1919-1995. The Diamond

.

Anniversary History Volume of the American Meteorological Society, ISBN 1-878220-17-9, 618 pp.

DeMaria, M., Knaff, J. A. and Connell, B. H. (2001). A tropical cyclone genesis parameter for the tropical Atlantic. *Wea. Forecasting,* **16**, 219–233.

De Ruijter, W.P.M., Ridderinkhof, H., Lutjeharms, J.R.E., Schouten, M.W. and Veth, C. (2002). Observations of the flow in the Mozambique Channel. *Geophys. Res. Lett*., **29**, 1401-1403.

De Ruijter, W. P. M., van Aken, H. M., Beier, E. J., Lutjeharms, J. R. E., Matano, R. P. and Schouten, M. W. (2003). Eddies and dipoles around South Madagascar: Formation, pathways and large-scale impact. *Deep Sea Res*., Part I, **51**, 383–400.

De Ruijter, W.P.M., Brummer G.-J.A., Drijfhout, S.S., Lutjeharms, J.R.E., Peeters, F., Ridderinkhof, H., van Aken, H. and van Leeuwen P.J. (2006). Observations of the inter-ocean exchange around South Africa. *Eos, Trans. Am. Geophys*. Un. 87, 97, 99, 101.

Dickey, T., Frye, D., McNeil, J., Manov, D., Nelson, N., Sigurdson, D., Jannasch, H., Siegel, D., Michaels, A. and Johnson, R. (1998). Upper-ocean temperature response to Hurricane Felix as measured by the Bermuda Testbed Mooring. *Mon. Wea. Rev*., **126**, 1195-1201.

DiMarco, S.F., Chapman, P., Nowlin, W.D., Hacker, P., Donohue, K., Luther, M.E., Johnson, G.C. and Toole, J.M. (2002). Volume transport and property distributions of the Mozambique Channel, *Deep-Sea Research* II **49**, 1481-1511.

Donlon, C.J., Minnett, P.J., Gentemann, C. Nightingale, T. J., Barton, I. J., Ward, B. and Murray, M. J. (2002). Toward Improved Validation of Satellite Sea Surface Skin temperature Measurements for Climate Research. *J. Climate*, **15**, 353-369.

Donelan, M.A. and Pierson W.J. (1987). Radar scattering and equilibrium ranges in wind-generated waves with application to scatterometry. *Geophys. Res., Lett.,* **28**, 575-578.

Donguy, J.R. and Piton, B. (1991). The Mozambique Channel revisited. *Oceanologica Acta,* **14** pp. 549–558.

Donque, G. (1975). Contribution Géographique a l'étude du Climat de Madagascar. N. Impr. Art. Graph, Antananarivo, Madagascar. 417 pp

.

Ducet, N., Le Traon, P.Y. and Reverdin, G. (2000). Global high-resolution mapping of ocean circulation from the combination of T/P and ERS-1/2. *J. Geophys. Res.*, **105**, 19477-19498.

Dunion, J. P. and Velden, C. S. (2004). The impacts of the Saharan Air Layer on Atlantic Cyclone Activity. *Bull. Amer. Meteor. Soc*., **85**, 353-365.

Dunn, P. (1985). An investigation into tropical cyclones in the Southwest Indian Ocean. Flood studies Tech. Note No1, 24. [Available from Dept. of Water affairs and Forest, Private Bag X313, Pretoria 0001, South Africa].

Dvorak, V.F., (1984). Tropical cyclone intensity analysis using satellite data. NOAA Tech. Rep. NESDIS 11, 47 pp.

Dvorak, V.F. (1975). Tropical cyclone intensity analysis and forecasting from satellite imagery. *Mon. Wea. Rev*. **103**, 420-430.

Ebuchi, N., Graber, H. C. and Caruso, M. J. (2002). Evaluation of wind vectors observed by QuikSCAT/SeaWinds using buoy data. *J.Atmos. Oceanic Tech.*, **19**, pp. 2049-2062.

Ecormier, J. (1992). Cyclone tropical du sud-ouest de l'Océan Indien: Le cas de l'Ile de la Réunion. Météo France, La Reunion. 479 pp.

Elsner, J. B. and Bossak, B. H. (2001). Bayesian analysis of U.S. hurricane climate. *J. Climate*, **14**, 4341-4350.

Elsner, J. B. and Jagger, T. H. (2004). A hierarchical Bayesian approach to seasonal hurricane modelling. *J. Climate*, **17**, 2813-2827.

Elsner, J. B. and Jagger, T. H. (2006). Prediction models for annual U.S hurricane counts. *J. Climate*, **19**, 2935-2952.

Emanuel, K. A. (1989). The finite-amplitude nature of tropical cyclogenesis. *J. Atmos. Sci*., **46**, 3431-3456.

Emanuel, K.A. (1999). Thermodynamic control of hurricane intensity. *Nature,* **401,** 665-669.

Emanuel, K. A. (2003). Tropical Cyclones. *Annu. Rev. Earth Planet. Sci.* 2003. 31:75–104. doi: 10.1146/annurev.earth.31.100901.141259.

Emanuel, K.A., 2005a: Increasing destructiveness of tropical cyclones over the past 30 years. Nature 436:686-688.

.

Emanuel, K. A. (2005b). Divine Wind: The History and Science of Hurricanes. *Oxford University Press. Inc*., New York, NY, 285 pp.

Emanuel, K. A. (2005). The dependence of hurricane intensity on climate. *Nature* **326**, 483-485.

Emery, W. J. and Thomson, R. E. (1998). Data and their analysis methods in physical oceanography. 1st and 2nd eds, Pergamon Press, Amsterdam, 634 pp.

Ffield, A. (2006). Amazon and Orinoco River Plumes and NBC Rings: Bystanders or Participants in Hurricane Events? *J. Climate* **20**, 316-333.

Fieux, M., & Stommel, H., 1977. Onset of the Southwest Monsoon over the Arabian Sea from marine reports of surface winds: structure and variability. *Mon. Wea. Rev.*, **105**, 231-236

Findlater, J. (1971). Mean monthly airflow at low levels over the western Indian Ocean. *Geophysical Memoirs*, **115**, 1-55.

Fink, H. A. and Speth, P. (1998). Tropical cyclones. *Naturwissenschaften* **85**, 482-493. Springer-Verlag 1998.

Frank, W. M. (1985). Tropical cyclone formation. In: Elsberry, R., Frank, W., Holland, G., Jarrel, J., Southern, R. (eds.) A global view of tropical cyclones. Office of Naval Research Marine Meteorology Program, Monterey, pp. 53-87.

Fratantoni D. M., Johns, W. E. and Townsend, T. L. (1995). Rings of the North Brazil Current: Their structure and behavior inferred from observations and a numerical simulation. *J. Geophys. Res*., **100**, 10633–10654.

Freilich, M. H. and Dunbar, S. (1999). The accuracy of NSCAT 1 vector winds: Comparison with National Data Buoy Center buoys. *J. Geophys. Res*., **104**, 11, 231-11,246.

Fu, L. L., and Cazenave, Ends. (2001). Satellite Altimetry and Earth Sciences: A Handbook of Techniques and Applications. Academic Press, 463 pp.

Fu, L.-L., Stammer, D., Leben, R.R. and Chelton, D.B. (2003). Improved Spatial Resolution of Ocean Surface Topography from the T/P-Jason-1 Altimeter Mission, *Eos, Trans. Am. Geophys Un.*, **84**, 241-248.

Fujita, T. T. (1971). Proposed Characterization of Tornadoes and Hurricanes by Area and Intensity. Satellite and Meteor. Res. Project. Department of the Geophy. Sci. The University of Chicago. 42 pp.

Gaffney, S. J. (2004). Probabilistic curve-aligned clustering and prediction with regression mixture models. Ph.D. thesis, University of California, Irvine, 281 pp.

.

[Available online at http://ftp.ics.uci.edu/pub/sgaffney/ outgoing/ sgaffney _thesis.pdf.].

Gaffney, S. J., Robertson, A. W., Smyth, P., Camargo, S. J. and Ghil, M. (2007). Probabilistic clustering of extratropical cyclones using regression mixture models. *Climate Dyn*., **29** (4), 423-440.

Geisler, J. E.: 1970, Linear theory of the response of a two-layer ocean to a moving hurricane. *Geophys. Fluid Dyn.* **1**, 249–272.

Gentemann, C. L., Wentz, F. J., Mears, C. A. and Smith, D. K. (2004). In situ validation of Tropical Rainfall Measuring Mission microwave sea surface temperatures. *J. Geophys. Res*., **109**, C04021.

Gibson, J. K., Kallberg, P., Uppala, S., Noumura, A., Hernandez, A. and Serrano, E. (1997). ERA Description. ECMWF Re-Analysis Project Report Series, 1. ECMWF, Reading, UK, 77 pp.

Gill, A. E. (1982). Atmosphere-Ocean Dynamics. *Academic press*, Inc. Vol. **30.**

Goldenberg, S. B., Landsea, C.W., Mestas-Nuñez, A.M. and Gray, W.M. (2001). The recent increase in Atlantic hurricane activity: Causes and implications. *Science,* **293,** 474-479

Goñi, G., Black, P. and Trinañes, J. (2003). Using satellite altimetry to identify regions of hurricane intensification des cyclones. *AVISO Newsletter* **8**.

Goni G. J., and Johns, W. E. (2001). A census of North Brazil Current Rings observed from T/P altimetry: 1992–1998. *Geophys. Res. Lett*., **28**, 1–4.

Goñi, G. and Trinañes, J. (2003). Ocean thermal structure monitoring could aid in the intensity forecast of tropical cyclones. EOS, vol. **84**, no. 51.

Gordon, A. L., Susanto, R. D. and Vranes, K. (2003). Cool Indonesian throughflow as a consequence of restricted surface layer flow. *Nature*, **425**(6960), 824-828.

Gray, W. M. (1968). Global view of origins of tropical disturbances and storms. *Mon. Wea. Rev*., **96**, 669-700

Gray, W. M. (1979). Hurricanes: Their formation, structure and likely role in the tropical circulation. *Meteorology over the Tropical Oceans*. D. B. Shaw Ed., *Roy. Meteor. Soc*., 155-218.

Gray, W. M. (1975). Tropical Cyclone Genesis. Department of Atmospheric Science. Paper No. 234 Colorado State University, Collins, CO, 121 pp.

.

Gray, W. M. (1984). Atlantic seasonal hurricane frequency. Part I: El Nino and 30 mb quasi-biennal oscillation influences. *Mon. Wea. Rev*., **112**. 1649-1668.

Gray, W. M., Neumann, C. and Tsui, T. L. (1991). Assessment of the role of aircraft reconnaissance on tropical cyclone analysis and forecasting. *Bull. Amer. Meteor. Soc*., **72**, 1867-1883.

Greatbatch, R. J. (1983). On the response of the ocean to a moving storm: The nonlinear dynamics. *J. Phys. Oceanogr.,* **13**. 357-367.

Greatbatch, R. J. (1984). On the response of the ocean to a moving storm: Parameters and scales. *J. Phys. Oceanogr*., **14**, 59-78.

Greatbatch, R. J. (1985). On the role played by upwelling of water in lowering sea surface temperature during passage of a storm. *J. Geophys. Res.,* **90**, 11751-11755

Gründlingh, M. L. (1984). An eddy over the northern Mozambique Ridge. *South African Journal of Science*, **80,** 324-329.

Gründlingh, M.L., Carter., R.A. and Stanton, R.C. (1991). Circulation and water properties of the southwest Indian Ocean, spring 1987. *Prog. Oceanogr.*, **28**, 305-342.

Gründlingh, M.L. (1995). Tracking eddies in the southeast Atlantic and South-West Indian Ocean with TOPEX/Poseidon. *J. Geophys. Res., **100**,* 24977-24986.

Guijarro, J., Auriol, A., Coste, M., Jayles, C. and Vicent, P. (2000). MWR and DORIS – supporting Envisat's radar altimetry mission. ESA *Bulletin*, **104**, online: http://esapub.esrin.esa.it/bulletin/bullet98.htm.

Guymer, T. H. (1983). A review of Seasat scatterometer data. *Phil. Trans. R. Soc. Lond*. A **309,** 399-414. Printed in Great Britain**.**

Harris, T. F.W. (1972). Sources of the Agulhas Current in spring of 1964. *Deep Sea Research* **19**, 633-650.

Hastenrath, S. (1985). Climate and Circulation of the Tropics. Doordrecht: D. Riedel, 455 pp.

Hellerman, S. and M, Rosenstein. (1993). Normal wind stress over the world ocean with error estimates. *J. Oceanogr.,* **13**, 1043-1104.

Henderson-Sellers, Zhang, H., Berz, G., Emanuel, K., Gray, W., Land Sea, C., Holland, G., Lighthill, J., Shieh, S.-L., and Webster, P. (1998). Tropical cyclones

.

and global climate change: A post IPCC assessment. *Bull. Amer. Meteorol. Soc.* **79**, 19-38.

Ho, C.-H., Kim, J.-H., Jeong, J.-H., Kim, H.-S. and Chen, C. (2006). Variation of tropical cyclone activity in the South Indian Ocean: El Niño–Southern Oscillation and Madden-Julian Oscillation effects. *J. Geophys*. *Res.*, **111**, D22101, doi: 10.1029/2006JD007289.

Hodges, K. I. (1994). A general method for tracking analysis and its applications to meteorological data. *Mon. Wea. Rev*., **122** (11), 2573–2586.

Hoffman, R. N. and Leidner, S. M. (2005). An introduction to the near-real-time QuikSCAT data. *Wea. Forecasting*, **20**, 476–493.

Hogan, T. F. and Rosmond, T. E. (1991). The description of the U.S. Navy Operational Global Atmospheric Prediction System's spectral forecast model. *Mon. Wea. Rev.,* **119**, 1786-1815.

Holland, G. J. (1981). On the quality of the Australian tropical cyclone data base. *Aust. Met. Mag*., **29**.

Holland G. J. and Lander, M. (1992). The meandering nature of tropical cyclone tracks. *J. Atmos. Sci*. **50**, 1254–1266.

Holland, G.J. (1993). "Ready Reckoner" - Chapter 9, Global Guide to Tropical Cyclone Forecasting. WMO/TC-No. 560, Report No. TCP-31, World.

Holland, G. J. and Merrill, R. T. (1984). On the dynamics of tropical cyclone structural changes. *Quart. J. Roy. Meteor. Soc* **110**: 723-745.

Holland, G. J. and Webster, P. J. (2007). Heightened tropical cyclone activity in the North Atlantic: natural variability or climate trend? Phil. *Trans. R. Soc*. A doi:10.1098/rsta.2007.2083.

Hsu, S. A. (1988). Coastal meteorology. Academic Press, San Diego.

Huang, N. E., Leitão, C. D. and Parra, C. G. (1978). Large scale Gulf study using Geos 3 radar altimeter data. *J. Geophy*. *Res*., **83**, 4673-4682.

Huffman, G., Adler, R., Morrissey, M., Curtis, S., Joyce, R., McGavock B. and Susskind. (2001): Global precipitation at one-degree daily resolution from multi-satellite observations. *J. Hydrometeor.*, **2**, 36-50.

Huffman, G. J., Adler R. F., Bolvin, D. T., Gu, G., Nelkin, E. R., Bowman, K. P., Hong, Y., Stocker, E. F. and Wolff, D. B. (2007). The TRMM Multi-satellite

.

Precipitation Analysis (TMPA): Quasi-Global, Multi-Year, Combined-Sensor Precipitation Estimates at Fine Scales. *J. Hydrometeo*. **8**, 38-55.

Imberger, J., Patterson, J. C. and Wiebe, W. J. (1979). Tropical cyclones: Nature's ploughs on the northwest shelf of Australia. Paper presented at International Conference on Tropical Cyclones, Perth, Australia, Royal Meteorological Society (Australian Branch) and American Meteorological Society.

IPCC[1]**.** (2001). The Scientific basis, Projections of Future Climate Change: An Assessment of Vulnerability. Special Report of IPCC Working Group II [Watson, R.T., M.C. Zinyowera, and R.H. Moss (eds.)]. Intergovernmental Panel on Climate Change, Cambridge University Press, Cambridge, United Kingdom and New York, USA, Ch 9.

Jiang, H., Halverson, J. B., Simpson, J. and Zipser, E. J. (2008). Hurricane "rainfall potential" derived from satellite observations aids overland rainfall prediction. *J. Appl. Meteor., **47**, 1310-1330.*

Johannessen J. A., Janssen, P., Minster, J. F., Robison, I. S., Rothrock, D. and Vachon, P.W. (1998). Preface to ERS Special Section. *J. Geophys. Res*., **103**, 7753

Jones, S., Harr, P.A., Abraham, J., Bosart, L.F., Bowyer, P.J., Evans, J.L., Hanley, D.E., Hanstrum, B.N., Hart, R.E., Lalaurette, F., Sinclair, M.R., Smith, R.K. and Thorncroft, C. (2003). The extratropical transition of tropical cyclones: Forecast challenges, current understanding and future directions. *Wea. Forecasting*, **18**, 1052-1092.

Josey, S. A., Kent, E. C. and Taylor, P. K. (1999). The insights into the ocean heat budget closure problem from analysis of the SOC air-sea flux climatology. *J. Climate*, **12**, 2856-2880.

Jury, M. R. and Pathack, B. (1991). A study of climate and weather variability over the tropical SW Indian Ocean. *Meteorol. Atmos. Phys*., **47**, 37-48.

Jury, M. R. (1993). A Preliminar Study of Climatological Associations and Characteristics of Tropical Cyclones in the SW Indian Ocean. *Meteorol. Atmos. Phys.*, **51**, 101-115.

Jury, M. R., Pathack, B. and Parker, B. (1999). Climatic determinants and statistical predictions of tropical cyclone days in the southwest Indian. Ocean. *J. Climate*, **12**, 1738-1746.

JTWC webpage. (2006). http://metocph.nmci.navy.mil/jtwc/best_tracks/shindex.html, consulted in May 2003.

.

Kalnay, E., Kanamistsu, M., Kistler, R., Collins, W., Deaven, D., Gandin, L., Iredell, M., Saha, S., White, G., Woolen, J., Zhu, Y., Leetmaa, A., Reynolds, B., Chelliah, M., Ebisuzaki, W., Higgins, W., Janowiak, J., Mo, K. C., Ropelewski, C., Wang, Jenne, R. and Joseph. D. (1996). The NCEP/NCAR 40-year reanalysis. *Bull. Am. Meteorol. Soc.* ***77***, 437-471.

Kanamitsu, M., Ebisuzaki, W., Woolen, J., Potter, J. and Fiorion, M. (2000). An overview of NCEP/DOE Reanalysis-2. Proc. Conf. 2nd Intl. Conf. on Reanalyses, Reading, England, 23-27 August 1999.

Karoly, D. J. and Vincent, D. G. (1998). Meteorology of Southern Hemisphere. 27(49). Am. Meteorol. Soc. Boston. 410 pp

Kato, H. and Phillips, O. M. (1969). On the penetration of a turbulent layer into stratified fluid. *J. Fluid Mech.,* **37**, pp 643–655.

Katsaros, K. B., Paris, W. V., Liu, W. T. and Black, P. G. (2002). Microwave Remote Sensing of Tropical Cyclones from Space. *J. Oceanogr.,* **58,** 137 to 151.

Kidder, S. Q. and Von der Haar, T. H. (1995). Satellite Meteorology. Academic press, London

Kidder, S. Q., Goldeberg, M. D., Zehr, R. M., De Grody, M. and Kusselson, S. J. (2000). Satellite analysis of tropical cyclones using the Advanced Microwave Sounding Unit (AMSU). *Bull. Amer. Meteor. Soc*., **81**, 1241-1259.

Kidder, S. Q., Knaff, J. A. and Kusselson, S. J. (2001). AMS Symposium on Precipitation Extremes. *Predictions, impacts, and response. P3.17.*

Kilpatrick, K. A., Podesta, G. P. and Evans, R. H. (2001). Overview of the NOAA/ NASA pathfinder algorithm for sea surface temperature and associated matchup database. *J. Geophys. Res.* **106**, pp. 9179–9198.

Kimball, S. K., and Mulekar, M. S. (2004). A 15-year climatology of North Atlantic tropical cyclones. Part I: Size parameters. *J. Climate*, **17**, 3555-3575.

Klinman, M. G. and Reason, C. J. C. (2008). On the peculiar storm track of TC Favio during the 2006-2007 South West Indian Ocean tropical cyclone season and relationship to ENSO. *Meteorol. Atmos. Phys.* 000, 1-10. DOI 10.1007/s00703-008-0306-7.

Klotzbach, P. J. (2006). Trends in global tropical cyclone activity over the past twenty years (1986-2005). *Geophys. Res. Lett.,* **33**, L10 805. (doi.1029/2006GL025881).

.

Knapp, K. R. and Kossin, J. P. (2007). New global tropical cyclone data set from ISCCP B1 geostationary satellite data. *J. Appl. Rem. Sens*, 1, 013505.

Kraus, E. B. and Turner, J. S. (1967). A one-dimensional model of the seasonal thermocline, II. The general theory and its consequences. *Tellus* **19,** 98-106.

Krayer, W. R. and Marshall, R. D. (1992). Gust factors applied to hurricane winds. *Bull. Amer. Met. Soc*. **73**, 613-617.

Kuleshov, Y. and de Hoedt, G. (2003). Tropical cyclone activity in the Southern Hemisphere. *Bull. Austr. Meteorol. Soc*., **16**, 135-137.

Kuleshov, Y., Qi, L., Fawcett, R. and Jones, D. (2008). On tropical cyclone activity in the Southern Hemisphere: Trends and the ENSO connection, *Geophys. Res. Lett*., **35**, L14S08, doi:10.1029/2007GL032983.

Kummerow, C., Barnes, W., Kozu, T., Shiue, J. and Simpson, J. (1998). The Tropical Rainfall Measuring Mission (TRMM) Sensor Package. *J. Atmos*. *and Ocean Tech*., **15**, 808-816.

Landman, W. A., Seth, A. and Camargo, S. J. (2005). The effect of regional climate model domain choice on the simulation of tropical cyclone-like vortices in the south-western Indian Ocean. *J. Climate* **18**, 1263-1274.

Landsea, C.W. (2000). Climate variability of tropical cyclones: Past, Present, and Future. In Storms, R.A. Pielke, Sr., and R.A. Pielke, Jr., Eds., Routledge, 220-241.

Landsea, C. W. (2007). Counting Atlantic tropical cyclones back to 1900. EOS **88**, 197–208.

Landsea, C. W., Harper, B. A., Hoarau, K. and Knaff, J. A. (2006). Can we detect trends in extreme tropical cyclones? *Science*, **313**, 452-454.

Landsea, C. W., Nicholls, N., Gray, W. M. and Avila, L. A. (1996). Downward trends in frequency of intense Atlantic hurricanes during the past five decades. Geophys. Res. Lett., **23**, 1697-1700.

Landsea, C. W., Pielke, Jr. R. A., Mestas-Nuñez, A. M. And Knaff, J .A. (1999). Atlantic basin hurricanes. Indices of climatic changes. *Climate Change*, **42**, 89-129.

Le Borne, J. (1987). Climatologie du sud-ouest de l'Océan Indien, Tome 1: Le cas de l'Ile Maurice. Collection travaux et documents Nº 204, ORSTOM, France. 356 pp.

.

Le Traon, P. Y., Faugère, Y., Hernandez, F., Dorandeu, J., Mertz, F. and Ablain, M. (2003). Can we Merge GEOSAT Follow-On with TOPEX/Poseidon and ERS-2 for an Improved Description of the Ocean Circulation? *J. Atmos. Oc. Tech*. Vol. **20,** pp. 889-895.

Legeckis, R. (1978). A survey of world-wide sea surface temperature fronts detected by environmental satellites, *J. Geophys. Res.,* 83, 4501-4522.

Leipper, D. F. and Volgenau, D. (1972). Hurricane heat potential of the Gulf of Mexico. *J. Phys. Oceanogr.,* **2**, 218-224.

Levitus, S. (1982). Climatological Atlas of the world ocean, NOAA Professional Paper 13. 173 pp., U.S. Govt. Print. Off., Washington, D.C.

Levitus, S., J. Antonov, and T. Boyer (2005), Warming of the world ocean, 1955–2003. *Geophys. Res. Lett.,* **32**, L02604, doi:10.1029/2004GL021592.

Lin, I. I., Wu, C. C. and Pun, I.-F. (2008). Upper ocean thermal structure and the Western North Pacific category 5 typhoons, part I: ocean features and Category-5 typhoons intensification. Mon.Wea. Rev., in press.

Lin, I.-I., Wu, C.-C., Emanuel, K.A., Lee, I.H., Wu, C. R. and Pun, I.-F. (2005). The interaction of supertyphoon Maemi (2003) with a warm ocean eddy. *Mon. Wea. Rev.,* **133**, 2635–2649.

Lin, I.-I., Liu, W. T., Wu, C.-C., Chiang, J. C. H. and Sui, C.-H. (2003). Satellite observations of modulation of surface winds by typhoon-induced upper ocean cooling. *Geophys. Res. Lett.*, **30**, 1131-1134.

Liu, W.T., Tang, W. and Polito, P. S. (1998). NASA scatterometer provides global ocean surface wind fields with more structures than numerical weather prediction. *Geophys. Res. Lett.*, **25**, 761-764.

Liu, W. T. (2002). Progress in scatterometer application. *J. Oceanogr*., **58**, 121–136.

Liu, Z., Xu, J., Zhu, B., Sun, C. and Zhang, L. (2006). The upper ocean response to tropical cyclones in the northwestern Pacific analyzed with Argo data. Chinese *J. Oceanol. Limnol.*, **25**, 23-131. DOI:10.1007/s00343-007-0123-8

LR-RMSC web page. (2003). www.meteo.fr/temps/domtom/La_Reunion/, consulted in January 2003).

Lutjeharms J. R. E. (1981). Features of the southern Agulhas Current circulation from satellite remote sensing. *S. Afr. J. Sci.* **77**, 231-236.

.

Lutjeharms, J. R. E. (1988). On the role of the East Madagascar Current as a source of the Agulhas Current. *S. Afr. J. Sci.* **84**, 236–238.

Lutjeharms, J. R. E. and Jorge da Silva, A. (1988). The Delagoa Bight eddy. *Deep-Sea Research*, **35,** 619-634.

Lutjeharms, J. R. E. Wedepohl, P. M. and Meeuwis, J. M. (2000). On the surface drift of the East Madagascar and Mozambique Currents. *S. Afr. J. Sci*. **96**, 141-147.

Lutjeharms, J. R. E. and Ansorge, I. J. (2001). The Agulhas Return Current. *J. Marine Sys.*, **30**, 115–138.

Lutjeharms, J. R. E. (2006a). The Agulhas Current. Springer-Verlag, Berlin, 329 pp.

Lutjeharms, J. R. E. (2006b). The ocean environment off the southeastern Africa: a review. *S. Afr. J. Sci*., **102**, 419-426.

Madden, R. A. and Julian, P. R. (1994). Observations of the 40-50 day tropical oscillation – A review. *Mon. Wea. Rev*., **122**, 814-837.

Mainelli, M., DeMaria, M., Shay, L. and Goni, G. (2008). Application of Oceanic Heat Content Estimation to Operational Forecasting of Recent Atlantic Category 5 Hurricanes, *Weather and Forecasting* (in press).

Mao, Q., Chang, S. W. and Pfeffer, R. L. (2000). Influence of large-scale initial oceanic mixed layer depth on tropical cyclones. *Mon. Wea.Rev*., **128**, 4058-4070.

Martin, A. K. (1981). Evolution of the Agulhas Current and its palaeo-ecological implications. *S. Afr. J. Sci*. **77,** 547-554.

Martin, J.D. (1988). Tropical cyclone observation and forecasting with and without aircraft reconnaissance. Dept. of Atmos. Sci. Paper 428, Colorado State University, Fort Collins, CO. 114 pp.

Martin, J.D. and Gray, W.M. (1993). Tropical cyclone observation and forecasting with and without aircraft reconnaissance. *Wea. Forecasting*, **8**, pp.519-532

Matsuura, T. and Yumoto, M. Iizuka, S. (2003). A mechanism of interdecadal variability of tropical cyclone activity over the western North Pacific. *Climate Dyn.,* **21**: 105-117.

McBride, J. L. and Keenan, T. D. (1982). Climatology of tropical cyclone genesis in the Australian region. *J. of Climatol.,* **2**, 13-33.

.

McBride J. L. (1995). Tropical cyclone formation. Global perspectives on tropical cyclones. *WMO Tech. Doc. WMO/TD-No*. **693**, 63–105.

McBride, J. and Coauthors. (2006). Statement on tropical cyclones and climate change. WMO/CAS Tropical Meteorology Research Program, Steering Committee for Project TC-2: Scientific Assessment of Climate Change Effects on Tropical Cyclones. [Available online at www.bom.gov.au/info/CAS-statement.pdf].

Mélice, J. L., Coron, A. and Berger, A. (2001). Amplitude and frequency modulations of the Earth's obliquity for the last million years. *J. Climate*, **14** (6), 1043-1054.

Ménard, Y., Escudier, P., Fu, L.-L. and Kunstmann, G. (2000). Cruising the Ocean from Space with Jason-1. EOS: Trans. Am. Geophys. Union, 81 (34), pp.381, 390–391.

Merril, R. T. (1984). A comparison of large and small tropical cyclones. *Mon. Wea. Rev*., **112**, 1408-1418.

Michaels, P. J., Knappenberger, P. C. and Davis, R. E. (2006). Sea surface temperatures and tropical cyclones in the Atlantic basin, *Geophys. Res. Lett.*, **33**, L09708, doi:10:10.1029/2006GLO2525757.

Miller, L. and B.C. Douglas. (2006). On the rate and causes of twentieth century sea level rise. *Phil. Trans. R. Soc. A,* **364**, 805-820.

Monaldo, F. M., Sikora, T. D., Babin, S. M. and Sterner, R. E. (1997). Satellite imagery of sea surface temperature cooling in the wake of Hurricane Edouard (1996). *Mon. Wea. Rev*., **125,** 2,716-2,721.

Monin, A. S. and Obkhov, A. M. (1954). Basic laws of turbulent mixing in the ground layer of the atmosphere. *Trudy Geofizecheskogo Instituta, Akademiya Nauk* SSSR **24**, pp. 163-187.

Morey, S. L., Bourassa, M. A., Dukhovskoy, D. S. and O'Brien, J. J. (2006). Modelling 56 studies of the upper ocean response to a tropical cyclone. Ocean Dynamics. doi:10.1007/s10236-006-0085-y.

Morlet, J. (1983). Sampling theory and wave propagation. Issue in Acoustic Signal/Image Processing and Recognition, C. H. Chen, Ed., NATO ASI Series, Vol. **1**, Springer, 233-261.

Mostovoy, G. V., Fitzpatrick, P. J. and Li, Y. (2005). Regional accuracy of QuikSCAT gridded winds. International Journal of Remote Sensing. Vol. 26, No. 18, 20 September 2005, 4117-4136.

.

Murray, R. J., and Simmonds, I. (1991). A numerical scheme for tracking cyclone centres from digital data Part I: development and operation of the scheme. *Aus. Meteo. Mag*., **39**, 155–166.

Naeraa, M. and Jury, M. R. (1997). Tropical cyclone composite structure and impacts over eastern Madagascar during January-March 1994. *Meteorol. Atmos. Phys*. **65**, 43-54

Nassor, A. and Jury, M. R. (1997). Intra-seasonal climate variability over Madagascar, part 1: Mean summer conditions. *Meteorol. Atmos. Phys.* **65**, 31.

Nazrul Islam, Md., Uyeda, H. (2006). Use of TRMM in determining the climatic characteristics of rainfall over Bangladesh. *Rem. Sens. Env*., **108**, pp.264–276.

New, A. L., Alderson, S.G., Smeed, D. A. and Stansfiel, K. L. (2007). On the circulation of water masses across the Mascarenhe Plateau in the South Indian Ocean. *Deep-Sea Research* I **54,** 42-47.

Nehring, D., Hagen, E., Jorge da Silva, A., Schemainda, R., Wolf, G., Mihelsen, N., Kaiser, W., Postel, L., Gosselck, F., Brenning, U., Kuhner, E., Arlt, G., Siegel, H., Gohs, L. and Bublitz G. (1987). Results of oceanological studies in the Mozambique Channel in February-March 1980. *Beiträge zur Meereskunde*, *Berlin*, **56**: 51-63.

Neumann, C. J. (1993). Global Overview, Chapter1 of Global Guide to Tropical Cyclone Forecasting. Edited by G. J. Holland WMO/TC-No. 560, Report No TCP-31, World Meteorological Organization, Geneva.

Nicholson, S. E. and Kim, J. (1997). The relationship of the El Niño–Southern Oscillation to African rainfall. *Int. J. Climatol*., **17**, 117–135.

Nilsson, J. (1996). Mixing in the ocean produced by tropical cyclones. *Tellus* A, **48**, 342-355 (14). doi: 10.1034/j.1600-0870.1996.t01-1-00010.x.

NIOZ ftp server. (2003). http://ftp.nioz.nl (consulted in January 2003).

Oberhuber, J. M. (1988). "An atlas based on `COADS' data set," Tech. Rep. 15, Max-Planck-Instutut für Meteorologie.

Ogallo, L. J. (1988). Relationship between seasonal rainfall in East Africa and Southern Oscillation. *Int. J. Climatol*, **8**, 31–43.

Olander, T.L. and Velden, C. (2007). The Advanced Dvorak Technique (ADT) - Continued Development of an Objective Scheme to Estimate TC Intensity Using Geostationary IR Satellite Imagery. *Wea. Forecasting*, **22**, 287-298.

.

Palastanga, V., van Leeuwen, P. J., Schouten, M. W. and de Ruijter, W. P. M. (2006). Flow structure and variability in the subtropical Indian Ocean: Instability of the South Indian Ocean Countercurrent. *J. Geophys*. *Res., doi*: 10.1029/2005JC003395, in press.

Palmén, E. (1948). On the formation and structure of tropical hurricanes. *Geophysica*, **3**, 26-38.

Payda, B. M. (1989). Weather and Climate of Mauritius. Mauritius: M. Gandhi Inst., 283 pp.

Penven, P., Lutjeharms, J. R. E. and Florenchie, P. (2006). Madagascar: A pacemaker for the Agulhas Current system? *Geophysical Research Letters*, **33**, L17609, doi: 10.1029/2006GL026854 pp. 1-5.

Pielke, R. A. Jr. (2005). Are there trends in hurricane destruction? *Nature, **438**. E11.*

Pielke, R. A. Jr. and Landsea, C. W. (1999). La Niña, El Niño, and Atlantic Hurricane Damages in the United States. *Bull. Amer. Met. Soc*., **80**, 10, 2027-2033.

Price, J. F. (1981). Upper ocean response to a hurricane. *J. Phys. Oceanogr*., **11**, 153-175.

Price, J. F. (1983). Internal wave wake of a moving storm. Part I: Scales, energy budget and observations. *J. Phys. Oceanogr*., **13**, 949-965.

Quartly, G. and Chen G. (2006). Introduction to Special issue on "Satellite altimetry: New sensors and new applications". *Sensors*, **6**, 616-619. *ISSN* 1424-8220.

Quilfen Y., Chapron, B., Elfouhaily, T., Katsaros, K. and J. Tournadre, (1998). Observation of tropical cyclones by high-resolution scatterometry. *J. Geophys. Res*., **103**, 7767–7786.

Ramage, C. S. (1984). Climate of the Indian Ocean north of 35°S. In Climates of the Oceans. Editor H. van Loon, World Survey of Climatology, *Volume* **15**, *Elsevier, Amsterdam*, *pp*. 693-697.

Rayner, N. A., Parker, D. E., Horton, E. B., Folland, C. K., Alexander, L. V., Rowell, D. P., Kent, E. C. and Kaplan, A. (2003). Global analyses of sea surface temperature, sea ice, and night marine air temperature since the late nineteenth century. *J. Geophys. Res*., **108**, 4407, doi:10.1029/2002JDOO2670.

.

Ridderinkhof, H. & de Ruijter, W. P. M. (2003). Moored current observations in the Mozambique Channel. *Deep-Sea Res.,* II, **50**, 1933-1955.

Ritchie, E.A., Simpson J., Liu, W.T., Halverson, J., Velden, C., Brueske, K.F. and Pierce H. (2003). In: Hurricanes! Coping with disaster, R.

Romero-Vadillo, E., Zaytsev, O. And Morales-Pérez, R. (2007). Tropical cyclone statistics in the Northeastern Pacific. *Atmosfera,* **20**, 197-213.

Reason, C. J. C. and Keibel, A. (2004). Tropical Cyclone Eline and its unusual penetration and impacts over the southern Africa mainland. *Weather and Forecasting*, **19,** 789-805.

Resti, A., Benveniste, J., Roca, M., Levrini, G., and Johannessen, J. (1999). The Envisat Radar Altimeter System (RA-2). ESA *Bulletin*, **98**, online: http://esapub.esrin.esa.it/bulletin/bullet98.htm.

Reynolds, R. W. and Smith, T. M. (1994). Improved global sea surface temperature analyses using optimum interpolation. *J. Climate*, **7**, 929-948.

Reynolds, R. W., Rayner, N. A., Smith, T. M., Stokes, D. C. and Wang, W. (2002). An improved in situ and satellite SST analysis for climate. *J. Climate* **15**: 1609-1625.

Reynolds, R. W., Gentemann CL and Wentz FJ. (2004). Impact of TRMM SSTs on a climate-scale SST analysis. *J. Climate,* **17,** 2938–2952.

Ridderinkhof, H. and de Ruijter, W. P. M. (2002). Moored current observations in the Mozambique Channel. *Deep Sea Research* II, **50**, 1933–1956.

Riehl, H. (1979). Climate and Weather of the Tropics. London: Academic Press, 611 pp.

Roberts, M. J. (2004). Signals and Sytems: Analysis Using Transform. Methods and Matlab. McGraw-Hill Professional. ISBN 0072499427

Roberts, M. J. (2008). ACEP 2008 overview and proposal. 63 pp. (unpublished).

Robinson, I. S. (2004). Measuring the Ocean from Space. The principles and methods of satellite oceanography. Springer-Verlag Berlin Heidelberg New York. Printed in Germany.

Rouault, M. and Lutjeharms, J.R.E. (2003). Estimation of sea-surface temperature around southern Africa from satellite-derived microwave observations. *S. Afr. J. Sci*. **99**, 489-494.

.

RSS home page. (2007). http://www.remss.com/tmi/tmi_3day.html (consulted in January, 2007)

Sætre, R. and Jorge da Silva, A. (1984). The circulation of the Mozambique Channel. *Deep-Sea Research*, **31,** 485-508.

Sætre, R. (1985). Surface currents in the Mozambique Channel. *Deep Sea Res.,* **32**, 1457-1467.

Sadhuram, Y., Rao, B. P., Rao, D. P., Shastri, P. N. M. and Subrahmanyam, M. V. (2004). Seasonal variability of cyclone heat potential in Bay of Bengal. *Natural Hazards,* **32**, 191-209.

Saffir, H. S. (1974). Saffir-Simpson Scale for Hurricanes, p21-23 in unknown volume issued by Herbert S. Saffir. Consulting Engineers. Coral Gables. Florida. 23 August 1974.

Saffir, H. S. and Simpson, R. H. (1974). Saffir-Simpson Scale for Hurricanes, p 21-23 in unknown volume issued by Herbert S. Saffir. Consulting Engineers. Coral Gables. Florida. 23 August 1974.

Sakaida, F., Kawamura, H. and Yoshiaki, T. (1998). Sea surface cooling caused by typhoons in the Tohoku Area in August 1989. *J. Geophys. Res*., **103**, 1053-1065.

Sampson, C. R., Jeffries, R. A. and Neumann, C. J. (1995). Tropical cyclone intensity. NRL Report NRL/PU/7541, 95-0012.

Sampson, C. R. and Schader. A. J. (2000). The automated tropical cyclone forecasting system (Version 3.2). *Bull. Amer. Meteor. Soc*., **81**: 1231-1240

Sandford, T.B., Price, J. F. and Girton, J. B. (2007). Highly resolved observations and simulations of the ocean response to a hurricane. *Geophys. Res. Lett.*, **34,** L13604.

Schouten, M.W., de Ruijter, W.P.M. and van Leeuwen, P.J. (2002b). Upstream control of the Agulhas ring shedding. *J. Geophys. Res*., doi: 10.1029/2001JC00804.

Schouten, M.W., de Ruijter, W.P.M., van Leeuwen, P.J. and Ridderinkhof, H. (2003). Eddies and variability in the Mozambique Channel. *Deep-Sea Res*. II, **50**, 1987-2003.

Scharroo, R. and Visser, P. N. A. M. (1998). Precise orbit determination and gravity field improvement for ERS satellites. *J. Geophys. Res*., **103**, 8113-8128.

.

Schott, F. A. and McCreary, J. P. (2001): The monsoon circulation of the Indian Ocean. *Prog. Oceanogr.*, **51**, 1-123.

Schroeder, L. C., Boggs, D., Dome, G., Halbersam, I. M., Jones, W. L., Pierson, W. J. and Wentz F. J. (1982). The relationship between the wind vector and and normalized radar cross section used to derive SEASAT-A satellite scatterometer winds. *J. Geophys. Res.,* **87**, 3318-3336.

Schulz, J., Meywerk, J., Ewald, S. and Schlussel, P. (1997). Evaluation of satellite-derived latent heat fluxes. *J. Climate*, **10**, 2782-2795.

Sen, P. K. (1968). Estimates of the regression coefficient based on Kendall's tau. *J. Amer. Stat. Assoc*., **63**, 1379-1389.

Shay, L. K., Black, P. G., Mariano, A. J., Hawkins, J. D. and Elsberry, R. L. (1992). Upper ocean response to Hurricane Gilbert. *J. Geophys. Res*., **97**, 20227-20248.

Shchepetkin A. F. and McWilliams J. C. (2005). Regional Ocean Model System: a split-explicit ocean model with a free-surface and topography-following vertical coordinate. *Ocean Modelling* **9**, 347–404.

Shay, L. K., Goni, G. J. and Black, P.G. (2000). Effects of warm oceanic feature on Hurricane Opal. *Mon. Wea. Rev*., **128**, 1366–1383.

Siedler, G., Rouault, M. and Lutjeharms, J. R. E. (2006). Structure and origin of the subtropical South Indian Ocean Countercurrent. *Geophys. Res. Lett.*, **33**, L24609, doi: 10.1029/2006GL027399, 1-5.

Slutz, R. J., Lubker, S. J., Hiscox, J. D., Woodruff, S. D., Jenne, R. L., Joseph, D. H., Seurer, P. M. and Elms, J. D. (1985). COADS - Comprehensive Ocean Atmosphere Data Set, CIRES/ERL/NCAR/NCDC, Boulder, Colorado, 268 pp.

Sikka, D. R. and Gadgil, S. (1980). On the maximum cloud zone and the ITCZ over Indian longitude during the southwest monsoon. *Mon. Wea. Rev.,* **108,** 11, pp. 1840–1853.

Simpson, R. H. and Riehl, H. (1981). The Hurricane and its Impact. (Oxford: Louisiana State University Press, 1960), 3-397. Simpson, eds. American Geophysical Union, Washington, D.C., 10.1029/055SP02.

Smith, S. D. (1980). Wind stress and heat flux over the ocean in gale force winds. *J. Phys. Oceanogr*., **10**, 709–726.

Smith, W. H. F. and Sandwell, D. T. (1997). Global seafloor topography from satellite altimetry and ship depth soundings. Science, **277**, 1957-1962.

.

Sneyers, R. (1990). On the statistical analysis of series of observations. WMO Technical Note No. 143.

Sobel and Maloney (2000). Effect of ENSO and MJO on western north Pacific tropical cyclones. *Geophys. Res. Lett.,* **27**, 1739-1742.

Spencer, M. W., Wu, C. and Long, D. G. (2000). Improved resolution backscatter measurements with SeaWinds pencil-Beam scatterometer. *IEEE Trans. Geosci. Remote Sens*., vol. **38**, no.1, pp. 89-104.

Sriver, R. and Huber, M. (2006). Low frequency variability in globally integrated tropical cyclone power dissipation. Geophys. Res. Lett., **33**, L11705. doi:10.1029/2006GL026167.

Stanley, H. R. (1979). The Geos-3 Project, J. Geophys. Res., **84,** 3779-3783.

Stramma, L., Cornillon, P. and Price. J. F. (1986). Satellite observations of sea surface cooling by hurricanes. *J. Geophys. Res*., **91**, 5031-5035.

Stramma, L. and Lutjeharms, J.R.E. (1997). The flow field of the subtropical gyre in the South Indian Ocean. *J. Geophys. Res.* **102**, 5513–5530.

Subrahmanyam, B., Murty, V. S. N., Sharp, R. J. and O'Brien, J. J. (2005). Air-sea Coupling During the Tropical Cyclones in the Indian Ocean: A Case study Using Satellite Observations. *Pure Appl. Geophys*., **162**, 1643–672. Birkhauser Verlag, Basel.

Subrahmanyam, B. and Robinson, I. S. (2000). Sea surface height Variability in the Indian Ocean from TOPEX/POSEIDON Altimetry and Model simulations. *Marine Geodesy*, **23,** 167–195.

Sugg, A. L. (1968). Beneficial aspects of the tropical cyclone. *J. App. Meteor*., **7**, 39-45.

Swallow, J.C., Fieux, M. and Schott, F (1988). The boundary currents east and north of Madagascar, Part I: Geostrophic currents and transports. *J. Geophys. Res.*, **93**, 4951-4962.

Swallow, J.C., Schott, F. Fieux, M. (1991). Structure and transport of the East African Coastal Current. *J. Geophys. Res*. **96**, 2254-22257.

Taljaard, J.J. and van Loon, H. (1984). Climate of the Indian Ocean south of 35°S. In Climates of the Oceans. Editor H. van Loon, World Survey of Climatology, *Volume* **15**, *Elsevier, Amesterdam*, *pp*. 693-697.

.

Tapley, B. D., Born, G. H. and Park, M. E. (1982). The Seasat altimeter data and its accuracy assessment. *J. Geophys. Res.*, **87**, 3179-3188.

Taylor P., Ed. (2000). Intercomparison and validation of ocean–atmosphere energy flux fields. Final Report of the Joint WCRP/SCOR Working Group on Air–Sea Fluxes (SCOR Working Group 110), Tech. Rep. WCRP-112, WMO/TD-136, WMO, Switzerland, Geneva, 303 pp.

Tomczak, M. and Godfrey, J. S. (1994). Regional Oceanography: an Introduction Pergamon. Oxford, 442 pp.

Tomczak, M. and Godfrey, J. S. (2003). Regional Oceanography: an Introduction. 2nd improved edition. Daya Publishing House, Delhi. 390p.

Tomczak, M. (2006). How good is your data? *Oceanography* I. Vol. 19. No.2

Torrence, C. and Compo, G. P. (1998). A practical guide to wavelet analysis. *Bull. Am. Meteorol. Soc* **79**, 61-78.

Trenberth, K. E (1997). The definition of El Niño. *Bull. Am. Meteorol*, **78** (12): 2771-2777

Trenberth, K. E. (2005). Uncertainty in hurricanes and global warming. *Science*, **308**, 1753-1754.

Tripp, R.T. (1967). An Atlas of Coastal Surface Drifts; Cape Town to Durban. South Africa Oceanographyc Data Centre, Department of Oceanography, University of Cape Town, Rondebosch, South Africa, 12 pp.

Turner, J. S. (1973). Buoyancy Effects in Fluids. Cambridge University Press, 368 pp.

Tyson, P. D. and Preston-Whyte, R. A. (2000). The Weather and Climate of Southern Africa. Oxford University Press Southern Africa. Cape town, South Africa

UNISYS Corporation Web page. (2006). www.weather.unisys.com/hurricanes/s_indian/ (consulted in January, 2006)

Van Heerden, J. and Taljaard, J. J. (1988). Africa and surrounding waters. Meteorology of the Southern Hemisphere. D. J. Karoly and D. G. Vicent, Eds., *Amer. Meteor. Soc.*, 141-174

Vitart, F., Anderson, J. L. and Stockdale, T. (2003). Seasonal forecasting of tropical cyclone landfall over Mozambique. *J. Climate* **16**, 3932–3945.

.

Vitart, F. and Stockdale, T. (2001). Seasonal forecasting of tropical storms using coupled GCM integrations. *Mon. Wea. Rev*., **129**, 2521–2537.

Von Ahn, J. M., Sienkiewicz, J. M. and Chang, P. S. (2006). Operational Impact of QuikSCAT winds at the NOAA Ocean Prediction Center. *Wea. Forecasting*, **21**. 523-539.

Walin, G. (1982). On the relation between sea-surface heat flow and thermal circulation in the ocean. *Tellus*, **34**, 187-195.

Walker, N. D., Leben, R. R. and Balasubramanian, S. (2005). Hurricane-forced upwelling and chlorophyll a enhancement within cold-core cyclones in Gulf of Mexico. *Geophys. Res. Lett.*, **32**, L18610, doi: 101029/2005GL023716.

Wallace J. M. and Hobbs, P. V. (1977). Atmospheric Science: An Introductory Survey. *Academic Press*, 467 pp.

Wang, Y. and Wu, C.-C. (2003). Current understanding of tropical cyclone structure and intensity changes – a review. *Meteorol. Atmos. Phys*. 000, 1-22. doi 10.1007/s00703-003-0055-6.

Webster, P. J., Holland, G. J., Curry, J. A. and Chang, H.-R. (2005). Changes in tropical cyclone number, duration, and intensity in a warming environment. Science, **309**, 1844–1846. (doi:10.1126/science.1116448).

Wentz, F. J. (1997). AMSR ocean algorithm, RSS Tech. Report 120296.

Wentz, F. J. and Smith, D. (1999). A model function for the ocean-normalized radar cross-section at 14 GHz derived from NSCAT observation. *J.Geophys. R.,* **104**, 11449-11514.

Wentz, F. J., Gentemann, C. and Smith, D. (2000). Satellite measurements if sea surface temperature through clouds. *Science* **288**, 847-850.

Wentz, F. J., Ashcroft, P., Gentemann, C. L. Meissner., T. (2001). The retrieval of ocean products from AMSR, IGARSS.

Wentz, F. J., Smith, D. and Mears, C. (2001). Advanced algorithm for QuikSCAT and SeaWinds/AMSR. *Proc. of IGARSS 2001*, IEEE (in press).

WHOI ftp server. (2007). ftp://ftp.whoi.edu/pub/science/oaflux/data data_v3/daily/ turbulence_1985-2006 (consulted in March, 2007).

.

Williams, J. B. (1990). Some temporal and regional variations of climate in Madagascar, Tech. Rep. Overseas Devep. Nat. Res. Inst., Chatham Maritime, Kent, pp 144.

WMO. (2006). Tropical Cyclone operational plan for the South-West Indian Ocean. WMO/TD-No. 577. Report No. TCP-12. World Meteorological Organization, Geneva.

Wong, A. P. S., Johnson, G.C. and Owens, W. B. (2003). "Delayed-mode calibration of autonomous CTD profiling float salinity data by theta-S climatology*". J. Atmos. Oceanic Tech.,* **20**, 308-318.

Wyrtki K. (1973a). An equatorial jet in the Indian Ocean. *Science* **181**, 262-264.

Xie, S.-P., Annamalai, H., Schott, F. A. and McCreary, J. P. (2002). Structure and mechanisms of south Indian Ocean climate variability. *J. Climate,* **15**, 64-878.

Xu, J.-S. (1992). On the relationship between the stratospheric quasi-biennial oscillation and the tropospheric southern oscillation. *J. Atmos*. *Sci*., **49**, 725-734.

Yelland, M. J., and Taylor, P. K. (1996). Wind stress measurements from the open ocean. *J. Phys. Oceanogr*., **26**, 541–558.

Yu, L. and Weller, R. A. (2007). Objectively Analyzed air-sea heat Fluxes (OAFlux) for the global oceans. *Bull. Ameri. Meteor. Soc.*, **88**, 527-539.

Yu, L., Weller, R. A. and Sun, B. (2004). Improving latent and sensible heat estimates for the Atlantic Ocean (1988-1999) by a synthesis approach. *J. Climate* **17**, 373-393.

Yue, S., Pilon, P. & Cavadias, G. (2002) Power of the Mann-Kendall and Spearman's rho tests for detecting monotonic trends in hydrological series. *J. Hydrol.* **259**, 254–271.

Yueh, S. H., Stiles, B., Tsai, W.-Y., Hu, H. and Liu, W. T. (2001). QuikSCAT geophysical model function for tropical cyclones and application to Hurricane Floyd. *IEEE Trans. Geosci. Remote Sens*. (in press).

Zehr, R. M., 1992: Tropical cyclogenesis in the western North Pacific. NOAA Tech. Report NESDIS 61, U.S. Department of Commerce, Washington, DC 20233, 181 pp.

Zhang, Y., Rossow, W. B., Lacis, A. A., Oinas, V. and Mishchenko, M. I. (2004). Calculation of radiative fluxes from the surface to top of atmosphere based on ISCCP and other global data sets: Refinements of the radiative transfer model and the input data. *J. Geophys. Res*., **109**, D1910, DOI: 10.1029/2003JD00447.

.

Chapter 12: Appendices

This chapter consists of a list of appendices along with contents mainly describing in more detail methodology, tables etc., that have been mentioned in Chapter 5 and in some cases highlighted in subsequent chapters. Some of the methods already incorporated within the body of the thesis at the first point of use may appear once again in this chapter. This chapter is organized according to the forthcoming Table of Appendices (from I-XLVIII).

Table of Appendices

Appendix A: Data description, Methods and Tools

Table A1. Hourly and 6-hourly data

Variable	*Spatial resolution*	*Temporal resolution*	*Data source*	*Temporal coverage*
Track information (wind speed, central pressure, translation speed, etc)	-	6-hourly	http://www.meteo.fr/temps/domtom/La_Reunion/# LR-RSMC http://www.npmoc.navy.mil/jtwc.html http://weather.unisys.com/hurricane/	1950-2003 (not available) 2004-2007 (new) 1950-2004 2004-2007
Track information (wind speed, central pressure, translation speed, etc)	-	6-hourly	Merged (JTWC+LR-RSMC) Merged (JTWC+LR-RSMC)	1980-2007 1952-2007

Table A2. Daily and 3-daily data

Variable	*Spatial resolution*	*Temporal resolution*	*Data source*	*Temporal coverage*
Sea surface temperature* (TMI/TRMM satellite)	0.25 x 0.25	daily and 3-day	ftp.ssmi.com/tmi/bmaps_v04	Nov.1998-Apr. 2005
SST (AVHRR/AOML)	4km	daily	ftp://ftp.aoml.noaa.gov/pub	1994-1997
Sea Winds (CERSAT)	0.5°x0.5°	daily	ftp.ifremer.fr/ifremer/cersat/products/gridded/	5 Aug 1991-2 June 1996
NCEP/NCAR-R2	2.5° x 2.5°	daily	ftp.cdc.noaa.gov/datasets/reanalysis2/dailyaverages	1979-2004

Table A3. Weekly data

Variable	*Spatial resol*	*Temp resol*	*Data source*	*Temporal coverage*
Sea level anomaly (TP/J-1+ERS-1/2,ENV)	1/3° x 1/3°	weekly	ftp.cls.fr/pub/oceano/AVISO/MSLA/	Oct. 1992-May 2005
Sea surface temperature (TMI/TRMM)	0.25°x0.25°	weekly	ftp.ssmi.com/tmi/bmaps_v04	Dec.1998-Apr. 2007

Table A4. Monthly data

Variable	*Spatial resolution*	*Temporal resolution*	*Data source*	*Temporal coverage*
SSHA (TP/J-1+ERS-1/2,ENV)	1° x 1°	monthly	ftp.cls.fr/pub/oceano/AVISO/MSLA/	Jan1993-July2005
OISST(NCEP)	1° x 1°	monthly	ftp://podaac.jpl.nasa.gov/pub/sst/oisst	1982-2007
SST (TMI/TRMM)	1° x 1°	monthly	ftp.ssmi.com/tmi/bmaps_v04	1999-2007

Table A6. Meteorological and Hydrographic data

Variable	*Spatial resolution*	*Temporal resolution*	*Data source*	*Temporal coverage*
Precipitation (INAM)	In-situ	Daily	http://www.inam.gov	1998-2006
T, S, currents (ACSEX)	In-situ	Daily	http://www.nioz.nl/nioz_nl/acsex/	March-April 2000
Temperature (WOA01)	In-situ	Climatology	ftp.data.nodc.noaa.gov/pub/WOA01	1999-2000
Bathymetry (ETOPO 2)	In-situ	2-mn lat-lon	http://www.ngdc.noaa.gov/mgg/fliers /01mgg04.html	-
T,S Profiles (ARGO)	In-situ	Daily	ftp.ifremer.fr/ifremer/cersat/products /gridded/	2002-2007

Appendix A1: Scatterometry

A1.1 Instrument characteristics

Scatterometers, operating on polar-orbiting satellites, provide wind speed and direction through multiple looks (Katsaros et al., 2002) at any one pixel in the swath as the spacecraft travels over the Earth's surface. Microwave pulses are transmitted to the ocean surface and the backscatter power, caused by ripples and waves, received at the instrument, is observed.

Table A8: Scatterometer instruments and their characteristics: on Seasat (operating June-September 1978); on ERS I-II (1991-2000); on ADEOS-I (August 1996-June 1997); on QuikSCAT (August 1999-) and ADEOS-II (2002-).

Instrument	SASS	ESCAT	NSCAT	QSCAT*
	Seasat	ERS	ADEOS	QuikSCAT
Frequency (GHz)	14.6	5.3	14.0	13.4
Scanning mode	Fan-beam (2 sides)	Fan-beam (1 side)	Fan-beam (2 sides)	Pencil-beam (conical)
Azimuth angle	45°, 135°	45°, 90°,135°	45°, 115°,135°	0-360
Swath width (km)	500 + 500	500	600 + 600	1800
Spatial resolution (km)	50	50	25	25 (12.5)
Daily coverage (%)	Variable	41	77	93
Life span	3 months	10 years	9 months	7 years+

Two wavelength bands, the C-band and Ku-band at frequencies of approximately 5 and 14 GHz, respectively have been used with the scatterometers (Table A8). The Ku-band allows greater sensitivity at low wind speeds but also exhibits stronger influence from rainfall, as compared to the lower frequencies of the C-band. The geophysical model functions, from which ocean surface wind vectors are retrieved, using the measured radar cross sections, are largely based on empirical fits to data (e.g. Wentz and Smith, 1999).

A1.2 Instrument history

The first scatterometers were tested on the Skylab missions in 1973-74, and on Seasat-A, which was launched by NASA in 1978**.** The latter instrument returned 100 days of data before a power failure occurred (Gymer, 1983). In 1991, a single-swath scatterometer operating at C-band was launched on the European Remote Sensing Satellite (ERS-1). It was followed by an identical instrument on the ERS-2, launched in April 1995. The NASA scatterometer (NSCAT) was launched in August 1996 on the Japanese Advanced Earth Observing Satellite (ADEOS-I; Midori). Unexpected destruction of the solar array caused the early demise of NSCAT (Liu et al., 1998; Katsaros et al., 2002). In 1999, NASA mounted SeaWinds, a Ku-band scatterometer with a new design, on board QuickSCAT, to fill the gap after ADEOS-I. QuikSCAT has a continuous 1,800 km swath that covers 93% of the global ocean daily. Calibrated against buoy data (e.g Ebuchi et al. 2002; Mostovoy et al. 2005), each QuikSCAT point represents a 10-m wind vector averaged over an area of about 25 km x 25 km. Special products with 12.5-km resolution has been produced (Liu et al., 2002). In 2002, SeaWinds was also mounted on board of ADEOS-II (Midori-II), but also that satellite had a power failure and terminated its mission the same year.

A1.3 QuikSCAT wind data

As indicated in Section 5.3.3 maximum winds using Equation 5.1 was approx 20 ms-1. To obtain a more relevant figure for the wind-speed the suggested 10-m wind was calculated according to;

$$U_{10,corr} = \kappa\sqrt{|u^3| + |v^3|} \quad \text{with } k = 0.5\left[\frac{s}{m}\right]^{\frac{1}{3}} \qquad (A3.1)$$

Figure A3.1 the performance of the original U_{10} and $U_{10,corr}$, respectively.

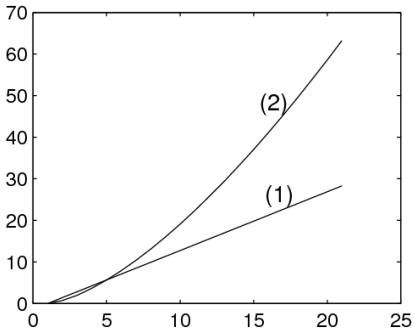

Figure A3.1: Wind speed (1) at the reference height (10-m) for the QuikSCAT winds (5.1) *and the interpolated (2) wind determined from* $(A3.1)$ *.*

Figure A3.2: shows the 10-m wind, U_{10} and the $U_{10,corr}$ while TC Japhet reached the level of Intense TC with estimated MSW > 50 ms^{-1}.

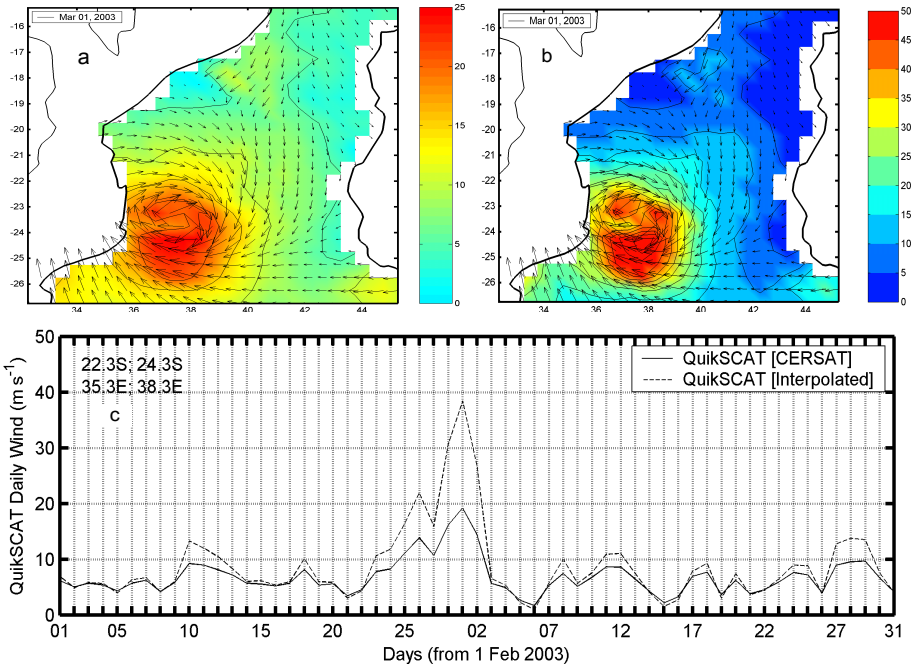

Figure A1.2: (a) daily mean winds from QuikSCAT data. (b) Indicate wind velocity using the algorithm of Equation A1.1 (fitted data). (c) Compares original and fitted data for a larger area and a longer period.

Although the Equation A1.1 is not physically sound, it seems to give a realistic fit between QuikSCAT data and the estimated MSW. Averaged over a larger area, as shown in Figure 5.5c, the result also looks realistic. Corrected wind data will be used to calculate upwelling and kinetic energy input used for mixing. The discussion (in Chapter 8) involves the algorithm used here.

Appendix A2: Radiometry

A2.1 Microwave Radiometers history

A Special Sensor Microwave Imager (SSM/I) was first deployed in 1987. It has been employed on a series of satellites launched and operated by Defence Meteorological Satellite Programme. Currently, SSM/I is mounted on three operational satellites and its observations provide a variety of oceanographic and atmospheric parameters with essentially global coverage in less than 24 hours (e.g. Wentz, 1997). The Tropical Rainfall Measuring Mission (TRMM), orbiting along the Equator, is a joint US-Japanese satellite launched in November 1997, carrying a suite of sensors aimed basically at measuring rainfall in tropical regions.

Table A9: *Microwave instrument comparison [After Kidder and Von Haar (1995)]. TMI information from Kummerow et al. (1998). Swathwidth in km.*

Parameter satellites	SSM/T DMSP	SSM/T-2 DMSP	SSM/I DMSP	TMI TRMM	MSU NOAA6-14	AMSU-A NOAA-15+	AMSU-B NOAA-15+
Channels	7	5	7	9	4	15	5
Frequency range (GHz)	50.5-59.4	91.6-183.3	19.35-85.5	10.65-85.5	50.3-57.95	23.8-89.0	89.0-183.3
NEΔT (K)	0.4-0.6	0.5	0.4-1.7	0.3-0.9	0.3	0.25-1.20	0.8
Beam-width	14	3.3-6.0	0.3-1.2	0.4-3.7	7.5	3.3	1.1
Scan type	Cross track	Cross track	Conical	Conical	Cross track	Cross track	Cross track
Best ground resolution*	204	48-84	12.5-50	5-37	110	48	16
Scan steps	7	28	64-128	26-208	11	30	90
Swath width*	2053	2053	1394	759	2347	2179	2179

The payload includes TRMM Microwave Imager (TMI), precipitation radar (PR), a visible and IR scanner (VIRS), an instrument to measure the clouds and the Earth's radiant energy (CERES) using shortwave, thermal, and total radiation detectors scanning from horizon to horizon, and a Lightning Imaging Sensor (LIS). The next generation of SSM/I, the Special Sensor Microwave Imager Sounder (SSMIS), was launched in 2003. It possesses additional channels, measuring vertical profiles of temperature, humidity, and water vapour in the troposphere. The advanced Microwave Scanning Radiometer (AMSR-E) aboard the EOS AQUA spacecraft and the TMI represent more advanced passive instruments (Table A9).

Appendix A3: Altimetry

A3.1 History of the altimeters

There have been a number of satellite altimeters flown in the past. Below is a description of the past present and some of the planed future altimeter missions.

Past altimeters

The first altimeter was mounted on Skylab in 1973 (Quartly and Chen, 2006). However the accuracy of this instrument was too low to be useful for oceanographic applications. Skylab was followed by the Geodynamics Experimental Ocean Satellite-3 (GEO-3), launched in 1975. The lack of an onboard data recorder limited its coverage to areas near ground receiving stations in United States (Stanley, 1979). Notwithstanding, GEOS-3 altimeter, with its fairly low precision of 20-30 cm, demonstrated the value of such data for estimating the variability of the sea surface from repeated passages over the same spot (Huang et al, 1978; Chelton et al., 2001).

Current altimeters

With the SEASAT (SEAfaring SATellite) launched in 1978 and its altimeter accuracy of 5 cm, the first scientific results were shown. Although it lasted three months only, it marked an advance in instrument accuracy, spawning many applications. This was the first altimeter to provide global information on ocean sea level (Cheney at al., 1983). SEASAT gave the first view of ocean circulation, waves, winds and heat storage. The data also revealed new information about the Earth's gravity field and the topography of the ocean floor.

The GEOSAT (GEOdetic SATellite) was lunched in March 1985 by US Navy, in an effort to more precisely map the influences of geoid. After 18-months of geodetic mission the satellite was put on a 17-day exact repeated orbit, using the same orbit as the previous SEASAT satellite (Tapley et al., 1982). The GEOSAT altimeter continued to function until 1989 providing almost three years of repeated measurements. It had a

range accuracy of 5-8 cm and orbit error of about 2 m. Although GEOSAT gave excellent opportunity to scientific community in studying ocean's height variability, it should be stressed that detailed knowledge of the earth's geoid is crucial to compute absolute currents (Emery and Thompson, 1998). Since then considerable experience was gained in computing the various corrections that are needed to correct satellite altimetry data (Le Traon et al., 2003).

ERS-1 was launched and operated from July 1991 to 2000, and ERS-2 has operated from June 1995 until May 2003. The radar altimeter operated reliably and accurately for more than a decade (Robinson, 2004). The ERS orbit is sun-synchronous at an altitude of 780 km, by no means an optimum orbit for altimetry since it experiences increased drag that makes precise modelling difficult. Also, the ERS-1 orbit was switched several times between a 3-day repeat, a 35-day, and a 350-day repeat cycle, preventing an accurate mean surface topography from being obtained. ERS-2 offered a steady 35-day repeat cycle during its life, achieving a ground track separation of about 80 km at the Equator. However, this was too long a revisit interval for monitoring mesoscale dynamics (Johannessen et al., 1998; Robinson, 2004).

The TOPEX-POSEIDON (T/P) satellite was launched in August 1992 into a non-sun-sycnchronous circular orbit at an inclination of 66° and an altitude of 1336 km at the equator. It describes 127 orbits during its ~10 day repeat cycle resulting in a cross track separation at the equator of 315 km for all the tracks within a cycle (Robinson, 2004). The mission was jointly conducted and sponsored by NASA and French Space Agency, CNES. It supplied the world ocean topography, or sea surface height, with unprecedented accuracy. Carrying two altimeters with a single antenna, T/P marked a significant step forward in altimetric remote sensing. The NASA altimeter, TOPEX (TOPographic EXperiment) is a dual-frequency altimeter (13.6 GHz – Ku-band and 5.3 GHz – C-band) which was able to compensate for the influence of ionosphere changes. The CNES French altimeter, called Poseidon, was the first solid-state instrument to be deployed in space. The Poseidon Ku-band altimeter operates at 13.65 GHz and has a bandwidth of 320 MHz (Robinson, 2004).

These altimeters were reducing the orbit errors to a few centimeters and have enabled the errors in the height measurements to be further reduced. The low error of 2–3 cm in locating the absolute height of the sea surface has enabled very precise mean sea surface topography (geoid plus the dynamic topography) to be established.

Another US-French collaborative mission, Jason-1 (Ménard et al., 2000) was launched in late 2001 with a suite of instruments similar to T/P although the use of new technology has led to a significant reduction of the instrument mass and power requirements, which should help it to achieve its minimum mission duration of three years and, like T/P, exceed its design life of five years. It is equipped with one single instrument, the CNES-supplied Poseidon-2 altimeter based on Poseidon-1 design, but with dual-frequency, like TOPEX; a 13.6-GHz Ku-band channel and a C-band channel at 100 MHz. The orbit is an exact copy of that of T/P, and the Jason cycles are in perfect phase with those of T/P, which has been shifted from its original track to make space (Robinson, 2004).

The large ESA Earth observation platform Envisat, launched in 2002, also carries an altimeter, RA-2 (Resti et al., 1999). This is a dual-frequency altimeter, the main channel operating at 13.6 GHz (Ku-band) with a pulse repetition frequency (PRF) of 1795 Hz, and a secondary channel at 3.2 GHz (S-band) with PRF of 448.8 Hz. The difference between travel times at the two frequencies is used to derive ionosphere correction. The Ku-band altimeter can operate in any one of three modes with bandwidths of 320, 80 and 20 MHz, respectively (Robinson, 2004).

Appendix B: Climatology of South-West Indian Ocean cyclones

Appendix B1: Temporal distribution and characterization of the tropical cyclones

The criteria used in the Tables B1-B16 (at the end of Appendices B-E) for temporal distribution of cyclones are the same as defined in Anonymous (2006) as follows: (i) if a tropical cyclone was first observed on during the last two days of a particular month and continued into the next month for longer than two days, then the system was attributed to the second month. (ii) if a tropical cyclone was observed on prior to the last two days of a month, it was attributed to the first month, regardless of how long the system lasted. (iii) if a tropical cyclone began on the last day of the month and ended on the first day of the next month, that system was attributed to the first month. However, if a tropical cyclone began on the last day of the month and continued into the next month for only two days, then it was attributed to the second month.

(iv) The South-west Indian Ocean (SWIO) study area is defined as the region west of 100°E. That is rather convenient since the majority of cyclones falling in the LR-RSMC area of responsibility (east of 90°E) still have significant portions of their tracks between 90 and 100°E. Therefore SWIO TCs are defined as the tropical cyclones with at least a portion of their track within the SWIO, though the genesis location does not necessarily need to be within SWIO. On the other hand the Mozambique Channel is the area west of 50°E from 10-21°S and west of 46°E from 21-28°S.

(v) The cyclone season is from November-April. The TC season 2007, for example, refers to the period November 2006 to April 2007. However cyclones may form outside the season at any time of the year. Those that occurred before November and after April were eliminated in the constructed data set.

(vi) Data are from JTWC+LR-RSMC

The main reason for merging these data sets was to include cyclones that may have escaped notice completely in one of the databases, to reduce missing data and other inconsistencies.

(vii) All maximum surface sustained winds are larger than 17 ms^{-1} and estimated over 1 minute. Winds with different averaging periods were translated according to conversion factors (Section 5.2.1).

(viii) Tropical depressions (TD; Wind < 17 ms^{-1}) were not included in the analysis and the earlier data records have many missing values in both wind and pressure. The exclusions of these systems were mainly based on the very limited information (e.g. track data, metadata, reports, etc.,) available from the data centers. However, it is assumed that the average values of TD per season and cyclones formed outside the season are not significant (see Ho et al., 2006). The procedure assumes that the total number of cyclones will not be affected. That is, even lacking measures of intensity and conceivable errors in exclusion, all remaining cyclones are considered as Tropical cyclones and Tropical storms (TC+TS).

(ix) All categories are defined according to the Saffir-Simpson Scale (Chapter 5; Table 5.2).

Appendix B2: Using tropical cyclone data and tracking program

This thesis uses a self-tracking program written in MATLAB (track.m, not shown) to plot tropical cyclone tracks on a map background by year and storm number using input data from the from the U.S. Navy's Joint Typhoon Warning center (JTWC) and La Reunion Regional Specialized Meteorological Center (LR-RSMC), covering the South-West Indian Ocean. The map background is either provided by a *worldo.mat* file for those using MATLAB environment only or by the directory m_map and all its contents which must be placed in MATLAB path so that they can be accessed by tracking program. The m_map package and documentation is obtainable free of charge from the web (http://www.eos.ubc.ca/~rich/private/mapug.html).

Also the geographycal boundaries may also be included as an option in the script when tracking using m_map and the corresponding data may be obtained by downloading the political boundary files at http://www.maproom.psu.edu/dcw/

Running tracking program or simply loading one of the data files (e.g. *yyyybshnnstorm.txt*, where yyyy stands for year number, *bsh* the basin i.e best southern hemisphere and *nn storm number for the JTWC data*). Files representing LR-RSMC data have similar format (e.g. *yyyyblrnnstorm.txt*, where yyyy stands for year number, *blr* the basin i.e best la reunion and *nn storm number*). Note that the SWIO season begins in November and runs through April and it is labeled by the second year, so that for example, a December 2003 storm will appear in the 2004 storm file.

Loading each '...*txt'* files yields arrays with dimensions of N X 4, where N is the total number of six hourly observations for each storm. The second dimension represents the six hour datum for a particular storm. The arrays contain year, month, day, hour (or UTC), latitude (0-40 degrees, with negative indicating the southern hemisphere), longitude (20-120 degrees) and maximum wind speed for each record. Missing values are indicated by NaNs.

Appendix B3: Categorization of the South-West Indian Ocean cyclone season for ENSO years

The analysis methods in this study uses definition of El Niño and La Niña based upon the ONI (Oceanic Niño Index) Niño 3.4 month running mean of ERSST.v3 SST anomalies warmer than or equal to +0.5 and La Niña for the same index but with ERSST.v3 SST anomalies cooler than or equal to -0.5 in the region 5N-5S, 120-170W. The El Niño and La Niña periods are defined when the threshold is met for a minimum of 5 consecutive over-lapping seasons (Table B17). Similar index have be used in the same study region (e.g. Ho et al. 2006) although a combination of various indices has been done (e.g. Kuleshov et al., 2008).

Table B17: Categorization of the South-West Indian Ocean cyclone season(DJF/JFM; 1980-2007) into El-Niño and La Niña seasons.

Current study [(1)]Ocean Niño Index ONI ERSST.v2 SST anomalies (1980-2007)	El Niño years	1982/83, 1986/87, 1987/88, 1991/92, 1994/95, 1997/98, 2002/03, 2004/05, 2006/07
	La Niña years	1983/84, 1984/85, 1985/86, 1988/89, 1995/96, 1998/99, 1999/00, 2000/01, 2005/06
	Neutral years	1979/80, 1980/81, 1981/82/, 1989/90, 1990/91, 1992/93, 1993/94, 1996/97, 2001/02, 2003/04

[(1)] *Information consulted in May 2008 at CPC site (http://www.cpc.ncep.noaa.gov/products/analysis_monitoring/ensostuff/ensoyears.shtml)*

Appendix B4: Time-Frequency representation and Spectrum of a Signal with Continuous Wavelet Transform

"…. Mélice et al., 2001)

The CWT (e.g Torrence and Compo) allows the decomposition of a signal *x(t)* into a elementary contributions localized in time and in frequency with the help of mathematical tools called wavelets. These wavelets are obtained from a single function ψ by translations and dilatations

$$\psi_{b,a}(t) = \frac{1}{a}\psi\left(\frac{t-b}{a}\right), \qquad (B1)$$

where a > 0 is the dilatation or scale parameter and *b* is the time translation parameter. The CWT of the signal *x(t)* with the analysing wavelet ψ is the convolution of *x(t)* with a set of dilated and translated wavelets

$$W(b,a) = \frac{1}{a}\int_{-\infty}^{\infty} x(t)\psi^*\left(\frac{t-b}{a}\right)dt, \qquad (B2)$$

Where * denotes the complex conjugate. The wavelet transform is defined as continuous since a and *b* may be varied continuously. The CWT expands the time series *x(t)* into the two-dimensional parameter space (*b*, *a*) and yields a measure of the relative amplitude of local activity (over an interval proportional to a) at scale a and time *b*. The choice of the wavelet ψ depends on the signal to be analyzed. In our case the periodicity of landfall is well localized in the frequency and we select the Morlet (Morlet, 1983) for its good frequency resolution properties. This wavelet is a complex cosine wave modulated by a Gaussian function

$$\psi_{b,a}(t) = \pi^{1/4} e^{-t^2/2} e^{i\omega_0 t}, \qquad (B3)$$

With $i = (-1)^{1/2}$ and where $\omega = \pi(2/\ln 2)^{1/2}$ (Daubechies, 1992) is chosen large enough to ensure that ψ *(t)* satisfies the admissibility condition which practically is equivalent to

$$\int_{-\infty}^{\infty}\psi(t)dt = 0 \qquad (B4)$$

As the Morlet wavelet is complex, the wavelet transform coeffiicient W(*b*, a) is also complex and may be expressed in terms of real and imaginary parts, modulus and phase. Moreover, for this wavelet, it make sense to identify the inverse of the scale to a frequency and the CWT is then a time-frequency analysis where the dilatation parameter a corresponds to a period and the translation parameter *b* corresponds to the time. In $(B1)$, the normalization $1/a$ is used, instead of the usual $1/(a)^{1/2}$. With this

normalization, the components of CWT may be directly compared to each other and the Morlet wavelet can be interpreted as a bandpass linear filterof the extraction of the different local components of the signal such as its local value, amplitude and phase for each point of the (b, a) time-frequency space.

Generally speaking, the CWT is infinitely redundant, the 1D original signal being transformed into a 2D time frequency image. Nevertheless, the fundamental information can be extracted from the so-called of the CWT (Mélice et al., 2001). These ridges are made of the points in the time frequency representation for which the frequency of the dilated-translated wavelet coincides with the partial derivative of the phase. More precisely, the ridges are set of couples (b, a) for which the relation

$$\frac{\partial \phi(b,a)}{\partial b} = \frac{\omega_0}{a}, \qquad (B5)$$

is satisfied and where $\phi(b,a)$ is the phase of $W(b,a)$ and ω_0 / a is the frequency of the dilated wavelet. The ridge procedure is used when there is a need of signal filtering (e.g. (e.g. Mélice et al., 2001).

Appendix B5: Characteristics of landfalling tropical cyclones affecting Mozambique and Madagascar

Table B18: List of tropical storms making landfall in Mozambique and Madagascar during 1980-2008, from the analysis data

Year	bsh ID	System	Period	MSW (1-min) [kts]I[ms^{-1}]		MSLP [hPa]	Category (Saffir-Simpson)	Area of landfall	$Date/time of landfall [mm.dd.hh]	Category at landfall /intensity (knots)
1980	22	bsh_un	14-20 Mar	40	21	994	TS	G	03/19/18Z	TS (35 kt)
1981	13	Helyette	28 Jan-04 Feb	45	23	991	TS	I	02/03/06Z	TS (40 kt)
1981	17	Iadine	16-23 Feb	55	28	984	TS	G	02/17/18Z	TS (35 kt)
1982	16	Electre	30 Jan-06 Feb	45	23	991	TS	H	02/03/00Z	TS (40 kt)
1984	14	Domoina	19-29 Jan	55	28	984	TS	H, C	01/22/00Z, 01/28/00Z	TS (35 kt, 55)
1985	19	Esitera	05-11 Feb	50	26	987	TS	H	02/10/00Z	TS (40 kt)
1985	23	Feliska	13-19 Feb	50	26	987	TS	D	02/18/06Z	TS (35 kt)
1986	04	Berobia	06-10 Jan	50	26	987	TS	B	01/09/18Z	TS (45 kt)
1988	02	bsh_un	20-26 Nov	40	21	994	TS	A	11/25/00Z	TS (40 kt)
1988	05	Benandro	24 Dec-01 Jan	35	18	997	TS	G	01/01/06Z	TD (25 kt)
1988	18	Hely	25 Mar-01 Apr	40	21	994	TS	H	03/27/18Z	TS (35 kt)
1991	10	Cynthia	16-18 Feb	50	26	987	TS	E	02/17/12Z	TS (50 kt)
1992	10	Bryna	30 Dec-02 Jan	45	23	991	TS	G	01/02/06Z	TS (35 kt)
1993	11	Dessilia	16-21 Jan	35	18	997	TS	E	01/20/12Z	TS (35 kt)
1995	09	Fodah	19-27 Jan	45	23	990	TS	B	01/22/00Z	TD (20 kt)
1997	14	Fabriola	25 Dec-09 Jan	60	31	980	TS	G	01/04/06Z	TS (60 kt)
1998	13	A19798	17-23 Jan	35	18	997	TS	A	01/17/06Z	TD (30 kt)
1998	21	Bsh21	01-10 Feb	35	18	997	TS	E	02/05/00Z	TD (25 kt)
2000	15	Gloria	27 Feb-05 Mar	50	26	987	TS	G	03/01/18Z	TS (50 kt)
2002	08	Cyprien	30 Dec-03 Jan	50	26	987	TS	F	01/02/06Z	TS (45 kt)
2003	02	Atang	06-13 Nov	45	23	991	TS	A	11/13/00Z	TD (25 kt)
2003	08	Delfina	30 Dec-09 Jan	55	28	984	TS	B	01/01/00Z	TS (50 kt)
2005	13	Felapi	26 Jan-03 Feb	40	21	997	TS	F	01/28/12Z	TD (34 kt)

Data sources: JTWC and LR-RSMC

All maximum surface sustained winds (MSW) are estimated over 1 minute

MSLP data for 1980-2001 were converted from estimated maximum surface winds using wind-pressure relationships described in Atkinson and Holliday (1977), Source: http://metocph.nmci.navy.mil/jtwc/atcr/ [1980atcr-2007atcr].

$Obtained from lat/lon data at the crossing point

Table B19: List of Category 1-2 tropical cyclones making landfall in Mozambique and Madagascar during 1980-2008, from the analysis data

Year	bsh ID	System	Period	MSW (1-min) [kts]l	[ms^{-1}]	MSLP [hPa]	Category (Saffir-Simpson)	Area of landfall	$Date/time of landfall [mm.dd.hh]	Category at landfall
1982	24	Justine	16-25 Mar	75	39	967	1	G	03/18/06Z	1 (70 kt)
1988	08	Calidera	11-18 Jan	65	33	976	1	H	01/15/00Z	1 (65 kt)
1988	14	Filão	24 Feb-02 Mar	85	44	958	2	B	03/02/00Z	1 (65 kt)
1989	06	Calasanjy	06-15 Jan	75	39	968	1	E	01/14/12Z	1 (75 kt)
1994	08	Daisy	08-16 Jan	95	49	949	2	H	01/13/18Z	1 (80 kt)
1996	14	Doloresse	11-19 Feb	75	39	967	1	D	02/19/00Z	TS (45 kt)
1996	16	Edwige	18-29 Feb	95	39	991	2	H	02/27/00Z	2 (95 kt)
1997	23	Josie	01-17 Feb	90	46	954	2	G	02/09/06Z	TS (50 kt)
1997	30	Lisette	25 Feb-02 Mar	75	39	968	1	B	03/02/06Z	TS (60 kt)
2000	03	Astride	23 Dec-03 Jan	65	33	976	1	G	12/31/18Z	TS (45 kt)
2004	03	Cela	04-21 Dec	65	33	976	1	G	12/09/18Z	TS (35 kt)
2004	09	Elita	25 Jan-05 Feb	65	33	976	1	D	01/28/12Z	TS (60 kt)
2007	06	Clovis	29 Dec-04 Jan	65	33	976	1	H	01/03/18Z	TS (45 kt)

Data sources: JTWC and LR-RSMC

All maximum surface sustained winds (MSW) are estimated over 1 minute

MSLP data for 1980-2001 were converted from estimated maximum surface winds using wind-pressure relationships described in Atkinson and Holliday (1977), Source: http://metocph.nmci.navy.mil/jtwc/atcr/ [1980atcr-2007atcr].

$Obtained from lat/lon data at the crossing point

Table B20: List of Category 3-5 tropical cyclones making landfall Mozambique and Madagascar during 1980-2008, from the analysis data

Year	bsh ID	System	Period	MSW (1-min) [Kts]I[ms^{-1}]		MSLP [hPa]	Category (Saffir-Simpson)	Area of landfall	$Date/time of landfall [mm.dd.hh]	Category at landfall
1984	07	Andry	5-16 Dec	130	67	927	4	D	12/12/06Z	3 (100 kt)
1984	32	Kamisy	3-15 Apr	100	52	927	3	G	04/09/00Z	3 (100 kt)
1985	33	Helisaonin	10-19 Apr	110	57	932	3	G	04/18/06Z	TD (30kt)
1986	25	Honorinina	07-20 Mar	110	57	933	3	H	03/15/06Z	2 (85 kt)
1988	09	Doaza	21 Jan-1Feb	115	59	927	4	G	01/25/18Z	TS (45 kt)
1990	08	Alibera	14 Dec-5 Jan	135	69	904	4	I	01/01/18Z	1 (70 kt)
1994	13	Geralda	25 Jan-5Feb	145	75	892	5	H	02/02/12Z	3 (105 kt)
1994	20	Litane	05-17 Mar	130	67	910	4	H	03/15/18Z	3 (110 kt)
1994	23	Nadia	17 Mar-2Apr	120	62	922	4	G, A	03/23/00Z, 03/24/18Z	2 (95 kt), 1 (75 kt)
1996	06	Bonita	31 Dec-15 Jan	135	69	904	4	H, B	01/11/00Z, 01/14/00Z	3 (110 kt), 1 (70 kt)
1997	20	Gretelle	18-31 Jan	115	59	927	4	I	01/24/12Z	4 (115 kt)
2000	11	Eline	03-23 Feb	115	59	927	4	H, B	02/17/18Z, 02/22/06Z	1 (75 kt), 4 (115 kt)
2000	21	Hudah	22 Mar-09 Apr	125	64	916	4	G, B	04/02/18Z, 04/08/06Z	4 (115 kt), 1 (80 kt),
2002	18	Hary	05-14 Mar	140	72	898	5	G	03/10/06Z	4 (140 kt)
2003	19	Japhet	24 Feb-04 Mar	115	59	927	4	C	03/02/12Z	2 (90 kt)
2004	16	Gafilo	01-11 Mar	140	72	898	5	G	03/07/00Z	4(130 kt)
2006	03	Boloetse	22 Jan-06 Feb	100	52	944	3	H	01/29/00Z	TD (30 kt)
2007	05	Bondo	16-26 Dec	135	69	921	4	D	12/25/12Z	TS (60 kt)
2007	14	Favio	11-23 Feb	120	62	933	4	C	02/22/06Z	3 (100 kt)
2007	19	Indlala	12-16 Mar	120	62	933	3	G	03/15/06Z	3 (100 kt)
2007	22	Jaya	30 Mar-04 Apr	110	57	940	3	G	04/03/06Z	1 (80 kt)

Data sources: JTWC and LR-RSMC

All maximum surface sustained winds (MSW) are estimated over 1 minute

MSLP data for 1980-2001 were converted from estimated maximum surface winds using wind-pressure relationships described in Atkinson and Holliday (1977), Source: http://metocph.nmci.navy.mil/jtwc/atcr/ [1980atcr-2007atcr].

$Obtained from lat/lon data at the crossing point

Appendix C: Intensification of TCs and sea surface cooling in the Mozambique Channel and adjacent waters: Some examples.

Table C1: The temporal distribution of the consecutive weeks used in the analysis of SSHA at pre-cyclone, during-cyclone and at post-cyclone conditions from the years 2000, 2003, 2004 and 2007.

Week	Dates	Mean Day
	Geralda, 25 Jan – 05 Feb 1994	
67	16 Jan – 22 Jan, 1994	19 Jan 1994
68	23 Jan – 29 Jan, 1994	26 Jan 1994
69	30 Jan –05 Feb, 1994	02 Feb 1994
70	06 Feb – 12 Feb, 1994	09 Feb 1994
	Litanne, 05 Mar – 17 Mar 1994	
72	20 Feb – 26 Feb, 1994	23 Feb 1994
73	27 Feb – 05 Mar, 1994	02 Mar 1994
74	06 Mar – 12 Mar, 1994	09 Mar 1994
75	13 Mar – 19 Mar, 1994	16 Mar 1994
	Nadia, 17 Mar – 02 Apr 1994	
74	06 Mar – 12 Mar, 1994	09 Mar 1994
75	13 Mar – 19 Mar, 1994	16 Mar 1994
76	20 Mar – 26 Mar, 1994	23 Mar 1994
77	27 Mar – 02 Apr, 1994	30 Apr 1994
	Bonita, 31 Dec – 15 Jan 1996	
168	24 Dec – 30 Dec, 1995	27 Dec 1995
169	31 Dec – 06 Jan, 1996	03 Jan 1996
170	07 Jan – 13 Jan, 1996	10 Jan 1996
171	14 Jan – 20 Jan, 1996	17 Jan 1996
	Gretelle, 18 Jan – 31 Jan 1997	
170	07 Jan – 13 Jan, 1996	10 Jan 1996
171	14 Jan – 20 Jan, 1996	17 Jan 1996
172	21 Jan – 27 Jan, 1996	24 Jan 1996
173	28 Jan – 03 Feb, 1996	31 Jan 1996
	Eline, 03 Feb – 23 Feb 2000	
381	23 Jan - 29 Jan, 2000	
382	30 Jan - 05 Feb, 2000	02 Feb 2000
383	06 Feb – 12 Feb, 2000	09 Feb 2000
384	13 Feb – 19 Feb, 2000	16 Feb 2000
385	20 Feb – 26 Feb, 2000	23 Feb 2000
	Hudah, 22 Mar – 09 Apr 2000	
388	12 Mar – 18 Mar, 2000	15 Mar 2000
389	19 Mar – 25 Mar, 2000	22 Mar 2000
390	26 Mar – 01 Apr, 2000	29 Mar 2000
391	02 Apr – 08 Apr, 2000	05 Apr 2000
392	09 Apr – 15 Apr, 2000	12 Apr 2000

(Cont.)

Table C2: The temporal distribution of the consecutive weeks used in the analysis of SSHA at pre-cyclone, during-cyclone and at post- cyclone conditions from the years 2000, 2003, 2004 and 2007.

Week	Dates	Mean Day
	Hary, 05 Mar – 14 Mar 2002	
490	24 Feb – 02 Mar, 2002	27 Feb 2002
491	03 Mar – 09 Mar, 2002	06 Mar 2003
492	10 Mar – 16 Mar, 2002	13 Mar 2003
	Japhet, 24 Feb – 04 Mar 2003	
541	16 Feb – 22 Feb, 2003	19 Feb 2003
542	23 Feb – 01 Mar, 2003	26 Feb 2003
543	02 Mar – 08 Mar, 2003	05 Mar 2003
544	09 Mar – 15 Mar, 2003	12 Mar 2003
	Gafilo, 01 Mar – 11 Mar 2004	
594	22 Feb – 28 Feb, 2004	25 Feb 2004
595	29 Feb – 06 Mar, 2004	03 Mar 2004
596	07 Mar – 13 Mar, 2004	10 Mar 2004
597	14 Mar – 20 Mar, 2004	17 Mar 2004
	Boloestse, 22 Jan – 05 Feb 2006	
693	15 Jan – 21 Jan 2006	18 Jan 2006
694	22 Jan – 28 Jan 2006	25 Jan 2006
695	29 Jan – 04 Feb 2006	01 Feb 2006
696	05 Feb – 11 Feb 2006	08 Feb 2006
	Bondo, 16 Dec – 26 Jan 2007	
739	03 Dec – 09 Dec 2006	06 Dec 2006
740	10 Dec – 16 Dec 2006	13 Dec 2006
741	17 Dec – 23 Dec 2006	20 Dec 2006
742	24Dec - 30 Dec 2006	27 Dec 2006
	Favio, 11 Feb – 23 Feb 2007	
748	04 Feb – 10 Feb, 2007	07 Feb 2007
749	11 Feb – 17 Feb, 2007	14 Feb 2007
750	18 Feb – 24 Feb, 2007	21 Feb 2007
751	25 Feb – 03 Mar, 2007	28 Feb 2007
	Indlala, 07 Mar – 17 Mar 2007	
751	25 Feb – 03 Mar, 2007	
752	04 Mar – 10 Mar, 2007	07 Mar 2007
753	11 Mar – 17 Mar, 2007	14 Mar 2007
754	18 Mar – 24 Mar, 2007	21 Mar 2007
	Jaya, 30 Mar – 04 Apr 2007	
754	18 Mar – 24 Mar, 2007	21 Mar 2007
755	25 Mar – 31 Mar, 2007	28 Mar 2007
756	01 Apr – 07 Apr, 2007	04 Apr 2007
757	08 Apr – 14 Apr, 2007	11 Apr 2007

Figure C1: SSHA Fields associated with ITC Geralda and ITC Litanne

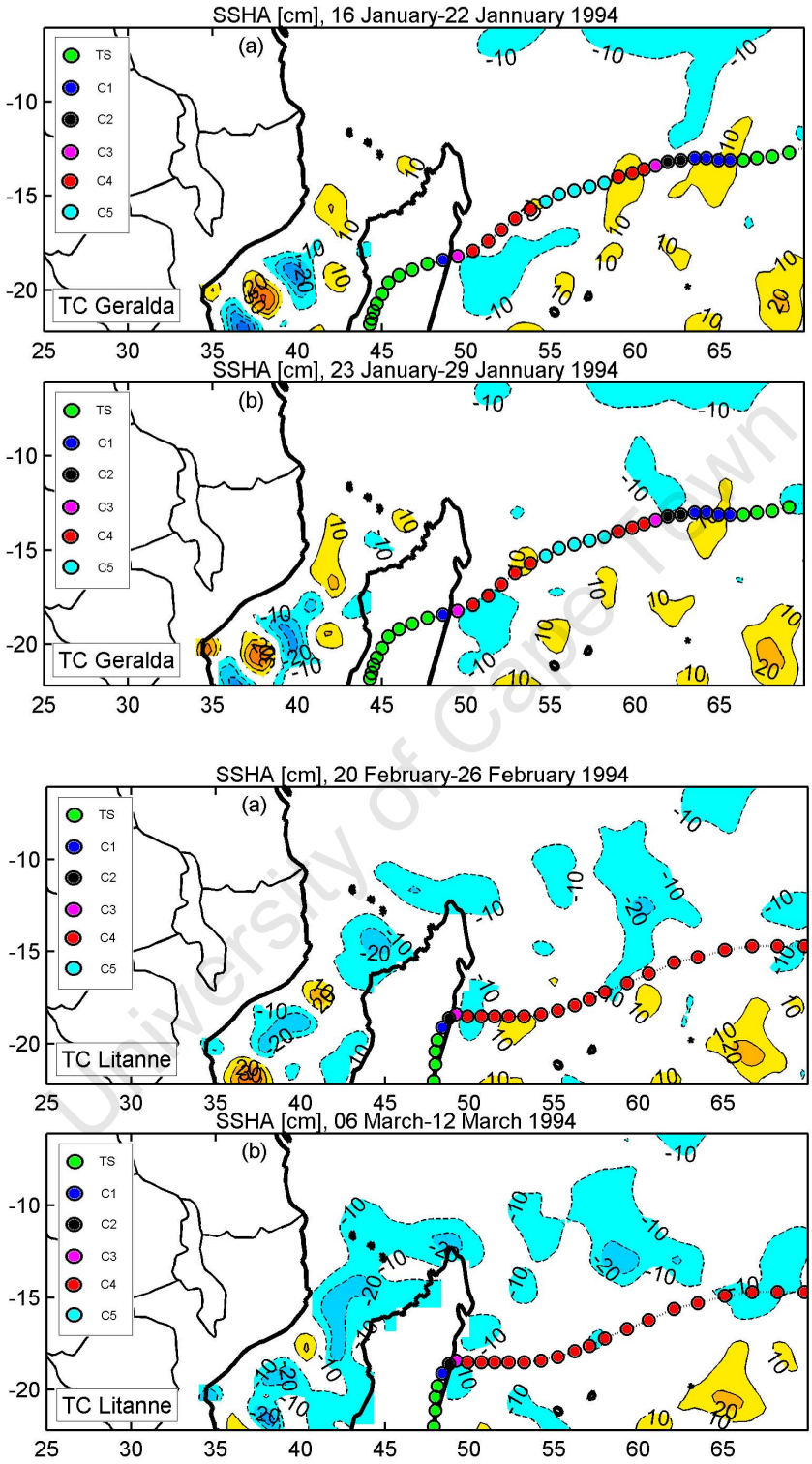

Figure C2: SSHA Fields associated with ITC Nadia and ITC Bonita

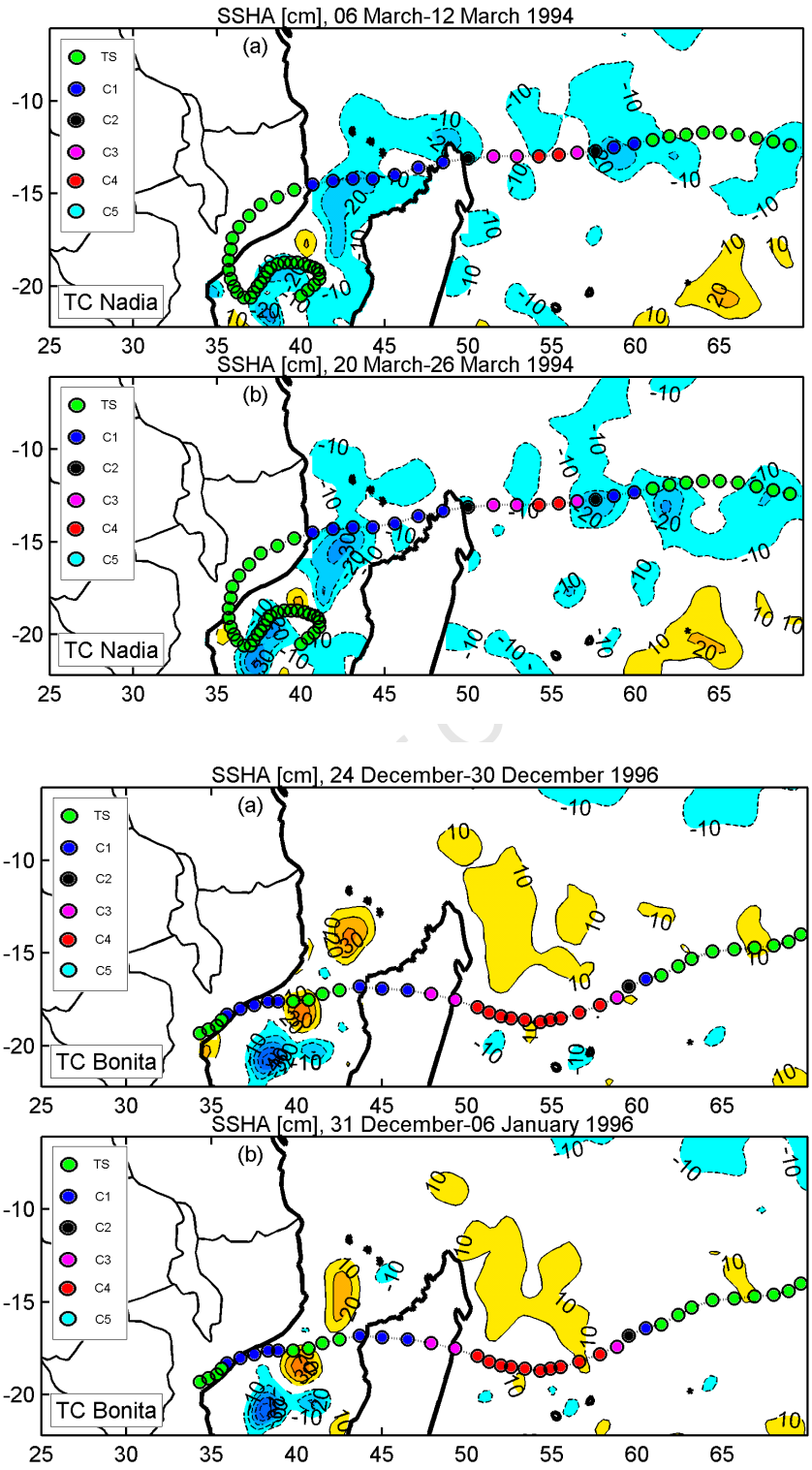

Figure C3: SSHA Fields associated with ITC Gretelle and ITC Eline

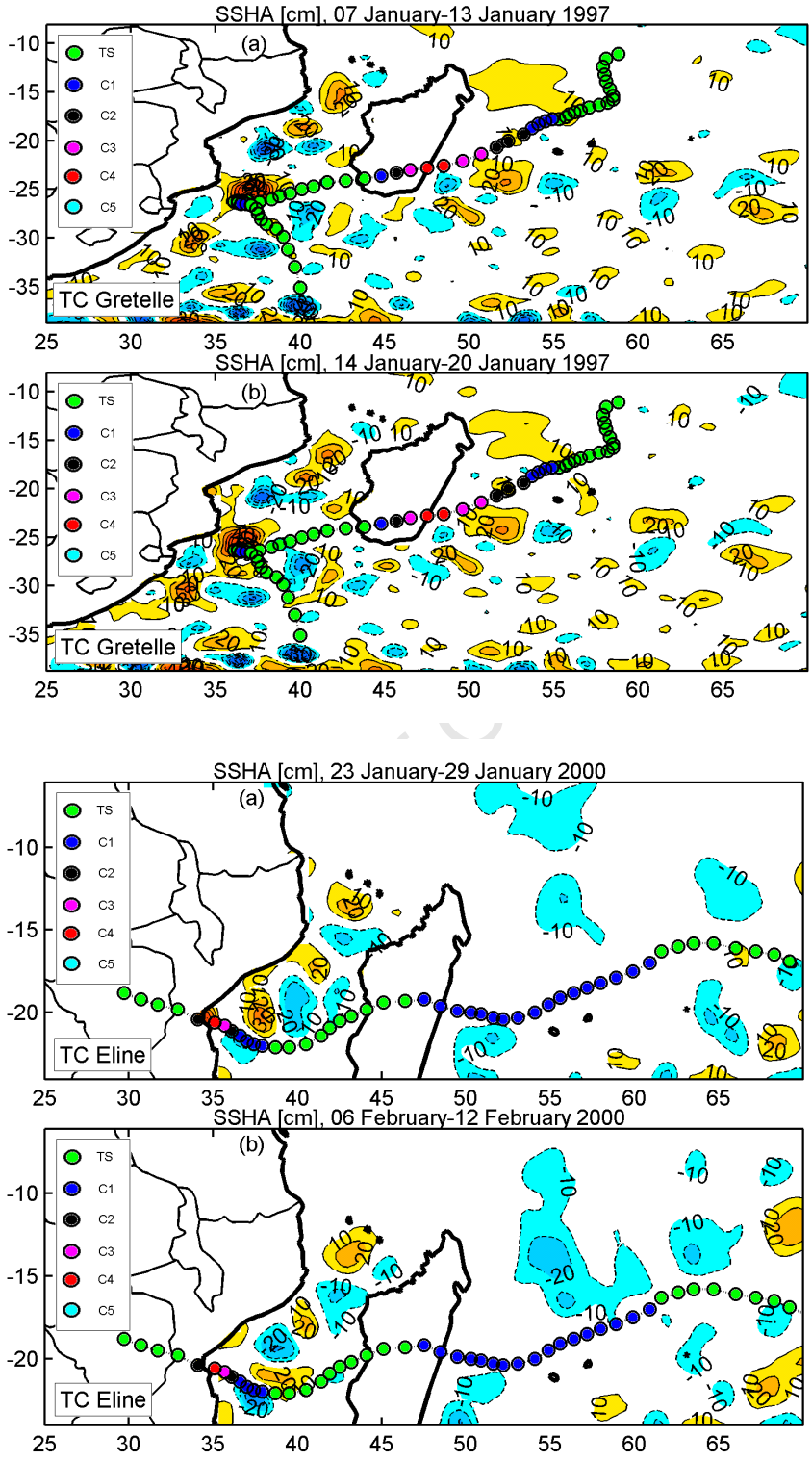

Figure C4: SSHA Fields associated with ITC Hudah and ITC Hary

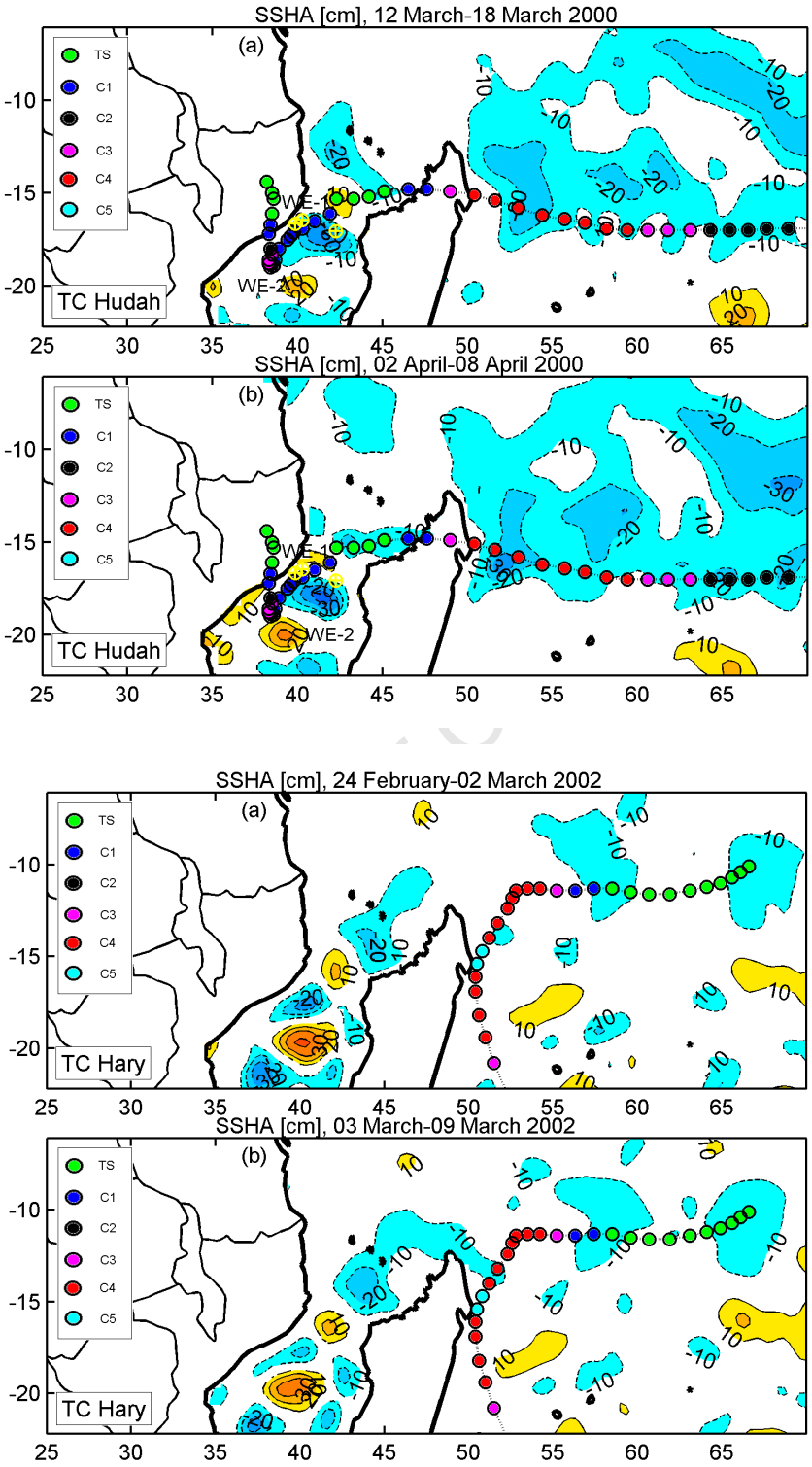

Figure C5: SSHA Fields associated with ITC Japhet

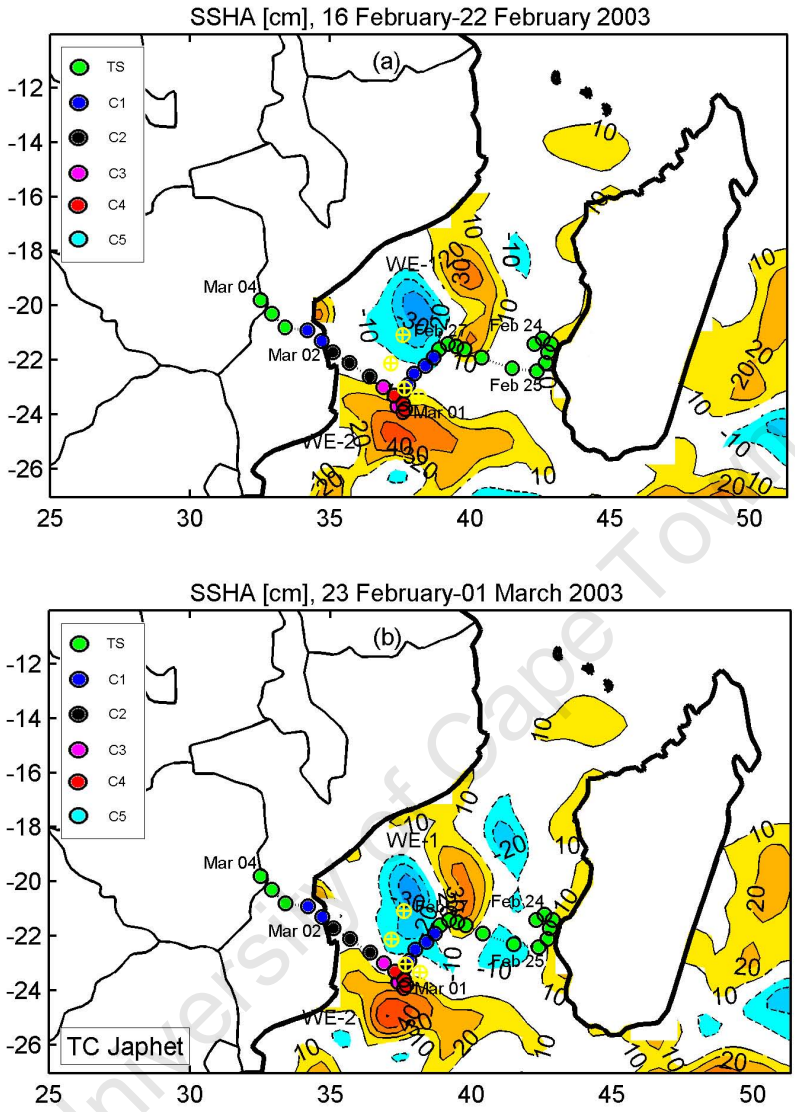

Figure C6: SSHA Fields associated with ITC Gafilo and ITC Boloetse

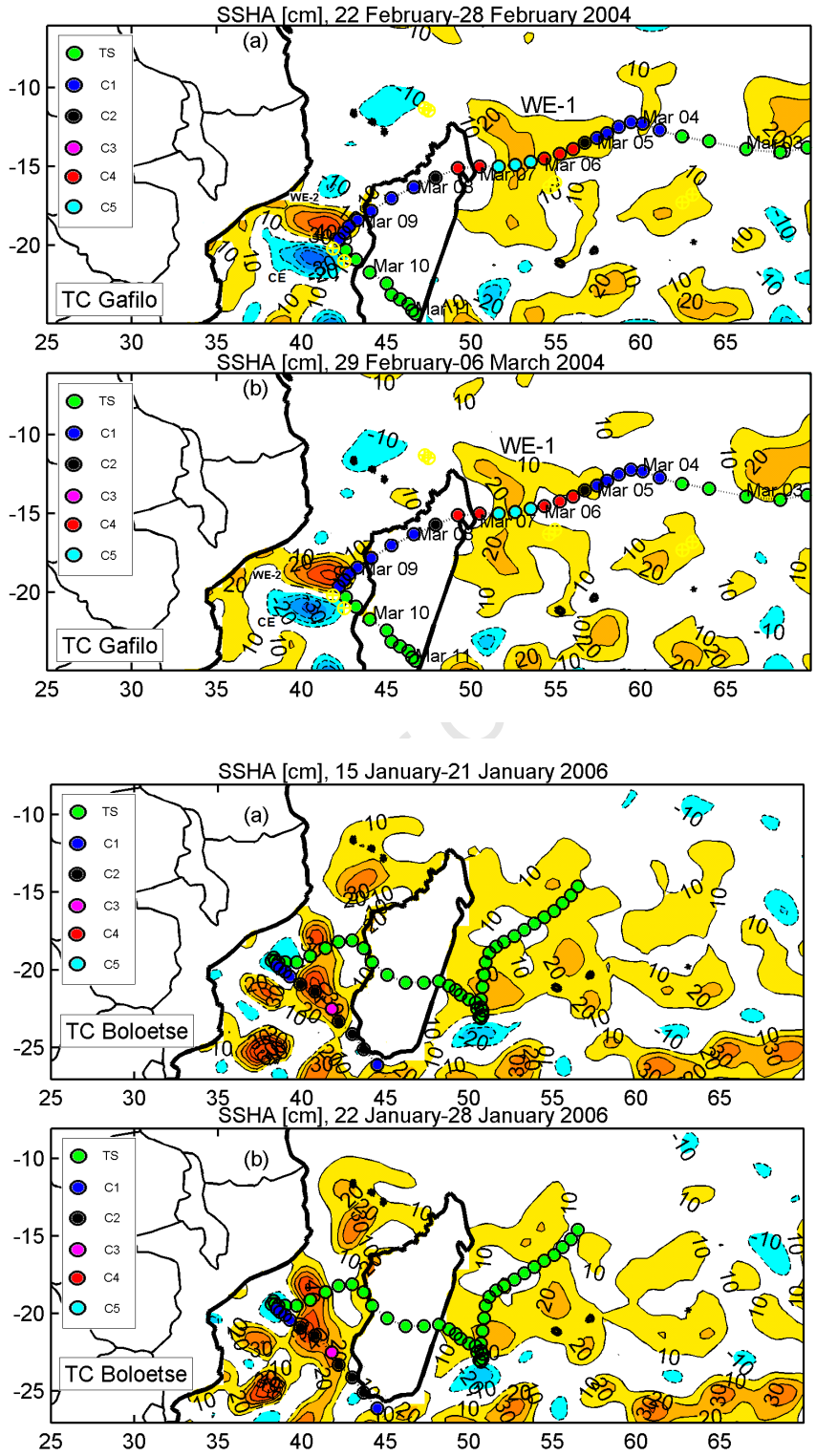

Figure C7: SSHA Fields associated with ITC Bondo and ITC Favio

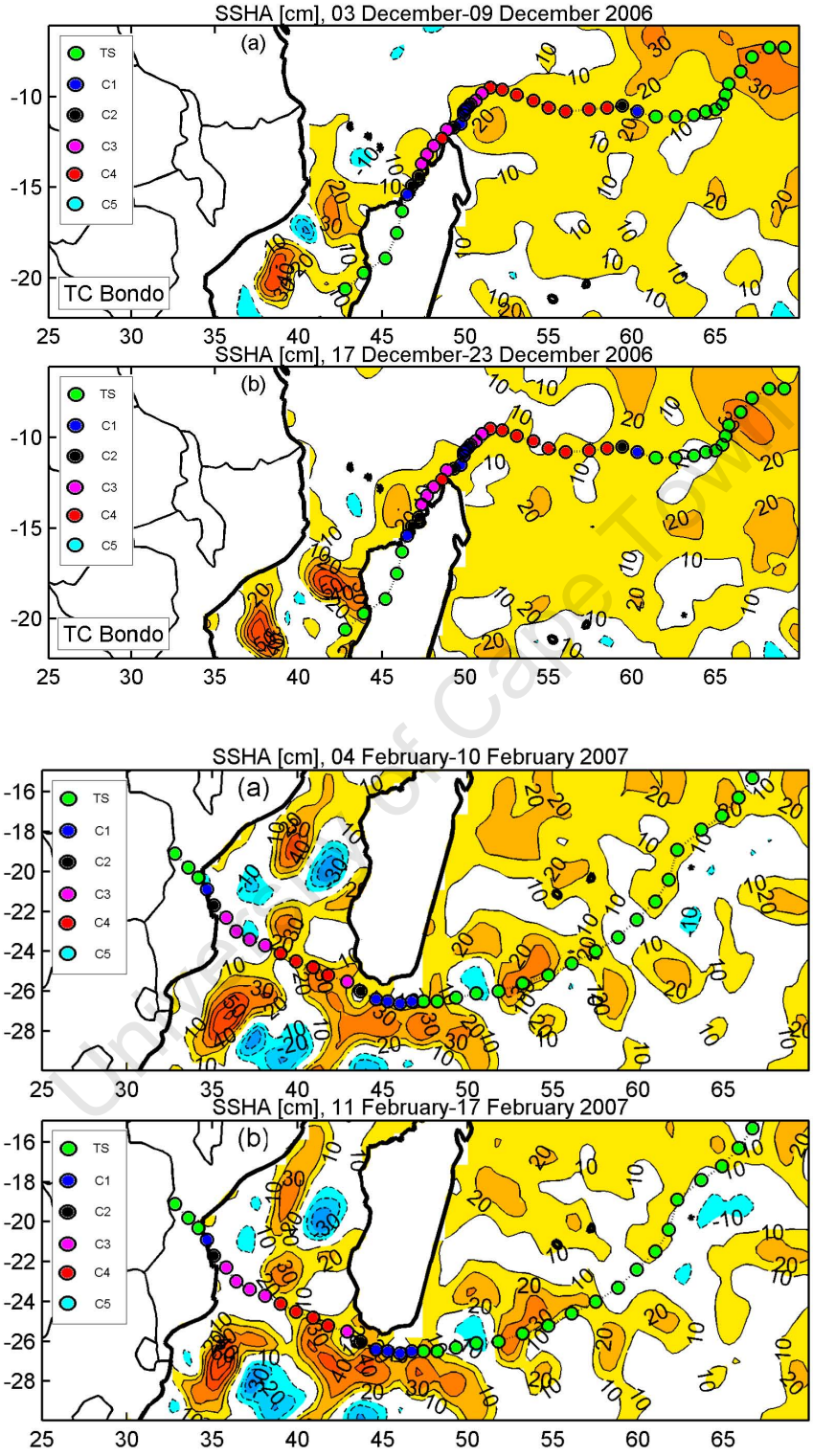

Figure C8: SSHA Fields associated with ITC Indlala and ITC Jaya

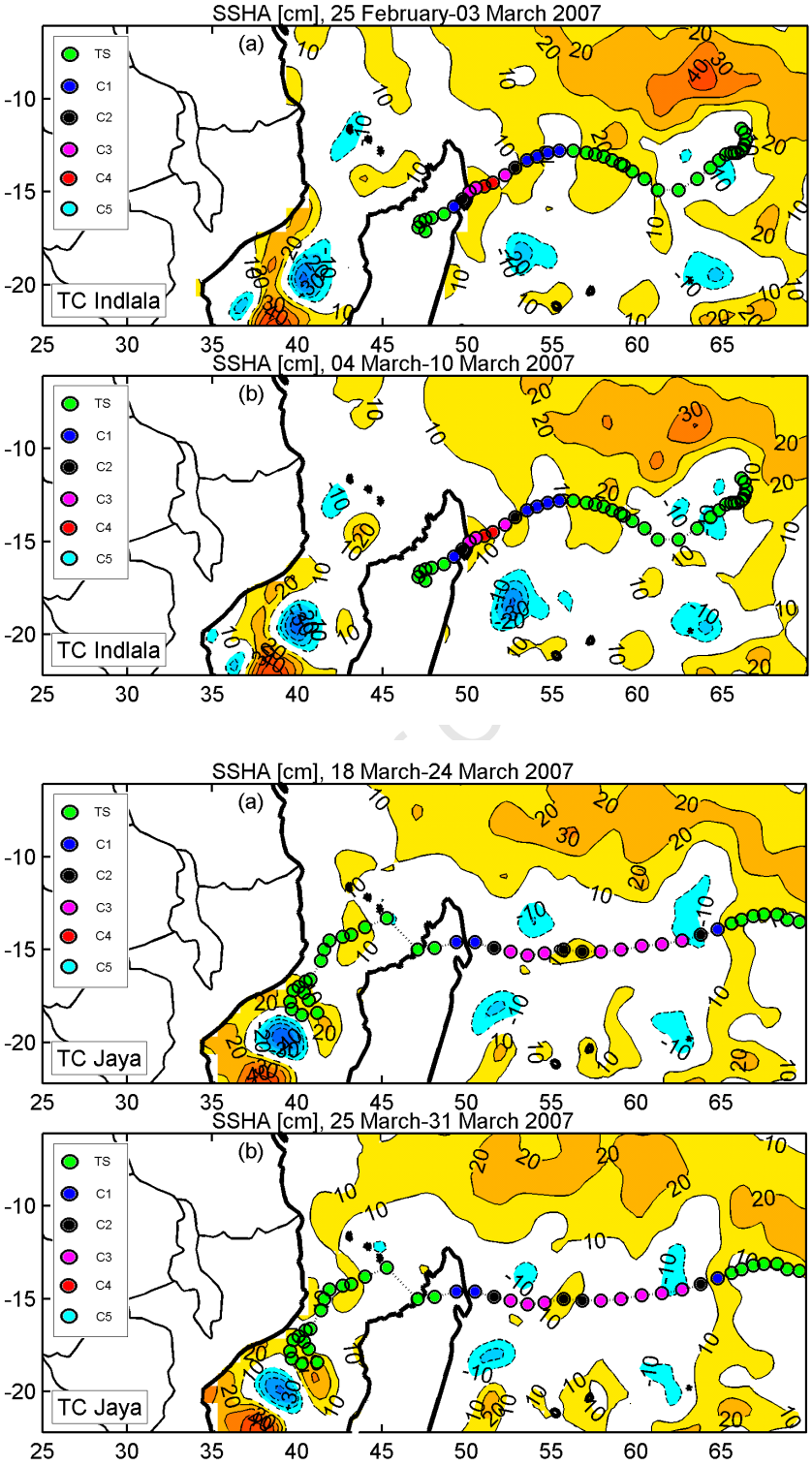

Table C3: The temporal distribution of the consecutive days used in the analysis of SST at pre-cyclone, during-cyclone and at post-cyclone conditions from the years 1994, 1996, 1997 and 2000.

Index	Dates	Mean Day
	Geralda, 25 Jan – 05 Feb 1994	
1	24 January 1994	24 January 1994
2	05 February 1994	05 February 1994
	Litanne, 05 Mar – 17 Mar 1994	
3	05 March 1994	05 March 1994
4	17 March 1994	17 March 1994
	Nadia, 17 Mar – 02 Apr 1994	
5	17 March 1994	17 March 1994
6	02 April 1994	02 April 1994
	Bonita, 31 Dec – 15 Jan 1996	
7	31 December 1996	31 December 1996
8	16 January 1996	16 January 1996
	Gretelle, 18 Jan – 31 Jan 1997	
9	18 January 1996	18 January 1996
10	01 February 1996	01 February 1996
	Eline, 03 Feb – 23 Feb 2000	
11	02 February 2000	02 February 2000
12	23 February 2000	23 February 2000
	Hudah, 22 Mar – 09 Apr 2000	
13	20 March 2000	22 Mar 2000
14	10 April 2000	29 Mar 2000

(Cont.)

Table C4: The temporal distribution of the consecutive days used in the analysis of SST at pre-cyclone, during-cyclone and at post-cyclone conditions from the years 2002, 2003, 2004, 2006 and 2007.		
Index	Dates	Mean Day
	Hary, 05 Mar – 14 Mar 2002	
14	04 March 2002	04 March 2002
15	13 March 2002	13 March 2002
	Japhet, 24 Feb – 04 Mar 2003	
16	22 February 2003	22 February 2003
17	04 March 2003	04 March 2003
	Gafilo, 01 Mar – 11 Mar 2004	
18	28 February 2004	28 February 2004
19	08 March 2004	08 March 2004
	Boloestse, 22 Jan – 05 Feb 2006	
20	20 January 2006	20 January 2006
21	05 Febraury 2006	05 Febraury 2006
	Bondo, 16 Dec – 26 Jan 2007	
22	13 December 2006	13 December 2006
23	26 December 2006	26 December 2006
	Favio, 11 Feb – 23 Feb 2007	
24	10 February 2007	10 February 2007
25	23 February 2007	23 February 2007
	Indlala, 07 Mar – 17 Mar 2007	
26	05 March 2007	05 March 2007
27	16 March 2007	16 March 2007
•	Jaya, 30 Mar – 04 Apr 2007	
28	27 March 2007	27 March 2007
29	04 April 2007	04 April 2007

Figure C9: SST Fields associated with ITC Geralda and ITC Litanne

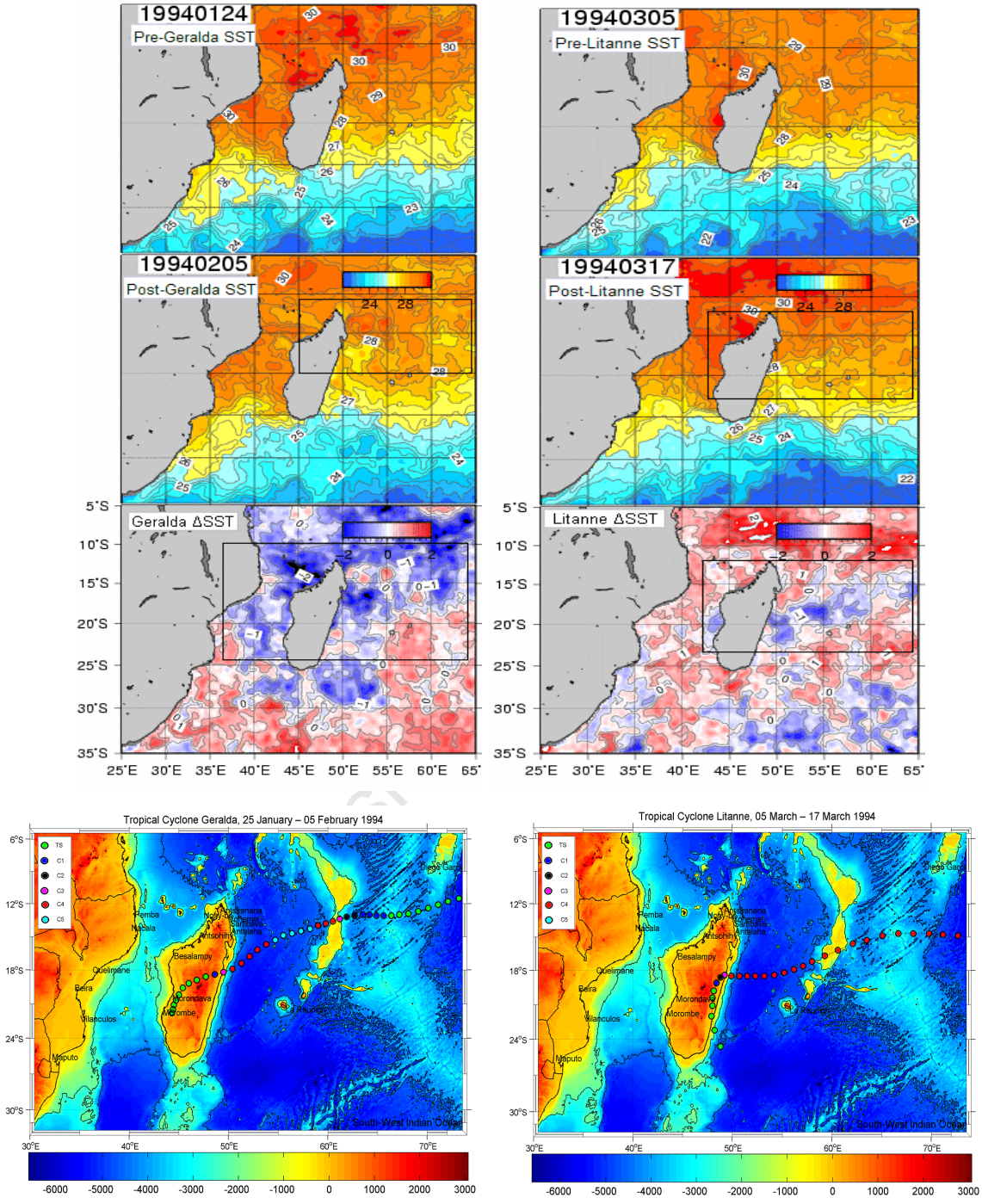

Bottom: Tropical cyclone *paths (circles colored marks) overlay the ocean and land topography (ETOPO-2).*

Figure C10: SST Fields associated with ITC Nadia

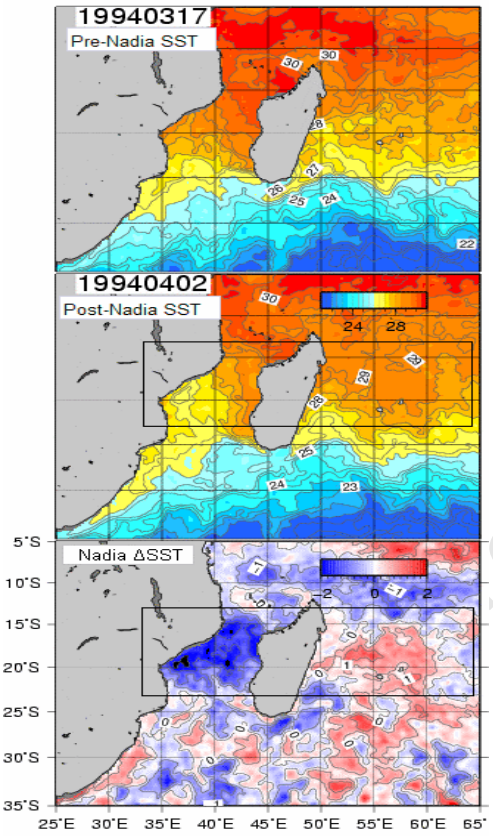

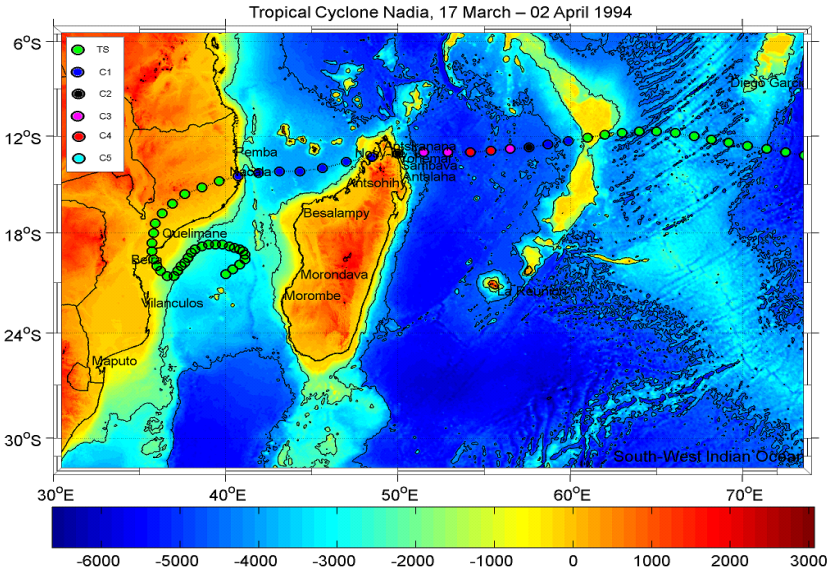

Bottom: Tropical cyclone *path (circles colored marks) overlain the ocean and land topography (ETOPO-2).*

Figure C11: SST Fields associated with ITC Bonita and ITC Gretelle

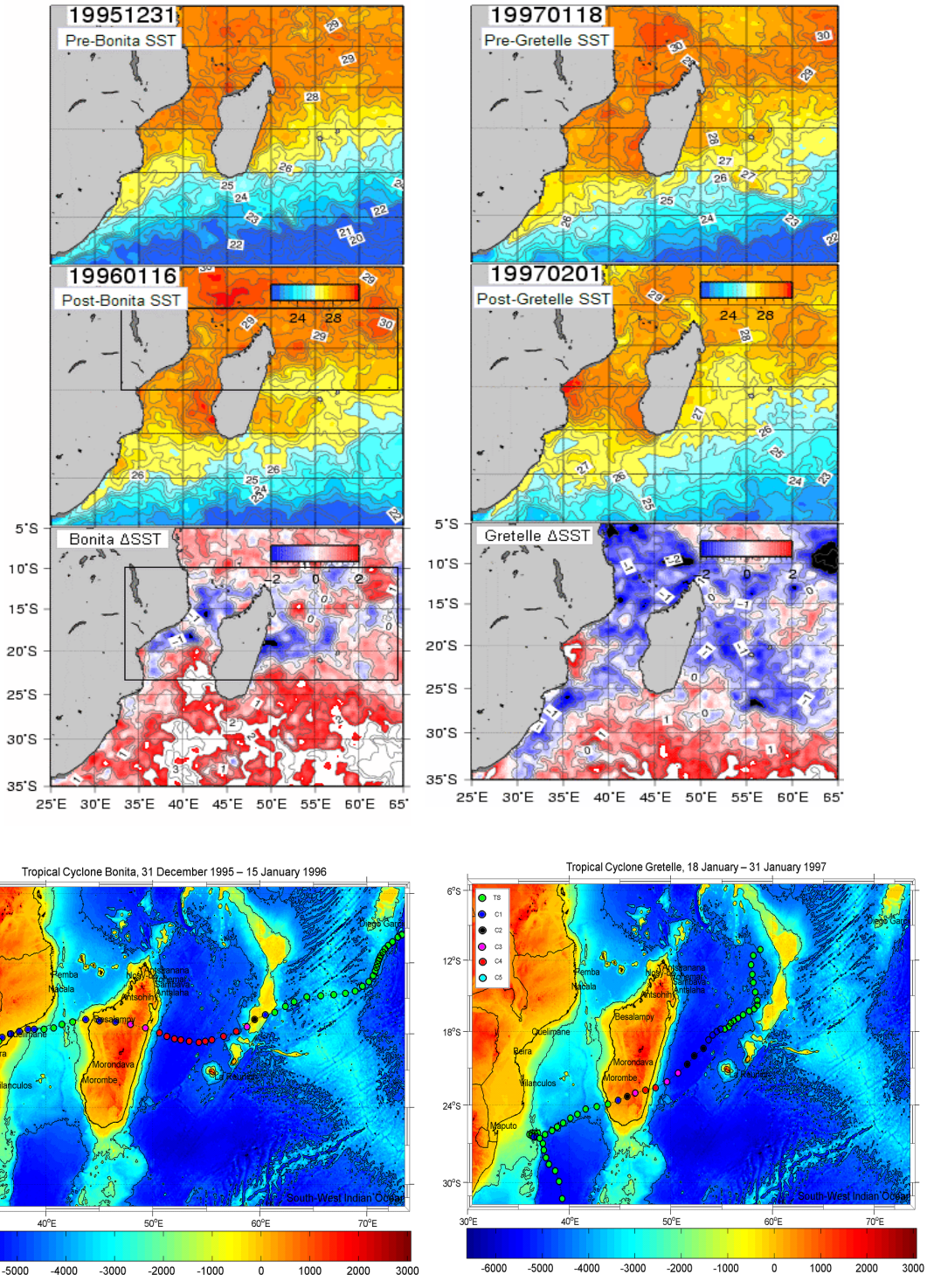

Bottom: Tropical cyclone *paths (circles colored marks) overlay the ocean and land topography (ETOPO-2).*

Figure C12: SST Fields associated with ITC Eline and ITC Hudah

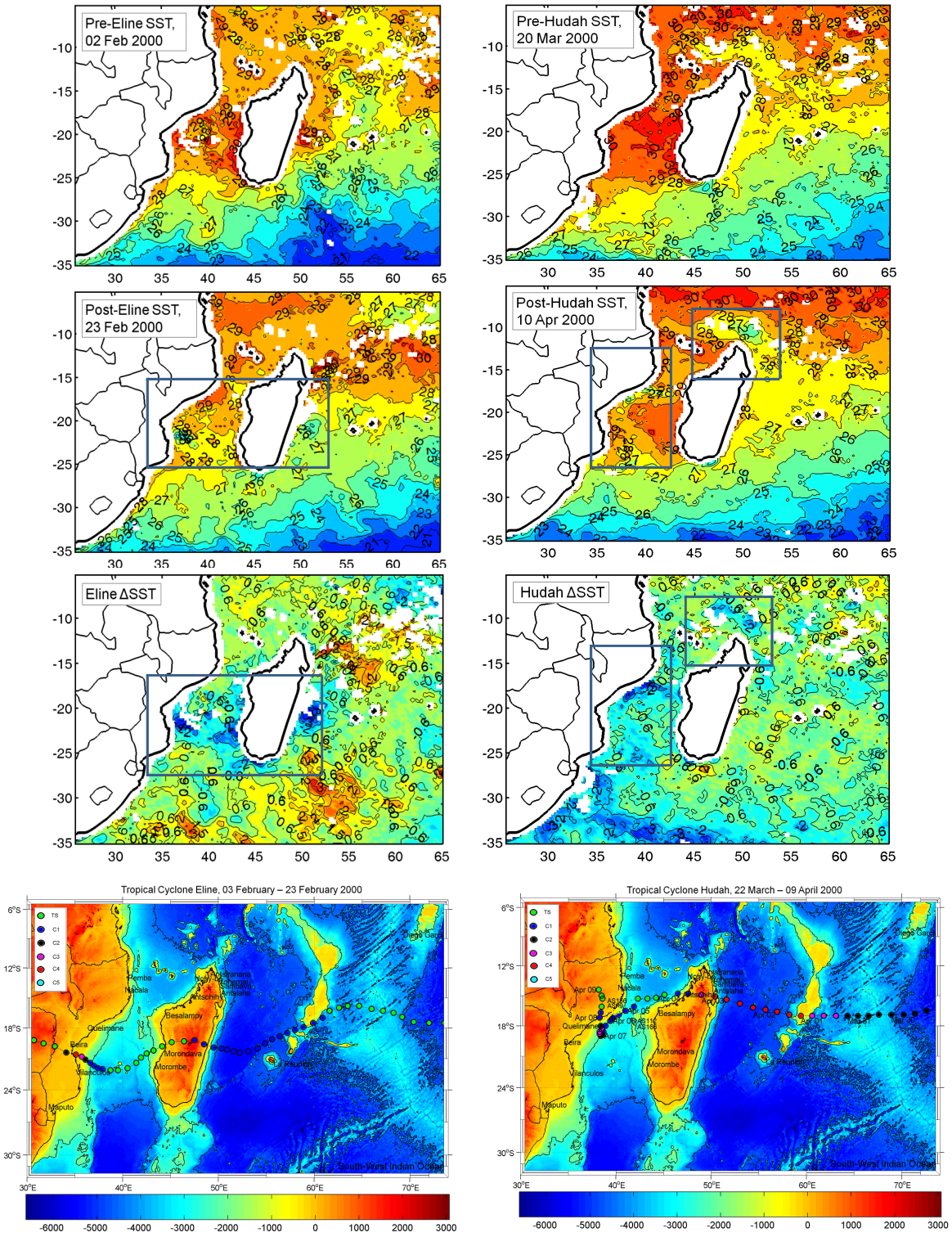

Bottom: Tropical cyclone *paths (circles colored marks) overlay the ocean and land topography (ETOPO-2).*

Figure C13: SST Fields associated with ITC Hary and ITC Japhet

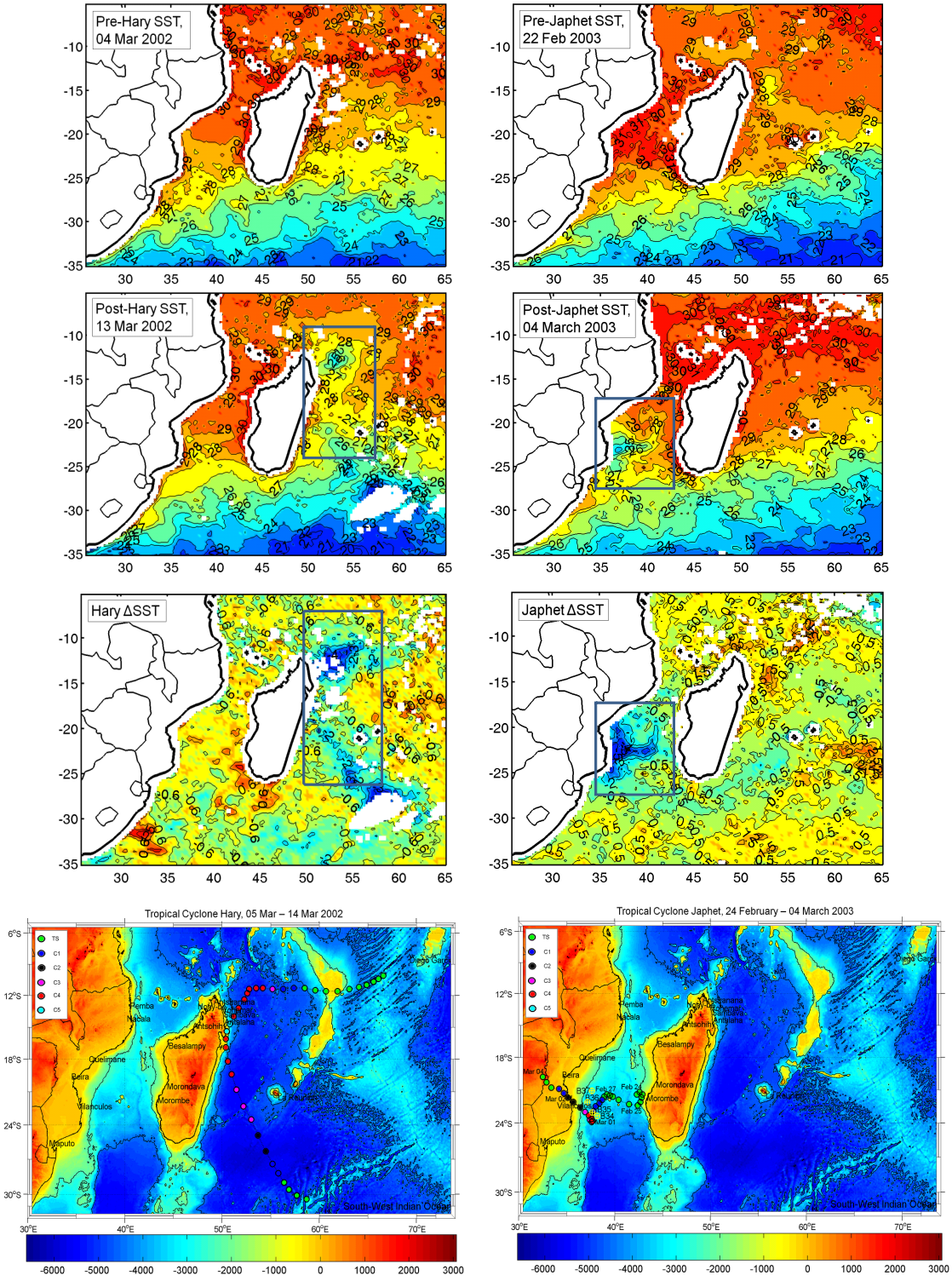

Bottom: Tropical cyclone *paths (circles colored marks) overlay the ocean and land topography (ETOPO-2).*

Figure C14: SST Fields associated with ITC Gafilo and ITC Boloetse

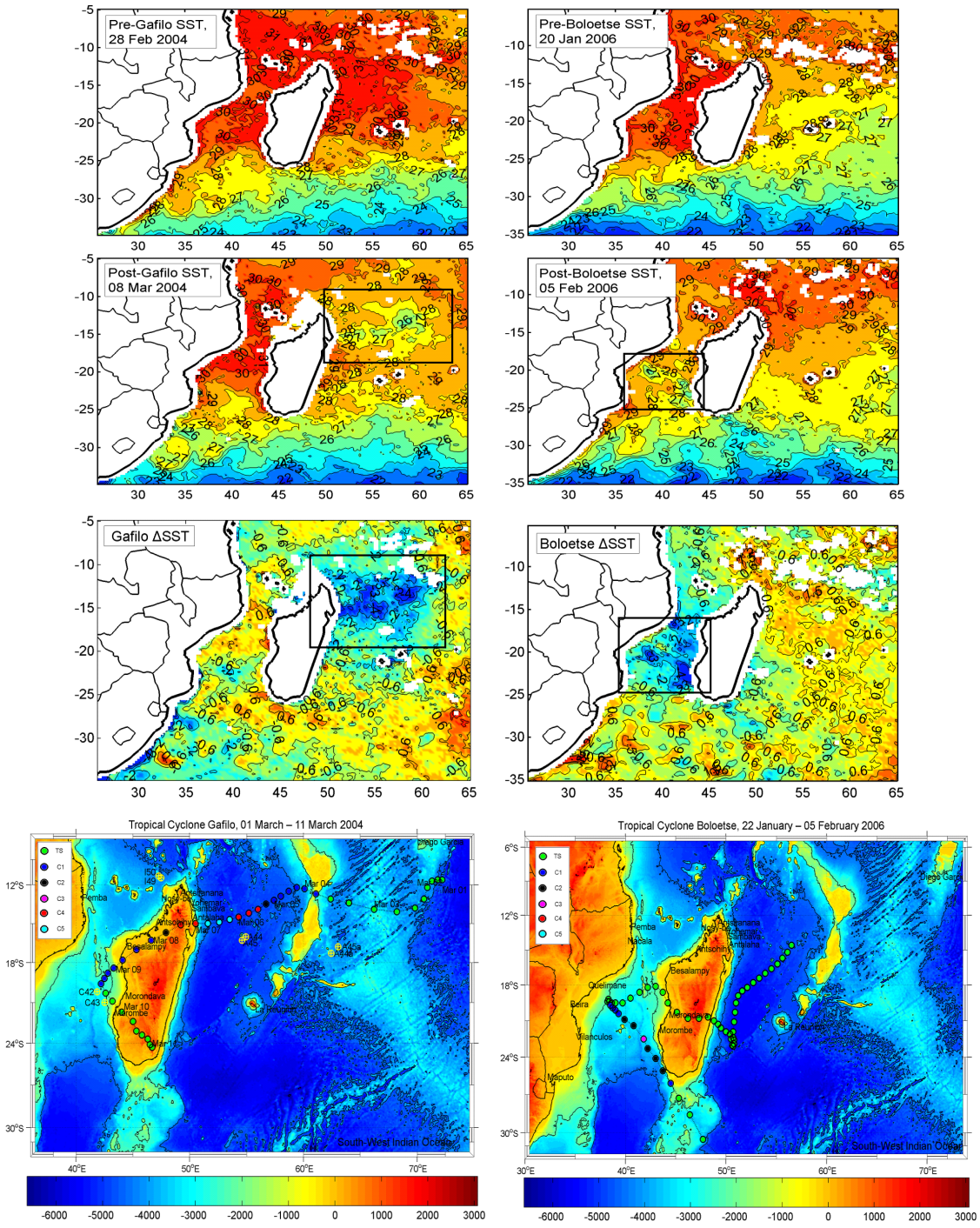

Bottom: Tropical cyclone *paths (circles colored marks) overlay the ocean and land topography (ETOPO-2).*

Figure C15: SST Fields associated with ITC Bondo and ITC Favio

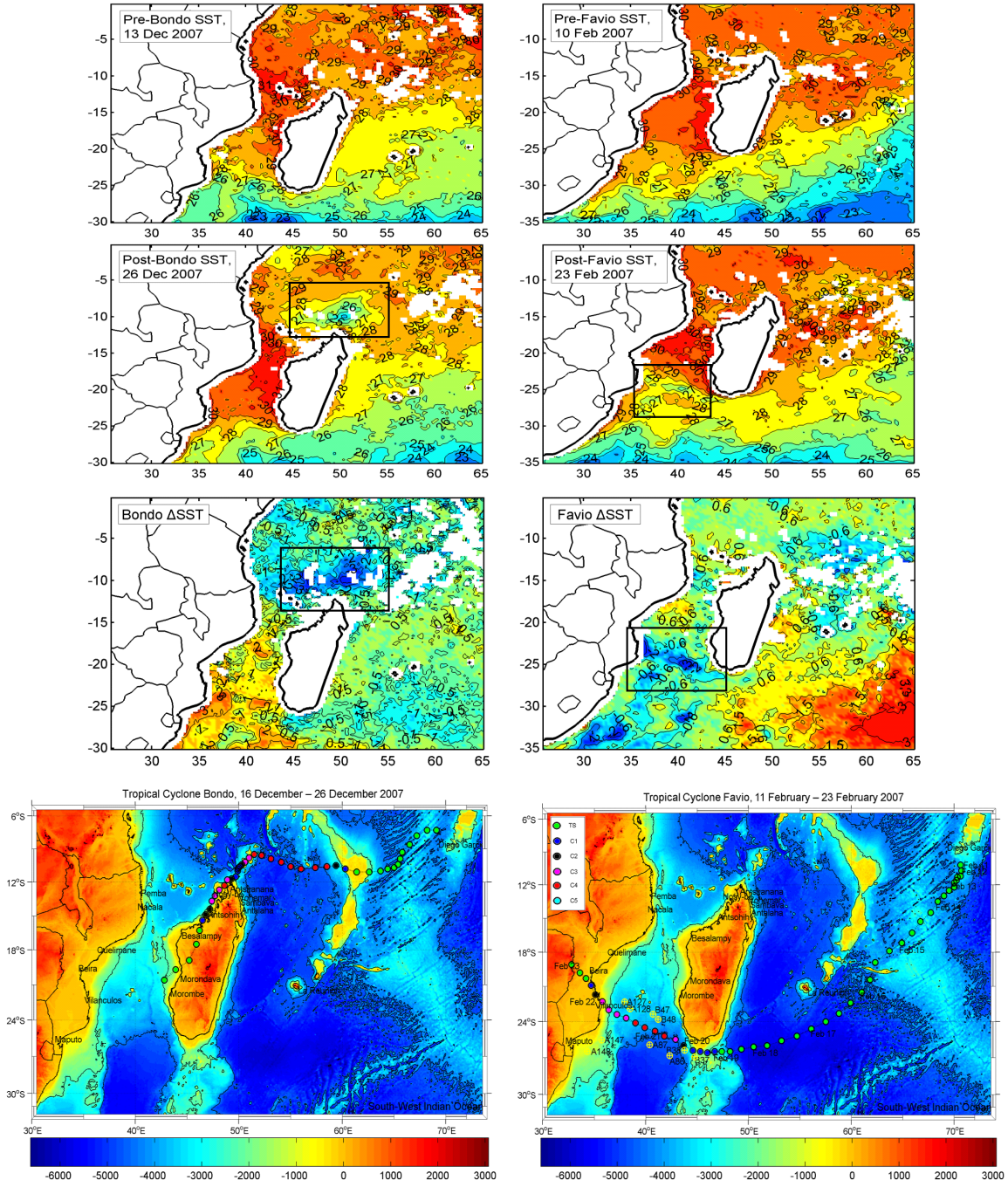

Bottom: Tropical cyclone *paths (circles colored marks) overlay the ocean and land topography (ETOPO-2).*

Figure C16: SST Fields associated with ITC Indlala and ITC Jaya

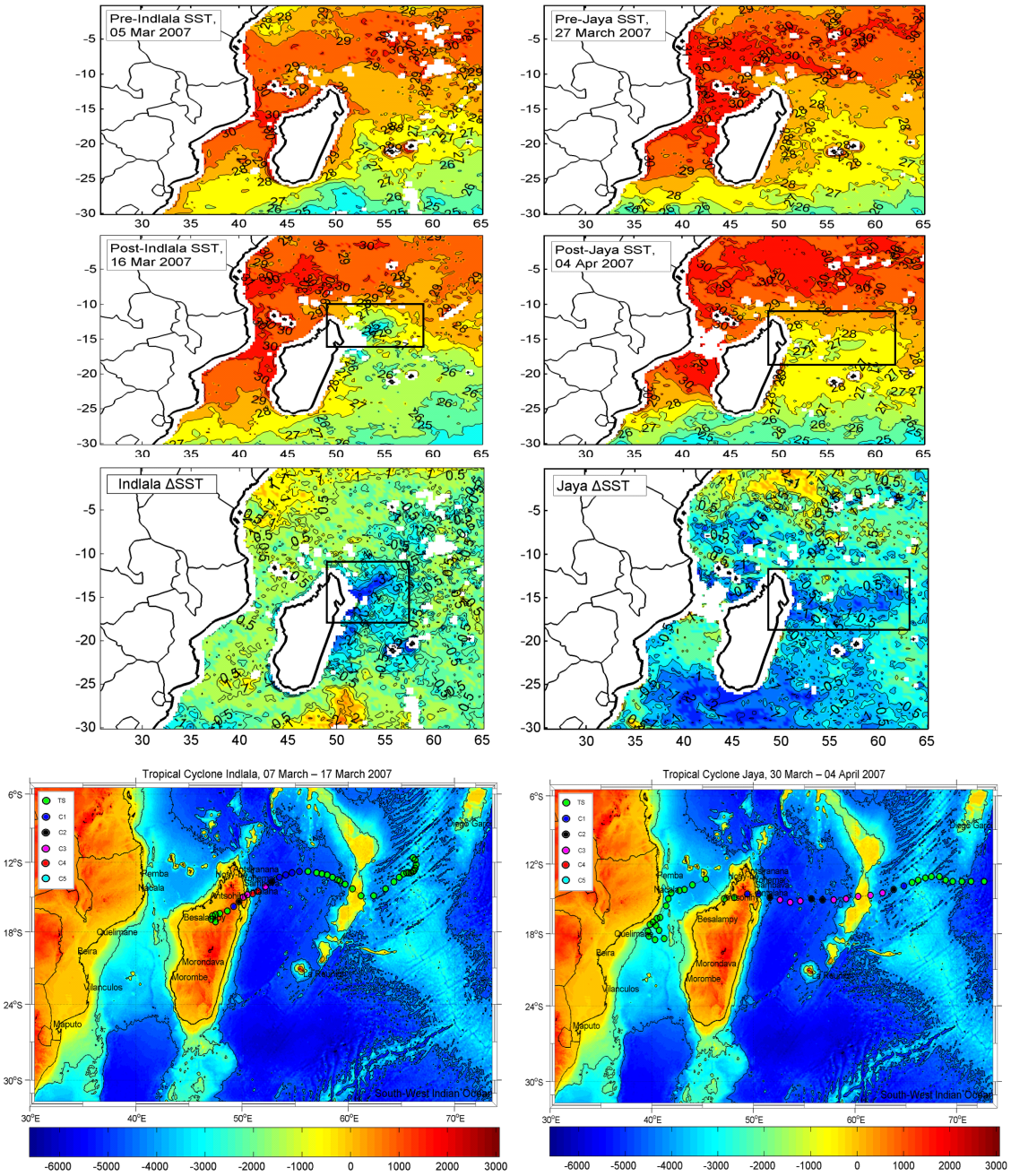

Bottom: Tropical cyclone *paths (circles colored marks) overlay the ocean and land topography (ETOPO-2)*

Table C5: HUDAH Stations

#	Date	Lat	Lon	XBT/CTD	Period
1	20000401	-17.0567	42.2697	AS112	Before
2	20000408	-17.0552	42.2707	AS166	After
3	20000331	-16.6545	39.8902	AS99	Before
4	20000406	-16.4562	40.2767	AS156	After
5					

Table C6: JAPHET Stations

#	date	Lat	Lon	PF	Period
1	20030212	-23.349	38.173	B34	Before
2	20030222	-23.035	37.662	B35	Before
3	20030304	-22.123	37.156	B36	After
4	20030314	-21.069	37.618	B37	After

Table C7: GAFILO Stations

#	date	Lat	Lon	PF	Period
1	20040303	-16.019	54.945	A44	Before
2	20040314	-16.295	54.588	A45	After
3	20040304	-17.296	62.442	A44a	Before
4	20040314	-16.791	63.052	A45a	After
5	20040305	-11.456	47.485	I49	Before
6	20040315	-11.309	47.268	I50	After
7	20040302	-20.196	41.844	C42	before
8	20040312	-20.987	42.509	C43	After

Table C8: FAVIO Stations

#	date	Lat	Lon	PF	Period
1	20070213	-26.932	44.756	B37	Before
2	20070223	-26.387	43.783	B38	After
3	20070215	-26.838	42.337	A86	Before
4	20070226	-25.941	40.375	A87	After
5	20070217	-25.543	35.722	A147	Before
6	20070227	-26.49	34.326	A148	After
7	20070212	-23.377	40.72	A47	Before
8	20070222	-23.798	41.218	A48	After
9	20070209	-22.32	37.953	A127	Before
10	20070220	-22.9	38.477	A128	After

PF: profiling float; A: AOML; B: BODC; C: Coriolis; I: INCOIS

Appendix C1: TC at maximum intensity and associated rainfall.

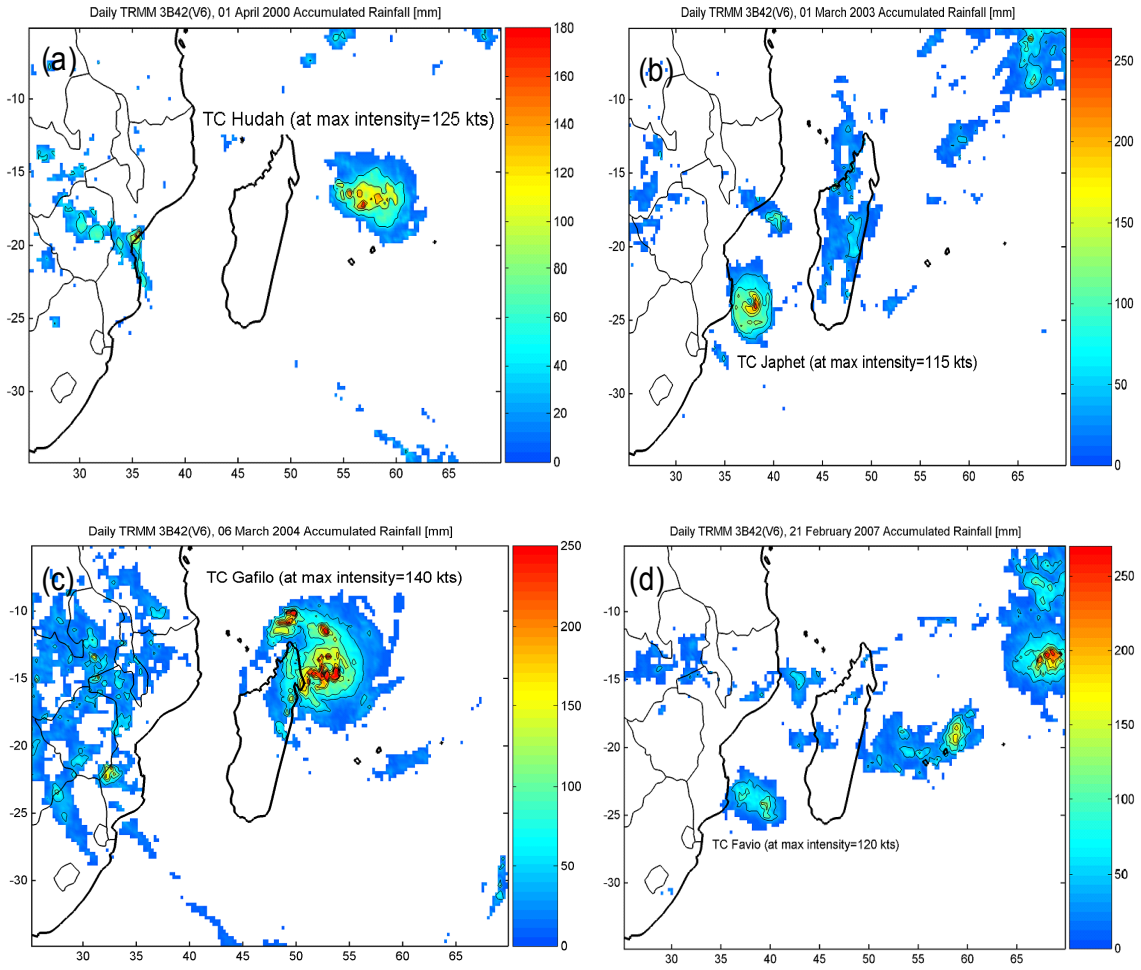

Figure C2.1: Storm total rainfall amounts (mm) for the four selected tropical cyclones reaching their peak intensity near Madagascar or Mozambique during: (a) 2000, TC Hudah; (b) 2003, Japhet; (c) 2004, TC Gafilo; and (d) 2007, TC Favio.

Appendix C2: Landfalling TCs and associated rainfall

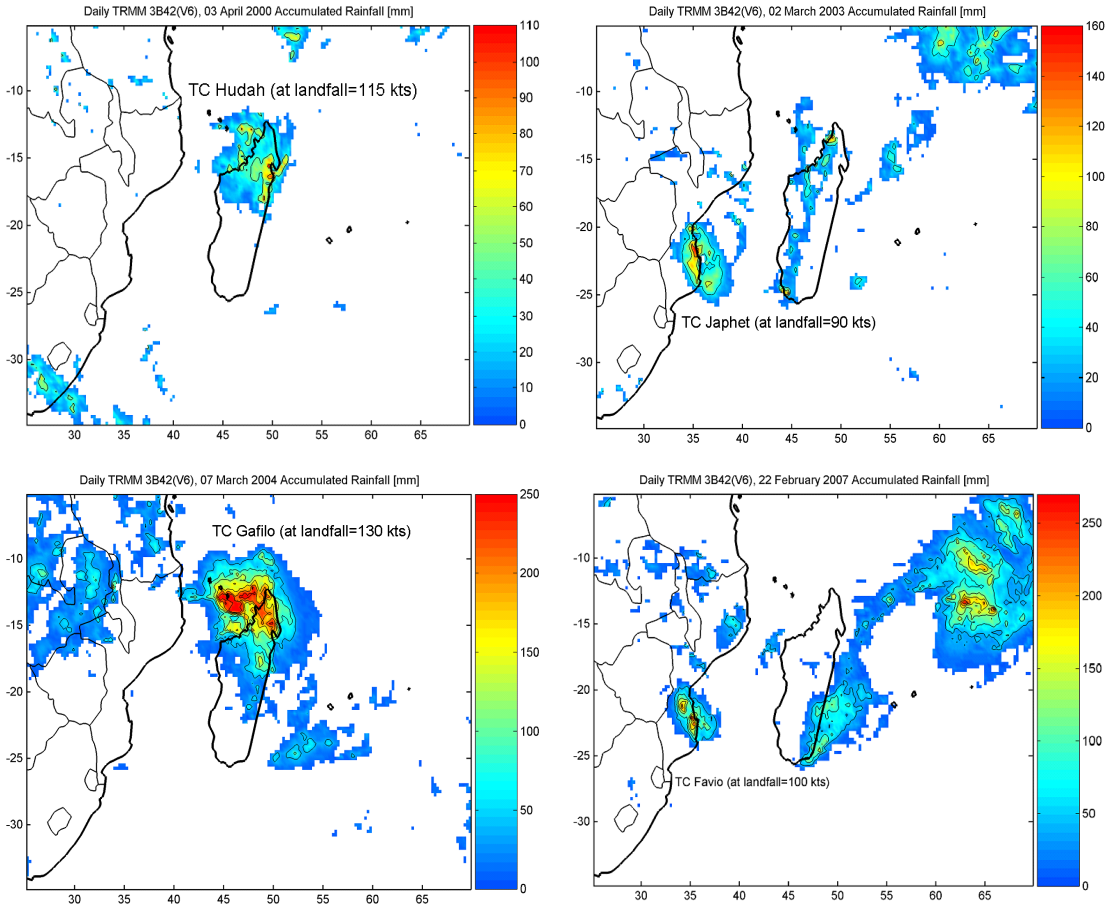

Figure C2.2: Storm total rainfall amounts (mm) for the four selected tropical cyclones that struck Madagascar and Mozambique during: (a) 2000, TC Hudah; (b) 2003, Japhet; (c) 2004, TC Gafilo; and (d) 2007, TC Favio.

Appendix D: Sea surface cooling, entrainment in the wake of a TC. Tropical cyclone heat potential.

Appendix D1: Two layer model approximation

The commonly used two-layer model (Figure D1.1) will result in more rapidly decreasing sea surface temperature than a model with a finite thermocline depth and also in much smaller entrainment velocities.

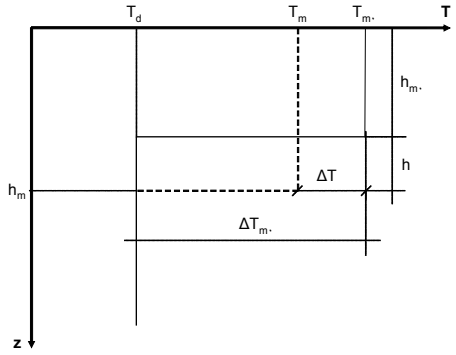

Figure D1.1: Two-layer model representation

In a two-layer system, heat conservation requires $h(\Delta T_{m\cdot} - \Delta T) = \Delta T h_{m\cdot}$. Then, the entrainment velocity is;

$$w_e = \frac{dh}{dt} = \frac{d}{dt}\left(\frac{\Delta T h_{m\cdot}}{\Delta T_{m\cdot} - \Delta T}\right)$$

Here, the solution for this equation for the region of the Mozambique Channel, affected by the cyclone is determined using daily SST ($T_s(t)$) data from TMI. The temperature change, $\Delta T = T_{m0} - T_m$ is determined for each grid point, and $\Delta SST = SST(dayX) - SST(day\cdot)$;

Two layer case; h_{m0} = 50 m, ΔT_{m0}= 8˚C (NB that this definition sets the value of T_d), C_p=4200Ws kg^{-1},^{0}C

The change in heat content due to decreasing SST is calculated according to $\Delta H = \rho C_p h_{m0} \Delta T$. It means that ΔH is assumed directly proportional to ΔT, where the calculation is based on the changes in the upper 50m only. However, we calculate the entrainment velocity, thus the heat flux from below, $Q_e = \rho C_p \Delta T w_e$, offers a better way to express the total change in heat caused by entrainment. Therefore it can also calculate

$$\Delta H_W = \int_T \rho C_p \Delta T w_e dt = \rho C_P \Delta T h ,$$

which, gives the total change in heat content in the mixed layer, independent of depth (for $T > T_d$).

The potential energy

The change in potential energy ΔPE from is calculated from the expression

$$\Delta PE = g(\Delta \rho_{m0} - \Delta \rho) h \frac{h_{m0} + h}{2}$$

Appendix D2: World Ocean Atlas Climatology (WOA05)

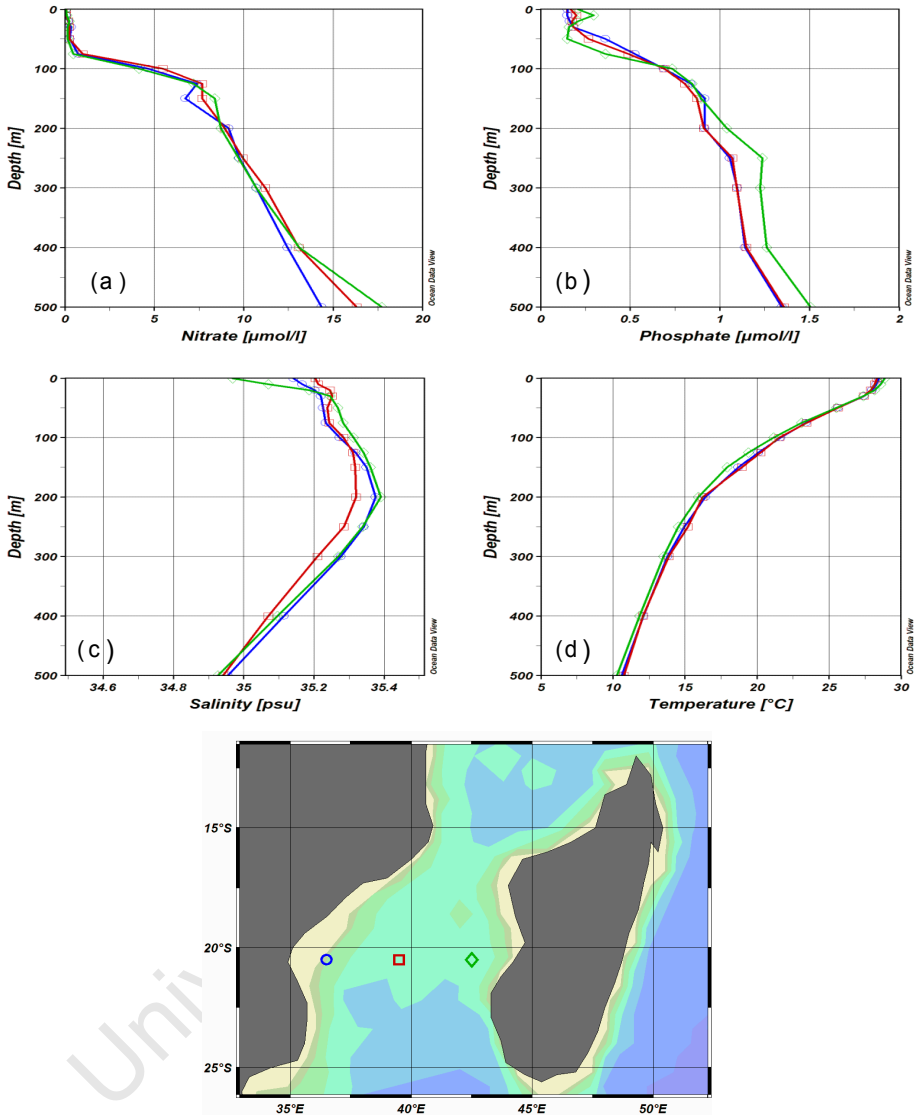

Figure D1.2: Profiles (a) Nitrate, (b) phosphate, (c) salinity and (d) temperature profiles during Jan-Mar from mid Mozambique Channel.

Appendix E: Linear Regression and Mann-Kendall analysis

Appendix E1: Least-Square Linear Regression

Trends in TCs and SST and their statistical significance show in Tables E1.1-E1.7 are assessed using least-squares linear regression (MyRegression function; Cardillo, 2007). This function computes a least-square linear regression supplying several output information. More details for the input/output information is found at http://www.mathworks.com/matlabcentral/fileexchange/15473.

E1.1: Trend in All Cyclone Categories (SWIO)

Slope			
Value	S.E.	95% C.I.	
0.39241	0.49234	-0.62159	1.40640
Intercept			
Value	S.E.	95% C.I.	
56.28691	8.14531	39.51133	73.06248
Pearson's Correlation Coefficient			
Value	95% C.I.		ADJ
0.15742	-0.23676	0.50710	0.12371
Spearman's Correlation Coefficient: 0.1397			
Other Parameters			
R.S.E. Value	Total	Variability by regression	Residual
20.97111	11274.05185	279.36981 (2.5%)	10994.68204 (97.5%)
Student's t-test on slope=0			
t	Critical Value	p	test not passed
0.7970	0.7970	0.4329	slope = 0

E1.2: Trend in Category 3-5 Cyclones (SWIO)

Slope			
Value	S.E.	95% C.I.	
1.20642	0.32326	0.54065	1.87219
Intercept			
Value	S.E.	95% C.I.	
14.9746	5.33463	3.98772	25.96148
Pearson's Correlation Coefficient			
Value	95% C.I.		ADJ
0.59816	0.28231	0.797	0.58208
Spearman's Correlation Coefficient: 0.6168			
Other Parameters			
R.S.E. Value	Total	Variability by regression	Residual
13.73766	7346.64	2628.55451 (35.8%)	4718.08549 (64.2%)
Student's t-test on slope=0			
t	Critical Value	p	test passed
3.7320	2.0595	0.0010	slope ~= 0

E1.3: Trend in Category 1-2 Cyclones (SWIO)

Slope			
Value	S.E.	95% C.I.	
-0.24606	0.21463	-0.68810	0.19597
Intercept			
Value	S.E.	95% C.I.	
21.56937	3.55080	14.25636	28.88237
Pearson's Correlation Coefficient			
Value	95% C.I.		ADJ
-0.22349	-0.55626	0.17105	-0.19243
Spearman's Correlation Coefficient: -0.2407			
Other Parameters			
R.S.E. Value	Total	Variability by regression	Residual
9.14197	2199.24000	109.85125 (5.0%)	2089.38875 (95.0%)
Student's t-test on slope=0			
t	Critical Value	p	test not passed
1.1465	2.0595	0.2625	slope = 0

E1.4: Trend in Category TS Cyclones (SWIO)

Slope			
Value	S.E.	95% C.I.	
-0.36788	0.15548	-0.68878	-0.0469
Intercept			
Value	SE	95% C.I.	
17.24239	2.61454	11.84625	22.63853
Pearson's Correlation Coefficient			
Value	95% C.I.		ADJ
-0.43491	-0.70371	-0.05719	-0.41136
Spearman's Correlation Coefficient: -0.3798			
Other Parameters			
R.S.E. Value	Total	Variability by regression	Residual
6.26068	1160.14038	219.43265 (18.9%)	940.70774 (81.1%)
Student's t-test on slope=0			
t	Critical Value	p	test passed
t = 2.3661	2.0639	0.0264	slope ~= 0

E1.5: Trend in sea surface temperature (MC)

Slope			
Value	S.E.	95% C.I.	
0.01622	0.00576	0.00429	0.02816
Intercept			
Value	SE	95% C.I.	
28.15334	0.08693	27.97306	28.33363
Pearson's Correlation Coefficient			
Value	95% C.I.		ADJ
0.51516	0.14109	0.76051	0.49312
Spearman's Correlation Coefficient: 0.5096			
Other Parameters			
R.S.E. Value	Total	Variability by regression	Residual
0.20449	1.25225	0.33234 (26.5%)	0.91992 (73.5%)
Student's t-test on slope=0			
t	Critical Value	p	test passed
2.8192	2.0739	0.0100	slope ~= 0

E1.6: Trend in sea surface temperature (SWIO)

Slope			
Value	S.E.	95% C.I.	
0.00599	0.00600	-0.00645	0.01842
Intercept			
Value	SE	95% C.I.	
27.71632	0.08883	27.53210	27.90055
Pearson's Correlation Coefficient			
Value	95% C.I.		ADJ
0.20821	-0.21309	0.56422	0.17222
Spearman's Correlation Coefficient: 0.2200			
Other Parameters			
R.S.E. Value	Total	Variability by regression	Residual
0.21538	1.06679	0.04625 (4.3%)	1.02055 (95.7%)
Student's t-test on slope=0			
t	Critical Value	p	test not passed
0.9985	2.0739	0.3289	slope = 0

E1.7: Trend in sea surface temperature (SIO)

Slope			
Value	S.E.	95% C.I.	
0.01031	0.00497	-0.00004	0.02065
Intercept			
Value	SE	95% C.I.	
27.67949	0.07529	27.52292	27.83607
Pearson's Correlation Coefficient			
Value	95% C.I.		ADJ
0.41198	-0.00027	0.70454	0.38398
Spearman's Correlation Coefficient: 0.3725			
Other Parameters			
R.S.E. Value	Total	Variability by regression	Residual
0.16823	0.71578	0.12149 (17.0%)	0.59429 (83.0%)
Student's t-test on slope=0			
t	Critical Value	p	test not passed
2.0719	2.0796	0.0508	slope = 0

Appendix E2: Mann-Kendall Tau (aka Tau-b) with Sen's Method.

The Mann-Kendall test is performed to confirm/evaluate trends in tropical cyclones as detected by least-square regression analysis. This is also done for tropical cyclones of categories as well as for the SST development during the cyclone season (November-April) in the SWIO including the Mozambique Channel. Tropical cyclone data runs from 1980-2007 while SST data is from 1980-2007. Tropical cyclones of Cat 3-5 are chosen to exemplify and confirm the performance of this test. The Mann-Kendall test is a non-parametric test for identifying trends in time series of data. The test compares the relative magnitudes of sample data rather than the data values themselves. For theoretical details see Yue et al. (2002), Sneyers (1990), and Sen (1968).

Appendix E2.1 An example for Mann-Kendall test for Category 3-5 TCs

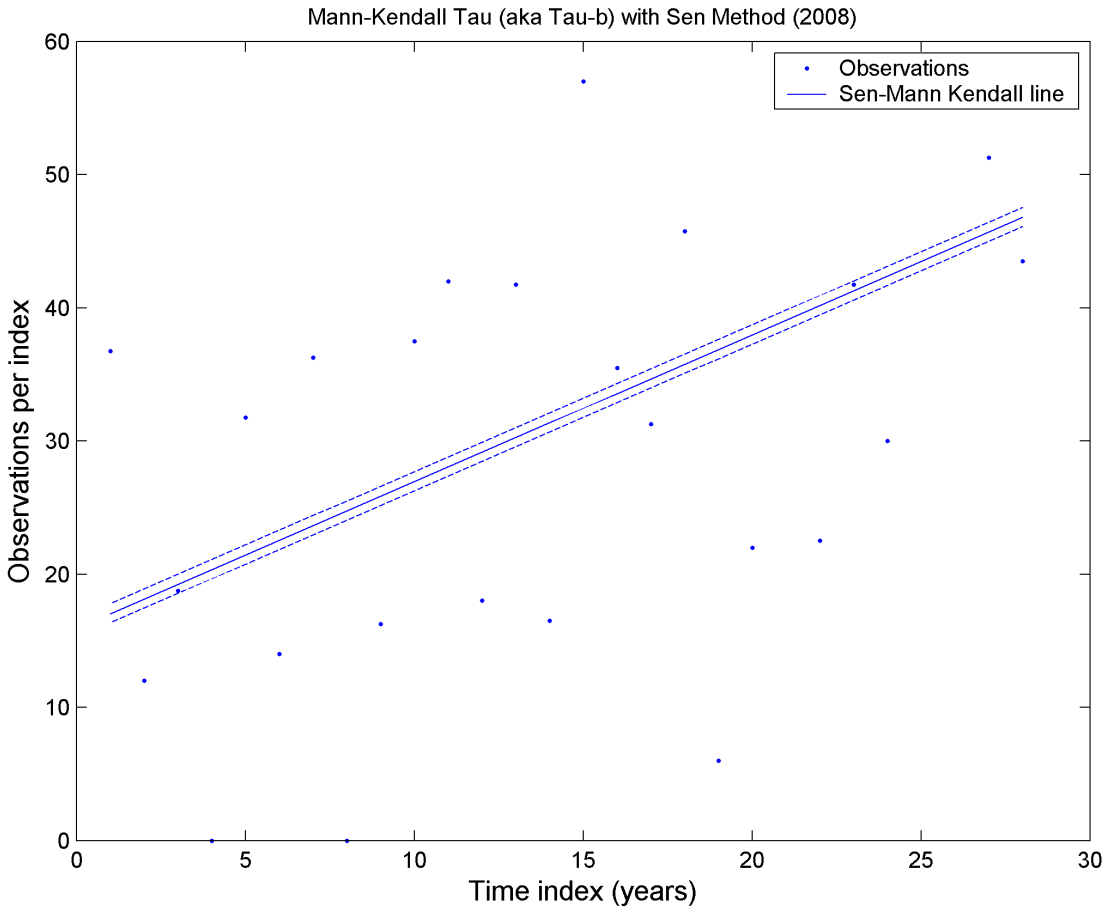

APPENDIX B1: Temporal distribution and characterization of the tropical cyclones (Cont.)

TABLES B1-B16

Temporal distribution

Tropical cyclones + Tropical storms

(South-West Indian Ocean + Mozambique Channel)

Table B1: Tropical cyclone statistics in the South-West Indian Ocean for *1952-1979*

Year	Nov	Dec	Jan	Feb	Mar	Apr	Tot
1952	1	1	4	3	3	2	14
1953	0	2	4	2	3	1	12
1954	0	1	2	0	3	1	7
1955	1	0	1	3	3	0	8
1956	0	1	3	3	3	1	11
1957	0	0	3	2	2	0	7
1958	0	2	3	5	4	1	15
1959	2	1	3	3	3	1	13
1960	2	2	2	1	1	1	9
1961	2	2	3	1	0	0	8
1962	0	2	4	3	3	1	13
1963	0	2	3	5	3	0	13
1964	0	2	2	4	2	1	11
1965	0	6	4	6	1	0	17
1966	0	4	6	3	6	1	20
1967	1	6	1	1	0	2	11
1968	0	2	8	2	2	1	15
1969	0	4	2	4	1	1	12
1970	1	0	4	3	3	0	11
1971	2	2	3	5	2	0	14
1972	0	1	1	6	2	0	10
1973	1	1	6	3	3	1	15
1974	0	2	2	1	0	1	6
1975	0	1	4	3	2	1	11
1976	1	1	2	0	3	2	9
1977	1	1	2	5	0	0	9
1978	1	4	4	2	5	0	16
1979	1	2	2	3	3	2	13
Avg	0.61	1.96	3.14	2.97	2.34	0.79	11.8
# TCs	17	55	88	82	66	22	330

Table B2: Tropical cyclone statistics in the Mozambique Channel for 1952-1979

Year	Nov	Dec	Jan	Feb	Mar	Apr	Tot
1952	1	1	1	0	2	1	6
1953	0	1	2	1	0	0	4
1954	0	1	1	0	2	0	4
1955	0	0	0	0	1	0	1
1956	0	0	2	3	1	1	7
1957	0	0	1	1	1	0	3
1958	0	1	1	2	0	0	4
1959	0	0	2	2	0	0	4
1960	1	1	1	0	1	0	4
1961	0	0	1	0	0	0	1
1962	0	1	1	1	1	0	4
1963	0	0	0	2	0	0	2
1964	0	0	1	1	1	0	3
1965	0	2	2	1	0	0	5
1966	0	1	0	2	0	0	3
1967	0	3	0	0	0	0	3
1968	0	0	3	0	0	0	3
1969	0	1	0	2	0	0	3
1970	1	0	2	0	0	0	3
1971	0	0	1	1	1	0	3
1972	0	1	0	2	1	0	4
1973	0	0	3	1	0	0	4
1974	0	0	1	0	0	1	2
1975	0	1	3	2	0	0	6
1976	0	0	2	0	1	1	4
1977	0	0	1	2	0	0	3
1978	0	0	1	1	0	0	2
1979	0	1	0	1	0	0	2
Avg	0.11	0.57	1.19	1	0.46	0.14	3.5
# TCs	3	16	33	28	13	4	97

Temporal distribution

Category 2 + Category 3

(South-West Indian Ocean+ Mozambique Channel)

Table B7: Category 2 (wind 43-49 ms^{-1}) statistics in the South-West Indian Ocean for 1980-2007

Year	Nov	Dec	Jan	Feb	Mar	Apr	Tot
1980	0	0	1	1	0	0	2
1981	0	0	0	0	0	0	0
1982	0	0	0	0	0	0	0
1983	0	0	0	0	0	0	0
1984	0	1	0	0	0	0	1
1985	0	0	0	0	0	0	0
1986	0	0	0	1	0	0	1
1987	0	0	0	0	0	0	0
1988	0	0	0	2	0	0	2
1989	0	0	1	0	0	0	1
1990	0	0	1	1	0	0	2
1991	0	0	0	1	1	0	2
1992	0	0	0	0	0	0	0
1993	0	0	1	0	0	0	1
1994	0	1	2	0	1	0	4
1995	0	0	0	0	1	0	1
1996	0	0	0	1	0	1	2
1997	0	0	1	1	0	0	2
1998	0	0	0	0	1	0	1
1999	0	0	0	0	0	0	0
2000	0	0	1	0	0	0	1
2001	0	0	0	0	1	1	2
2002	0	0	0	0	0	0	0
2003	0	1	0	0	0	0	1
2004	0	0	0	0	0	0	0
2005	0	0	0	0	0	0	0
2006	0	0	0	0	0	0	0
2007	0	0	0	0	0	0	0
Avg	0	0.11	0.29	0.29	0.18	0.07	0.93
# TCs	0	3	8	8	5	2	26

Table B8: Category 3 (wind 50-58 ms^{-1}) statistics in the South-West Indian Ocean for 1980-2007

Year	Nov	Dec	Jan	Feb	Mar	Apr	Tot
1980	1	1	0	1	1	0	4
1981	0	0	1	0	0	0	1
1982	0	0	0	0	0	1	1
1983	0	0	0	0	0	0	0
1984	0	0	0	1	0	1	2
1985	0	0	0	0	0	1	1
1986	0	0	1	0	2	0	3
1987	0	0	0	0	0	0	0
1988	0	0	0	0	0	0	0
1989	1	0	0	0	0	1	2
1990	0	0	0	0	2	0	2
1991	0	0	0	0	1	0	1
1992	0	1	0	0	0	0	1
1993	0	0	1	0	0	0	1
1994	0	0	0	2	0	1	3
1995	0	0	1	1	0	0	2
1996	0	0	0	0	0	0	0
1997	0	0	0	0	0	0	0
1998	0	0	0	0	0	0	0
1999	0	0	0	0	1	0	1
2000	0	0	0	0	0	0	0
2001	0	0	2	0	0	0	2
2002	0	0	0	0	1	1	2
2003	0	0	0	2	0	0	2
2004	1	0	0	0	0	0	1
2005	0	1	1	0	0	0	2
2006	0	0	1	0	0	0	1
2007	0	0	0	1	1	0	2
Avg	0.11	0.11	0.29	0.29	0.32	0.21	1.32
# TCs	3	3	8	8	9	6	37

Temporal distribution

Category 4 + Category 5

(South-West Indian Ocean+ Mozambique Channel)

Table B9: Category 4 (wind 59-69 ms^{-1}) statistics in the South-West Indian Ocean for 1980-2007

Year	Nov	Dec	Jan	Feb	Mar	Apr	Tot
1980	0	0	0	0	0	0	0
1981	0	0	0	0	0	1	1
1982	0	0	1	0	0	0	1
1983	0	0	0	0	0	0	0
1984	0	1	0	0	0	0	1
1985	0	0	0	0	1	0	1
1986	0	0	0	1	0	0	1
1987	0	0	0	0	0	0	0
1988	0	0	1	0	1	0	2
1989	0	0	1	1	0	0	2
1990	0	1	0	0	1	0	2
1991	0	0	1	0	0	0	1
1992	0	1	0	1	1	1	4
1993	0	0	0	0	0	1	1
1994	0	0	0	0	2	0	2
1995	1	0	0	0	0	1	2
1996	0	0	1	1	0	0	2
1997	1	1	2	0	0	0	4
1998	0	0	0	1	0	0	1
1999	0	0	0	0	0	0	0
2000	0	0	1	1	2	1	5
2001	0	0	1	0	0	0	1
2002	0	0	1	2	0	0	3
2003	0	0	0	1	0	0	1
2004	0	0	0	1	1	0	2
2005	0	0	0	0	0	1	1
2006	1	0	0	1	0	0	2
2007	0	1	0	2	1	0	4
Avg	0.11	0.18	0.36	0.46	0.36	0.21	1.68
# TCs	3	5	10	13	10	6	47

Table B10: Category 5 (wind > 69 ms^{-1}) statistics in the South-West Indian Ocean for 1980-2007

Year	Nov	Dec	Jan	Feb	Mar	Apr	Tot
1980	0	0	0	0	0	0	0
1981	0	0	0	0	0	0	0
1982	0	0	0	0	0	0	0
1983	0	0	0	0	0	0	0
1984	0	0	0	0	0	0	0
1985	0	0	0	0	0	0	0
1986	0	0	0	0	0	0	0
1987	0	0	0	0	0	0	0
1988	0	0	0	0	0	0	0
1989	0	0	0	0	0	0	0
1990	0	0	0	0	0	0	0
1991	0	0	0	0	0	0	0
1992	0	0	0	0	0	0	0
1993	0	0	0	0	0	0	0
1994	0	0	1	0	0	0	1
1995	0	0	0	0	0	0	0
1996	1	0	0	0	0	1	2
1997	0	0	0	0	0	0	0
1998	0	0	0	0	0	0	0
1999	0	0	0	0	0	1	1
2000	0	0	0	0	0	0	0
2001	0	0	0	0	0	0	0
2002	0	0	0	0	1	0	1
2003	0	0	0	0	1	0	1
2004	0	0	0	0	1	0	1
2005	1	0	0	0	0	0	1
2006	0	0	0	0	0	0	0
2007	0	0	0	0	0	0	0
Avg	0.07	0	0.04	0	0.11	0.07	0.29
# TCs	2	0	1	0	3	2	8

Temporal distribution

Tropical storm + Category 1

(Mozambique Channel)

Table B11: Tropical Storm (wind 18-32 ms^{-1}) statistics in the Mozambique Channel for 1980-2007

Year	Nov	Dec	Jan	Feb	Mar	Apr	Tot
1980	0	0	0	0	1	0	1
1981	0	0	1	1	0	0	2
1982	0	0	0	1	0	0	1
1983	0	0	0	0	0	0	0
1984	0	0	1	1	0	0	2
1985	0	0	0	1	0	0	1
1986	0	0	1	0	1	0	2
1987	0	0	0	0	0	0	0
1988	1	0	0	0	0	0	1
1989	0	0	0	0	1	0	1
1990	0	1	0	0	0	1	2
1991	0	0	0	1	0	0	1
1992	0	0	0	0	0	0	0
1993	0	0	1	0	0	0	1
1994	0	0	0	0	0	0	0
1995	0	0	1	0	0	0	1
1996	0	0	0	0	0	0	0
1997	0	0	1	0	0	0	1
1998	0	0	1	2	0	0	3
1999	0	0	0	1	0	0	1
2000	0	1	0	0	0	0	1
2001	0	0	0	0	0	0	0
2002	0	0	1	0	0	0	1
2003	1	1	0	0	0	0	2
2004	0	0	0	0	0	0	0
2005	0	0	1	0	0	0	1
2006	0	0	0	0	0	0	0
2007	0	1	0	0	0	0	1
Avg	0.07	0.14	0.32	0.29	0.11	0.04	0.96
# TCs	2	4	9	8	3	1	27

Table B12: Category 1 (wind 33-42 ms^{-1}) statistics in the Mozambique Channel for 1980-2007

Year	Nov	Dec	Jan	Feb	Mar	Apr	Tot
1980	0	0	0	0	0	0	0
1981	0	0	0	0	0	0	0
1982	0	0	0	0	1	0	1
1983	0	0	1	0	0	0	1
1984	0	0	0	0	0	0	0
1985	0	0	0	0	0	0	0
1986	0	0	0	0	0	0	0
1987	0	0	0	0	0	1	1
1988	0	0	0	0	0	0	0
1989	0	0	1	0	0	0	1
1990	0	0	0	0	0	0	0
1991	0	0	0	0	0	0	0
1992	0	0	0	0	0	0	0
1993	0	0	0	0	0	0	0
1994	0	0	0	0	0	0	0
1995	0	0	0	0	1	0	1
1996	0	0	1	1	0	0	2
1997	0	0	1	1	0	0	2
1998	0	0	0	0	0	0	0
1999	0	0	1	0	0	0	1
2000	0	0	0	0	0	0	0
2001	0	0	0	0	0	0	0
2002	0	0	0	0	0	0	0
2003	0	0	0	0	0	0	0
2004	0	1	1	0	1	0	3
2005	0	0	0	0	0	0	0
2006	0	0	0	0	0	0	0
2007	0	0	0	0	0	0	0
Avg	0	0.04	0.21	0.07	0.11	0.04	0.46
# TCs	0	1	6	2	3	1	13

Temporal distribution

Category 2 + Category 3

(Mozambique Channel)

Table B13: Category 2 (wind 43-49 ms^{-1}) statistics in the Mozambique Channel for 1980-2007

Year	Nov	Dec	Ja	Feb	Mar	Apr	Tot
1980	0	0	0	0	0	0	0
1981	0	0	0	0	0	0	0
1982	0	0	0	0	0	0	0
1983	0	0	0	0	0	0	0
1984	0	0	0	0	0	1	1
1985	0	0	0	0	0	0	0
1986	0	0	0	1	0	0	1
1987	0	0	0	0	0	0	0
1988	0	0	0	1	0	0	1
1989	0	0	0	0	0	0	0
1990	0	0	0	0	0	0	0
1991	0	0	0	1	0	0	1
1992	0	0	0	0	0	0	0
1993	0	0	0	0	0	0	0
1994	0	0	0	0	1	0	1
1995	0	0	0	0	0	0	0
1996	0	0	0	0	0	0	0
1997	0	0	0	1	0	0	1
1998	0	0	0	0	0	0	0
1999	0	0	0	0	0	0	0
2000	0	0	0	0	0	0	0
2001	0	0	0	0	1	0	1
2002	0	0	0	0	0	0	0
2003	0	0	0	0	0	0	0
2004	0	0	0	0	0	0	0
2005	0	0	0	0	0	0	0
2006	0	0	0	0	0	0	0
2007	0	0	0	0	0	0	0
Avg	0	0	0	0.14	0.1	0.04	0.25
#TCs	0	0	0	4	2	1	7

Table B14: Category 3 (wind 50-58 ms^{-1}) statistics in the Mozambique Channel for 1980-2007

Year	Nov	Dec	Jan	Feb	Mar	Apr	Tot
1980	0	0	0	0	0	0	0
1981	0	0	0	0	0	0	0
1982	0	0	0	0	0	0	0
1983	0	0	0	0	0	0	0
1984	0	0	0	0	0	0	0
1985	0	0	0	0	0	0	0
1986	0	0	0	0	0	0	0
1987	0	0	0	0	0	0	0
1988	0	0	0	0	0	0	0
1989	0	0	0	0	0	0	0
1990	0	0	0	0	0	0	0
1991	0	0	0	0	0	0	0
1992	0	0	0	0	0	0	0
1993	0	0	0	0	0	0	0
1994	0	0	0	0	0	0	0
1995	0	0	0	0	0	0	0
1996	0	0	0	0	0	0	0
1997	0	0	0	0	0	0	0
1998	0	0	0	0	0	0	0
1999	0	0	0	0	0	0	0
2000	0	0	0	0	0	1	1
2001	0	0	0	0	0	0	0
2002	0	0	0	0	0	0	0
2003	0	0	0	0	0	0	0
2004	0	0	0	0	0	0	0
2005	0	0	1	0	0	0	1
2006	0	0	1	0	0	0	1
2007	0	0	0	0	0	0	0
Avg	0	0	0.07	0	0	0.04	0.11
# TCs	0	0	2	0	0	1	3

Temporal distribution

Category 4 + Category 5

(Mozambique Channel)

Table B15: Category 4 (wind 59-69 ms^{-1}) statistics in the Mozambique Channel for 1980-2007

Year	Nov	Dec	Jan	Feb	Mar	Apr	Tot
1980	0	0	0	0	0	0	0
1981	0	0	0	0	0	0	0
1982	0	0	0	0	0	0	0
1983	0	0	0	0	0	0	0
1984	0	1	0	0	0	0	1
1985	0	0	0	0	0	0	0
1986	0	0	0	0	0	0	0
1987	0	0	0	0	0	0	0
1988	0	0	1	0	0	0	1
1989	0	0	0	0	0	0	0
1990	0	0	0	0	0	0	0
1991	0	0	0	0	0	0	0
1992	0	0	0	0	0	0	0
1993	0	0	0	0	0	0	0
1994	0	0	0	0	0	0	0
1995	0	0	0	0	0	0	0
1996	0	0	0	0	0	0	0
1997	0	0	0	0	0	0	0
1998	0	0	0	0	0	0	0
1999	0	0	0	0	0	0	0
2000	0	0	0	0	0	1	1
2001	0	0	0	0	0	0	0
2002	0	0	0	0	0	0	0
2003	0	0	0	1	0	0	1
2004	0	0	0	0	0	0	0
2005	0	0	0	0	0	0	0
2006	0	0	0	0	0	0	0
2007	0	1	0	1	0	0	2
Avg	0	0.07	0.04	0.07	0	0.04	0.21
# TCs	0	2	1	2	0	1	6

Table B16: Category 5 (wind > 69 ms^{-1}) statistics in the Mozambique Channel for 1980-2007

Year	Nov	Dec	Ja	Feb	Mar	Ap	Tot
1980	0	0	0	0	0	0	0
1981	0	0	0	0	0	0	0
1982	0	0	0	0	0	0	0
1983	0	0	0	0	0	0	0
1984	0	0	0	0	0	0	0
1985	0	0	0	0	0	0	0
1986	0	0	0	0	0	0	0
1987	0	0	0	0	0	0	0
1988	0	0	0	0	0	0	0
1989	0	0	0	0	0	0	0
1990	0	0	0	0	0	0	0
1991	0	0	0	0	0	0	0
1992	0	0	0	0	0	0	0
1993	0	0	0	0	0	0	0
1994	0	0	0	0	0	0	0
1995	0	0	0	0	0	0	0
1996	0	0	0	0	0	0	0
1997	0	0	0	0	0	0	0
1998	0	0	0	0	0	0	0
1999	0	0	0	0	0	0	0
2000	0	0	0	0	0	0	0
2001	0	0	0	0	0	0	0
2002	0	0	0	0	0	0	0
2003	0	0	0	0	0	0	0
2004	0	0	0	0	0	0	0
2005	0	0	0	0	0	0	0
2006	0	0	0	0	0	0	0
2007	0	0	0	0	0	0	0
Avg	0	0	0	0	0	0	0
# TCs	0	0	0	0	0	0	0